

## **INFORMATION TO USERS**

This manuscript has been reproduced from the microfilm master. UMI films the text directly from the original or copy submitted. Thus, some thesis and dissertation copies are in typewriter face, while others may be from any type of computer printer.

**The quality of this reproduction is dependent upon the quality of the copy submitted.** Broken or indistinct print, colored or poor quality illustrations and photographs, print bleedthrough, substandard margins, and improper alignment can adversely affect reproduction.

In the unlikely event that the author did not send UMI a complete manuscript and there are missing pages, these will be noted. Also, if unauthorized copyright material had to be removed, a note will indicate the deletion.

Oversize materials (e.g., maps, drawings, charts) are reproduced by sectioning the original, beginning at the upper left-hand corner and continuing from left to right in equal sections with small overlaps.

Photographs included in the original manuscript have been reproduced xerographically in this copy. Higher quality 6" x 9" black and white photographic prints are available for any photographs or illustrations appearing in this copy for an additional charge. Contact UMI directly to order.

Bell & Howell Information and Learning  
300 North Zeeb Road, Ann Arbor, MI 48106-1346 USA  
800-521-0600

**UMI<sup>®</sup>**



**Spatiotemporal Stochastic Models for Earth Science  
and Engineering Applications**

**By**

**Xiaochun Luo**

**A Thesis Submitted to the Faculty of Graduate Studies and Research in partial  
fulfillment of the requirement for the Degree of Doctor of Philosophy**

**Department of Mining and Metallurgical Engineering**

**McGill University**

**Montreal, Canada**

**June 1998**

**Copyright © 1998 Xiaochun Luo**



National Library  
of Canada

Acquisitions and  
Bibliographic Services

395 Wellington Street  
Ottawa ON K1A 0N4  
Canada

Bibliothèque nationale  
du Canada

Acquisitions et  
services bibliographiques

395, rue Wellington  
Ottawa ON K1A 0N4  
Canada

*Your file Votre référence*

*Our file Notre référence*

The author has granted a non-exclusive licence allowing the National Library of Canada to reproduce, loan, distribute or sell copies of this thesis in microform, paper or electronic formats.

The author retains ownership of the copyright in this thesis. Neither the thesis nor substantial extracts from it may be printed or otherwise reproduced without the author's permission.

L'auteur a accordé une licence non exclusive permettant à la Bibliothèque nationale du Canada de reproduire, prêter, distribuer ou vendre des copies de cette thèse sous la forme de microfiche/film, de reproduction sur papier ou sur format électronique.

L'auteur conserve la propriété du droit d'auteur qui protège cette thèse. Ni la thèse ni des extraits substantiels de celle-ci ne doivent être imprimés ou autrement reproduits sans son autorisation.

0-612-44665-4

**Canada**

SPATIOTEMPORAL STOCHASTIC MODELS FOR EARTH  
SCIENCE AND ENGINEERING APPLICATIONS

Xiaochun Luo

Ph.D.

1998

To my wife, lovely daughter  
and my parent

## Abstract

Spatiotemporal processes occur in many areas of earth sciences and engineering. However, most of the available theoretical tools and techniques of space-time data processing have been designed to operate exclusively in time or in space, and the importance of spatiotemporal variability was not fully appreciated until recently. To address this problem, a systematic framework of spatiotemporal random field (S/TRF) models for geoscience/engineering applications is presented and developed in this thesis.

The space-time continuity characterization is one of the most important aspects in S/TRF modelling, where the space-time continuity is displayed with experimental spatiotemporal variograms, summarized in terms of space-time continuity hypotheses, and modelled using spatiotemporal variogram functions. Permissible spatiotemporal covariance/variogram models are addressed through permissibility criteria appropriate to spatiotemporal processes.

The estimation of spatiotemporal processes is developed in terms of spatiotemporal kriging techniques. Particular emphasis is given to the singularity analysis of spatiotemporal kriging systems. The impacts of covariance functions, trend forms, and data configurations on the singularity of spatiotemporal kriging systems are discussed. In addition, the tensorial invariance of universal spatiotemporal kriging systems is investigated in terms of the space-time trend.

The conditional simulation of spatiotemporal processes is proposed with the development of the sequential group Gaussian simulation techniques (SGGS), which is actually a series of sequential simulation algorithms associated with different group sizes. The simulation error is analyzed with different covariance models and simulation grids. The simulated annealing technique honoring experimental variograms is also proposed, providing a way of conditional simulation without the covariance model fitting which is prerequisite for most simulation algorithms.

The proposed techniques were first applied for modelling of the pressure system in a carbonate reservoir, and then applied for modelling of springwater contents in the Dyle watershed. The results of these case studies as well as the theory suggest that these techniques are realistic and feasible.

## Résumé

Le processus spatio-temporel se présente dans un grand nombre de domaines des sciences de la terre et de l'ingénierie. Cependant, la plupart des outils théoriques disponibles et des techniques pour traiter les données dans l'espace et le temps ont été établis indépendamment dans le temps ou dans l'espace; l'importance de la variabilité spatio-temporelle n'était pas appréciée jusqu'à maintenant. En ce qui concerne ce problème, un cadre systématique du modèle spatio-temporel aléatoire (S/TRF) pour les applications géoscientifiques et de génie est présenté et aussi développé dans cette thèse.

La caractérisation de la continuité dans l'espace et le temps est l'un des plus importants aspects de la modélisation S/TRF, où la continuité dans l'espace et le temps est démontrée par le variogramme spatio-temporel expérimental. Elle est résumée en terme d'hypothèse de continuité dans l'espace et le temps et, modélisée en utilisant les fonctions du variogramme spatio-temporel. Les modèles permisibles de covariance/variogramme spatio-temporel sont adressés par des critères de permmissibilité appropriés au processus spatio-temporel.

L'estimation du processus spatio-temporel est développée en terme de Krigeage spatio-temporel. Le point clé est l'analyse de singularité du système de Krigeage spatio-temporel. L'influence de la fonction de covariance, de tendances et de configurations des données sur la singularité du système de Krigeage spatio-temporel sont discutés. De plus, l'invariance tensorielle du système de Krigeage spatio-temporel universel est analysée en termes de tendances dans l'espace et le temps.

La simulation conditionnelle du processus spatio-temporel est proposée avec le développement d'une technique de simulation gaussienne en groupe séquentiel (SGGS), qui est actuellement une série de simulations séquentielles associées à des groupes de taille différente. L'erreur de simulation a été analysée avec différents modèles de covariance et grilles de simulation. La technique de détrempe simulée pour reproduire les variogrammes expérimentaux est aussi proposée, donnant ainsi une méthode de simulation conditionnelle sans simuler le modèle covariance qui est une condition préalable pour la plupart des algorithmes de simulation.

Les techniques proposées ci-dessus ont été appliquées à la modélisation du système de pression dans un réservoir au sein de carbonates, puis, elles sont utilisées pour la modélisation du chimisme d'eaux de source dans la région de ligne de partage des eaux de la Dyle. Les résultats des études sur ces exemples ainsi que ceux de la théorie suggèrent que les techniques présentées sont réalistes et faisables.

## Acknowledgments

I would like to express my thanks to all those who helped me to complete this study. In particular, I wish to express my thanks to my supervisor, Professor R. Dimitrakopoulos for his guidance, encouragement and support in every aspect of my life at McGill University, without him I could not have undertaken this work. I wish to thank Professor M.L. Bilodeau for his careful correction of my thesis. I also wish to thank other staff members in the Department of Mining and Metallurgical Engineering at McGill University who made me welcome and had their doors open for discussions.

I wish to thank M. Dagbert for his constructive comments and recommendations on estimation and conditional simulation techniques, B. Noland for providing pressure data and valuable advice on the case study of reservoir pressure modelling, and P. Goovaerts for providing the spring data.

The financial support for this work was provided by the National Science and Engineering Research Council of Canada (OGP0105803), to R. Dimitrakopoulos.

Finally, I wish to thank my wife Ping and my little daughter Kathy for their support in my endeavors, and my parents for their forever encouragement in my life.

## Statement of Originality

Based on the distinct characteristics of spatiotemporal processes in geoscience applications, this research develops a theoretical framework and applicable techniques of spatiotemporal stochastic models with regard to three aspects: the space-time continuity characterization, the estimation of spatiotemporal processes, and the conditional simulation of spatiotemporal processes. The following paragraphs describe the author's original contributions to the development of spatiotemporal stochastic models.

The space-time continuity characterization is established in terms of the space-time continuity description, continuity hypotheses, and covariance/variogram modelling. The permissibility criteria of space-time covariance models are proposed. Two types of permissible covariance functions are introduced for covariance modelling, estimation, and conditional simulation of spatiotemporal processes. The properties of these permissible covariance functions are also analyzed.

The estimation of spatiotemporal processes is developed in terms of space-time kriging techniques. The singularity analysis of space-time kriging is introduced with regards to covariance models, trend models, and data configurations. Many failures of kriging computations in practice can be interpreted using this singularity analysis. In addition, the tensorial invariance of universal spatiotemporal kriging systems is analyzed with space-time trend models, and the result indicates several constraints in the selection of trend models.

The conditional simulation techniques of spatiotemporal processes are developed in terms of sequential group Gaussian simulation (SGGS) and the simulated annealing honoring experimental variograms. After proving that the LU decomposition technique (LUD) is equivalent to the sequential Gaussian simulation technique (SGS) in terms of simulation results, this research proposes the SGGS technique which is a series of sequential simulation algorithms including SGS and LUD. The optimal SGGS is the  $0.5v$ -SGGS whose group size is around half of the neighborhood size  $v$ . The simulation error caused by ignoring farther information during the SGGS implementation is introduced in terms of the screen effect approximation loss and investigated with popular covariance models using different simulation grids. The simulated annealing honoring experimental variograms is proposed, providing a way of generating realizations of spatiotemporal

processes without the covariance or variogram model fitting, which is prerequisite for most simulation algorithms.

# TABLE OF CONTENTS

Abstract.....	i
Résumé .....	ii
Acknowledgments .....	iv
Statement of Originality.....	v
Table of Contents .....	vii
List of Figures .....	xi
List of Tables.....	xiv
List of Symbols.....	xv
<b>Chapter 1</b>	
<b>Research Goal and Objectives .....</b>	<b>1</b>
1.1 Introduction .....	1
1.2 Stochastic Analysis of Spatiotemporal Processes: Problem Definition .....	3
1.3 Spatiotemporal Random Field Models: Problem Statement .....	4
1.4 Goal and Objectives .....	5
1.5 Thesis Outline .....	6
1.6 Basic Definitions .....	7
<b>Chapter 2</b>	
<b>Literature Review.....</b>	<b>10</b>
2.1 Overview .....	10
2.2 Current Stochastic Models of Spatiotemporal Processes.....	10
2.2.1 Averaged Models .....	11
2.2.3 Multivariate Models .....	13
2.2.4 Simple Combination Models.....	14
2.2.5 Moving Space Models.....	15
2.2.6 S/TRF Models.....	16
<b>Chapter 3</b>	
<b>Space-Time Continuity Characterization .....</b>	<b>18</b>
3.1 Introduction.....	18
3.2 Space-Time Continuity Description .....	19

3.3	Space-Time Continuity Hypotheses .....	20
3.4	Spatiotemporal Covariance/Variogram Functions .....	23
3.4.1	Permissibility Criteria.....	23
3.4.2	Two Types of Spatiotemporal Covariance/Variogram Models .....	25
3.4.2.1	Separable models.....	25
3.4.2.2	Joint distance models.....	27
3.4.3	A General Form of Spatiotemporal Covariance/Variogram Models.....	28
3.4.4	The Strictly Positive Definite Property.....	29
<b>Chapter 4</b>		
<b>Estimation of Spatiotemporal Processes .....</b>		<b>31</b>
4.1	Introduction .....	31
4.2	Spatiotemporal Simple Kriging (S/T SK).....	32
4.2.1	Singularity Analysis of S/T SK .....	33
4.2.1.1	Strictly positive definite requirement.....	33
4.2.1.2	The influence of data configurations .....	36
4.3	Spatiotemporal Ordinary Kriging (S/T OK).....	39
4.4	Spatiotemporal Universal Kriging (S/T UK) .....	40
4.4.1	Linear Independence and Tensorial Invariance of Trend Models .....	41
4.4.2	Practical S/T Trend Models.....	46
4.4.3	Singularity Analysis of S/T UK.....	47
4.4.3.1	Singularity Problems in $R^1 \times T$ .....	49
4.4.3.2	A general result in $R^n \times T$ .....	50
4.5	Summary.....	52
<b>Chapter 5</b>		
<b>Conditional Simulation of Spatiotemporal Processes .....</b>		<b>54</b>
5.1	Introduction .....	54
5.1.1	The LU Decomposition Algorithm.....	56
5.1.1.1	Summary of the LU Decomposition Computations .....	57
5.1.2	The Sequential Simulation Techniques.....	60
5.1.2.1	Summary of the SGS Computations.....	61
5.1.2.2	SGS Using the Screen-Effect Approximation.....	62
5.1.2.3	Summary of the SGS Computations Using the SEA.....	63

5.2	Equivalence of the LU Decomposition Algorithm and SGS .....	64
5.3	Sequential Group Gaussian Simulation .....	65
5.3.1	Problem Definition .....	65
5.3.2	Theory .....	66
5.3.3	Summary of the SGGs Computations.....	67
5.3.4	Optimal SGGs in Terms of Group Size .....	69
5.3.5	Implementation Process of SGGs.....	71
5.3.6	The SEA Loss.....	72
5.3.6.1	Assessment of the RSEA loss .....	75
5.3.6.2	Optimal size of neighborhood with required RSEA loss .....	76
5.4	The Simulated Annealing Technique Honoring Experimental Variograms .....	86
5.4.1	Problem Definition .....	86
5.4.2	Simulated Annealing Techniques .....	87
5.4.3	Experimental Variogram Reproduction.....	88
5.4.4	The Implementation Procedure.....	88
5.4.3	An Improvement of Implementation .....	91
5.5	Summary.....	92

## **Chapter 6**

### **Space-Time Modelling of the Pressure System in a Carbonate Reservoir ..... 94**

6.1	Introduction .....	94
6.2	Statistics of Pressure Measurements .....	95
6.3	Spatiotemporal Continuity Characterization of the Reservoir Pressure .....	97
6.4	Space-Time Mapping of the Reservoir Pressure.....	101
6.5	Conditional Simulations of the Reservoir Pressure .....	110
6.6	Pressure Monitoring Scheme .....	118
6.6.1	Implementation Steps .....	119
6.6.2	Computations and Results .....	120
6.7	Summary.....	124

## **Chapter 7**

### **Space-Time Modelling of Springwater Contents ..... 125**

7.1	Introduction .....	125
7.2	Statistics and Space-Time Continuity of Spring Data .....	127

7.3	Recognition of a Space-Time Trend .....	132
7.4	Statistics and Space-Time Continuity of Ion Residuals.....	133
7.5	Space-Time Mapping of Springwater Contents.....	144
7.5.1	Different Trend Models in Subareas.....	144
7.5.2	Mapping Results.....	145
7.6	Conditional Simulations of Ca Residuals.....	149
7.6.1	Conditional Simulations of Ca Residuals Using SGGs.....	149
7.6.2	Conditional Simulations of Ca Residuals Using Simulated Annealing .....	156
7.7	Monitoring Scheme of Ca Concentrations .....	164
7.7.1	Sampling Results.....	164
7.8	Summary.....	167
 <b>Chapter 8</b>		
<b>Conclusions and Recommendations .....</b>		<b>169</b>
8.1	Conclusions.....	169
8.2	Recommendations .....	170
 <b>BIBLIOGRAPHY .....</b>		<b>172</b>

## LIST OF FIGURES

Figure 2.1	Space-Time data measured in specific space-time domains.....	14
Figure 2.2	An example of a moving space model.....	16
Figure 3.1	A space-time data set in $R^2 \times T$ .....	18
Figure 3.2	Parameters in s/t experimental variogram calculation.....	21
Figure 3.3	A plot of experimental spatiotemporal variograms.....	21
Figure 3.4	A plot of s/t anisotropic continuity.....	22
Figure 3.5	The variogram structures at three fixed time intervals.....	23
Figure 3.6	A separable covariance model.....	26
Figure 3.7	A joint distance exponential model.....	28
Figure 4.1	A rectangular configuration in $R^2 \times T$ .....	37
Figure 4.2	A 2-location configuration in $R^1 \times T$ .....	50
Figure 5.1	Overlapped neighborhoods.....	66
Figure 5.2	The ratios between the 0.5v-SGGS and SGS.....	70
Figure 5.3	An inverse-direction combination of internal / external paths.....	72
Figure 5.4	Four neighborhoods with regular grid.....	78
Figure 5.5	Convergence of posterior variance of the spherical model.....	78
Figure 5.6	Convergence of posterior variance of the exponential model.....	78
Figure 5.7	Upper bound of the RSEA loss of the exponential model.....	79
Figure 5.8	Upper bound of the RSEA loss of the spherical model.....	80
Figure 5.9	The RSEA loss of exponential model.....	81
Figure 5.10	The RSEA loss of spherical model for grid ratio=0.01, 0.05, 0.07.....	82
Figure 5.11	The RSEA loss of spherical model for grid ratio=0.10, 0.12, 0.15.....	83
Figure 5.12	The RSEA loss of spherical model for grid ratio=0.20, 0.25, 0.30.....	84
Figure 5.13	The RSEA loss of Gaussian model for grid ratio=0.15, 0.20, 0.25.....	85
Figure 5.14	Three conditions in a swap.....	90
Figure 5.15	Variogram updating involved in swaps.....	92
Figure 6.1	The well locations in the study area.....	95
Figure 6.2	Histogram of the pressure data from production wells.....	96
Figure 6.3	Histogram of the pressure data from injection wells.....	96
Figure 6.4	S/T experimental variogram of pressure data in the E-W direction.....	98
Figure 6.5	S/T experimental variogram of pressure data in the NE 45°.....	98
Figure 6.6	S/T experimental variogram of pressure data in the N-S direction.....	99
Figure 6.7	S/T experimental variogram of pressure data in the SW 45°.....	99
Figure 6.8	The elliptical-shaped directional graph.....	100

Figure 6.9	The spatiotemporal variogram model of the reservoir pressure.....	100
Figure 6.10	S/T mapping of reservoir pressure in first two quarters of 1989 .....	102
Figure 6.11	S/T mapping of reservoir pressure in last two quarters of 1989 .....	103
Figure 6.12	S/T mapping of reservoir pressure in first two quarters of 1990 .....	104
Figure 6.13	S/T mapping of reservoir pressure in last two quarters of 1990 .....	105
Figure 6.14	S/T mapping of reservoir pressure in first two quarters of 1991 .....	106
Figure 6.15	S/T mapping of reservoir pressure in last two quarters of 1991 .....	107
Figure 6.16	S/T mapping of reservoir pressure in first two quarters of 1992 .....	108
Figure 6.17	S/T mapping of reservoir pressure in last two quarters of 1992 .....	109
Figure 6.18	Histograms of two conditional simulations by using SGGS .....	111
Figure 6.19	Experimental variograms of one simulation using SGGS .....	112
Figure 6.20	Experimental variograms of one simulation using SGGS .....	113
Figure 6.21	Conditional simulations at January/April 1990 using SGGS.....	114
Figure 6.22	Conditional simulations at July/October 1990 using SGGS .....	115
Figure 6.23	Conditional simulations at January/April 1990 using SGGS.....	116
Figure 6.24	Conditional simulations at July/October 1990 using SGGS .....	117
Figure 6.25	Two neighborhoods used to estimate the blocks .....	118
Figure 6.26	Average local estimation error vs. space spacing for 1990.....	122
Figure 6.26	Average local estimation error vs. space spacing for 1991.....	123
Figure 7.1	Locations of 68 springs .....	126
Figure 7.2	The histogram of Ca concentrations.....	127
Figure 7.3	The histogram of Cl concentrations .....	128
Figure 7.4	The histogram of NO <sub>3</sub> concentrations .....	128
Figure 7.5	Experimental variograms of Ca concentrations .....	129
Figure 7.6	Experimental variograms of Cl concentrations .....	130
Figure 7.7	Experimental variograms of NO <sub>3</sub> concentrations.....	131
Figure 7.8	The histogram of Ca residuals.....	140
Figure 7.9	The histogram of Cl residuals .....	140
Figure 7.10	The histogram of NO <sub>3</sub> residuals .....	140
Figure 7.11	Experimental variograms of Ca residuals.....	141
Figure 7.12	Experimental variograms of Cl residuals .....	142
Figure 7.13	Experimental variograms of NO <sub>3</sub> residuals.....	143
Figure 7.14	A neighborhood configuration .....	144
Figure 7.15	Space-Time mapping of Ca concentrations from 1980 to 1982.....	146
Figure 7.16	Space-Time mapping of Cl concentrations from 1980 to 1982 .....	147
Figure 7.17	Space-Time mapping of NO <sub>3</sub> concentrations from 1980 to 1982 .....	148

Figure 7.18	Histograms of two conditional simulations of Ca residuals .....	150
Figure 7.19	Omnidirectional variograms of Ca residuals .....	151
Figure 7.20	A conditional simulation of Ca residuals at three time slices .....	152
Figure 7.21	A conditional simulation of Ca residuals at three time slices .....	153
Figure 7.22	A conditional simulation of Ca concentrations at three time slices .....	154
Figure 7.23	A conditional simulation of Ca concentrations at three time slices .....	155
Figure 7.24	Histograms of two conditional simulations of Ca residuals .....	158
Figure 7.25	Space-Omnidirectional variograms of Ca residuals and space- Omnidirectional variograms of two conditional simulations of Ca residuals .....	159
Figure 7.26	A conditional simulation of Ca residuals at three time slices using the simulated annealing .....	160
Figure 7.27	A conditional simulation of Ca residuals at three time slices using the simulated annealing .....	161
Figure 7.28	A conditional simulation of Ca concentrations at three time slices .....	162
Figure 7.29	A conditional simulation of Ca concentrations at three time slices .....	163
Figure 7.30	Average local estimation error vs. spatial spacing (SGGS) .....	166
Figure 7.31	Average local estimation error vs. spatial spacing (simulated annealing) .....	167

## LIST OF TABLES

Table 2.1	Current stochastic models of spatiotemporal processes .....	11
Table 4.1	Practical space-time trend models .....	47
Table 4.2	Neighborhood requirements for S/T trend models .....	52
Table 5.1	Optimal size of the neighborhood for the exponential model.....	77
Table 5.2	Optimal size of the neighborhood for the spherical model.....	77
Table 7.1	The average results of trend-surface analysis for Ca concentrations.....	134
Table 7.2	The average results of trend-surface analysis for Cl concentrations.....	135
Table 7.3	The average results of trend-surface analysis for NO <sub>3</sub> concentrations.....	136
Table 7.4	The coefficients of trend models for Ca concentrations .....	137
Table 7.5	The coefficients of trend models for Cl concentrations .....	138
Table 7.6	The coefficients of trend models for NO <sub>3</sub> concentrations .....	139

## LIST OF SYMBOLS

S/TRF = spatiotemporal random field  
S/T SK = spatiotemporal simple kriging  
S/T OK = spatiotemporal ordinary kriging  
S/T UK = spatiotemporal universal kriging  
SGS = sequential Gaussian simulation  
LUD = triangular decomposition simulation  
SGGS = sequential group Gaussian simulation  
SEA = screen effect approximation  
ALEE = average local estimation error  
 $h$  = spatial distance  
 $\tau$  = temporal interval  
 $v$  = number of data in the neighborhood  
 $\xi$  = order of spatial trend  
 $\zeta$  = order of temporal trend

# Chapter 1

## Research Goal and Objectives

### 1.1 Introduction

Spatiotemporal processes develop simultaneously in space and time. These processes occur in many areas of earth sciences and engineering, such as environmental engineering, the mining industry, petroleum reservoir engineering, geohydrology, renewable energy engineering, and meteorology.

Environmental engineers monitor the concentrations of atmospheric pollutants. These concentrations and their effects depend on meteorological conditions such as precipitation, air turbulence, wind direction and speed, cloud cover, as well as on the sources and the locations of the pollutants. These conditions may vary from location to location, and from time to time. Groundwater pollutant concentrations also show a strong spatiotemporal variation that depends on geological and geographical settings, weather variations, and human activities (e.g., Gilbert, 1987; Switzer, 1988).

In the mining industry, several problems relate to space-time variability. For example, in mining environmental management, environmental contamination, such as acid mine drainage, varies in space and time simultaneously. In rock mechanics, certain parameters such as the stress in a pillar, as well as rock deformations caused by mineral extraction, can change in different locations and in time. In mineral reserve assessment and evaluation, the dollar equivalence of mining blocks in polymetallic deposits varies depending on their spatial locations as well as on market fluctuations.

In petroleum reservoir engineering, reservoir properties may not only be variant in space, as present modelling techniques assume, but also simultaneously variant with production time -- particularly when enhanced oil recovery techniques are applied. For instance, one of the most important dynamic attributes, the reservoir pressure, varies simultaneously in space and in time. Some properties of the reservoir fluids may also change in the space-time domain, such as the oil, gas, and water viscosity, saturation, density, and compressibility.

In geohydrology, rainfall structures are commonly described as spatiotemporal processes -- varying simultaneously with geographical location and time. The head of the water table changes not only spatially but also temporally depending on the variation of groundwater recharge rates (e.g., Zawadzki, 1973; Mejia and Rodriguez-Iturbe, 1974; Rouhani and Wackernagel, 1990).

In renewable energy engineering, the occurrence and intensity of wind are functions that change with respect to space locations and time instances, and solar irradiation changes daily, monthly and yearly, and varies depending on location (e.g., Haslett and Raftery, 1989; Loutfi and Khtira, 1992). Similar situations may also be found in the study of sea waves and tidal energy.

In meteorology, weather observations including temperature, pressure, humidity, wind velocity, and various special elements are made hourly at numerous stations or even more frequently during a time of rapid weather changes. These observations are interpreted in terms of weather systems which are fitted onto a weather map. The spatiotemporal variations of weather parameters are apparent from the change and the movement of these systems on a sequence of weather maps.

Perhaps the most helpful information that can be used in the modelling of spatiotemporal natural processes is a description of how the space-time phenomenon in question was generated. In certain situations, the physical or chemical processes that generated the data set might be known in sufficient detail, therefore, a deterministic model might be adequate.

Unfortunately, very few geoscientific processes are understood well enough to permit the application of deterministic models. Even though we do know the physics or chemistry of many spatiotemporal processes, the variables of interest in geoscientific data sets are typically the end result of a vast number of processes whose complex interactions we are not yet able to describe quantitatively. For the vast majority of geoscientific space-time data sets, we are forced to admit that there is a significant amount of uncertainty about how the phenomenon behaves in the space-time domain. Stochastic analysis of spatiotemporal processes recognizes this fundamental uncertainty and gives us tools for modelling space-time variations in terms of stochastic processes.

## 1.2 Stochastic Analysis of Spatiotemporal Processes: Problem Definition

The development of a method for the stochastic analysis of spatiotemporal processes that is able to model spatiotemporal variations systematically is still in the primitive stages. In some geoscience/engineering fields, an awareness of the problem of stochastic modelling of spatiotemporal variates exists. However, most approaches are simplistic and consider space and time separately.

In geohydrology, methods of analysis either create artificial decomposition of the hydrologic variates of interest -- one in time and one in space -- and study each separately (e.g., Mejia and Rodriguez-Iturbe, 1974), or focus on moving space modelling by accounting for invariant velocities (e.g., Zawadzki, 1973). Other methods of analysis focus on multivariate modelling, in the sense of mutually related spatial variables (e.g., Rouhani and Wackernagel, 1990).

In environmental engineering, the existing stochastic models have been designed to handle different problems. They refer to either specific space-time interaction systems in which the variates are treated at each spatial location as a separate time series (e.g., Gilbert, 1987), or the averaged models which simplify the spatiotemporal variation into averaged spatial variations (e.g., Switzer, 1988).

In renewable energy engineering, the available models either independently investigate temporal variations at different locations in the study of solar irradiation (e.g., Loutfi and Khtira, 1992), or separately estimate spatial variations at different time instances by ignoring temporal dependence, as in the study of wind power resources (e.g., Haslett and Raftery, 1989). In renewable energy engineering, a procedure to describe space-time interactions does not exist.

In petroleum reservoir characterization, there is currently no method of spatiotemporal stochastic analysis. Most available techniques account exclusively for the spatial variation of geological reservoir processes. Also, most current practices in data collection do not account for time.

The reasons for such clearly inadequate analysis of space-time data may be attributed to two facts: (i) most of the available theoretical tools and techniques of space-time data processing have been designed to operate exclusively in time or exclusively in space, and (ii) the importance of spatiotemporal variability in the study of space-time phenomena was not fully appreciated until recently.

### **1.3 Spatiotemporal Random Field Models: Problem Statement**

In order to perform a systematic analysis of space-time data, we will employ the concept of the spatiotemporal random field (S/TRF). Within the framework of the S/TRF model:

- a. Space and time form a combined process having simultaneous and interrelated effects on the evolution of the physical variate represented.
- b. Suitable hypotheses and operational tools assure that the mathematical concept of a S/TRF is compatible with the physics of the variate it describes and, thus, it is applicable in practice.

S/TRF models have not been developed until recently. A general framework of mathematical definitions for S/TRF models was developed by Christakos (1992). However, despite this systematic introduction of some basic notations for S/TRF models, several aspects remain to be developed:

1. Space-Time continuity characterization. Space-Time continuity needs to be described in such a way that the space-time simultaneousness can be characterized. After an appropriate description of space-time continuity, a systematic investigation of space-time continuity in terms of second-order moments needs to be performed, including the development of a reasonable hypotheses of space-time continuity, suitable covariance/variogram models, and permissibility criteria of covariance/variogram models.
2. Spatiotemporal kriging techniques. Spatiotemporal kriging techniques that can handle various space-time covariance/variogram models and space-time drifts need to be developed. Stability analysis of spatiotemporal kriging systems in terms of data configuration also needs to be investigated.

3. Spatiotemporal conditional simulation techniques.
4. Applications of S/TRF models in applied geosciences and engineering.

#### **1.4 Goal and Objectives**

On the strength of the foregoing considerations, the goal of this research project is to develop S/TRF models for earth science and engineering applications. To achieve this goal, the following specific objectives are set:

1. The development of the space-time continuity description by means of spatiotemporal experimental covariances and variograms, and the hypotheses that can reflect and summarize adequately the characteristics of the space-time continuity of the data.
2. The development of the required second-order models of S/TRF that match the hypotheses of the space-time continuity. The permissibility and inference of these models will be emphasized.
3. The development of the spatiotemporal point/block ordinary kriging systems and its singularity analysis, and the implementation of the corresponding computational equivalent.
4. The development of the spatiotemporal point/block universal kriging systems and its singularity analysis, and the implementation of the corresponding computational equivalent.
5. The development of conditional spatiotemporal simulation techniques that may handle large scale simulations, and the simulation algorithms that can reproduce experimental covariance/variogram characteristics.
6. Demonstrate the applicability of spatiotemporal stochastic models in various geoscience and engineering applications.

## 1.5 Thesis Outline

Chapter 2 surveys previous work and developments in spatiotemporal stochastic analysis applied to the geosciences. Six types of spatiotemporal stochastic models are summarized: averaged models, moving trend models, multivariate models, simple combination models, moving space models, and S/TRF models.

Chapter 3 provides the space-time continuity characterization in terms of three aspects: the space-time continuity description, hypotheses, and space-time covariance/variogram models. The space-time continuity description is investigated with spatiotemporal experimental covariance/variograms. The space-time continuity hypotheses are summarized with respect to four aspects. The permissibility criteria of space-time covariance/variogram models are proposed, and two types of permissible covariance models are introduced.

Chapter 4 presents the estimation of spatiotemporal processes in terms of spatiotemporal kriging techniques, along with the singularity analysis of the kriging system with regard to covariance models, trend models, and data configurations. The permissibility of trend models in terms of tensorial invariance is also investigated.

Chapter 5 describes spatiotemporal simulation techniques. After proving that sequential Gaussian simulation (SGS) is equivalent to the LU decomposition algorithm (LUD) in the sense of simulation results, a new simulation technique, called sequential group Gaussian simulation (SGGS), is introduced. The screen-effect error associated with sequential simulation algorithms is analyzed, and optimal grid size under the required error level is discussed. In addition, another new simulation technique, called simulated annealing honoring experimental variograms, is proposed.

A case study of a reservoir pressure system is given in Chapter 6. This case study illustrates the spatiotemporal ordinary kriging technique developed in Chapter 4, and SGGS developed in Chapter 5. The methods of Chapter 3 are applied to characterize the space-time continuity of the reservoir pressure and the fitted covariance model is used in spatiotemporal ordinary kriging to estimate the pressure distribution in the space-time domain. The sampling design is investigated using simulation results generated by SGGS.

A case study of spatiotemporal modelling of springwater contents is given in Chapter 7. It illustrates the spatiotemporal universal kriging technique developed in Chapter 4, SGGs and the simulated annealing technique honoring experimental variograms developed in Chapter 5. The spring data set of  $\text{Ca}^+$ ,  $\text{Cl}^+$ , and  $\text{NO}_3^+$  concentrations are decomposed into the space-time trend components and residuals using trend-surface analysis. The space-time mapping of springwater contents is performed using spatiotemporal universal kriging. The monitoring scheme of springwater contents is investigated using the simulation results generated by both SGGs and simulated annealing.

Chapter 8 contains conclusions and recommendations.

## 1.6 Basic Definitions

The following definition of an ordinary S/TRF, based on Christakos' works (1991, 1992), will be quoted in the following chapters.

The space-time domain can be defined as the Cartesian product  $\mathbb{R}^n \times T$ , with  $(s, t) \in \mathbb{R}^n \times T$  being space-time coordinates, and  $X(s, t)$  being a S/TRF from  $\mathbb{R}^n \times T$  into  $[0, \infty]$ .

An ordinary S/TRF (OS/TRF)  $X(s, t)$  can be defined as the function on the space-time domain  $\mathbb{R}^n \times T$  with values in the Hilbert space  $L_2(\Omega, F, P)$ ; that is,

$$X: \mathbb{R}^n \times T \rightarrow L_2(\Omega, F, P)$$

All OS/TRFs are considered to be continuous in the mean square sense.

The most common type of OS/TRF is the second-order OS/TRF; that is, the analysis will be based on all S/TRFs up to second-order statistical moments assumed to be continuous and finite. More precisely, a second-order OS/TRF  $X(s, t)$  will be characterized by

(1) the spatiotemporal mean value

$$m(s, t) = E[X(s, t)] = E[X(z)] = \int_{-\infty}^{+\infty} \chi dF(\chi) \quad (1.1)$$

where  $F(\chi)$  denotes the probability function of  $X(s, t)$  such that

$$F(\chi) = P\{\chi \leq X(s, t)\} = P\{\chi \leq X(z)\}$$

(2) the spatiotemporal variance

$$\text{Var}\{X(s, t)\} = E\{[X(s, t) - m(s, t)]^2\} = \int_{-\infty}^{+\infty} (\chi - m)^2 dF(\chi) \quad (1.2)$$

(3) the spatiotemporal covariance function

$$\begin{aligned} C(\mathbf{s}, t; \mathbf{s}', t') &= E\{[X(\mathbf{s}, t) - m(\mathbf{s}, t)][X(\mathbf{s}', t') - m(\mathbf{s}', t')]\} \\ &= \int_{-\infty}^{+\infty} \int_{-\infty}^{+\infty} (\chi - m)(\chi' - m') dF(\chi, \chi') \end{aligned} \quad (1.3)$$

(4) the spectral density of the spatiotemporal covariance function

$$S(\boldsymbol{\lambda}, \omega; \boldsymbol{\lambda}', \omega') = \frac{1}{(2\pi)^{-(n+1)/2}} \int_T \int_{R^n} \int_T \int_{R^n} e^{-i(\boldsymbol{\lambda}^T \mathbf{s} + \boldsymbol{\lambda}'^T \mathbf{s}' + \omega t + \omega' t')} C(\mathbf{s}, t; \mathbf{s}', t') d\mathbf{s} dt d\mathbf{s}' dt' \quad (1.4)$$

(5) the spatiotemporal variogram function

$$\gamma(\mathbf{s}, t; \mathbf{s}', t') = \frac{1}{2} E[X(\mathbf{s}, t) - X(\mathbf{s}', t')]^2 = \frac{1}{2} \int_{-\infty}^{+\infty} \int_{-\infty}^{+\infty} (\chi - \chi')^2 dF(\chi, \chi') \quad (1.5)$$

Very often S/TRFs used in applications may be stationary, or are considered locally stationary: An OS/TRF  $X(\mathbf{s}, t)$  will be called stationary in the wide sense if its mean and covariance do not change under a shift of the parameters; that is,

$$m_x(\mathbf{s}, t) = \text{constant} \quad (1.6)$$

and

$$C_x(\mathbf{s}, t; \mathbf{s}', t') = C_x(\mathbf{h}, \tau) \quad (1.7)$$

$$\gamma_x(\mathbf{s}, t; \mathbf{s}', t') = \gamma_x(\mathbf{h}, \tau) \quad (1.8)$$

where  $\mathbf{h} = \mathbf{s} - \mathbf{s}'$ , and  $\tau = t - t'$ . It is easy to show that the covariance and the variogram are related by

$$C_x(\mathbf{h}, \tau) = C_x(\mathbf{0}, 0) - \gamma_x(\mathbf{h}, \tau) \quad (1.9)$$

An OS/TRF  $X(\mathbf{s}, t)$  will be called space-isotropic/time-stationary, if its covariance becomes

$$C(\mathbf{h}, \tau) = C(r, \tau)$$

and

$$\gamma(\mathbf{h}, \tau) = \gamma(r, \tau)$$

where  $r = |\mathbf{h}|$  and  $\lambda = |\boldsymbol{\lambda}|$ .

An OS/TRF  $X(\mathbf{s}, t)$  that does not satisfy Equation 1.6 or 1.7 will be called a nonstationary RF. Very often a nonstationary RF  $X(\mathbf{s}, t)$  may be assumed to have the following form

$$X(\mathbf{s}, t) = Y(\mathbf{s}, t) + m(\mathbf{s}, t) \quad (1.10)$$

where  $Y(\mathbf{s}, t)$  is stationary with a mean of zero and a covariance function  $C_Y(\mathbf{h}, \tau)$ , and  $m(\mathbf{s}, t)$ , called the drift or trend of  $X(\mathbf{s}, t)$ , is a function of the coordinates  $(\mathbf{s}, t) \in R^n \times T$ . The expectation of  $X(\mathbf{s}, t)$  is given by

$$E[X(\mathbf{s}, t)] = m(\mathbf{s}, t)$$

and its covariance function is given by

$$C_x(\mathbf{h}, \tau) = C_y(\mathbf{h}, \tau)$$

This indicates that the covariance function of  $X(\mathbf{s}, t)$  is identical to that of the residual  $Y(\mathbf{s}, t)$ .

## Chapter 2

### Literature Review

#### 2.1 Overview

This chapter reviews previous work and developments in the stochastic analysis of spatiotemporal processes in applied geosciences and engineering. The two main objectives of past attempts were to make models and estimate spatiotemporal variates.

Most applications of the stochastic analysis of spatiotemporal processes in applied geosciences and engineering is focused on two areas: geohydrology and environmental engineering. In geohydrology, the main focus is on the space-time modelling of rainfall related processes, and most research selects separable models that are rather simplistic and easily investigated by available spatial techniques. In environmental engineering, the majority of work focuses on the space-time estimation of pollutant concentrations. To accomplish this task, researchers have employed many techniques including the spatial estimation technique based on time-averaged spatial covariance models, multivariate estimation techniques (cokriging) to interpolate missing data, and intuitively developed estimation techniques based on joint distance spatiotemporal covariance or variogram models, but without permissibility and singularity considerations.

Stochastic spatiotemporal conditional simulations have not yet been developed. Stochastic conditional simulation is a statistical method which, with known data from available control locations, assigns simulated values of the characteristics of interest to a grid of points with the desired density. The simulated variable, while reproducing the known information at the sample locations, also faithfully mimics the variability between sample locations. Stochastic conditional simulation was introduced into geostatistics literature by Journel (1974), and several other developments on spatial conditional simulations have been presented recently (e.g., Verly, 1993; Deutsch, 1992; Issaks, 1991; Dimitrakopoulos, 1990; Journel, 1989; Davis, 1987; Mantoglou, 1987).

#### 2.2 Current Stochastic Models of Spatiotemporal Processes

There are a variety of stochastic models used for modelling spatiotemporal processes in geoscience and engineering applications. In this section, six types of current models are introduced. Despite the fact that these models can not entirely cover the field of

spatiotemporal stochastic modelling, they summarize a general trend of spatiotemporal stochastic analysis in applied geoscience and engineering.

Table 2.1 provides a summary of these models, the details of which are discussed in the rest of this section.

### 2.2.1 Averaged Models

A typical and simple way of traditional spatiotemporal analysis is that of averaged models. Consider the data observed in the space-time domain, at any specific time instance  $t_k$ , the corresponding spatial experimental covariance can be calculated by

$$C^*(\mathbf{h}, t_k) = \frac{1}{N(\mathbf{h}, t_k)} \sum_{i=1}^{N(\mathbf{h}, t_k)} \{ [x(\mathbf{s}_i, t_k) - m_k^*] [x(\mathbf{s}_i + \mathbf{h}, t_k) - m_k^*] \} \quad (2.1)$$

where  $N(\mathbf{h}, t_k)$  denotes the number of data pairs separated by the distance vector  $\mathbf{h}$  at the time instance  $t_k$ , and  $m_k^*$  denotes the mean of available data at  $t_k$ . Furthermore, if one assumes that  $C^*(\mathbf{h}, t_k)$  is approximately invariant over time, the overall spatial experimental covariance can then be achieved by averaging spatial experimental covariances with respect to the time series. Thus, the space-time estimation is simplified to a regular spatial estimation, based on the time-averaged spatial covariance models (e.g., Bilonick, 1983; Switzer, 1988).

In a study of atmospheric acid deposition in the northeastern part of the United States, Egbert and Lettenmaier (1986) introduced a similar consideration. They proposed that a RF in the space-time domain can be expressed by

$$Z_{st}(\mathbf{x}) = W_{st}(\mathbf{x}) + Y_{st}(\mathbf{x}) + M_{st}(\mathbf{x}) \quad (2.2)$$

where  $W_{st}(\mathbf{x})$ ,  $Y_{st}(\mathbf{x})$  and  $M_{st}(\mathbf{x})$  represent week-to-week variations, year-to-year variations, and a long-term mean, respectively. Consequently the spatiotemporal variations become a linear combination of week-averaged spatial variations, year-averaged spatial variations, and long-term-averaged spatial variations, and therefore the covariance model used in the estimation is composed of these three types of averaged spatial covariances.

Averaged models are incompatible with the fact that spatiotemporal variates vary simultaneously in time and in space. Furthermore, space-time continuity is not taken into consideration.

Table 2.1 Current Stochastic Models of Spatiotemporal Processes

<b>Model</b>	<b>Characteristics</b>	<b>Space-time continuity</b>	<b>References</b>
<b>Averaged</b>	no account for temporal variability.	unaccounted	Bilonick (1983), Egbert and Lettenmaier (1986), Switzer (1988).
<b>Moving trend</b>	separately models spatial variations in time series.	unaccounted	Berkowitz et al. (1992).
<b>Multivariate</b>	interpolates missing data by cokriging, based on the interactions between location variables.	partially accounted	Solow and Gorelick (1986), Rouhani and Wackerngel (1990), Rouhani et al. (1997), Goovaerts and Sonnet (1992).
<b>Simple combination</b>	Spatiotemporal variations are simplified into a product or a sum of spatial variations and temporal variations.	simplified	Mejia and Rodriguez-Iturbe (1974), Eynon and Switzer (1983), Bilonick (1985), Rodriguez-Iturbe and Eagleson (1987), Rouhani and Hall (1989).
<b>Moving space</b>	is only suitable for unidirectional variations with a constant velocity.	limited	Zawadzki (1973), Waymire et al. (1984).
<b>S/TRF</b>	systematically studies spatiotemporal variations in the entire space-time domain.	fully accounted	Varmarcke (1983), Bilonick (1987), Christakos (1991, 1992), Buxton and Pate (1993).

### 2.2.2 Moving Trend Models

A moving trend model was proposed by Berkowitz et al. (1992) in the estimation of hydrologic data, by representing the groundwater table as

$$H(x, y, t) = \phi(x, y | \Theta_t) + \varepsilon(x, y, t) \quad (2.3)$$

where  $\varepsilon(x, y, t)$  is white noise,  $\phi(x, y | \Theta_t)$  is a trend function of spatial coordinates with the time-dependent coefficient vector  $\Theta_t$ . When this trend function is linear, we have

$$\phi(x, y | \Theta_t) = \lambda_t + \alpha_t x + \beta_t y \quad (2.4)$$

the coefficient vector  $\Theta_t = (\lambda_t, \alpha_t, \beta_t)$ . This approach is actually a 'moving trend analysis' in the sense that the coefficients of trend analysis vary in time. The estimation at every specific time is achieved by contemporaneous data only, indicating that there is no relation between information in different times. This model does not account for the space-time continuity.

### 2.2.3 Multivariate Models

In order to interpolate missing streamflow data in the space-time domain, Solow and Gorelick (1986) proposed that the temporal variation in each location in space could be regarded as a separate variable, thus  $n$  locations provide  $n$  variables that are mutually related. From this viewpoint spatiotemporal variations are characterized by multivariate fields with  $n$  separate 'location variables', each variates in time. Consequently, co-kriging was used for the space-time estimation.

Rouhani and Wackernagel developed this work by accounting for the impact of different time scales (1990). The cross variogram between the  $i$ th and  $j$ th location variables is expressed as a combination of variograms in different time scales. The variogram at the specific time scale is given by an elementary variogram function, with a coefficient determined through principal component analysis. Similar works can also be seen in Rouhani et al. (1992). Goovaerts and Sonnet (1992) focus on the situation where the sampling is denser in space than in time, so that the spatiotemporal variations are characterized by 'time instance variables' instead of space location variables.

The multivariate model can estimate the spatiotemporal variations at observed space locations or at observed time instances. It, however, fails to model and estimate the spatiotemporal variations in the entire space-time domain. For example, if data is measured at four locations in  $R^1 \times T$ , shown in Figure 2.1(a), or at four time instances,

shown in (b), then the multivariate models can only represent and estimate spatiotemporal variations on lines, Therefore the multivariate models cannot systematically represent space-time continuity.

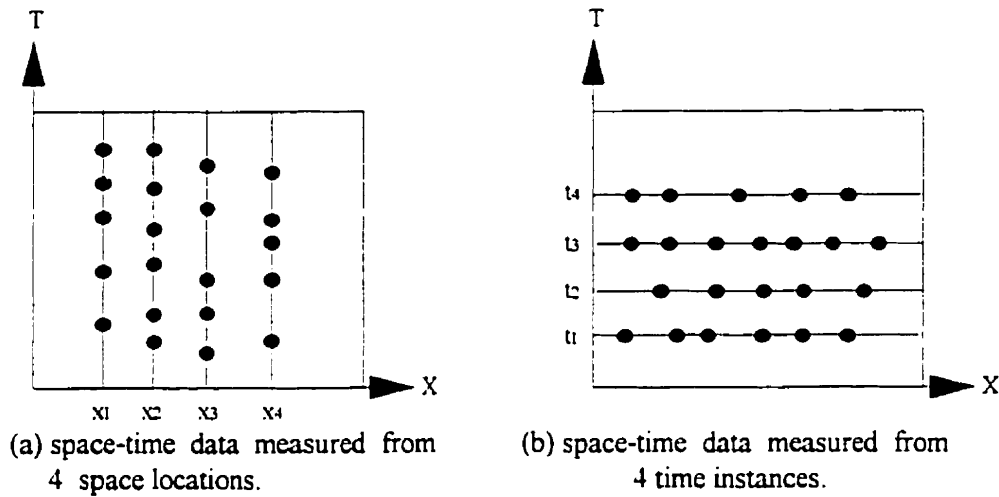


Figure 2.1 Space-time data measured in specific space-time domains (represented by shaded areas) in  $R^1 \times T$ . The Multivariate model cannot model and estimate the variations in the shaded areas except those at 4 space locations in (a) or at 4 time instances in (b).

### 2.2.4 Simple Combination Models

Mejia and Rodriguez-Iturbe (1974), in the study of rainfall networks, proposed that a space-homogeneous/time-stationary RF  $Z(\mathbf{s}, t)$  could be represented as

$$Z(\mathbf{s}, t) = \sum_{i=1}^N X_i(\mathbf{s})Y_i(t) \quad (2.5)$$

where  $X_i(\mathbf{s})$  are spatial random functions, and  $Y_i(t)$  are temporal random functions independent of  $X_i(\mathbf{s})$ . The corresponding covariance function is a separable model

$$C(\mathbf{h}, \tau) = C_s(\mathbf{h})C_t(\tau) \quad (2.6)$$

where  $\mathbf{h}$  denotes a distance vector in space,  $t$  denotes an interval in time, and  $C_s(\mathbf{h})$  and  $C_t(\tau)$  are spatial and temporal covariances, respectively. Similar discussion can also be found in Rodriguez-Iturbe and Eagleson (1987), where the mean of the rainfall intensity process was considered to be a function of time and therefore, a space-homogeneous/time-nonstationary covariance model was used.

Bilonick (1985) in a study of sulfate deposition in the Northeastern United States, proposed that the sum of a spatial covariance and a temporal covariance could represent the spatiotemporal covariance, such that

$$C(\mathbf{h}, \tau) = C_s(\mathbf{h}) + C_t(\tau) \quad (2.7)$$

where  $C_s(\mathbf{h})$  and  $C_t(\tau)$  are spatial and temporal covariances, respectively. This amounts to a decomposition of the spatiotemporal covariance into the sum of independent purely spatial and purely temporal components. Ordinary kriging (OK) and universal kriging (UK) in  $\mathbf{R}^3$  were used for estimations in  $\mathbf{R}^2 \times T$ . Similar work can also be found in Eynon and Switzer (1983). Rouhani and Hall (1989) used the same model in spatiotemporal universal kriging to estimate groundwater data.

Simple combination models reduce spatiotemporal variates to some combination of separate and independent spatial variates (where the time variate can be regarded as a one-dimensional spatial variate). All concepts and methods of spatial random fields can be directly applied to these separable spatiotemporal variates. Separability implies that there is no connection between the correlation structures of the random variation in time and space. In addition, when the model of Equation 2.7 is used in kriging systems, a singularity problem could occur (Dimitrakopoulos and Luo, 1993). The space-time continuity is taken into account as a simple combination of spatial and temporal continuities.

### 2.2.5 Moving Space Models

In the study of rainfall data, Zawadski (1973) suggested that by considering the velocity of the storm system  $U_x$  and  $U_y$ , the space-time domain could be transformed into 'storm space', which is represented by  $(x-U_x t, y-U_y t)$ . The rainfall rate  $R(x, y, t)$  can be rewritten in so called 'storm coordinates'  $x$

$$R(x, y, t) = R(x-U_x t, y-U_y t) \quad (2.8)$$

All the statistical characteristics of the rainfall rates can then be studied in the light of 'storm coordinates'. Both the theory and the techniques of spatial random field are directly applicable to this special type of the space-time domain. This consideration was developed by Bras and Rodriguez-Iturbe (1976), where a spatiotemporal covariance is written as

$$C(x_i, y_i, t'; x_j, y_j, t'') = C \{ (y_j - y_i)^2 + [(x_j + U_x t'') - (x_i + U_x t')]^2 \}^{1/2}$$

where  $U_x$  denotes the average storm velocity in direction  $x$ . Letting  $\Delta x = x_j - x_i$ ,  $\Delta y = y_j - y_i$ , and  $\Delta t = t'' - t'$ , we obtain

$$C(x_i, y_i, t'; x_j, y_j, t'') = C(\Delta x, \Delta y, \Delta t) = C \{ [\Delta y^2 + (\Delta x + U_x \Delta t)^2]^{1/2} \} \quad (2.9)$$

Waymire et. al (1984) introduced a similar but rather complicated way to deal with the rainfall intensity at ground level. The rainfall intensity is regarded as a RF which has the form

$$X(s, t) = \sum X_1(t-t_i)X_2[s-(s_i + U(t-t_i))] \quad (2.10)$$

where  $X_1$  and  $X_2$  are RF and independent,  $s_i$  and  $t_i$  are coordinates of birth center points in a rain band, and  $U$  denotes the velocity. The covariance function, derived from the integration of the joint density of  $X(s, t)$ , is a non-stationary model.

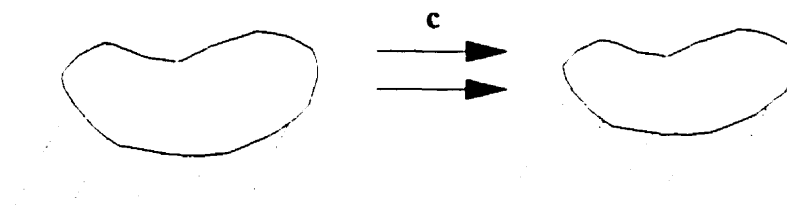


Figure 2.2 An example of a moving space model, a storm moving along one direction with a constant velocity  $c$ .

The key point of moving space models is that spatiotemporal variates are transformed into spatial variates by means of velocities, and the space-time continuity becomes a moving spatial continuity. Moving space models are compatible with unidirectional random processes with constant velocities, a simple example is illustrated in Figure 2.2. Unfortunately, in practice most spatiotemporal processes are neither unidirectional nor have constant velocities. This greatly limits the application of moving space models.

### 2.2.6 S/TRF Models

S/TRF models have not been explicitly mentioned until recently. Varmarcke (1983) discussed space-homogeneous/time-stationary random processes  $X(s, t)$  in terms of second-order analysis, where  $s \in \mathbb{R}^n$  and  $t \in T$ . The space-time covariance function is, by definition, the covariance between two observations at different points  $(s, t)$  and  $(s', t')$

$$C(s, t; s', t') = E[(X(s, t) - m(s, t))(X(s', t') - m(s', t'))] = C_x(\mathbf{h}, \tau)$$

where  $\mathbf{h} = s - s'$ , and  $\tau = t - t'$ . Varmarcke also discussed the exponential covariance models in terms of a 'joint distance structure'

$$C(\mathbf{h}, \tau) = \exp\{-(a^2|\mathbf{h}|^2 + b^2\tau^2)^{1/2}\} \quad (2.11)$$

with the corresponding spectral density

$$S(\lambda, \omega) = S_0[1 + |\lambda|^2/a^2 + \omega^2/b^2]^{-3/2} \quad (2.12)$$

where  $S_0$  is a positive constant, and  $\lambda$  and  $\omega$  denote frequencies with respect to  $\mathbf{h}$  and  $\tau$ , respectively. Finally, he mentioned that a general autoregressive (Markov) spatiotemporal covariance model has the following spectral density

$$S(\lambda, \omega) = S_0[1 + |\lambda|^2/a^2 + \omega^2/b^2]^{-m}, \quad m > 1. \quad (2.13)$$

When  $m = 3/2$  one obtains the exponential model.

Buxton and Pate (1993), in the estimation of hazardous pollutants in the urban air of Atlanta, empirically proposed a spatiotemporal variogram model with zonal anisotropy structures, such that

$$\gamma(\mathbf{h}, \tau) = \gamma_0 + \gamma_s(\mathbf{h}) + \gamma_t(\tau) + \gamma[(a^2|\mathbf{h}|^2 + b^2\tau^2)^{1/2}] \quad (2.14)$$

where  $\gamma_0$  is a positive constant,  $\gamma_s(\mathbf{h})$  and  $\gamma_t(\tau)$  are variogram models in space and time, respectively, and  $\gamma[(a^2|\mathbf{h}|^2 + b^2\tau^2)^{1/2}]$  is a joint distance model in  $\mathbb{R}^n \times T$ . Unfortunately, the permissibility of the selected model in the space-time domain was not taken into consideration. Similar discussions can also be found in Bilonick (1987).

The systematic definition of S/TRF was provided by Christakos (1991, 1992). After giving the definition of the space-time domain as a Cartesian product  $\mathbb{R}^n \times T$  and the definition of the space-time distance  $|(s, t)|^2 = |s|^2 + t^2$ , he proposed the basic definitions of ordinary and generalized S/TRFs, and the fundamental permissibility criteria of spatiotemporal covariance functions. Spatiotemporal estimation techniques were formulated in terms of Wiener-Kolmogorov estimators, and spatiotemporal simulation techniques were mentioned in the light of the turning bands method by rotating  $\mathbb{R}^1 \times T$  simulations into  $\mathbb{R}^n \times T$ .

S/TRF models provide a distinct framework for the systematic characterization of space-time continuity. In accordance with S/TRF theory, space-time phenomena are studied by using stochastic processes that vary simultaneously in space and in time. Under adequate hypotheses, S/TRF models allow us to represent, predict, and simulate spatiotemporal variations in the entire space-time domain.

## Chapter 3

### The Space-Time Continuity Characterization

#### 3.1 Introduction

The space-time continuity is a property that characterizes the relation between data at different places in the space-time domain. Consider two data points  $x(s_a, t_a)$  and  $x(s_b, t_b)$ . Their relation usually depends on the separation  $(s_a - s_b, t_a - t_b)$ . Figure 3.1 shows a simple example where three data points  $x(s_1, t_1)$ ,  $x(s_2, t_2)$ , and  $x(s_3, t_3)$  are mutually separated by  $(h_{12}, \tau_{12})$ ,  $(h_{13}, \tau_{13})$ , and  $(h_{23}, \tau_{23})$ . It is common that the relation between  $x(s_1, t_1)$  and  $x(s_2, t_2)$  may be closer than that between  $x(s_1, t_1)$  and  $x(s_3, t_3)$  since  $h_{12} < h_{13}$  and  $\tau_{12} < \tau_{13}$ .

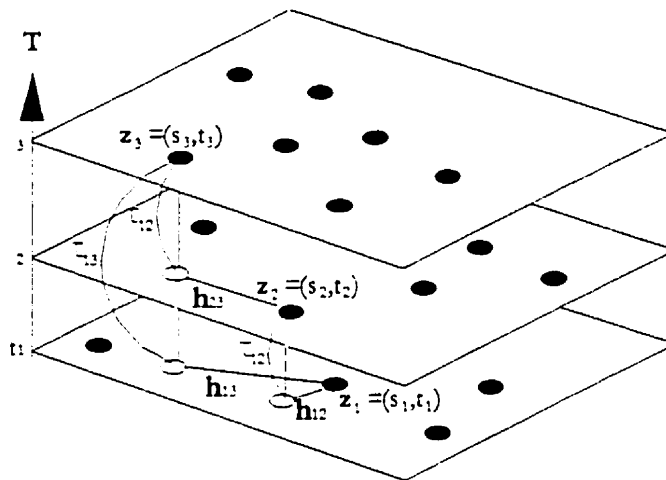


Figure 3.1 A space-time data set in  $R^2 \times T$ .

In general, the space-time continuity characterization includes:

- (a) The description of the space-time continuity along with the experimental covariance or variogram to provide the experimental basis for the hypotheses of the space-time continuity and for fitting of the spatiotemporal covariance/variogram models.
- (b) The investigation of the hypotheses made in modelling the space-time continuity that could reflect and summarize adequately the characteristics of the experimental

covariances or variograms, which provides the foundation of covariance/variogram model fitting.

- (c) The fitting of permissible covariance/variogram models to characterize the space-time continuity of the natural process.

### 3.2 Space-Time Continuity Description

The space-time continuity can be described using various tools. These include data postings where each data location is plotted along with its corresponding data value, contour maps of data values, and h-scatterplots that show all possible pairs of data values whose locations are separated by certain space distances and time intervals in certain directions. Also, the space-time continuity can be appropriately described by the experimental spatiotemporal covariance or variogram.

The experimental spatiotemporal covariance can be expressed as

$$C^*(\mathbf{h}, \tau) = \frac{1}{N_{(\mathbf{h}, \tau)}} \sum_{i=1}^{N_{(\mathbf{h}, \tau)}} \{[x(s_i, t_i) - m^*][x(s_i + \mathbf{h}, t_i + \tau) - m^*]\} \quad (3.1)$$

and the experimental spatiotemporal variogram

$$\gamma^*(\mathbf{h}, \tau) = \frac{1}{2N_{(\mathbf{h}, \tau)}} \sum_{i=1}^{N_{(\mathbf{h}, \tau)}} \{[x(s_i, t_i) - x(s_i + \mathbf{h}, t_i + \tau)]^2\} \quad (3.2)$$

where  $m^*$  denotes the mean of the data and  $N_{(\mathbf{h}, \tau)}$  denotes the number of sample pairs separated by the space distance vector  $\mathbf{h}$  and time interval  $\tau$ .

Figure 3.2 shows the parameters involved in the experimental spatiotemporal covariance or variogram calculation. These parameters include the space lag  $h$  and its tolerance  $dh$ , the specific direction  $v$  and its directional tolerance  $dv$ , the time interval  $\tau$  and its tolerance  $d\tau$ .

To take a specific example, the experimental spatiotemporal variogram of the pressure data measured in a petroleum reservoir is shown in Figure 3.3. The behavior of the experimental variogram at the origin area (Q) shows a good space-time continuity, that is, the space-time continuity of a data pair increases as its separation  $(\mathbf{h}, \tau)$  decreases. The space-time continuity tends to be invariant when the data separation  $(\mathbf{h}, \tau)$  is beyond the

range line, which indicates that two pressure measurements will not be influenced by each other when their separation is large enough. Therefore, the range line may be seen as the influence zone of the pressure measurements. On the space boundary ( $\tau = 0$ ), the influence zone is around one kilometer, implying that two pressure measurements at the same time will not be influenced to each other if their distance is larger than one kilometer. The influence zone (range) changes from the space boundary towards the time boundary ( $h = 0$ ) along the range line, with the time interval increasing but the space distance decreasing, say, (0.8 km, 6 months), (0.6 km, 9 months), and so on. On the time boundary the influence zone is over one year.

Some of the implications of the space-time continuity description in the above example are (1) the space-time continuity can be described by the experimental variogram, in terms of space-time separation ( $h, \tau$ ); (2) the behavior of the experimental variogram around the origin area may indicate the characteristics of the regularity; (3) the behavior of the experimental variogram at large separations may imply the homogeneity of the space-time continuity.

### 3.3 Space-Time Continuity Hypotheses

In order to characterize the space-time continuity of a natural process, it is necessary to propose some hypotheses for the space-time continuity in accordance with the characteristics of the experimental variogram. The study of space-time continuity hypotheses can be imaginatively regarded as the 'bridge' between the experimental variograms and variogram models. It will, on one hand, reflect and summarize the characteristics of the experimental covariances/variograms. On the other hand, it provides the basis for the selection of covariance or variogram models. In general, space-time continuity hypotheses include the following:

- (a) Homogeneity. The homogeneity of the space-time continuity, as we mentioned earlier, may correspond to the existence of the range line. However, a detailed discussion of homogeneity should be based on moving window techniques. It may be possible that the homogeneity only exists in space (or time), indicating a range line parallel to the time boundary (or space boundary). The two parameters used to describe the main features of the homogeneity are the width of the influence zone (range) and the height of the plateau outside the range line (sill).

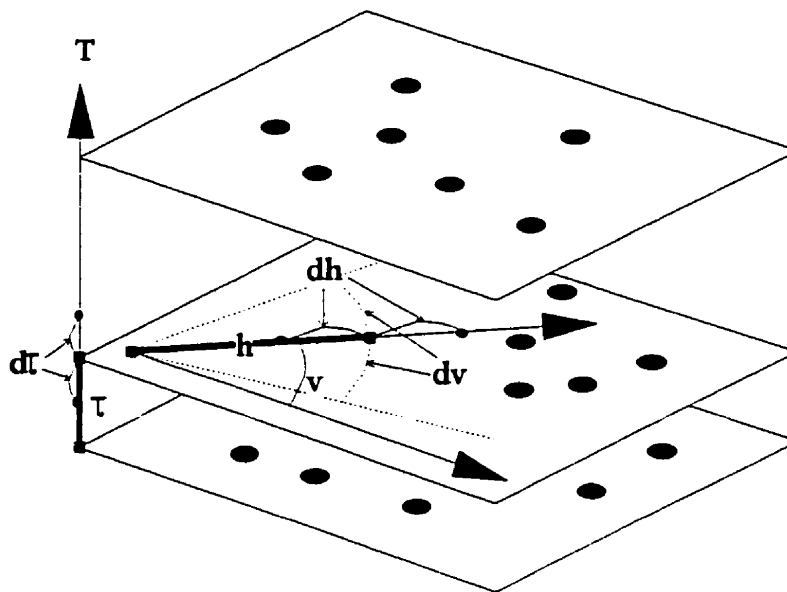


Figure 3.2 An illustration of the parameters used in the experimental spatiotemporal covariance or variogram calculation.

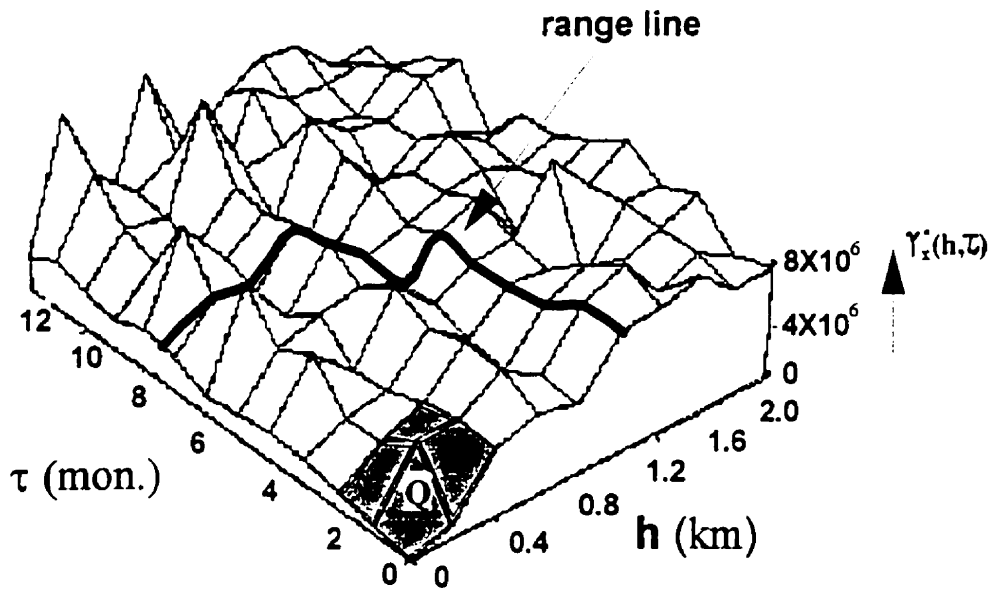


Figure 3.3 Plot of experimental spatiotemporal variograms of the pressure data measured from a petroleum reservoir.

- (b) Anisotropy. The space-time continuity is called 'anisotropic' if it is not the same in different directional space-time surfaces. For example, a specific spatiotemporal anisotropic continuity in  $R^2 \times T$  is shown in Figure 3.4. These three experimental variograms show apparent differences with each other. If the differences only lie in the range lines, then it is possible that these differences can be reduced by a specific linear transformation of the spatial coordinates. An anisotropy that can be reduced to isotropy by a mere linear transformation of the spatial coordinates is called a geometric anisotropy, otherwise it is called a zonal anisotropy.
- (c) Regularity. The behavior of the experimental variogram at the origin area decreases the type of spatiotemporal regularity and continuity. The three popular types of regularity are parabolic, linear, and nugget effect. Nugget effect corresponds to a discontinuity around the origin area of the experimental variogram that may be caused by sampling error and short scale continuity. More precisely, the jump from the value of 0 at the origin to the value of the variogram at extremely small distances is called the nugget effect.

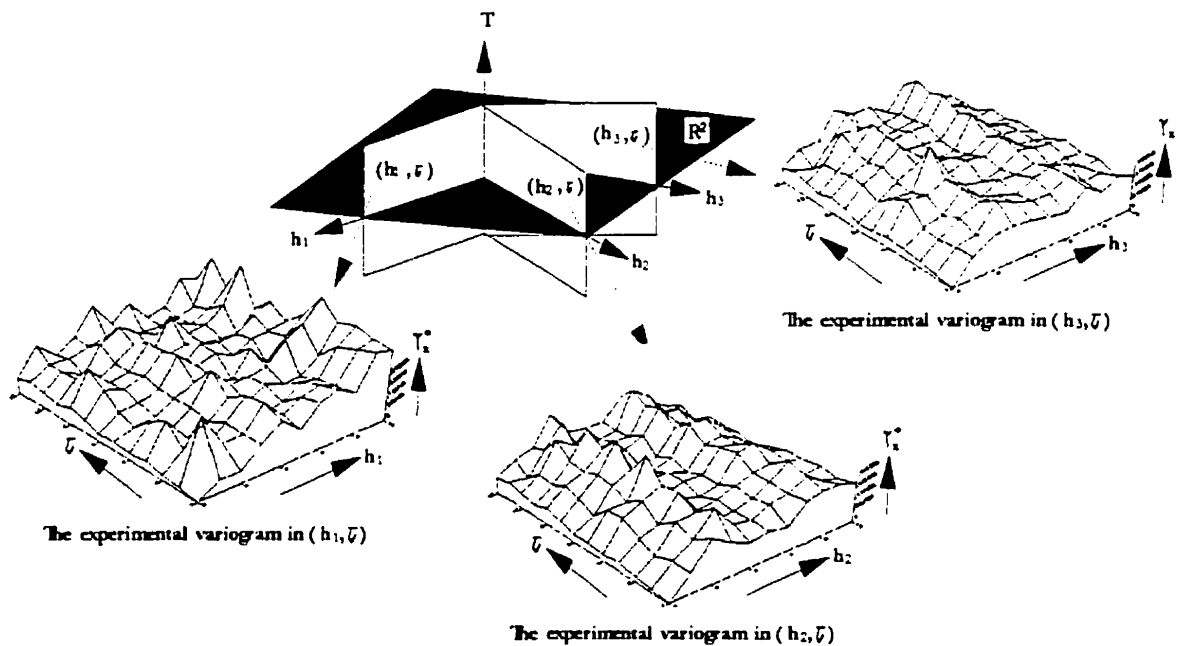


Figure 3.4 A spatiotemporal anisotropic continuity demonstrated by experimental variograms of three directional space-time surfaces  $(h_1, \tau)$ ,  $(h_2, \tau)$ , and  $(h_3, \tau)$ .

- (d) Separability. The plot of the experimental variogram at a specific time interval shows the variogram structure at a fixed time interval. Figure 3.5 shows the experimental variogram structures at three fixed time intervals:  $\tau = 0$ ,  $\tau = 4$ , and  $\tau = 8$ . The differences between these structures are distinct. If the differences between these variogram structures are indistinct, a separability of the space-time continuity may be taken into account, that is, the space-time continuity can be represented by the product of the spatial continuity and the temporal continuity.

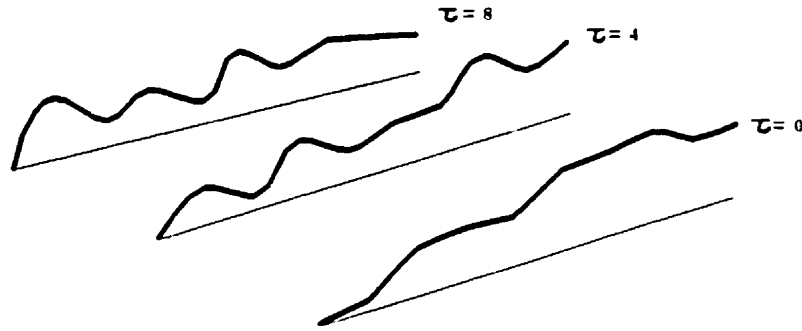


Figure 3.5 The variogram structure at three time intervals, associated with Figure 3.3.

### 3.4 Spatiotemporal Covariance/Variogram Functions

The study of covariance/variogram models is the final stage of the space-time continuity characterization. It also, in most cases, provides the foundation for spatiotemporal stochastic estimations and simulations.

#### 3.4.1 Permissibility Criteria

Covariance/variogram functions must satisfy certain permissibility criteria to ensure nonnegative variances. A continuous function  $C(\mathbf{s}, t; \mathbf{s}', t')$  can be the covariance function of an OS/TRF  $X(\mathbf{s}, t)$  if and only if it satisfies the nonnegative-definiteness condition

$$\sum_{i=1}^N \sum_{j=1}^N a_i a_j C(\mathbf{s}_i, t_i; \mathbf{s}_j, t_j) \geq 0 \quad (3.3)$$

for all integers  $N \geq 1$ , all  $(\mathbf{s}_i, t_i)$  and  $(\mathbf{s}_j, t_j) \in \mathbb{R}^n \times T$ , and all numbers  $a_i, a_j$  (real or complex). This entails that the spatiotemporal permissible covariance function is defined by

$$C(\mathbf{s}, t; \mathbf{s}', t') = \int_T \int_{\mathbb{R}^n} \int_T \int_{\mathbb{R}^n} e^{i(\lambda^T \mathbf{s} + \lambda'^T \mathbf{s}' + \omega t + \omega' t')} S(\lambda, \omega; \lambda', \omega') d\lambda d\omega d\lambda' d\omega' \quad (3.4)$$

where the spectral density  $S(\lambda, \omega; \lambda', \omega')$  is a positive summable function in  $R^n \times T$ . Correlatively, a function  $\gamma(s, t; s', t')$  is permitted to be the variogram function of an OS/TRF  $X(s, t)$  if and only if it satisfies the nonpositive-definite condition

$$\sum_{i=1}^N \sum_{j=1}^N a_i a_j \gamma(s_i, t_i; s'_j, t'_j) \leq 0 \quad \forall \sum_{i=1}^N a_i = 0 \quad (3.5)$$

By definition,  $-\gamma(s, t; s', t')$  is said to be a 'conditional positive definite' function.

A covariance function of a stationary RF is permissible if its corresponding spectral density satisfies the nonnegative condition

$$S(\lambda, \omega) = \frac{1}{(2\pi)^{(n+1)/2}} \int_{R^n} \int_T e^{-i(\lambda^T \mathbf{h} + \omega \tau)} C(\mathbf{h}, \tau) d\mathbf{h} d\tau \geq 0 \quad (3.6)$$

for all  $\lambda$  and  $\omega$ . Consequently, a permissibility criterion of a variogram function,  $\gamma(\mathbf{h}, \tau)$ , is that its auxiliary function

$$C(\mathbf{h}, \tau) = \gamma^{upp} - \gamma(\mathbf{h}, \tau) \quad (3.7)$$

has a spectral density that satisfies Equation 3.6, where the constant  $\gamma^{upp}$  denotes the upper bound of  $\gamma(\mathbf{h}, \tau)$

$$\gamma(\mathbf{h}, \tau) \leq \gamma^{upp}$$

For example, the function  $\gamma(\mathbf{h}, \tau) = 1 - \exp\{-(a^2|\mathbf{h}|^2 + b^2\tau^2)^{1/2}\}$  has the auxiliary function  $\exp\{-(a^2|\mathbf{h}|^2 + b^2\tau^2)^{1/2}\}$  (here  $\gamma^{upp}=1$ ), whose spectral density satisfies Equation 3.6, therefore, it is a permitted variogram function.

A function,  $C(r, \tau)$ , is permitted to be a covariance model of a space-isotropic/time-stationary RF if it can be expressed as follows (Yaglom, 1962; Gandin, 1963),

$$C(r, \tau) = \int_{-\infty}^{+\infty} \int_0^{+\infty} \frac{J_{(n-2)/2}(\lambda r)}{(\lambda r)^{(n-2)/2}} \times \exp[i\omega \tau] \lambda^{n-1} S(\lambda, \omega) d\omega d\lambda \quad (3.8)$$

where  $J_{(n-2)/2}$  is the Bessel function of the first kind of order  $(n-2)/2$ ,  $S(\lambda, \omega) \geq 0$  on the half-plane  $(\lambda, \omega)$ ,  $\lambda \in (-\infty, \infty)$ , and  $\omega \in [0, \infty)$ .

It is worth noting that a permitted covariance/variogram function in a higher dimensional space-time domain is also permissible in a lower dimensional space-time domain, but the opposite is not necessarily true.

Moreover, the following properties are useful for the construction of covariance models:

- (1) every combination of positive definite functions with positive coefficients is also positive definite;
- (2) any product of positive definite functions is also positive definite.

These properties also hold true for conditional nonpositive definite functions.

The following criteria are convenient to check the permissibility of a candidate spatiotemporal variogram function.

*Alternative criterion 1:* If  $\gamma(\mathbf{h}, \tau)$  is a permissible spatiotemporal variogram function, then it should satisfy

$$\lim \frac{\gamma(\mathbf{h}, \tau)}{|\mathbf{h}|^2 + \tau^2} = 0 \quad \text{when } |\mathbf{h}| \rightarrow \infty \text{ and } \tau \rightarrow \infty.$$

*Alternative criterion 2:* If  $\gamma(\mathbf{h}, \tau)$  is a permissible spatiotemporal variogram model, then the function  $\exp[-\alpha\gamma(\mathbf{h}, \tau)]$  must be positive definite for all positive values of  $\alpha$ .

This criterion is a direct expansion from Gelfand and Vilenkin (1964, pp. 279). Consider the following, as an example, in  $\mathbb{R}^2 \times \mathbb{T}$ :

$$\gamma(\mathbf{h}, \tau) = \sqrt{|\mathbf{h}|^2 + \tau^2}$$

it is a permissible variogram model since  $\exp[-\alpha\sqrt{|\mathbf{h}|^2 + \tau^2}]$  is positive definite for all positive values of  $\alpha$ .

### 3.4.2 Two Types of Spatiotemporal Covariance/Variogram Models

#### 3.4.2.1 Separable models

The covariance function  $C(\mathbf{h}, \tau)$  will be called space-time separable if it has the form of Equation 2.6. This entails that its spectral density is also permissible:

$$S(\boldsymbol{\lambda}, \omega) = S_s(\boldsymbol{\lambda})S_t(\omega)$$

The separable model corresponds to the separability hypothesis, its variogram function given by

$$\gamma(\mathbf{h}, \tau) = C_s(\mathbf{0})\gamma_t(\tau) + \gamma_s(\mathbf{h})C_t(0) - \gamma_s(\mathbf{h})\gamma_t(\tau) \quad (3.9)$$

A separable covariance model has the following properties:

(a) The function  $C(\mathbf{h}, 0)$  is called the space boundary function of the covariance model  $C(\mathbf{h}, \tau)$ , which reflects the marginal spatial structure of the spatiotemporal covariance. Similarly,  $C(\mathbf{0}, \tau)$  is called the time boundary function of  $C(\mathbf{h}, \tau)$ , corresponding to the marginal temporal structure of  $C(\mathbf{h}, \tau)$ . Thus, for a separable covariance model, its marginal spatial structure could be different from its marginal temporal structure, as shown in Figure 3.6, where the space boundary curve demonstrates an exponential structure while the time boundary curve shows a periodic structure. This is because the covariance model

$$C(\mathbf{h}, \tau) = C_s(\mathbf{h})C_t(\tau) = \exp(-0.1\mathbf{h})\cos(0.1\tau)$$

has the following space boundary function

$$C(\mathbf{h}, 0) = C_s(\mathbf{h}) = \exp(-0.1\mathbf{h})$$

and time boundary function

$$C(\mathbf{0}, \tau) = C_t(\tau) = \cos(0.1\tau)$$

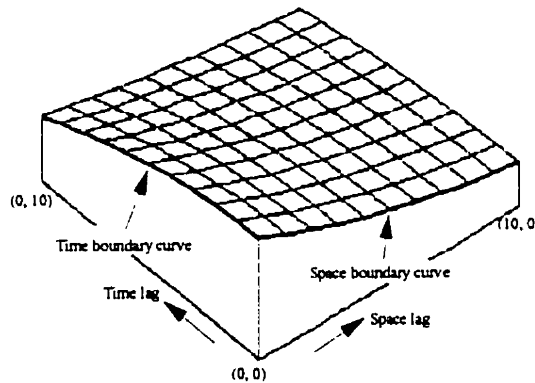


Figure 3.6 A separable covariance model  $C(\mathbf{h}, \tau) = \exp(-0.1\mathbf{h})\cos(0.1\tau)$

(b) The relation between covariances with different fixed space distances or time intervals is proportional; that is,

$$\frac{C(\mathbf{h}_i, \tau)}{C(\mathbf{h}_j, \tau)} = \frac{C_s(\mathbf{h}_i)C_t(\tau)}{C_s(\mathbf{h}_j)C_t(\tau)} = \frac{C_s(\mathbf{h}_i)}{C_s(\mathbf{h}_j)} = \text{constant} \quad \forall \tau \geq 0.$$

where  $\mathbf{h}_i$  and  $\mathbf{h}_j$  are fixed space distances, or

$$\frac{C(\mathbf{h}, \tau_i)}{C(\mathbf{h}, \tau_j)} = \frac{C_s(\mathbf{h})C_t(\tau_i)}{C_s(\mathbf{h})C_t(\tau_j)} = \frac{C_t(\tau_i)}{C_t(\tau_j)} = \text{constant} \quad \forall \mathbf{h} \geq 0.$$

where  $\tau_i$  and  $\tau_j$  are fixed time intervals. This indicates that the spatial structure of the spatiotemporal covariance is invariant with respect to time intervals, and also that the temporal structure of the spatiotemporal covariance is invariant with respect to space distances.

A separable covariance/variogram model is permissible if its spatial component is permissible in space and its temporal component is permissible in time:

$$S(\lambda, \omega) = S_s(\lambda)S_t(\omega) \geq 0$$

Separable models correspond to the subcases of S/TRF where a S/TRF  $X(s, t)$  is considered to be a product of a SRF  $X_s(s)$  and a TRF  $X_t(t)$

$$X(s, t) = X_s(s)X_t(t)$$

where  $X_s(s)$  is independent of  $X_t(t)$ .

### 3.4.2.2 Joint distance models

The covariance  $C(\mathbf{h}, \tau)$  will be called a joint distance model if it is given by

$$C(\mathbf{h}, \tau) = C[(a^2|\mathbf{h}|^2 + b^2\tau^2)^{1/2}] \quad (3.10)$$

where  $|\mathbf{h}|^2 = \mathbf{h}^T\mathbf{h}$ , and  $a$  and  $b$  are the coefficients. For example,  $\exp[-(a^2|\mathbf{h}|^2 + b^2\tau^2)^{1/2}]$  indicates a joint distance exponential model, while  $\exp[-(a^2|\mathbf{h}|^2 + b^2\tau^2)]$  indicates a joint distance Gaussian model. Consequently, the corresponding variogram function is also a joint distance model

$$\gamma(\mathbf{h}, \tau) = C(0, 0) - C[(a^2|\mathbf{h}|^2 + b^2\tau^2)^{1/2}] = \gamma[(a^2|\mathbf{h}|^2 + b^2\tau^2)^{1/2}]$$

It can be shown that a joint distance model is permissible in  $\mathbf{R}^n \times T$  if and only if it is permissible in  $\mathbf{R}^{n+1}$ . For a joint distance covariance function,  $C[(a^2|\mathbf{h}|^2 + b^2\tau^2)^{1/2}]$ , its spectral density is given by

$$S(\lambda, \omega) = S(\lambda_1, \dots, \lambda_n, \omega) = (2\pi)^{-(n+1)/2} \int_{-\infty}^{+\infty} \dots \int_0^{+\infty} C(r^2) \exp[-i(\lambda^T\mathbf{h} + \omega\tau)] d\mathbf{h}_1 \dots d\mathbf{h}_n d\tau$$

where  $\lambda^T\mathbf{h}$  denotes the inner product  $\lambda_1 h_1 + \dots + \lambda_n h_n$ , and  $r^2 = a^2(h_1^2 + h_2^2 + \dots + h_n^2) + b^2\tau^2$ . If one sets  $h'_1 = ah_1, \dots, h'_n = ah_n, h'_{n+1} = b\tau, \lambda'_1 = \lambda_1/a, \dots, \lambda'_n = \lambda_n/a$ , and  $\lambda'_{n+1} = \omega/b$ , then

$$r^2 = h_1^2 + h_2^2 + \dots + h_n^2 + h_{n+1}^2 = r'^2$$

and

$$\lambda^T\mathbf{h} + \omega\tau = \lambda'_1 h'_1 + \dots + \lambda'_n h'_n + \lambda'_{n+1} h'_{n+1} = \lambda'_1 h_1 + \dots + \lambda'_n h_n + \omega\tau = \lambda'^T\mathbf{h}' + \omega\tau$$

Consequently,

$$\begin{aligned} S(\lambda, \omega) &= S(\lambda_1, \dots, \lambda_n, \omega) = S(a\lambda'_1, \dots, a\lambda'_n, b\lambda'_{n+1}) \\ &= (2\pi)^{-(n+1)/2} 2^{-1} a^{-n} b^{-1} \int_{-\infty}^{+\infty} \dots \int_{-\infty}^{+\infty} C(r'^2) \exp[-i(\lambda'^T\mathbf{h}')] d\mathbf{h}'_1 \dots d\mathbf{h}'_n d\mathbf{h}'_{n+1} \end{aligned}$$

If  $C(\mathbf{h}')$  is a nonnegative definite function in  $\mathbf{R}^{n+1}$ , it follows that

$$S(\lambda, \omega) = S(a\lambda', b\lambda'_{n+1}) \geq 0, \text{ for all } \lambda, \omega.$$

A joint distance model corresponds to the following hypothesis. The spatiotemporal covariance has a uniform structure in the entire space-time domain, such as a spherical structure, an exponential structure, etc., which implies that the type of marginal spatial structure is the same as that of the marginal temporal structure. This property is shown in Figure 3.7, where the covariance model is given by

$$C(\mathbf{h}, \tau) = \exp[-(0.05|\mathbf{h}|^2 + 0.07\tau^2)^{1/2}]$$

which follows the space boundary function

$$C(\mathbf{0}, \tau) = \exp[-(0.07\tau^2)^{1/2}]$$

and the time boundary function

$$C(\mathbf{h}, 0) = \exp[-(0.05|\mathbf{h}|^2)^{1/2}]$$

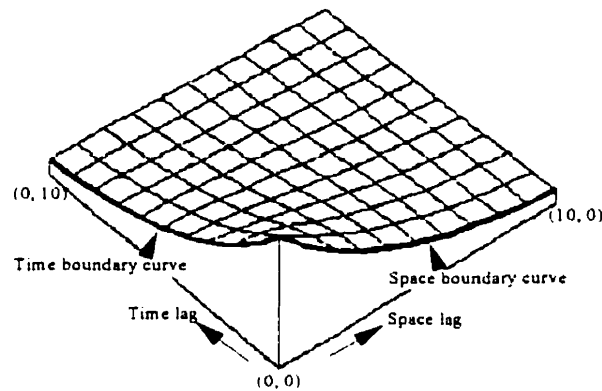


Figure 3.7 A joint distance exponential model  $C(\mathbf{h}, \tau) = \exp[-(0.05|\mathbf{h}|^2 + 0.07\tau^2)^{1/2}]$

### 3.4.3 A General Form of Spatiotemporal Covariance/Variogram Models

Let  $\mathbf{r}^T = (\mathbf{h}, \tau)^T = (h_1, \dots, h_n, \tau)^T$  be the separation vector in  $\mathbb{R}^n \times \mathbb{T}$ , where  $h_j$  denotes the distance in the  $j$ th coordinate ( $j = 1, \dots, n$ ),  $\mathbf{A}_i$  denotes a linear transformation matrix of the vector  $(h_1, \dots, h_n, \tau)^T$ , and the transformed vector  $\mathbf{r}_i^T$  is given by

$$\mathbf{r}_i^T = \mathbf{A}_i \cdot (h_1, \dots, h_n, \tau)^T$$

Thus, every subvector of  $\mathbf{r}^T$ , say,  $(h_1, \dots, h_n, \tau)^T$ ,  $(h_1, \dots, h_{n-1}, \tau)^T$ , ...,  $(h_1), (\tau)$ , corresponds to a specific transformed vector  $\mathbf{r}_i^T$ . Furthermore, if  $C_i(\mathbf{r}_i)$  is used to define the sum of different covariance models in terms of  $\mathbf{r}_i$ ,  $C_i(\mathbf{r}_i)$  can be used to define the sum of separable model and a joint distance model in terms of  $\mathbf{r}_1$  (where  $\mathbf{r}_1 = (h_1, h_2, \tau)$ )

$$C_i(\mathbf{r}_1) = C_i(h_1, h_2, \tau) = \cos(\tau)\exp[-(h_1^2 + h_2^2)^{1/2}] + \exp\{-[a^2(h_1^2 + h_2^2) + b^2\tau^2]\}$$

A general form of a spatiotemporal covariance function can be given by

$$C(\mathbf{h}, \tau) = \sum_{i=1}^K C_i(\mathbf{r}_i) \quad (3.11)$$

The form of Equation 3.11 represents a nested structure of the spatiotemporal covariance  $C(\mathbf{h}, \tau)$ , with the differences among the components  $C_1(\mathbf{r}_1), \dots, C_K(\mathbf{r}_K)$  reflecting zonal anisotropies in different directional space-time surfaces. For example, a general form of a spatiotemporal covariance function in  $R^2 \times T$  can be represented as

$$C(h_x, h_y, \tau) = C_0 + C_1(h_x, h_y, \tau) + C_2(h_x, h_y) + C_3(h_x, \tau) + C_4(h_y, \tau) + C_5(h_x) + C_6(h_y) + C_7(\tau) \quad (3.12)$$

where  $C_0$  is a positive constant, and  $C_1, C_2, \dots, C_7$  are the sums of permissible models in  $(h_x, h_y, \tau), (h_x, h_y), \dots, (\tau)$ , respectively. To take a specific example,  $C_3(h_x, \tau)$  could be given by

$$C_3(h_x, \tau) = \cos(\tau) \exp(-\tau) \exp(-h_x) + \text{Sph}\{-(a^2 h_x^2 + b^2 \tau^2)^{1/2}\}$$

the second term on the right hand side denoting a joint distance spherical model in terms of  $(h_x, \tau)$ .

In practice some components of the right hand side of Equation 3.11 and Equation 3.12 may be missing, indicating that the zonal anisotropies in some directional space-time surfaces may not exist. If, for example, all components of Equation 3.12 are missing except  $C_2(h_x, h_y)$  and  $C_7(\tau)$ , then Equation 3.12 is reduced to Equation 2.7.

All of the above discussion holds true for a general form of spatiotemporal variogram function.

#### 3.4.4 The Strictly Positive Definite Property

A covariance model  $C(\mathbf{h}, \tau)$  is called strictly positive definite if it satisfies

$$\sum_{i=1}^N \sum_{j=1}^N a_i a_j C(\mathbf{h}_{ij}, \tau_{ij}) > 0 \quad (3.13)$$

for all real values  $a_1, \dots, a_N$  (not all zero). Similarly, a variogram model  $\gamma(\mathbf{h}, \tau)$  is called strictly conditional negative definite if it satisfies

$$\sum_{i=1}^N \sum_{j=1}^N a_i a_j \gamma(\mathbf{h}_{ij}, \tau_{ij}) < 0, \quad \forall \sum_{i=1}^N a_i = 0. \quad (3.14)$$

The strictly positive definite property of a covariance model will result in the unique solutions of simple kriging and ordinary kriging systems, as well as the unique solutions of

LUD simulations and SGS. Therefore, the strictly positive definite property is of practical significance in both stochastic estimations and conditional simulations.

Several aspects of the strictly positive definite property are:

- (1) A separable covariance model is strictly positive definite in  $R^n \times T$  if both the spatial component and the temporal component are strictly positive definite in  $R^n$  and  $T$ , respectively;
- (2) A joint distance covariance model is strictly positive definite in  $R^n \times T$  if it is strictly positive definite in  $R^{n+1}$ ;
- (3) If the spatiotemporal covariance  $C(\mathbf{h}, \tau)$  is of a general form as defined by Equation 3.11, then it is strictly positive definite in  $R^n \times T$  if and only if its component in terms of  $(h_1, \dots, h_n, \tau)$  is strictly positive definite in  $R^n \times T$ . For example, if the covariance  $C(\mathbf{h}, \tau)$  is defined by Equation 3.12 in  $R^2 \times T$ , then it is strictly positive definite if and only if  $C_1(h_x, h_y, \tau)$  is strictly positive definite.

A strictly positive definite covariance entails a strictly conditional negative definite variogram,

$$\sum_{i=1}^N \sum_{j=1}^N a_i a_j \gamma(\mathbf{h}_{ij}, \tau_{ij}) = \sum_{i=1}^N \sum_{j=1}^N a_i a_j [C(\mathbf{0}, 0) - C(\mathbf{h}_{ij}, \tau_{ij})] = -\sum_{i=1}^N \sum_{j=1}^N a_i a_j C(\mathbf{h}_{ij}, \tau_{ij}) < 0, \quad \forall \sum_{i=1}^N a_i = 0.$$

Therefore, the above conclusions also hold true for spatiotemporal variograms.

## Chapter 4

### Estimation of Spatiotemporal Processes

#### 4.1 Introduction

The problem of spatiotemporal estimation is to, under specific constraints, find estimates of values at unsampled positions in the space-time domain. This problem may be stated as follows.

Let  $X(\mathbf{s}, t)$  be a S/TRF,  $(\mathbf{s}, t) \in \mathbb{R}^n \times T$ . We wish to find estimates  $\hat{x}(\mathbf{s}_0, t_0)$  of the actual values  $x(\mathbf{s}_0, t_0)$  at unsampled positions  $\{(\mathbf{s}_0, t_0), \nu = 1, \dots, K\}$ , using a set of available measurements  $\{x(\mathbf{s}_i, t_i), i = 1, \dots, N\}$ .

In practice we use a variety of spatial estimation techniques. Of these, the random field estimation methods are generally considered to be the optimum stochastic estimation methods, given the minimum mean square error criterion. The underlying concept behind optimal stochastic estimation was first introduced by Kolmogorov (1941) and Wiener (1949), and was subsequently applied in various fields. The main advantage of the so-called Wiener-Kolmogorov estimators, is that they reproduce the measurements at known data locations and also measure the accuracy of the estimates obtained.

Spatial kriging is a special case of a Wiener-Kolmogorov estimator which provides a linear unbiased estimator of the unknown characteristic with minimum estimation variance (Matheron, 1971; David, 1977; Journel and Huijbregts, 1978). Spatiotemporal kriging techniques will be presented in this chapter as an extension of these spatial kriging techniques.

A spatiotemporal kriging estimate  $\hat{x}(\mathbf{s}_0, t_0)$  has the following properties:

(i) Linearity:

$$\hat{x}(\mathbf{s}_0, t_0) = \sum_{i=1}^N \lambda_i x(\mathbf{s}_i, t_i) \quad (4.1)$$

where  $\lambda_i$  is the coefficient of the observation  $x(\mathbf{s}_i, t_i)$  to be calculated during the estimation process.

(ii) Impartiality:

$$E[\hat{x}(s_u, t_u) - x(s_u, t_u)] = 0 \quad (4.2)$$

(iii) Minimum estimation variance:

$$\sigma_k^2 = \min\{E[\hat{x}(s_u, t_u) - x(s_u, t_u)]^2\} \quad (4.3)$$

This chapter will attempt to develop spatiotemporal kriging systems in terms of spatiotemporal processes, and provide a singularity analysis of spatiotemporal kriging systems with regard to covariance models and data configurations. The impact of trend models on tensorial invariance and on singularities is also discussed in the case of spatiotemporal universal kriging systems.

## 4.2 Spatiotemporal Simple Kriging (S/T SK)

Spatiotemporal simple kriging deals with a space-homogenous/time-stationary RF  $X(s, t)$ , with a known mean. S/T SK considers the following linear estimator

$$\hat{x}(s_u, t_u) = m + \sum_{i=1}^N \lambda_i [x(s_i, t_i) - m] \quad (4.4)$$

Its estimation variance is given by

$$E[\hat{x}(s_u, t_u) - x(s_u, t_u)]^2 = C(0,0) - 2 \sum_{i=1}^N \lambda_i C(\mathbf{h}_{ui}, \tau_{ui}) + \sum_{i=1}^N \sum_{j=1}^N \lambda_i \lambda_j C(\mathbf{h}_{ij}, \tau_{ij})$$

using the Lagrange multiplier method the S/T SK system becomes

$$\sum_{i=1}^N \lambda_i C(\mathbf{h}_{ij}, \tau_{ij}) = C(\mathbf{h}_{uj}, \tau_{uj}), \quad j = 1 \text{ to } N \quad (4.5)$$

and its matrix formula can be given by

$$C\lambda = \theta$$

where  $C$  denotes the covariance matrix,  $\lambda$  denotes the vector of weights, and  $\theta$  denotes the vector of covariances on the right hand side of Equation 4.5. The weights can be obtained by

$$\lambda = C^{-1}\theta \quad (4.6)$$

and the corresponding S/T SK variance is

$$\sigma_{SK}^2(s_u, t_u) = C(\mathbf{h}_{uu}, \tau_{uu}) - \sum_{i=1}^N \lambda_i C(\mathbf{h}_{ui}, \tau_{ui}) \quad (4.7)$$

## 4.2.1 Singularity Analysis of S/T SK

We can easily conclude from Equation 4.6, that S/T SK has a unique solution if and only if the covariance matrix is positive definite, this entails that the covariance function must be strictly positive definite (e.g., Berg et al., 1984).

### 4.2.1.1 Strictly positive definite requirement

A spatiotemporal covariance function  $C(\mathbf{h}, \tau)$  is called strictly positive definite if and only if for all real values  $a_1, a_2, \dots, a_N$ , (which are not all zero),

$$\sum_{i=1}^m \sum_{j=1}^m a_i a_j C(\mathbf{h}_{ij}, \tau_{ij}) > 0 \quad (4.8)$$

where  $\mathbf{h}_{ij} = \mathbf{s}_i - \mathbf{s}_j$  and  $\tau_{ij} = t_i - t_j$ . The strictly positive definite property of a covariance function ensures the absence of singularity problems in the SK process.

For the purposes of the discussion, the spatiotemporal RF under study is assumed to be space-homogeneous/time-stationary with a joint distance covariance function. This discussion is therefore, easily adaptable, as other types of covariance functions can be expressed as a linear combination/production of joint distance covariance functions. Referring to the discussion in Section 3.4.2.2, the positive definite property of covariance functions in  $\mathbb{R}^n \times T$  is equivalent to that of covariance functions in  $\mathbb{R}^{n+1}$ .

A covariance function of a homogeneous RF in  $\mathbb{R}^{n+1}$  can be expressed by its spectral density  $S(\lambda)$

$$C(\mathbf{h}) = \int_{\mathbb{R}^{n+1}} \exp(i\lambda^T \mathbf{h}) S(\lambda) d\lambda \quad (4.9)$$

Putting Equation 4.9 into Equation 4.8 one gets

$$\begin{aligned} \sum_{i=1}^m \sum_{j=1}^m a_i a_j C(\mathbf{h}_{ij}) &= \sum_{i=1}^m \sum_{j=1}^m a_i a_j \int_{\mathbb{R}^{n+1}} \exp(i\lambda^T \mathbf{s}_i) \exp(i\lambda^T \mathbf{s}_j) S(\lambda) d\lambda \\ &= \int_{\mathbb{R}^{n+1}} \left( \sum_{i=1}^m a_i \exp(i\lambda^T \mathbf{s}_i) \right)^2 S(\lambda) d\lambda > 0 \end{aligned} \quad (4.10)$$

$\sum_{i=1}^m a_i \exp(i\lambda^T s_i) \neq 0$  almost everywhere. This indicates that a function  $C(\mathbf{h})$  is strictly positive definite if its spectral density  $S(\lambda)$  is positive with finite zeros (e.g., Berg et al., 1984).

*Example 4.1* The exponential model

$$C(\mathbf{h}) = e^{-a\mathbf{h}}, \quad a > 0 \quad (4.11)$$

has a spectral density in  $\mathbb{R}^5$

$$S(\lambda) = \frac{1}{4\pi^3 a \lambda^2 (a^2 + \lambda^2)^2} (3\lambda^2 + 2a^3 - a^2 + 1) > 0$$

Thus it is strictly positive definite in  $\mathbb{R}^3 \times \mathbb{T}$ .

*Example 4.2* The Gaussian model

$$C(\mathbf{h}) = e^{-a^2 \mathbf{h}^2} \quad (4.12)$$

has a spectral density in  $\mathbb{R}^5$

$$S(\lambda) = \frac{\sqrt{\pi}}{8a^5} (\lambda^2 + 4a^2) e^{-\lambda^2/4a^2} > 0$$

Therefore, it is also strictly positive definite in  $\mathbb{R}^3 \times \mathbb{T}$ .

*Example 4.3* The spherical model

$$C(\mathbf{h}) = \begin{cases} 1 - \frac{3\mathbf{h}}{2a} + \frac{\mathbf{h}^3}{2a^3} & \mathbf{h} \leq a; \\ 0 & \mathbf{h} > a. \end{cases} \quad (4.13)$$

has a spectral density in  $\mathbb{R}^3$

$$S(\lambda) = \frac{3}{2\pi\lambda^6} (\lambda^2 + \lambda^2 \cos \lambda - 4\lambda \sin \lambda - 4 \cos \lambda + 4) > 0$$

Therefore, it is strictly positive definite in  $\mathbb{R}^2 \times \mathbb{T}$ . However, the spherical model is prohibited in  $\mathbb{R}^n$  if  $n > 3$  (e.g., Christakos, 1984), and therefore, cannot be used in  $\mathbb{R}^3 \times \mathbb{T}$ . Instead, the following model is admissible in  $\mathbb{R}^5$  (Matern, 1960)

$$C(\mathbf{h}) = \begin{cases} 1 - \frac{15}{8} \frac{\mathbf{h}}{a} + \frac{5}{4} \frac{\mathbf{h}^3}{a^3} - \frac{3}{8} \frac{\mathbf{h}^5}{a^5} & \mathbf{h} \leq a; \\ 0 & \mathbf{h} > a. \end{cases} \quad (4.14)$$

with a spectral density in  $\mathbb{R}^5$  (Christakos, 1984)

$$S(\lambda) = \lambda^{-5} (J_{5/2}(\lambda))^2$$

where  $J_{5/2}$  is the Bessel function of 5/2th order, therefore, this function is strictly positive definite in  $\mathbb{R}^3 \times T$ .

The following criteria can be used to determine whether a covariance function is strictly positive definite.

**Criterion 4.1** A covariance function is not strictly positive definite if its spectral density is a linear combination of delta functions

$$S(\lambda) = \sum_{k=1}^K b_k \delta(\lambda - c_k) \quad (4.15)$$

where  $b_k$  are positive constants and  $c_k$  are constant vectors, and

$$\delta(\lambda - c_k) = \begin{cases} 1 & \lambda = c_k; \\ 0 & \text{otherwise.} \end{cases}$$

This criterion can be derived directly from Equation 4.10,

$$\begin{aligned} & \frac{1}{(2\pi)^{n+1}} \int_{-\infty}^{\infty} \dots \int_{-\infty}^{\infty} \left( \sum_{i=1}^m a_i \exp(i\lambda^T s_i) \right)^2 S(\lambda) d\lambda \\ &= \frac{1}{(2\pi)^{n+1}} \sum_{k=1}^K b_k \int_{-\infty}^{\infty} \dots \int_{-\infty}^{\infty} \left( \sum_{i=1}^m a_i \exp(i\lambda^T s_i) \right)^2 \delta(\lambda - c_k) d\lambda \\ &= \frac{1}{(2\pi)^{n+1}} \sum_{k=1}^K b_k \left( \sum_{i=1}^m \sum_{j=1}^m a_i a_j \exp(i c_k^T s_i) \right)^2 \end{aligned}$$

Then

$$\sum_{i=1}^m \sum_{j=1}^m a_i a_j C(h_{ij}) = 0 \quad \text{when} \quad \sum_{i=1}^m a_i \exp(i c_k^T s_i) = 0, \quad k = 1, \dots, K.$$

*Example 4.4* A counterpart example is the cosine function  $C(h) = \cos(h)$ , its spectral density in  $\mathbb{R}^1$  is given by

$$S(\lambda) = \frac{1}{4\pi} [\delta(\lambda + 1) + \delta(\lambda - 1)]$$

Therefore, the cosine function is not strictly positive definite.

This criterion is also useful in the discussion of zonal anisotropy structures. A covariance function in  $\mathbb{R}^2 \times T$  can be represented by the general form

$$C(h_x, h_y, \tau) = C_0 + C_1(h_x, h_y, \tau) + C_2(h_x, h_y) + C_3(h_x, \tau) + C_4(h_y, \tau) + C_5(h_x) + C_6(h_y) + C_7(\tau) \quad (4.16)$$

where  $C_0$  is a positive constant, and  $C_1, C_2, \dots, C_7$  are permissible covariance functions in  $R^2 \times T, R^2, R^1 \times T, R^1$  and  $T$ , respectively. The spectral density

$$\begin{aligned} S(\lambda_1, \lambda_2, \omega) &= \frac{1}{(2\pi)^3} \int_{-\infty}^{\infty} \int_{-\infty}^{\infty} \int_0^{\infty} C(h_x, h_y, \tau) \exp[-i(\lambda_1 h_x + \lambda_2 h_y + \omega \tau)] dh_x dh_y d\tau \\ &= S_0 \delta(\lambda_1) \delta(\lambda_2) \delta(\omega) + S_1(\lambda_1, \lambda_2, \omega) + S_2(\lambda_1, \lambda_2) \delta(\omega) + S_3(\lambda_2, \omega) \delta(\lambda_1) \\ &\quad + S_4(\lambda_1, \omega) \delta(\lambda_2) + S_5(\lambda_1) \delta(\lambda_2) \delta(\omega) + S_6(\lambda_2) \delta(\lambda_1) \delta(\omega) + S_7(\omega) \delta(\lambda_1) \delta(\lambda_2) \end{aligned}$$

where  $S_0$  is a positive constant, and  $S_1, \dots, S_7$  are spectral densities of  $C_1, \dots, C_7$ , respectively. Since there is no constraint for functions  $C_1, C_2, \dots, C_7$ , the following is true.

**Criterion 4.2** The covariance function represented by Equation 4.16 is a strictly positive definite function in  $R^2 \times T$  if and only if  $C_1(h_x, h_y, \tau)$  is strictly positive definite in  $R^2 \times T$ .

As for the separable models, it is obvious that the covariance model is strictly positive definite in  $R^n \times T$  if and only if both  $C_s(\mathbf{h})$  and  $C_t(\tau)$  are strictly positive definite in  $R^n$  and  $T$ , respectively.

#### 4.2.1.2 The influence of data configurations

Singularity problems may arise when the covariance function is not strictly positive definite, therefore, covariance functions of this type are undesirable in S/T SK applications.

In some cases, however, a covariance function which is not strictly positive definite is the most appropriate representation of the real data. To avoid singularities in these cases, we need to discuss the influence of data configurations.

Consider the cosine function. The following data configuration in  $R^1$  consists of three observations; at  $x_1, x_2$  and  $x_3$ , separated by the distances:  $|x_1 - x_2| = 2k\pi$  (with any positive integer  $k$ ),  $|x_2 - x_3| = \Delta$ ,  $|x_1 - x_3| = 2k\pi + \Delta$ . Then  $C(|x_1 - x_2|) = 1$ ,  $C(|x_2 - x_3|) = \cos(\Delta) = a$ ,  $C(|x_1 - x_3|) = \cos(2k\pi + \Delta) = a$ , and the kriging matrix

$$\mathbf{K} = \begin{pmatrix} 1 & 1 & a \\ 1 & 1 & a \\ a & a & 1 \end{pmatrix}$$

This matrix is singular because the first two rows are identical. Furthermore, note that regardless of the amount of data added to the configuration, the kriging matrix remains singular. This leads us to our next criterion.

**Criterion 4.3** For the covariance function  $\cos(h)$  in  $R^1$ , the simple kriging system will be singular if there are two samples among the data that are separated by a distance of  $2k\pi$ .

Interesting results are also obtained from the zonal anisotropy structure of Equation 4.16. Consider the case in which Equation 4.16 reduces to the following purely zonal anisotropy structure

$$C(\mathbf{h}, \tau) = C_2(h_x, h_y) + C_7(\tau) \quad (4.17)$$

Given four samples at the four corners of a 'rectangle':  $(x_1, y_1, t_1)$ ,  $(x_1, y_1, t_2)$ ,  $(x_2, y_2, t_1)$ ,  $(x_2, y_2, t_2)$ , as shown in Figure 4.1, the covariance terms are

$$C(\mathbf{h}_{11}, \tau_{11}) = C(\mathbf{h}_{22}, \tau_{22}) = C(\mathbf{h}_{33}, \tau_{33}) = C(\mathbf{h}_{44}, \tau_{44}) = C_2(0, 0) + C_7(0)$$

$$C(\mathbf{h}_{12}, \tau_{12}) = C_2(0, 0) + C_7(|t_2 - t_1|)$$

$$C(\mathbf{h}_{13}, \tau_{13}) = C_2(|x_2 - x_1|, |y_2 - y_1|) + C_7(0)$$

$$C(\mathbf{h}_{14}, \tau_{14}) = C_2(|x_2 - x_1|, |y_2 - y_1|) + C_7(|t_2 - t_1|)$$

$$C(\mathbf{h}_{23}, \tau_{23}) = C_2(|x_2 - x_1|, |y_2 - y_1|) + C_7(|t_2 - t_1|)$$

$$C(\mathbf{h}_{24}, \tau_{24}) = C_2(|x_2 - x_1|, |y_2 - y_1|) + C_7(0)$$

$$C(\mathbf{h}_{34}, \tau_{34}) = C_2(0, 0) + C_7(|t_2 - t_1|)$$

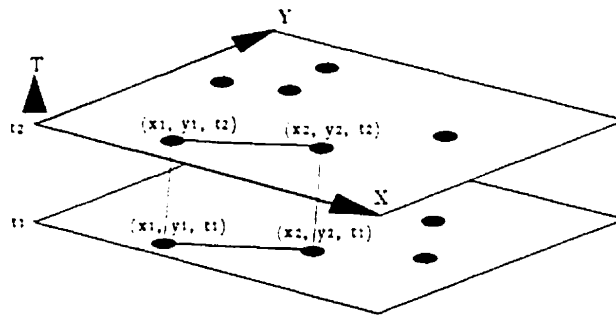


Figure 4.1 A rectangular configuration in  $R^2 \times T$ .

Setting  $a = C_2(|x_2 - x_1|, |y_2 - y_1|)$ ,  $b = C_7(|t_2 - t_1|)$ ,  $c = C_2(0, 0)$ , and  $d = C_7(0)$ , the kriging matrix is

$$\mathbf{K} = \begin{pmatrix} c+d & b+c & a+d & a+b \\ b+c & c+d & a+b & a+d \\ a+d & a+b & c+d & b+c \\ a+b & a+d & b+c & c+d \end{pmatrix}$$

Since the sum of rows one and four is the same as the sum of rows two and three, the matrix is singular. Furthermore, if one adds another sample at  $(x_5, y_5, t_5)$ , then we get the following

$$C(\mathbf{h}_{15}, \tau_{15}) = C_5(|x_5 - x_1|, |y_5 - y_1|) + C_7(|t_5 - t_1|)$$

$$C(\mathbf{h}_{25}, \tau_{25}) = C_5(|x_5 - x_1|, |y_5 - y_1|) + C_7(|t_5 - t_2|)$$

$$C(\mathbf{h}_{35}, \tau_{35}) = C_5(|x_5 - x_1|, |y_5 - y_1|) + C_7(|t_5 - t_1|)$$

$$C(\mathbf{h}_{45}, \tau_{45}) = C_5(|x_5 - x_1|, |y_5 - y_1|) + C_7(|t_5 - t_2|)$$

$$C(\mathbf{h}_{55}, \tau_{55}) = C_5(0, 0) + C_7(0)$$

and the matrix  $\mathbf{K}$  increases an extra column/row  $(C(\mathbf{h}_{15}, \tau_{15}), C(\mathbf{h}_{25}, \tau_{25}), C(\mathbf{h}_{35}, \tau_{35}), C(\mathbf{h}_{45}, \tau_{45}), c+d)^T$ . Since

$$C(\mathbf{h}_{15}, \tau_{15}) + C(\mathbf{h}_{45}, \tau_{45}) = C(\mathbf{h}_{25}, \tau_{25}) + C(\mathbf{h}_{35}, \tau_{35})$$

the matrix  $\mathbf{K}$  remains singular. This demonstrates that when the model 4.17 is chosen as the covariance function, the SK system will be singular as long as there are four samples among the data whose configuration is 'rectangular' in  $\mathbb{R}^2 \times T$ .

The aforementioned four data observations forming a 'rectangular' pattern represent a common case in many types of data sets. For example, this can occur in the case of two monitoring stations measuring the concentration of pollutants at the same time instant, or occur in the case of measuring the reservoir pressure at two wells taken on the same day, etc..

Note that  $C_2(h_x, h_y)$  and  $C_7(\tau)$  are not specified in this discussion, they can be any kind of covariance functions in  $\mathbb{R}^2$  and  $T$ . For example,  $C_2(h_x, h_y)$  may be the exponential function in  $\mathbb{R}^2$  and  $C_7(\tau)$  may be the spherical model in  $T$ , and thus strictly positive definite in  $\mathbb{R}^2$  and  $T$ . However, the linear combination of these functions is not strictly positive definite in  $\mathbb{R}^2 \times T$ , as discussed in Section 4.1.2.1. This indicates that the purely zonal anisotropy structure has a high risk of singularity in the SK process.

Analogous results are obtained for the general form in  $\mathbb{R}^3 \times T$ . Furthermore, the risk of singularity increases with the number of dimensions. Indeed since  $\mathbb{R}^2 \times T$  is only a sub-case of  $\mathbb{R}^3 \times T$ , any singular case occurring in  $\mathbb{R}^2 \times T$  will arise in  $\mathbb{R}^3 \times T$ .

### 4.3 Spatiotemporal Ordinary Kriging (S/T OK)

Spatiotemporal ordinary kriging deals with a space-homogenous/time-stationary RF  $X(\mathbf{s}, t)$ , with a constant but unknown mean  $\mu$ . Either the covariance or variogram function of  $X(\mathbf{s}, t)$  is known.

The S/T OK estimator is given by

$$\hat{x}(\mathbf{s}_0, t_0) = \sum_{i=1}^N \lambda_i x(\mathbf{s}_i, t_i)$$

To ensure the unbiased condition, the weights must satisfy  $\sum_{i=1}^N \lambda_i = 1$ . The spatiotemporal ordinary kriging system is given by

$$\begin{cases} \sum_{i=1}^N \lambda_i C(\mathbf{h}_{ij}, \tau_{ij}) - \mu = C(\mathbf{h}_{0j}, \tau_{0j}); j = 1 \text{ to } N \\ \sum_{i=1}^N \lambda_i = 1 \end{cases} \quad (4.18)$$

The corresponding matrix form is

$$\mathbf{K}\boldsymbol{\beta} = \boldsymbol{\Theta}$$

where  $\boldsymbol{\beta}$  denotes the vector of weights:  $\boldsymbol{\beta}^T = (\boldsymbol{\lambda}^T, \mu)$ ,  $\boldsymbol{\Theta}$  denotes the vector on the right hand side of Equation 4.18:  $\boldsymbol{\Theta}^T = (\boldsymbol{\theta}^T, 1)$ ,  $\mathbf{K}$  denotes the ordinary kriging matrix

$$\mathbf{K} = \begin{pmatrix} \mathbf{C} & \mathbf{1} \\ \mathbf{1}^T & 0 \end{pmatrix} \quad (4.19)$$

where  $\mathbf{1}$  denotes the vector with elements 1, and  $\mathbf{C}$  is the covariance matrix mentioned in SK. Obviously, the vector of weights,  $\boldsymbol{\beta}$ , is obtained from

$$\boldsymbol{\beta} = \mathbf{K}^{-1}\boldsymbol{\Theta} \quad (4.20)$$

The ordinary kriging variance can then be written as

$$\sigma_{OK}^2(\mathbf{s}_0, t_0) = C(\mathbf{0}, 0) + \mu - \sum_{i=1}^N \lambda_i C(\mathbf{h}_{0i}, \tau_{0i}) \quad (4.21)$$

Note that the above kriging system is S/T point OK dealing with estimation at a position rather than a block in the space-time domain. S/T block OK can be derived from Equation 4.18 by changing point-to-point covariances  $C(\mathbf{h}_{0j}, \tau_{0j})$  to point-to-block covariances  $\tilde{C}(\mathbf{h}_{A0j}, \tau_{A0j})$ , thereby obtaining

$$\begin{cases} \sum_{i=1}^N \lambda_i C(\mathbf{h}_{ij}, \tau_{ij}) - \mu = \tilde{C}(\mathbf{h}_{A_{0j}}, \tau_{A_{0j}}); j = 1 \text{ to } N \\ \sum_{i=1}^N \lambda_i = 1 \end{cases}$$

where  $A_{0j}$  denotes the grid block to be estimated, and  $\tilde{C}(\mathbf{h}_{A_{0j}}, \tau_{A_{0j}})$  is the average value of the point-to-point covariances between the sample  $z(s_j, t_j)$  and the discrete points within the grid block  $A_{0j}$ .

Equation 4.20 indicates that a S/T OK system has a unique solution if and only if the OK matrix,  $\mathbf{K}$ , is not singular. Furthermore, it is easy to show that the OK matrix is not singular if the covariance matrix is positive definite:

$$|\mathbf{K}| = |\mathbf{C}| \cdot |0 - \mathbf{1}'\mathbf{C}^{-1}\mathbf{1}| \neq 0$$

Therefore, analogous to the SK system, a strictly positive definite covariance function ensures the unique solution of the OK system.

#### 4.4 Spatiotemporal Universal Kriging (S/T UK)

Spatiotemporal universal kriging provides an unbiased linear estimator of the space-nonhomogeneous/time-nonstationary RF  $X(s, t)$ , which has the form of Equation 1.10, provided that the form of the drift  $m(s, t)$  is given (Matheron, 1973; David, 1977; Journel and Huijbregts, 1978).

Suppose a space-nonhomogeneous /time-nonstationary RF  $X(s, t)$ , as defined by Equation 1.10, has the following form of space-time trend  $m(s, t)$

$$m(s, t) = \sum_{j=1}^L \alpha_j f_j(s, t) = \mathbf{f}'\boldsymbol{\alpha} \quad (4.22)$$

where  $\mathbf{f}' = [f_1(s, t), \dots, f_L(s, t)]$  is a vector of known functions, and  $\boldsymbol{\alpha} = [\alpha_1, \dots, \alpha_L]$  are unknown coefficients.

For a set of  $N$  data  $\{z(s_i, t_i), i=1, \dots, N\}$ , a UK estimator at unknown location  $(s_0, t_0)$  is

$$\hat{x}(s_0, t_0) = \sum_{i=1}^N \lambda_i x(s_i, t_i)$$

To be unbiased, the weights must satisfy

$$\sum_{i=1}^N \lambda_i f_j(s_i, t_i) = f_j(s_u, t_u), \quad j = 1 \text{ to } L.$$

The S/T UK system can be expressed as follows,

$$\begin{cases} \mathbf{C}\boldsymbol{\lambda} - \mathbf{F}\boldsymbol{\mu} = \mathbf{C}_u \\ \mathbf{F}^T\boldsymbol{\lambda} = \mathbf{F}_u \end{cases} \quad (4.23)$$

with vectors  $\boldsymbol{\lambda}^T = [\lambda_1, \dots, \lambda_N]$ ,  $\boldsymbol{\mu}^T = [\mu_1, \dots, \mu_L]$ ,  $\mathbf{C}_u^T = [C(\mathbf{h}_{u1}, \tau_{u1}), \dots, C(\mathbf{h}_{uN}, \tau_{uN})]$ ,  $\mathbf{F}_u^T = [f_1(s_u, t_u), \dots, f_L(s_u, t_u)]$ , and the  $N \times L$  matrix  $\mathbf{F} = [F_{ij}] = [f_j(s_i, t_i)]$ . The corresponding matrix form is given by

$$\mathbf{K}\boldsymbol{\beta} = \boldsymbol{\Theta}$$

where  $\boldsymbol{\beta}$  is the vector of weights:  $\boldsymbol{\beta}^T = (\boldsymbol{\lambda}^T, \boldsymbol{\mu}^T)$ ,  $\boldsymbol{\Theta}$  is the vector on the right hand side of Equation 4.23:  $\boldsymbol{\Theta}^T = (\boldsymbol{\theta}^T, \mathbf{F}_u^T)$ ,  $\mathbf{K}$  is the universal kriging matrix

$$\mathbf{K} = \begin{pmatrix} \mathbf{C} & \mathbf{F} \\ \mathbf{F}^T & \mathbf{0} \end{pmatrix} \quad (4.24)$$

where  $\mathbf{C}$ , as previously mentioned, is the covariance matrix. The vector of weights,  $\boldsymbol{\beta}$ , is obtained by

$$\boldsymbol{\beta} = \mathbf{K}^{-1}\boldsymbol{\Theta} \quad (4.25)$$

The estimation variance is given by

$$\sigma_{UK}^2(s_u, t_u) = C(\mathbf{h}_{uu}, \tau_{uu}) - \mathbf{C}_u^T\boldsymbol{\lambda} + \mathbf{F}_u^T\boldsymbol{\mu} \quad (4.26)$$

#### 4.4.1 Linear Independence and Tensorial Invariance of Trend Models

The trend form,  $\mathbf{f}^T$ , includes a set of component functions which must satisfy the following two requirements (e.g., Matheron, 1971): (i) linear independence of the component functions  $f_1(s, t), \dots, f_L(s, t)$  is required for the unique solution of the S/T UK system, provided that the covariance matrix  $\mathbf{C}$  is positive definite; and (ii) tensorial invariance of the kriging system with regard to changing the origin/unit of the coordinate system, is also required to ensure the unique solution. The requirement of tensorial invariance is necessary, in practice, due to the fact that the coordinates of neighborhoods are usually reset to enhance the stability of the solutions of the kriging system.

It has been shown that the UK system has a unique solution if and only if the component functions  $f_i(s, t)$  are linearly independent on the set of  $n$  data (e.g., Journel and Huijbregts, 1978), that is, if the  $n$  following linear relations

$$\sum_{i=1}^L \lambda_i f_i(s_i, t_i) = 0, \quad \forall i=1 \text{ to } n,$$

This implies that  $\lambda_i = 0, \forall i = 1 \text{ to } L$ . This linear independence requirement can be further subdivided into two aspects: (i) the requirement of linear independence for the component functions, that is, the following linear relation

$$\sum_{i=1}^L \lambda_i f_i(s, t) = 0$$

implies that  $\lambda_i = 0, \forall i = 1 \text{ to } L$ . (ii) the second requirement is more complicated, as there are cases where the configuration of the data alone can make the component functions linearly dependent on the set of  $n$  data (a detailed discussion of the second requirement will be given in Section 4.4.3).

For most combinations of component functions, it is fairly easy to demonstrate whether or not the first requirement is satisfied. For example, the trend form  $f^T = [1, \cos t, \sin t, \cos^2 t, \sin^2 t]$  is not linearly independent since we can find a non-zero set of values  $(1, 0, 0, -1, -1)$  such that  $1 + 0 \times \cos t + 0 \times \sin t - 1 \times \cos^2 t - 1 \times \sin^2 t = 0$ .

However, tensorial invariance is somewhat more difficult to either prove or refute. The tensorial invariance indicates the following relations,

$$\hat{x}(s_u, t_u) = \hat{x}'(s'_u, t'_u)$$

and

$$\sigma_{UK}^2(s_u, t_u) = \sigma_{UK}^2(s'_u, t'_u)$$

where  $s'_u$  and  $t'_u$  denote the transformed space-time coordinates after the origin/unit has been changed, and  $\hat{x}'$  and  $\sigma_{UK}^2$  are the kriging estimator and kriging variance under these transformed coordinates. Even simple trend forms, such as  $f^T = [1, t^2]$ , may not be tensorially invariant. Since the UK process involves the change of the coordinate system's origin in the neighborhood setting, the discussion of permissible trend models in terms of tensorial invariance is, in practice, quite significant.

Three general types of trend forms are considered in the present work: the traditional polynomial functions, Fourier expressions, and combinations of the two. We will present the  $R^2 \times T$  case as an example but the same method can be expanded to include other dimensions.

The polynomial form of S/T trend, using the same notation as Equation 4.22, is given by

$$\mathbf{f}^T = [1, x, y, t, \dots, x^\xi, y^\zeta, t^\zeta] \quad (4.27)$$

where  $\xi$  and  $\zeta$  are orders in space and time, respectively.

A general Fourier form is given by

$$\mathbf{f}^T = [1, \sin\omega_x x \cdot \sin\omega_y y \cdot \sin\omega_t t, \sin\omega_x x \cdot \sin\omega_y y \cdot \cos\omega_t t, \dots, \cos\omega_x ix \cdot \cos\omega_y iy \cdot \sin\omega_t it, \cos\omega_x ix \cdot \cos\omega_y iy \cdot \cos\omega_t it] \quad (4.28)$$

where  $\omega_x$ ,  $\omega_y$  and  $\omega_t$  are frequencies in  $x$ ,  $y$ , and  $t$ , respectively,  $i$  denotes the order of the Fourier series.

The third form includes both polynomial and Fourier terms. This mixed type can be generated from  $m(s, t) = m(s)m(t)$ , where  $m(s)$  is the spatial trend and  $m(t)$  a temporal trend. For instance, a mixed s/t trend form could be

$$\mathbf{f}^T = [1, \sin\omega_t t, \cos\omega_t t, x\sin\omega_t t, x\cos\omega_t t, y\sin\omega_t t, y\cos\omega_t t, \dots] \quad (4.29)$$

Since a trend form with full polynomial terms or full Fourier terms is linearly independent, then, a trend combining full polynomial and full Fourier terms is also linearly independent.

Now we will develop some criteria for tensorial invariance.

**Criterion 4.4** A space-time trend of the form  $\mathbf{f}^T$  meets the requirements for tensorial invariance if there exists a regular matrix  $\mathbf{P}$  such that

$$\mathbf{f}^T = [f_1(s', t'), \dots, f_L(s', t')] = \mathbf{f}^T \mathbf{P} \quad (4.30)$$

where  $s'$  and  $t'$  denote linearly transformed coordinates in space and in time, and  $\mathbf{f}^T$  denotes the transformed form of the space-time trend.

To prove Criterion 4.4, it is easy to show that Equation 4.30 amounts to the trend matrix under the transformed coordinate system  $\mathbf{F}' = \mathbf{F}\mathbf{P}$ , this follows  $\mathbf{F}'^T = \mathbf{P}^T \mathbf{F}_0^T$ . The kriging system under the transformed coordinate system is therefore given by

$$\begin{cases} \mathbf{C}\lambda' - \mathbf{F}\mathbf{P}\mu' = \mathbf{C}_0 \\ \mathbf{P}^T \mathbf{F}'^T \lambda' = \mathbf{P}^T \mathbf{F}_0^T \end{cases} \quad (4.31)$$

Let  $\mu = \mathbf{P}\mu'$ .  $\mathbf{P}$  is regular, therefore, Equation 4.31 becomes

$$\begin{cases} \mathbf{C}\lambda' - \mathbf{F}\mu = \mathbf{C}_0 \\ \mathbf{F}'^T \lambda' = \mathbf{F}_0^T \end{cases} \quad (4.32)$$

Obviously, the kriging system is invariant with respect to  $\lambda'$  and  $\mu$ , which means that the kriging estimator is also invariant. Since  $\mathbf{F}_0^T \mu = \mathbf{F}_0^T \mathbf{P}\mathbf{P}^{-1}\mu' = \mathbf{F}_0^T \mu'$ , the kriging variance becomes

$$\sigma_{UK}^2(\mathbf{s}_U', t_U') = C(\mathbf{h}_{UU}, \tau_{UU}) - \mathbf{C}_U^T \boldsymbol{\lambda}' + \mathbf{F}_U'^T \boldsymbol{\mu}$$

Therefore, the kriging variance is also invariant.

Based on this criterion, it is easy to show that a S/T trend form with full polynomial terms,  $\mathbf{f}^T = [1, x, y, t, \dots, x^{\bar{s}}, y^{\bar{s}}, t^{\bar{s}}]$ , is acceptable since there exists an upper triangular matrix  $\mathbf{P}$  with non-zero diagonal elements such that  $\mathbf{f}^T = \mathbf{f}^T \mathbf{P}$ . Furthermore, it is easy to show that a polynomial trend form with some higher-order terms missing meets the criterion for tensorial invariance.

For a trend form with full Fourier expression terms, the terms with different orders are not related with respect to linear transformation of coordinates, thus,

$$[\sin \omega_x i x' \cdot \sin \omega_y i y' \cdot \sin \omega_t i t', \dots, \cos \omega_x i x' \cdot \cos \omega_y i y' \cdot \cos \omega_t i t'] = [\sin \omega_x i x \cdot \sin \omega_y i y \cdot \sin \omega_t i t, \dots, \cos \omega_x i x \cdot \cos \omega_y i y \cdot \cos \omega_t i t] \mathbf{P}_i, \quad \forall i = 1, 2, \dots$$

Consequently, it is sufficient to evaluate the trend form of order 1 below:

$$\mathbf{f}^T = [\sin \omega_x x \cdot \sin \omega_y y \cdot \sin \omega_t t, \dots, \cos \omega_x x \cdot \cos \omega_y y \cdot \cos \omega_t t] = [f_1(s, t), \dots, f_8(s, t)]$$

To show the terms under the transformed coordinate system, one has

$$\sin \omega_x x' = \sin \frac{\omega_x}{a_x} (a_x x + b_x) = \sin \omega_x x \cdot \cos b_1 + \cos \omega_x x \cdot \sin b_1$$

and

$$\cos \omega_x x' = \cos \omega_x x \cdot \cos b_1 - \sin \omega_x x \cdot \sin b_1$$

where  $b_1 = \frac{\omega_x b_x}{a_x}$ . Similarly,

$$\sin \omega_y y' = \sin \omega_y y \cdot \cos b_2 + \cos \omega_y y \cdot \sin b_2, \quad \cos \omega_y y' = \cos \omega_y y \cdot \cos b_2 - \sin \omega_y y \cdot \sin b_2$$

$$\sin \omega_t t' = \sin \omega_t t \cdot \cos b_3 + \cos \omega_t t \cdot \sin b_3, \quad \cos \omega_t t' = \cos \omega_t t \cdot \cos b_3 - \sin \omega_t t \cdot \sin b_3$$

with  $b_2 = \frac{\omega_y b_y}{a_y}$  and  $b_3 = \frac{\omega_t b_t}{a_t}$ . One can show that  $\mathbf{f}^T = \mathbf{f}^T \mathbf{P}$  with

$$\mathbf{P} = \begin{pmatrix} \cos b_1 \cdot \mathbf{D} & -\sin b_1 \cdot \mathbf{D} \\ \sin b_1 \cdot \mathbf{D} & \cos b_1 \cdot \mathbf{D} \end{pmatrix}$$

where

$$\mathbf{D} = \begin{pmatrix} \cos b_2 \cdot \mathbf{E} & -\sin b_2 \cdot \mathbf{E} \\ \sin b_2 \cdot \mathbf{E} & \cos b_2 \cdot \mathbf{E} \end{pmatrix}$$

and

$$\mathbf{E} = \begin{pmatrix} \cos b_3 & -\sin b_3 \\ \sin b_3 & \cos b_3 \end{pmatrix}$$

Since  $\mathbf{E}$ ,  $\mathbf{D}$  and  $\mathbf{P}$  are regular, this trend form is acceptable.

Though trend forms with full polynomial terms and full Fourier terms are acceptable, this is not necessarily the case with trend forms containing partial terms. The following criterion can be used to check for unacceptable trend forms.

**Criterion 4.5** A trend form  $\mathbf{f}^T = [f_1(s, t), \dots, f_L(s, t)]$  is unacceptable, with respect to the tensorial invariance of the kriging estimator/variance, if there exists a regular matrix  $\mathbf{P}$  and a non-zero matrix  $\mathbf{Q}$  such that

$$\mathbf{f}^T = [f_1(s', t'), \dots, f_L(s', t')] = \mathbf{f}^T \mathbf{P} + \mathbf{Q} \mathbf{w} \quad (4.33)$$

where  $\mathbf{w}^T = [f_{L+1}(s, t), \dots, f_{L+k}(s, t)]$  denotes a vector of additional terms with  $k > 0$ .

To verify this criterion, it is enough to show that the unbiased conditions under the transformed coordinate system are

$$\mathbf{P}^T \mathbf{F}^T \lambda' + \mathbf{W}^T \mathbf{Q}^T \lambda' = \mathbf{P}^T \mathbf{F}_0 + \mathbf{W}_0 \mathbf{Q}$$

where the  $N \times k$  matrix  $\mathbf{W} = [\mathbf{W}_{ij}] = [f_{L+i}(s_j, t_j)]$  and the vector  $\mathbf{W}_0 = [f_{L+1}(s_0, t_0), \dots, f_{L+k}(s_0, t_0)]^T$ . Consequently,

$$\mathbf{F}^T \lambda' = \mathbf{F}_0 + (\mathbf{P}^{T-1} \mathbf{F} \mathbf{W} \mathbf{Q} - \mathbf{P}^{T-1} \mathbf{W}^T \mathbf{Q}^T \lambda')$$

These unbiased conditions are not identical to that of Equation 4.32 since  $\mathbf{Q} \neq \mathbf{0}$ , indicating that the kriging estimator is no longer invariant.

Based on this criterion one may easily determine the acceptability of the trend form. For example,  $\mathbf{f}^T = [1, t^2]$  is not acceptable, as is shown here,

$$\mathbf{f}^T = [1, (a_t t + b_t)^2] = [1, t^2] \begin{pmatrix} 1 & b_t^2 \\ 0 & a_t^2 \end{pmatrix} + [0, 2a_t b_t] t$$

Moreover, it is not difficult to demonstrate that for any polynomial trend form with some lower-order terms missing, there always exists a regular  $\mathbf{P}$  and a non-zero  $\mathbf{Q}$  such that Equation 4.33 holds.

**Criterion 4.6** A polynomial trend form of order  $\xi/\zeta$  meets the criteria for tensorial invariance if and only if all lower-order terms up to  $(\xi-1)/(\zeta-1)$  are present.

Therefore, the trend form  $\mathbf{f}^T = [1, x, y, x^2, y^2, t^2, xy, xt, yt]$  is unacceptable even though all higher-order terms are present, while the trend form  $\mathbf{f}^T = [1, x, y, t, xy]$  is acceptable.

For a S/T trend form with Fourier terms, the following criterion is true due to the fact that each term under the transformed coordinate system is a linear combination of all terms under the original coordinate system,

$$f_i(s', t') = a_i f_1(s, t) + \dots + a_8 f_8(s, t), \quad \forall i = 1 \text{ to } 8.$$

**Criterion 4.7** A Fourier trend form is acceptable with respect to tensorial invariance if and only if all terms are present.

In practice one may also consider a S/T trend which is the product of a spatial trend  $m(s)$  and a temporal trend  $m(t)$

$$m(s, t) = m(s)m(t)$$

Very often  $m(s)$  has a polynomial form while  $m(t)$  has a Fourier form, indicating that the S/T trend form can be given by

$$f^T = [\sin\omega_1 t, \cos\omega_1 t, x\sin\omega_1 t, x\cos\omega_1 t, y\sin\omega_1 t, y\cos\omega_1 t, \dots]$$

Taking Criterion 4.6 and 4.7 into account, we can demonstrate that this type of S/T trend form is acceptable if and only if all lower-order terms are present and higher-order terms are in pairs of sine and cosine functions. In other words,  $f^T = [\sin\omega_1 t, \cos\omega_1 t, x\sin\omega_1 t, x\cos\omega_1 t, y\sin\omega_1 t, y\cos\omega_1 t]$  is acceptable while  $f^T = [\sin\omega_1 t, \cos\omega_1 t, x\sin\omega_1 t, x\cos\omega_1 t, y\sin\omega_1 t]$  is not acceptable, since  $y\cos\omega_1 t$  is missing.

#### 4.4.2 Practical S/T Trend Models

The polynomial, Fourier, and mixed space-time forms described previously can adequately model space-time trends in most practical cases (using lower orders). For polynomial trends, the space and time orders  $\xi$  and  $\zeta$  up to 2 are sufficient in most cases. In the majority of cases, a Fourier trend form of order  $i$  set to 1 appears to be sufficient. A larger order, either in time or in space, may generate a large number of terms which will encounter singularity more frequently in the estimation processes. Nevertheless, one may select the orders that seem appropriate to the data set to be modeled.

In practice, one may consider the following S/T trend models (see Table 4.1):

1. Polynomial terms both in space and in time, including: terms linear both in space and in time, linear in space and quadric in time, quadric in space and linear in time, and quadric both in space and in time.
2. Polynomial terms in space and Fourier terms in time, such as: linear terms in space and Fourier terms in time, i.e.

$$f^T = (1, x, y, \sin t, \cos t, x\sin t, x\cos t, y\sin t, y\cos t)$$

3. Fourier terms in space and polynomial terms in time, such as: linear terms in time and Fourier terms in space, i.e.

$$\mathbf{f}^r = (1, \sin\omega_x x, \cos\omega_x x, \sin\omega_y y, \cos\omega_y y, t, t\sin\omega_x x, t\cos\omega_x x, t\sin\omega_y y, t\cos\omega_y y)$$

Table 4.1 Practical space-time trend models.

spatial component ( $\xi$ )	temporal component ( $\zeta$ )			
	constant ( $\zeta=0$ )	linear ( $\zeta=1$ )	quadric ( $\zeta=2$ )	harmonic ( $\zeta=i$ )
constant ( $\xi=0$ )	N.A.	$\zeta=1$	$\zeta=2$	$\zeta=i$
linear ( $\xi=1$ )	$\xi=1$	$\xi=1/\zeta=1$	$\xi=1/\zeta=2$	$\xi=1/\zeta=i$
quadric ( $\xi=2$ )	$\xi=2$	$\xi=2/\zeta=1$	$\xi=2/\zeta=2$	N.A.
harmonic ( $\xi=i$ )	$\xi=i$	$\xi=i/\zeta=1$	N.A.	$\xi=i/\zeta=i$
linear+harmonic ( $\xi=1+i$ )	$\xi=1+i$	$\xi=1+i/\zeta=1$	N.A.	$\xi=1+i/\zeta=i$

In addition, one may also consider mixed terms (polynomial plus Fourier terms) in space or in time. Mixed spatial terms (linear + Fourier) with linear temporal terms may be expressed by

$$\mathbf{f}^r = (1, x, y, \sin\omega_x x, \cos\omega_x x, \sin\omega_y y, \cos\omega_y y, t, xt, yt, t\sin\omega_x x, t\cos\omega_x x, t\sin\omega_y y, t\cos\omega_y y)$$

#### 4.4.3 Singularity Analysis of S/T UK

Singularity problems may arise in the solution of the UK system (e.g., Rouhani and Myers, 1990). Understanding of the potential sources of these problems can be helpful in determining the criteria for selecting kriging neighborhoods, as well as the criteria for sampling location/instance design.

The unique solution of the kriging system (4.23) is determined by the kriging matrix

$$\mathbf{K} = \begin{pmatrix} \mathbf{C} & \mathbf{F} \\ \mathbf{F}^T & \mathbf{0} \end{pmatrix}$$

where  $\mathbf{F}$  is the  $N \times L$  trend matrix

$$\mathbf{F} = \begin{pmatrix} f_1(\mathbf{s}_1, t_1) & f_2(\mathbf{s}_1, t_1) & \dots & f_L(\mathbf{s}_1, t_1) \\ f_1(\mathbf{s}_2, t_2) & f_2(\mathbf{s}_2, t_2) & \dots & f_L(\mathbf{s}_2, t_2) \\ \dots & \dots & \dots & \dots \\ f_1(\mathbf{s}_N, t_N) & f_2(\mathbf{s}_N, t_N) & \dots & f_L(\mathbf{s}_N, t_N) \end{pmatrix}$$

The singularity of the kriging matrix  $\mathbf{K}$  depends on both the matrix  $\mathbf{C}$  and the matrix  $\mathbf{F}$ . The singularity of the covariance matrix is caused by the covariance function not being positive definite. In some cases, when the kriging matrix  $\mathbf{K}$  is not singular, the covariance

matrix  $C$  may be singular due to the impact of the trend matrix  $F$ . However, if the covariance matrix  $C$  is positive definite, then the determinant of the kriging matrix can be represented as

$$|K| = |C| |0 - F^T C^{-1} F| = (-1)^L |C| |F^T C^{-1} F|$$

indicating that the singularity of the kriging matrix  $K$  depends exclusively on the trend matrix  $F$ . In other words, in this case the kriging matrix is singular if and only if the trend matrix is singular. Here, the discussion will concentrate on the impact of trend models, assuming that the covariance matrix is positive definite.

The trend matrix  $F$  will be singular when the number of data points,  $N$ , is less than the number of trend terms,  $L$ , since it is a  $N \times L$  matrix. For the following discussion we will assume  $N \geq L$ . To unveil the impact of the space-time data configuration on the singularity of the trend matrix, it is convenient to introduce the following definition of the space-time data configuration.

***p*-location configuration:** Given  $N$  available data observations with coordinates  $(s_1, t_1), \dots, (s_N, t_N)$  in  $R^n \times T$ , including  $L_1$  samples located at  $s_1$  in  $R^n$ ,  $L_2$  samples at  $s_2$ , ..., and  $L_m$  samples at  $s_p$ ,  $s_1 \neq s_2 \neq \dots \neq s_p$  (when  $n = 2$ , for example,  $s_i$  denotes  $(x_i, y_i)$  and  $s_i = s_j$  if and only if  $x_i = x_j$  and  $y_i = y_j$  simultaneously) such that  $L_1 + L_2 + \dots + L_p = N$ , the data is said to form a *p*-location configuration in  $R^n \times T$ .

Every space-time data set forms a specific *p*-location configuration. For example, measurements of reservoir pressure at five wells form a 5-location configuration, measurements of pollutant concentrations at eight locations form a 8-location configuration, etc..

It is convenient to recall the following information from linear algebra: a matrix  $F$  is singular if and only if the set of its columns  $\{F_1, F_2, \dots, F_L\}$  is linearly dependent. Also, a  $N \times L$  matrix  $F$  is singular if it has a basis of  $k$  columns  $\{v_1, v_2, \dots, v_k\}$  with  $k < L$ .

To further our discussion we will now introduce the matrix  $A$

$$A = \begin{pmatrix} a_{11} & \dots & a_{1k} \\ \cdot & \dots & \cdot \\ a_{p1} & \dots & a_{pk} \end{pmatrix} \quad (4.34)$$

where  $\mathbf{a}_{ij} = a_{ij} \cdot \mathbf{1}_{L_i}$ ,  $a_{ij}$  is a value and  $\mathbf{1}_{L_i}$  is a vector with  $L_i$  elements 1,  $i = 1, \dots, p$ ;  $j = 1, \dots, k$ . Now we propose the following result.

**Criterion 4.8** The matrix  $\mathbf{A}$  represented in Equation 4.32 is singular if  $p < k$ .

Since a basis of the matrix  $\mathbf{A}$  in Equation 4.32 can be constructed by the following  $p$  columns  $\mathbf{v}_1, \mathbf{v}_2, \dots, \mathbf{v}_p$ :  $\mathbf{v}_1^T = [\mathbf{1}_{L_1}^T, \mathbf{0}^T, \dots, \mathbf{0}^T]$ ,  $\mathbf{v}_2^T = [\mathbf{0}^T, \mathbf{1}_{L_2}^T, \mathbf{0}^T, \dots, \mathbf{0}^T]$ , ...,  $\mathbf{v}_p^T = [\mathbf{0}^T, \dots, \mathbf{0}^T, \mathbf{1}_{L_p}^T]$ ,  $\mathbf{A}$  is singular when  $p < k$ .

In the next section we will show that every S/T trend matrix has certain columns which construct the matrix expressed by Equation 4.32. The number of columns is determined by the trend model chosen in the S/T UK system.

#### 4.4.3.1 Singularity Problems in $\mathbf{R}^1 \times \mathbf{T}$

The S/T trend with quadric spatial polynomials can be represented by

$$m(x, t) = a_0 + a_1 x + a_2 x^2 + \sum_{j=3}^L a_j f_j(x, t)$$

where the sum on the right-hand side denotes the terms related to  $t$ . Consider the case where samples form a 2-location configuration as shown in Figure 4.2.  $L_1$  denotes the number of samples located at  $x_1$  and  $L_2$ , the number of samples at  $x_2$ , with  $L_1 + L_2 = N$ . Then, the first three columns of the trend matrix  $\mathbf{T}$  are

$$\mathbf{F}_1 = (\mathbf{1}_{L_1}^T, \mathbf{1}_{L_2}^T)^T$$

$$\mathbf{F}_2 = (x_1, x_1, \dots, x_1, x_2, x_2, \dots, x_2)^T = (x_1 \cdot \mathbf{1}_{L_1}^T, x_2 \cdot \mathbf{1}_{L_2}^T)^T$$

$$\mathbf{F}_3 = (x_1^2, x_1^2, \dots, x_1^2, x_2^2, x_2^2, \dots, x_2^2)^T = (x_1^2 \cdot \mathbf{1}_{L_1}^T, x_2^2 \cdot \mathbf{1}_{L_2}^T)^T$$

which form a  $N \times 3$  matrix  $\mathbf{A}$

$$\mathbf{A} = \begin{pmatrix} \mathbf{1}_{L_1} & x_1 \cdot \mathbf{1}_{L_1} & x_1^2 \cdot \mathbf{1}_{L_1} \\ \mathbf{1}_{L_2} & x_2 \cdot \mathbf{1}_{L_2} & x_2^2 \cdot \mathbf{1}_{L_2} \end{pmatrix}$$

According to Criterion 4.8 the matrix  $\mathbf{A}$  is singular, and so is the trend matrix  $\mathbf{F}$ .

Analogous to the above discussion, it is not difficult to show that the trend matrix is singular if the S/T trend model has  $\xi$ -order spatial polynomials and the samples form a  $\xi$ -location configuration,  $\xi = 3, 4, \dots$ . The following is true.

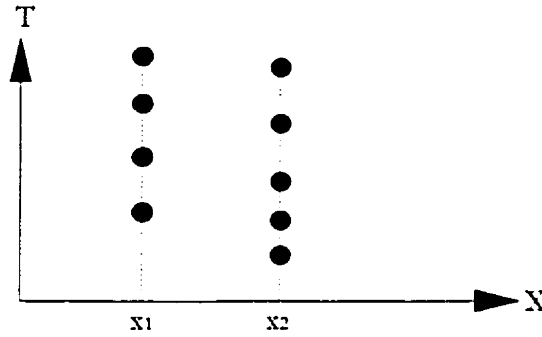


Figure 4.2 A 2-location configuration in  $R^1 \times T$  with  $L_1 = 4$  and  $L_2 = 5$ .

**Criterion 4.9** Given a S/T UK system in  $R^1 \times T$ , if the trend model has  $\xi$ -order spatial polynomials, then the kriging matrix is singular when samples form a p-location configuration with  $p \leq \xi$ .

More generally, it is easy to show that the kriging matrix is singular when the number of purely spatial terms is larger than  $p$  (the number of spatial locations), implying that  $p \leq 2$  for Fourier terms of order 1. Similar results can be obtained for mixed trend forms.

#### 4.4.3.2 A general result in $R^n \times T$

A general form of a s/t trend  $m(s, t)$  can be expressed as follows

$$m(s, t) = a_0 + \sum_{j=1}^{\alpha} a_j f_j(s) + \sum_{j=\alpha+1}^L a_j f_j(s, t) \quad (4.35)$$

where  $\alpha$  denotes the number of purely spatial terms. Assume that the samples form a p-location configuration, as previously defined. Then the first  $p + 1$  columns of the trend matrix  $F$  are

$$F_1 = (\mathbf{1}_{L_1}^T, \dots, \mathbf{1}_{L_p}^T)^T$$

$$F_2 = (f_1(s_1) \cdot \mathbf{1}_{L_1}^T, \dots, f_1(s_p) \cdot \mathbf{1}_{L_p}^T)^T$$

...

$$F_{p+1} = (f_p(s_1) \cdot \mathbf{1}_{L_1}^T, \dots, f_p(s_p) \cdot \mathbf{1}_{L_p}^T)^T$$

which form a  $N \times (p+1)$  matrix  $A$

$$\mathbf{A} = \begin{pmatrix} \mathbf{1}_{L_1} & f_1(\mathbf{s}_1) \cdot \mathbf{1}_{L_1} & \dots & f_p(\mathbf{s}_1) \cdot \mathbf{1}_{L_1} \\ \mathbf{1}_{L_2} & f_1(\mathbf{s}_2) \cdot \mathbf{1}_{L_2} & \dots & f_p(\mathbf{s}_2) \cdot \mathbf{1}_{L_2} \\ \vdots & \vdots & \ddots & \vdots \\ \mathbf{1}_{L_p} & f_1(\mathbf{s}_p) \cdot \mathbf{1}_{L_p} & \dots & f_p(\mathbf{s}_p) \cdot \mathbf{1}_{L_p} \end{pmatrix}$$

Due to criterion 4.8 the matrix  $\mathbf{A}$  is singular if  $p \leq \alpha$ .

**Criterion 4.10** For a S/T UK system in  $\mathbb{R}^n \times T$ , its s/t trend can be expressed by Equation 4.33 with  $\alpha$  purely spatial terms, and the kriging matrix will be singular when samples form a p-location configuration with  $p \leq \alpha$ .

For polynomial trend forms, the goal is to determine  $\alpha$ , the number of purely spatial terms. This is a combinatorial problem with repetitions and the value  $\alpha$  is given by (e.g., Dimitrakopoulos, 1989)

$$\alpha = (n+\xi)!/(n!\xi!) - 1 \quad (4.36)$$

where  $n$  denotes spatial dimensions and  $\xi$  is the order of spatial polynomials. Similarly, when the spatial terms are Fourier terms with an order of  $i$ , then the value  $\alpha$  is obtained by

$$\alpha = i2^n \quad (4.37)$$

The above two cases encompass all mixed trend forms.

**Remark 4.1** It is now possible to generate guidelines to be applied in specific cases. Previous discussions of singularity problems in UK system's have concluded the following. In  $\mathbb{R}^1 \times T$ ,  $\alpha = (1+\xi)!/(1!\xi!) - 1 = \xi$ , which explains Criterion 4.9. In addition,  $\alpha = 1 \times 2^1 = 2$  for Fourier terms of order 1. For  $\mathbb{R}^2 \times T$ ,  $\alpha = (2+\xi)!/(2!\xi!) - 1$  and  $\alpha = 4i$ . Table 4.2 summarizes the most common cases and provides guidelines that should be followed in constructing neighborhoods while performing S/T UK, and possibly used in monitoring and data collection schemes.

**Remark 4.2** We may also obtain analogous results based on p-instance configuration, that is, available data measured at  $p$  different time instances. Equation 4.33 can be rewritten as

$$m(\mathbf{s}, t) = a_0 + \sum_{j=1}^{\alpha} a_j f_j(t) + \sum_{j=\alpha+1}^L a_j f_j(\mathbf{s}, t)$$

where the first sum on the right-hand side represents purely temporal terms. Then, analogous to Criterion 4.10, the kriging matrix is singular when samples form a p-time-instance configuration with  $p \leq \alpha$ .

Table 4.2 Neighborhood requirements for S/T trend models up to  $\xi/\zeta = 2$  and  $i=1$ .

	S/T trend order-form	p-locations (space)	p-locations (time)
$R^1 \times T$	$\xi/\zeta = 2/2$	$>2$	$>2$
$R^1 \times T$	$i/i = 1/1$	$>2$	$>2$
$R^1 \times T$	$\xi/i = 2/1$	$>2$	$>2$
$R^1 \times T$	$i/\zeta = 1/2$	$>2$	$>2$
$R^2 \times T$	$\xi/\zeta = 2/2$	$>5$	$>2$
$R^2 \times T$	$i/i = 1/1$	$>4$	$>2$
$R^2 \times T$	$\xi/i = 2/1$	$>5$	$>2$
$R^2 \times T$	$i/\zeta = 1/2$	$>4$	$>2$

#### 4.5 Summary

Spatiotemporal kriging techniques are commonly derived as extensions of spatial kriging techniques because S/T kriging systems have similar structures. However, the covariances for S/T systems are obtained from special space-time covariance models.

S/T SK and OK require strictly positive definite space-time covariance models to avoid singularity. The criteria to determine whether or not a space-time covariance model is positive definite is outlined in this chapter. In the case of joint distance models, it has been shown that the selection of exponential models or Gaussian models ensures the unique solution of kriging systems in the space-time domain. However, the selection of spherical models ensures the unique solution only in  $R^1 \times T$  and  $R^2 \times T$ . An alternate model for obtaining a unique solution in  $R^3 \times T$  is given in Equation 4.14.

Selected space-time trend forms must meet two requirements: linear independence and tensorial invariance. Criteria developed in this chapter demonstrate that a polynomial trend form of S/T order  $\xi/\zeta$  meets the tensorial invariance requirement if and only if all lower-

order terms up to  $\xi^{-1}/\zeta^{-1}$  are present. A Fourier trend form of order  $i$  is acceptable if and only if all terms are present. Mixed trend forms must satisfy similar conditions.

Finally, a method is derived which can be used to avoid singularities in the S/T UK system caused by the form of the space-time trend model. This formula indicates that in  $R^n \times T$  the kriging matrix is singular if samples in the neighborhood have a  $p$ -location configuration and the trend has  $\alpha$  purely spatial trend terms with  $p \leq \alpha$ . Similar results are derived for data configuration in time. These results contain the potential for further development in the interest of establishing guidelines with which to evaluate kriging neighborhoods with respect to trend models and sampling configurations.

## Chapter 5

### Conditional Simulation of Spatiotemporal Processes

#### 5.1 Introduction

Conditional simulations of spatiotemporal processes provide realizations,  $x(\mathbf{u})$ , of a S/TRF,  $X(\mathbf{u})$ , which share the same second-order statistics with the original, and reproduce the known information at data locations. Due to the distinct properties of the space-time domain, not every spatial simulation technique can be directly adapted to generate realizations of spatiotemporal processes. The turning band method is a typical example of a method that is difficult to implement in the space-time domain. On the other hand, conditional simulation of spatiotemporal processes follows the same implementation procedure as that of spatial conditional simulation in order to generate the required second-order moments at simulated nodes and replicate the measured values at their locations. This allows conditional simulation techniques, whose implementation involves direct computation at simulated nodes, to be applicable to the space-time domain. This chapter will focus on the potential use of these techniques for conditional simulation of spatiotemporal processes. For convenience, spatiotemporal processes will be expressed by  $X(\mathbf{u})$  in this chapter rather than  $X(s, t)$  as in previous chapters, where  $\mathbf{u}$  denotes a position in the space-time domain. Therefore spatial processes can also be expressed by  $X(\mathbf{u})$  since spatial processes are special subcases of spatiotemporal processes. Under this expression the available conditional simulation techniques of spatial processes can be easily introduced and expanded for potential applications to spatiotemporal processes without notation modifications.

Current conditional simulation techniques may be classified into two categories: (i) two-step techniques, where an unconditional simulation step is prerequisite to the implementation of the required simulation, and (ii) direct conditional techniques, that perform conditioning concurrently with simulation. Conditional simulation was initially developed as a two-step technique in 1974 (Journel, 1974), and the domination of two-step techniques in conditional simulation applications continued until the introduction of LU decomposition simulations in 1987 (Davis, 1987a).

**Two-step techniques:** Journel (1974) proposes that the conditional simulation of stationary processes can be obtained using the following formula

$$x_{cs}(\mathbf{u}) = x_{ok}^*(\mathbf{u}) + [x_s(\mathbf{u}) - x_{sk}^*(\mathbf{u})]$$

where  $x_{cs}(\mathbf{u})$  denotes the required conditional simulation at the location  $\mathbf{u}$ ,  $x_{ok}^*(\mathbf{u})$  denotes the kriged value at  $\mathbf{u}$  deduced from the data,  $x_s(\mathbf{u})$  is the unconditional simulation at  $\mathbf{u}$ , and  $x_{sk}^*(\mathbf{u})$  is the kriged value at  $\mathbf{u}$  deduced from the unconditionally simulated values. The simulation procedure includes two steps. First, an unconditional simulation has to be computed at all grid and data locations. Then, the required conditional simulation is derived based on both the conditioning data and the unconditional simulation results.

**Direct conditional simulation techniques:** Since conditional simulations require the same results as measured values at data locations, an effective technique of conditional simulations should perform the conditional simulation without redundant calculations at data locations. This consideration led to the development of direct conditional simulation techniques which implement conditioning simultaneously with simulation, so that extra unconditional simulation processes and redundant calculations at data locations are unnecessary. Essentially, there are three popular types of direct conditional simulation techniques: the LU decomposition algorithm proposed by Davis (1987a), the sequential simulation approaches, devised by Johnson (1987) and developed by Alabert (1987) and Isaaks (1991), and the simulated annealing approaches developed by Farmer (1991) and Deutsch (1992).

Direct techniques are favorable to spatiotemporal conditional simulations due to the fact that they perform simulation directly on the simulation nodes, and the only prerequisite to the implementation process is the availability of covariance calculations between the simulation nodes and data. This requirement can be easily satisfied through the space-time continuity characterization process.

This chapter will show that all three of the above direct conditional simulation techniques are appropriate for spatiotemporal simulations. After proving that the LU decomposition algorithm is equivalent to the sequential Gaussian simulation (SGS), a fast simulation technique, called the sequential group Gaussian simulation (SGGS), will be developed. This technique consists of a series of algorithms, the first of which is linked to sequential Gaussian simulation and the last of which is linked to the LU decomposition algorithm. In addition, the simulated annealing technique which reproduces experimental variograms will be developed. This technique allows us to bypass covariance/variogram model fitting in conditional simulations.

### 5.1.1 The LU Decomposition Algorithm

Let the conditioning data set  $\{x'_i, i = 1, \dots, N\}$  be a realization of a Gaussian RF  $X(s)$  with a mean vector  $\mathbf{m}$ , and let  $\mathbf{C}$  be the covariance matrix associated with conditioning data locations and grid nodes. The LU decomposition algorithm is based on the LU triangular decomposition of the covariance matrix

$$\mathbf{C} = \mathbf{L}\mathbf{U} \quad \text{where } \mathbf{L}^T = \mathbf{U}$$

Now consider the vector

$$\mathbf{x} = \mathbf{L}\mathbf{w} + \mathbf{m} \quad (5.1)$$

where  $\mathbf{x} = (x'_1, \dots, x'_n, x_1, \dots, x_k)^T$ ,  $\{x'_1, \dots, x'_n\}$  and  $\{x_1, \dots, x_k\}$  respectively denote the conditioning data and the required conditional simulation,  $\mathbf{w}$  is a vector of independently  $N(0, 1)$  distributed random numbers,  $N(0, 1)$  denotes the standard normal distribution. The expectation of  $\mathbf{x}$  is given by

$$E\{\mathbf{x}\} = E\{\mathbf{L}\mathbf{w} + \mathbf{m}\} = \mathbf{m}$$

and the corresponding covariance matrix

$$E\{(\mathbf{x} - \mathbf{m})(\mathbf{x} - \mathbf{m})^T\} = E\{\mathbf{L}\mathbf{w}\mathbf{w}^T\mathbf{L}^T\} = \mathbf{L} E\{\mathbf{w}\mathbf{w}^T\} \mathbf{U} = \mathbf{L}\mathbf{I}\mathbf{U} = \mathbf{L}\mathbf{U} = \mathbf{C}$$

where  $\mathbf{I}$  is a unit matrix. Therefore, the vector  $\mathbf{x}$  is a conditional simulation of  $X(\mathbf{u})$ .

Partition  $\mathbf{C}$  as:

$$\begin{pmatrix} \mathbf{C}_{DD} & \mathbf{C}_{GD}^T \\ \mathbf{C}_{GD} & \mathbf{C}_{GG} \end{pmatrix}$$

where  $\mathbf{C}_{DD}$  is the covariance matrix between data locations,  $\mathbf{C}_{GD}$  is the covariance matrix between grid locations and data locations, and  $\mathbf{C}_{GG}$  is the covariance matrix between grid locations. This entails

$$\mathbf{C} = \begin{pmatrix} \mathbf{L}_{DD} & \mathbf{0} \\ \mathbf{L}_{GD} & \mathbf{L}_{GG} \end{pmatrix} \begin{pmatrix} \mathbf{U}_{DD} & \mathbf{U}_{GD} \\ \mathbf{0} & \mathbf{U}_{GG} \end{pmatrix} \quad (5.2)$$

Partition  $\mathbf{w}$  as:  $\mathbf{w} = (\mathbf{w}_D^T \ \mathbf{w}_G^T)^T$ , where  $\mathbf{w}_G$  is a vector of independently standard normally distributed random numbers, and  $\mathbf{w}_D$  is the conditioning vector such that

$$\mathbf{L}_{DD}\mathbf{w}_D = \mathbf{x}_D - \mathbf{m}_D \quad (5.3)$$

where  $\mathbf{x}_D$  and  $\mathbf{m}_D$  are vectors of the data and means, respectively. The required simulation is then obtained by

$$\mathbf{x}_G = [\mathbf{L}_{GD}\mathbf{L}_{DD}^{-1}(\mathbf{x}_D - \mathbf{m}_D) + \mathbf{m}_G] + \mathbf{L}_{GG}\mathbf{w}_G \quad (5.4)$$

Note that  $[\mathbf{L}_{GD}\mathbf{L}_{DD}^{-1}(\mathbf{x}_D - \mathbf{m}_D) + \mathbf{m}_G]$  is the simple kriging vector deduced from the conditioning values.

### 5.1.1.1 Summary of the LU Decomposition Computations

The computation of the LU decomposition algorithm includes (1) the computation of the lower triangular matrix  $L$  from a given covariance matrix  $C$ , (2) the computation of  $L_{DD}^{-1}$  from the given  $L_{DD}$ , and (3) the computation of Equation 5.4. We are assuming that the random numbers and the covariance matrix have been previously computed.

The pseudocode for the computation of the lower triangular matrix is presented as a procedure called LU-DECOMPOSITION( $L$ ,  $n+K$ ) where  $L$  denotes a lower triangular matrix and  $n+K$  denotes the number of columns of  $L$ . Note that the covariance matrix is symmetric, therefore it is convenient to build only the lower triangular part of the covariance matrix. The input matrix  $L$  loads the lower triangular part of the covariance matrix. The output is the required lower triangular matrix which is also loaded by  $L$ . The pseudocode is shown below.

LU-DECOMPOSITION( $L$ ,  $n+K$ )

```

1  for i = 1 to n+K
2    do  $L_{ii} = \sqrt{L_{ii}}$ 
3    for k = i+1 to n+K
4      do  $L_{ki} = L_{ki}/L_{ii}$ 
5    for j = i+1 to n+K
6      do for k = j to n+K
7         $L_{kj} = L_{kj} - L_{ki}L_{ji}$ 
8  return L

```

The number of additions in LU-DECOMPOSITION,  $N_{add}(LU, n+K)$ , are calculated from Step 7:

$$N_{add}(LU, n+K) = \sum_{i=1}^{n+K} \sum_{j=i+1}^{n+K} (n+K-j+1) = \frac{1}{6}(n+K)^3 - \frac{1}{2}(n+K)^2 + \frac{1}{12}(n+K)$$

The number of multiplication's,  $N_{mul}(LU)$ , are calculated from Step 2, 4, and 7:

$$N_{mul}(LU, n+K) = \sum_{i=1}^{n+K} \sum_{j=i+1}^{n+K} (n+K-j+1) + \sum_{i=1}^{n+K} (n+K-i) = \frac{1}{6}(n+K)^3 - (n+K)^2 + \frac{7}{12}(n+K)$$

The pseudocode for the inverse of the lower triangular matrix,  $L_{DD}^{-1}$ , is presented as a procedure called INVERSE shown below.

```

INVERSE( $\mathbf{L}_{DD}$ , n)
1  for i = 1 to n
2     $L_{ii} = 1./L_{ii}$ 
3    for k = 1 to i-1
4      do for j = k to i-1
5        tmp = tmp +  $L_{ij}L_{jk}$ 
6         $L_{ik} = -tmp \times L_{ji}$ 
7  return  $\mathbf{L}_{DD}^{-1}$ 

```

The number of additions required in INVERSE can be calculated from Step 5:

$$N_{\text{add}}(\text{INVERSE}, n) = \sum_{i=1}^n \sum_{k=1}^{i-1} (i-k) = \frac{1}{6}n^3 - \frac{1}{6}n$$

the number of multiplication's are calculated from Step 2, 5, and 6:

$$N_{\text{mul}}(\text{INVERSE}, n) = \sum_{i=1}^n \sum_{k=1}^{i-1} (i-k) + \sum_{i=1}^n (i-1) + n = \frac{1}{6}n^3 + \frac{1}{2}n^2 + \frac{1}{3}n$$

Finally, the computation of Equation 5.4 consists of two parts: the operations involved in the first term,  $[\mathbf{L}_{GD}\mathbf{L}_{DD}^{-1}(\mathbf{x}_D - \mathbf{m}_D) + \mathbf{m}_G]$ , and the operations involved in the second term,  $\mathbf{L}_{GG}\mathbf{w}_G$ . The first term requires  $\frac{1}{2}K(n^2+n) + Kn + (n+K)$  additions and  $\frac{1}{2}K(n^2+n) + Kn$  multiplications, and the second term requires  $\frac{1}{2}K(K+1)$  additions and multiplications. Therefore, the total number of arithmetic operations of the LU decomposition algorithm,  $N_{\text{add}}(\text{LUD})$  and  $N_{\text{mul}}(\text{LUD})$ , are as follows.

$$N_{\text{add}}(\text{LUD}) = \frac{1}{6}(n+K)^3 - \frac{1}{2}(n+K)^2 + \frac{1}{12}(n+K) + \frac{1}{6}n^3 - \frac{1}{6}n + \frac{1}{2}K(n^2+n) + Kn + (n+K) + \frac{1}{2}K(K+1)$$

$$= \Theta((n+K)^3)$$

$$N_{\text{mul}}(\text{LUD}) = \frac{1}{6}(n+K)^3 - (n+K)^2 + \frac{7}{12}(n+K) + \frac{1}{6}n^3 + \frac{1}{2}n^2 + \frac{1}{3}n + Kn + \frac{1}{2}K(K+1)$$

$$= \Theta((n+K)^3)$$

Here the notation  $\Theta$  indicates that for a given function  $g(n)$ ,  $\Theta(g(n))$  represents the set of functions such that

$$\Theta(g(n)) = \{f(n): \text{there exist positive constants } c_1, c_2, \text{ and } n_0 \text{ such that}$$

$$0 \leq c_1g(n) \leq f(n) \leq c_2g(n) \text{ for all } n \geq n_0\}$$

A function  $f(n)$  belongs to the set  $\Theta(g(n))$  if there exist positive constants  $c_1$  and  $c_2$  such that the function  $f(n)$  can be 'sandwiched' between  $c_1g(n)$  and  $c_2g(n)$ , for sufficiently large  $n$  (e.g., Cormen, Leiserson, and Rivest, 1990).

In addition, the amount of storage required in the LU decomposition algorithm is mainly determined by the size of the lower triangular matrix  $L$ , which is  $\Theta((n+K)^2)$ .

The advantages of the LU decomposition algorithm are that it is simple to implement, and performs conditioning simultaneously with simulation. Also it is not limited to particular forms of covariance functions and automatically handles anisotropies. The main drawbacks of this method are the amount of memory required, which increases with the square of the number of grid nodes and conditioning data, and the computing time which increases with the cube of the number of grid nodes and conditioning data. In practice, storage effectively limits this method to applications in at most two dimensions and with not more than several thousand grid nodes, which makes it inapplicable in the space-time domain.

Several attempts have been made to reduce storage limitations and calculations. Alabert (1987) introduced a way to reduce memory requirements by using this technique in conjunction with a moving neighborhood. The main drawback of this method is that the discontinuities between contiguous neighborhoods could alter the covariance structure, thus introducing additional noise and banding. Davis (1987b) introduced a matrix polynomial approximation method as a further development of the LU decomposition approach. Although this approach simplified some calculations, it did not reduce memory requirements. In 1993, Dietrich suggested an algorithm that under some specific conditions reduced the memory requirement from  $\Theta(m_1^2 m_2^2)$  to  $\Theta(2m_1^2 m_2)$ , where  $m_1$  denotes the number of grid rows,  $m_2$  denotes the number of grid columns, and the total number of grid nodes is  $m_1 \cdot m_2$ . In that same year Dowd and Sarac used a ring decomposition algorithm which, similar to Dietrich's approach, took advantage of the block Toeplitz property of covariance matrices to reduce memory requirements and calculations. To date, despite these improvements, problems concerning the amount of required storage and computing time still exist.

### 5.1.2 The Sequential Simulation Techniques

Based on the theorem of sequential simulation introduced by Johnson in 1987, Alabert (also in 1987) proposed the sequential indicator simulation (SIS) for categorical variable simulation, and Issaks in 1991, introduced the sequential Gaussian simulation (SGS) for continuous variable simulation. In 1992, Verly developed the joint sequential simulation (JSS) which expanded the sequential simulation technique from one Gaussian field to multiGaussian fields.

The SIS is implemented through a sequential procedure by means of indicator kriging, and generates conditional probabilities of RF  $X(\mathbf{u})$  at  $K$  locations  $\mathbf{u}_i$  for  $L$  thresholds  $x_l$   $\{\text{Prob}(X(\mathbf{u}_i) \leq x_l | (n)), i \text{ from } 1 \text{ to } K; l \text{ from } 1 \text{ to } L\}$ . The main advantage of sequential indicator simulation is the possibility of controlling  $L$  spatial covariances instead of a single one, as in other simulation techniques. For details about SIS and its development see Alabert (1987) and Journel (1989).

SGS has become the most extensively used algorithm for conditional simulations of continuous variables. SGS requires sampling from the following  $K$ -variant distribution posterior to the data set  $(n)$  (Isaaks, 1991):

$$f(\mathbf{u}_1, \dots, \mathbf{u}_K; x_1, \dots, x_K | (n)) = P(X(\mathbf{u}_1) \leq x_1, \dots, X(\mathbf{u}_K) \leq x_K | (n)) \quad (5.5)$$

with a density equal to the product of the  $K$  single-variate posterior probability density functions

$$f(x(\mathbf{u}_1), \dots, x(\mathbf{u}_K) | (n)) = f(x(\mathbf{u}_K) | (n+K-1)) \dots f(x(\mathbf{u}_1) | (n)) \quad (5.6)$$

where  $K$  denotes the number of grid nodes,  $n$  denotes the number of data, and  $\mathbf{u}_i$  denotes the locations of grid nodes. The posterior probability density functions are given by

$$f(\mathbf{u}_i; x_i | (n_i)) = N(m(x(\mathbf{u}_i) | (n_i)), \text{var}(x(\mathbf{u}_i) | (n_i))) \quad (5.7)$$

where  $N(m(x(\mathbf{u}_i) | (n_i)), \text{var}(x(\mathbf{u}_i) | (n_i)))$  denotes the normal probability density function of  $x(\mathbf{u}_i)$  with the mean  $m(x(\mathbf{u}_i) | (n_i))$  and the variance  $\text{var}(x(\mathbf{u}_i) | (n_i))$ , posterior to the information  $(n_i)$  ( $(n_i) = (n+i)$  indicates the data plus simulated values). Therefore the simulated value can be obtained by

$$x(\mathbf{u}_i | (n_i)) = E\{x(\mathbf{u}_i) | (n_i)\} + \sqrt{\text{var}(x(\mathbf{u}_i) | (n_i))} \cdot e_i \quad (5.8)$$

where the random number  $e_i \sim N(0,1)$ . The posterior mean and variance can be obtained from the following equation,

$$E\{x(\mathbf{u}_i) | (n_i)\} = m_i + C_{ii}^{-1}(\mathbf{x}_I - \mathbf{m}_I) \quad (5.9)$$

and

$$\text{var}(x(\mathbf{u}_i) | (n_I)) = C_{ii} - C_{ii} C_{II}^{-1} C_{ii} \quad (5.10)$$

Equation 5.8 can be rewritten as follows,

$$x(\mathbf{u}_i | (n_I)) = m_i + C_{ii} C_{II}^{-1} (\mathbf{x}_I - \mathbf{m}_I) + \sqrt{C_{ii} - C_{ii} C_{II}^{-1} C_{ii}} \cdot \mathbf{e}_i \quad (5.11)$$

where  $m_i$  and  $C_{ii}$  are the prior mean and variance of  $x(\mathbf{u}_i)$ ,  $\mathbf{m}_I$  and  $C_{II}$  denote respectively the prior mean vector and covariance matrix of the information  $(n_I)$ , vector  $\mathbf{x}_I$  denotes the values of the information  $(n_I)$ , and the vector  $C_{ii}$  denotes the covariances between  $x(\mathbf{u}_i)$  and  $(n_I)$ .

The implementation of SGS proceeds as follows:

1. define a path that visits each node of the grid (K);
2. at each node  $\mathbf{u}_i$  generate the simulated value by Equation 5.11;
3. add the simulated value into the data set;
4. proceed to the next node until all nodes are simulated.

### 5.1.2.1 Summary of the SGS Computations

The computation of SGS at the  $i$ th node during the sequential process involves the following:

- (1) The inverse of the lower triangular matrix of the covariance matrix,  $L_{II}^{-1}$ , requires  $N_{add}(LU, n+i-1) + N_{add}(INVERSE, n+i-1)$  additions and  $N_{mul}(LU, n+i-1) + N_{mul}(INVERSE, n+i-1)$  multiplications, obtaining

$$\begin{aligned} \# \text{ of additions: } & \frac{1}{6}(n+i-1)^3 - \frac{1}{2}(n+i-1)^2 + \frac{1}{12}(n+i-1) + \frac{1}{6}(n+i-1)^3 - \frac{1}{6}(n+i-1) \\ & = \frac{1}{3}(n+i-1)^3 - \frac{1}{2}(n+i-1)^2 + \frac{11}{12}(n+i-1) \end{aligned}$$

$$\begin{aligned} \# \text{ of multiplications: } & \frac{1}{6}(n+i-1)^3 - (n+i-1)^2 + \frac{7}{12}(n+i-1) + \frac{1}{6}(n+i-1)^3 + \frac{1}{2}(n+i-1)^2 + \frac{1}{3}(n+i-1) \\ & = \frac{1}{3}(n+i-1)^3 - \frac{1}{2}(n+i-1)^2 + \frac{11}{12}(n+i-1) \end{aligned}$$

- (2) since  $C_{ii} C_{II}^{-1} (\mathbf{x}_I - \mathbf{m}_I) = (L_{II}^{-1} C_{ii})' (L_{II}^{-1} (\mathbf{x}_I - \mathbf{m}_I))$  and  $C_{ii} C_{II}^{-1} C_{ii} = (L_{II}^{-1} C_{ii})' (L_{II}^{-1} C_{ii})$ , the computations of these two matrix products include the computations of  $(L_{II}^{-1} C_{ii})'$  and  $(L_{II}^{-1} (\mathbf{x}_I - \mathbf{m}_I))$ , requiring  $(n+i)(n+i-1) + 2(n+i-1)$  additions and  $(n+i)(n+i-1)$  multiplications, plus another  $(n+i-1)$  additions and multiplications. The total computation at this step requires  $(n+i-1)^2 + 4(n+i-1)$  additions and  $(n+i-1)^2 + 2(n+i-1)$  multiplications.

Thus, the total computation at the  $i$ th node includes approximately  $\frac{1}{3}(n+i-1)^3 - \frac{1}{2}(n+i-1)^2 + 4\frac{11}{12}(n+i-1)$  additions and  $\frac{1}{3}(n+i-1)^3 + \frac{1}{2}(n+i-1)^2 + 2\frac{11}{12}(n+i-1)$  multiplications. The overall computation of SGS can be approximated as follows:

$$\begin{aligned}
N_{\text{add}}(\text{SGS}) &\approx \sum_{i=1}^K \left[ \frac{1}{3}(n+i-1)^3 - \frac{1}{2}(n+i-1)^2 + 4\frac{11}{12}(n+i-1) \right] \\
&= \frac{1}{12}[(n+K)^2(n+K-1)^2 - n^2(n-1)^2] - \frac{1}{12}[(n+K-1)(n+K)(2(n+K)-1) - n(n-1)(2n-1)] + 4\frac{11}{12}K(n+K) \\
&= \Theta((n+K)^4) \\
N_{\text{mul}}(\text{SGS}) &= \sum_{i=1}^K \left[ \frac{1}{3}(n+i-1)^3 + \frac{1}{2}(n+i-1)^2 + 2\frac{11}{12}(n+i-1) \right] \\
&= \frac{1}{12}[(n+K)^2(n+K-1)^2 - n^2(n-1)^2] + \frac{1}{12}[(n+K-1)(n+K)(2(n+K)-1) - n(n-1)(2n-1)] + 2\frac{11}{12}K(n+K) \\
&= \Theta((n+K)^4)
\end{aligned}$$

SGS is much slower than the LU decomposition algorithm. This is because the number of computations required by SGS quadruple relative to the number of grid nodes and conditioning data. Also, the storage requirement increases with the square of the number of grid nodes and conditioning data, this makes the SGS algorithm impractical. In practice, the following so-called 'screen-effect approximation' (SEA) has to be used in the SGS implementation.

### 5.1.2.2 SGS Using the Screen-Effect Approximation

**Screen-effect approximation:** the probability density function at a node posterior to all information can be approximated by that posterior to the information closest to this node:

$$f(\mathbf{x}(\mathbf{u}_i) \mid (n_i)) \approx f(\mathbf{x}(\mathbf{u}_i) \mid (nn_i)) \quad (5.12)$$

where  $(nn_i)$  denotes the information within a neighborhood of  $\mathbf{u}_i$ ,  $(nn_i) \subseteq (n_i)$ .

Based on the SEA, the overall conditional density function is approximated by

$$f(\mathbf{x}(\mathbf{u}_1), \dots, \mathbf{x}(\mathbf{u}_K) \mid (n)) \approx f(\mathbf{x}(\mathbf{u}_K) \mid (nn_K)) \dots f(\mathbf{x}(\mathbf{u}_1) \mid (nn_1)) \quad (5.13)$$

Therefore, SGS is approximated by

$$\begin{aligned}
\mathbf{x}(\mathbf{u}_i \mid (n_i)) &\approx E\{\mathbf{x}(\mathbf{u}_i) \mid (nn_i)\} + \sqrt{\text{var}(\mathbf{x}(\mathbf{u}_i) \mid (nn_i))} \cdot \mathbf{e}_i \\
&= \mathbf{m}_i + \mathbf{C}_{ii} \mathbf{C}_{ii}^{-1} (\mathbf{x}_i - \mathbf{m}_i) + \sqrt{\mathbf{C}_{ii} - \mathbf{C}_{ii} \mathbf{C}_{ii}^{-1} \mathbf{C}_{ii}} \cdot \mathbf{e}_i
\end{aligned} \quad (5.14)$$

The implementation of SGS using the SEA is, in terms of the steps defined below,

1. define a path,
2. define a neighborhood for the node in question
3. calculate the mean and variance posterior to the information in this neighborhood
4. generate a value by Equation 5.14
5. add the simulated value into the data set
6. proceed to the next node and repeat the procedure until all nodes have been visited.

### 5.1.2.3 Summary of the SGS Computations Using the SEA

Define the upper bound of samples in a neighborhood as  $v$ , and assume that  $v$  is adopted as the neighborhood size at most nodes. In practice,  $v=10\sim 50$  on most occasions. There are two parts to the computation of SGS using the SEA at the  $i$ th node: (a) the operations for neighborhood searching, and (b) the operations involved in Equation 5.14.

Assuming that the optimal neighborhood searching algorithm is adopted in  $R^2 \times T$  using super blocks, then the average number of distance calculations involved in neighborhood searching at each node is approximately  $\alpha v$ , and each distance calculation requires 2 additions and 3 multiplications, where  $\alpha$  is a positive number and usually  $\alpha \leq v$ . The total number of additions involved in neighborhood searching is approximately  $2K\alpha v$ , and the total number of multiplications is approximately  $3K\alpha v$ .

Analogous to the discussion in Section 5.1.2.1, the computations involved in Equation 5.14 require  $K(\frac{1}{3}v^3 - \frac{1}{2}v^2 + 4\frac{11}{12}v + 3)$  additions and  $K(\frac{1}{3}v^3 + \frac{1}{2}v^2 + 2\frac{11}{12}v + 2)$  multiplications. The overall number of arithmetic operations can then be estimated as follows.

$$\begin{aligned}
 N_{\text{add}}(\text{SGS with SEA}) &\approx K\left(\frac{1}{3}v^3 - \frac{1}{2}v^2 + 4\frac{11}{12}v + 3\right) + 2K\alpha v \\
 &\approx K\left(\frac{1}{3}v^3 - \frac{1}{2}v^2 + 2K\alpha v\right) \\
 &= \Theta(Kv^3)
 \end{aligned}$$

$$\begin{aligned}
 N_{\text{mul}}(\text{SGS with SEA}) &\approx K\left(\frac{1}{3}v^3 + \frac{1}{2}v^2 + 2\frac{11}{12}v + 2\right) + 3K\alpha v \\
 &\approx K\left(\frac{1}{3}v^3 + \frac{1}{2}v^2 + 3K\alpha v\right) \\
 &= \Theta(Kv^3)
 \end{aligned}$$



$$\begin{aligned}
&= \mathbf{C}_{ii} \mathbf{L}_{ii}^{\tau-1} \mathbf{L}_{ii}^{-1} \mathbf{L}_{ii} \mathbf{w}_i \\
&= \mathbf{C}_{ii} \mathbf{C}_{ii}^{-1} \mathbf{L}_{ii} \mathbf{w}_i
\end{aligned}$$

Since  $\mathbf{L}_{ii} \mathbf{w}_i$  forms the values of the information ( $n_i$ ):  $\mathbf{L}_{ii} \mathbf{w}_i = \mathbf{x}_i - \mathbf{m}_i$ ,  $\mathbf{L}_i^{\tau} \mathbf{w}_i + \mathbf{m}_i$  is but the posterior mean,

$$\mathbf{L}_i^{\tau} \mathbf{w}_i + \mathbf{m}_i = \mathbf{C}_{ii} \mathbf{C}_{ii}^{-1} (\mathbf{x}_i - \mathbf{m}_i) + \mathbf{m}_i$$

As for the element  $\mathbf{L}_{n+i, n+i}$ , from  $\mathbf{C}_{ii} = \mathbf{L}_{ii}^{\tau} \mathbf{L}_{ii} + \mathbf{L}_{n+i, n+i}^2$  and  $\mathbf{L}_{ii}^{\tau} = \mathbf{C}_{ii} \mathbf{C}_{ii}^{-1} \mathbf{L}_{ii}$ , one obtains

$$\mathbf{L}_{n+i, n+i}^2 = \mathbf{C}_{ii} - \mathbf{L}_{ii}^{\tau} \mathbf{L}_{ii} = \mathbf{C}_{ii} - \mathbf{C}_{ii} \mathbf{C}_{ii}^{-1} \mathbf{C}_{ii}$$

Equation 5.15 can then be rewritten as follows,

$$\mathbf{x}_i = \mathbf{m}_i + \mathbf{C}_{ii} \mathbf{C}_{ii}^{-1} (\mathbf{x}_i - \mathbf{m}_i) + \sqrt{\mathbf{C}_{ii} - \mathbf{C}_{ii} \mathbf{C}_{ii}^{-1} \mathbf{C}_{ii}} \cdot \mathbf{w}_i$$

This is equivalent to Equation 5.11.

In practice SGS using the SEA is highly preferable to the LU decomposition algorithm since the computation is greatly reduced from  $\Theta((n+K)^3)$  to  $\Theta(Kv^3)$ . More importantly, the storage required is reduced from  $\Theta(K^2)$  to  $\Theta(v^2)$ , where  $v$  is the upper bound of samples in a neighborhood, as has been mentioned previously. This indicates that the storage problem which exists in the LU decomposition algorithm does not exist in SGS using the SEA. For convenience, SGS using the SEA will be referred to simply as SGS in all further discussion.

## 5.3 Sequential Group Gaussian Simulation

### 5.3.1 Problem Definition

The implementation of SGS is entirely based on the computation of the kriging system. As Chapter 4 indicates, the spatiotemporal kriging system is quite similar to the spatial kriging system, the difference being that the covariances are obtained by space-time covariance models. This implies that SGS is applicable to conditional simulations of spatiotemporal processes.

The implementation of SGS is actually a node-by-node sequential process, implying that neighborhood searching and a kriging operation are required at each node. In practice, the simulation grid is usually large and dense, which usually leads to overlapping of neighborhoods among closest nodes (see Figure 5.1). Therefore, it is rational to consider sharing neighborhood searching and kriging operations among closest nodes.

The sequential group Gaussian simulation (SGGS), proposed in this section, takes advantage of neighborhood sharing for closest nodes. Analogous to SGS, SGGS is also a sequential process. However, this sequential process is performed from one group of closest nodes to the next group rather than node by node, and simulated values of each group are generated simultaneously.

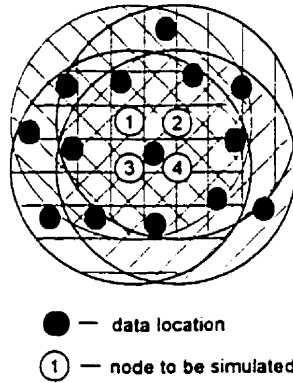


Figure 5.1 Four neighborhoods of four closest nodes are overlapped.

### 5.3.2 Theory

Cluster the  $K$  nodes into  $k$  groups such that the nodes in each group are close to each other:  $(K_1) = (\mathbf{u}_1, \dots, \mathbf{u}_{K_1}), \dots, (K_k) = (\mathbf{u}_{K_{k-1}+1}, \dots, \mathbf{u}_K), K_1 + \dots + K_k = K$ . Analogous to SGS which partitions the posterior probability density into  $K$  posterior probability densities for  $K$  nodes, we can decompose the posterior probability density into  $k$  posterior probability densities for  $k$  groups of  $K$  nodes,

$$f(\mathbf{x}(\mathbf{u}_1), \dots, \mathbf{x}(\mathbf{u}_K) | (n)) = f((K_k) | (n+K-K_k)) \dots f((K_1) | (n)) \quad (5.16)$$

If we denote the neighborhood of the  $i$ th group  $(K_i)$  by  $(nn_i)$ ,  $i, I = 1$  to  $K$ , then Equation 5.18 can be approximated with the SEA as follows,

$$f(\mathbf{x}(\mathbf{u}_1), \dots, \mathbf{x}(\mathbf{u}_K) | (n)) \approx f((K_k) | (nn_k)) \dots f((K_1) | (nn_1)) \quad (5.17)$$

The posterior probability density of the  $i$ th group,  $f((K_i) | (nn_i))$ , is determined by the following posterior mean vector and posterior covariance matrix,

$$E\{(K_i) | (nn_i)\} = \mathbf{m}_i + \mathbf{C}_{ii} \mathbf{C}_{ii}^{-1} (\mathbf{x}_i - \mathbf{m}_i) \quad (5.18)$$

and

$$\mathbf{C}((K_i) | (nn_i)) = \mathbf{C}_{ii,1} = \mathbf{C}_{ii} - \mathbf{C}_{ii} \mathbf{C}_{ii}^{-1} \mathbf{C}_{ii} \quad (5.19)$$

where vector  $\mathbf{m}_i$  and  $\mathbf{m}_i$  respectively denote the original means of  $(K_i)$  and of  $(nn_i)$ ; vector  $\mathbf{x}_i$  denotes the information in the neighborhood,  $\mathbf{C}_{ii}^{-1}$  denotes the inverse of the prior

covariance matrix of  $(n_{n_i})$ ,  $C_{ii}$  denotes the covariance matrix of  $(K_i)$ , and vector  $C_{ii}^T = C_{ii}$  denotes the prior covariances between  $(K_i)$  and  $(n_{n_i})$ . Let  $C_{ii} = L_{ii} L_{ii}^T$ , where  $L_{ii}$  is the lower triangular matrix of  $C_{ii}$ , then the simulated values of the  $i$ th group can be obtained by

$$\mathbf{x}((K_i) | (n_{n_i})) = \mathbf{m}_i + C_{ii} C_{ii}^{-1} (\mathbf{x}_I - \mathbf{m}_I) + L_{ii} \mathbf{e}_i \quad (5.20)$$

where the vector of random numbers  $\mathbf{e}_i \sim N(\mathbf{0}, \mathbf{I})$ .

For convenience, the number of nodes in most groups can be identically designed, that is,  $K_1 = \dots = K_k = \kappa$  and  $K = k \cdot \kappa$ , the proposed algorithm can then be defined by the  $\kappa$ -SGGS. Notice that when  $\kappa = 1$ , the 1-SGGS is but SGS; and when  $\kappa = K$ , the  $K$ -SGGS is exactly equivalent to the LU decomposition algorithm. Therefore, SGGS is a series of sequential Gaussian simulation algorithms associated with different group sizes which progresses from SGS to the LU decomposition algorithm.

### 5.3.3 Summary of the SGGS Computations

Recall that the upper bound  $v$  is assumed to be the neighborhood size for most groups. Corresponding to the discussion of SGS using the SEA, the computations of SGGS for each group can be summarized as follows

- (1) the implementation of neighborhood searching discussed in Section 5.1.2.3, requires  $(2\beta-1)\alpha v$  additions and  $(\beta+1)\alpha v$  multiplications, where  $\alpha$  and  $\beta$  are constants as mentioned in Section 5.1.2.3.
- (2) the computation of  $L_{ii}^{-1}$  for a given  $C_{ii}$  requires  $\frac{1}{3}v^3 - \frac{1}{2}v^2 + \frac{11}{12}v$  additions and  $\frac{1}{3}v^3 - \frac{1}{2}v^2 + \frac{11}{12}v$  multiplications;
- (3) the computation of two matrix products,  $C_{ii} C_{ii}^{-1} (\mathbf{x}_I - \mathbf{m}_I) = (L_{ii}^{-1} C_{ii}) (L_{ii}^{-1} (\mathbf{x}_I - \mathbf{m}_I))$  and  $C_{ii}^{-1} (L_{ii}^{-1} C_{ii}) (L_{ii}^{-1} C_{ii})$ , requires  $\frac{1}{2}v(v+1)(\kappa+1) + \kappa v + \kappa^2 v + \kappa^2 + v$  additions and  $\frac{1}{2}v(v+1)(\kappa+1) + \kappa v + \kappa^2 v$  multiplications.
- (4) the computation of  $L_{ii}$  from a given  $C_{ii}$  requires  $N_{\text{add}}(\text{LU}, \kappa) = \frac{1}{6}\kappa^3 - \frac{1}{2}\kappa^2 + \frac{1}{12}\kappa$  additions and  $N_{\text{mul}}(\text{LU}, \kappa) = \frac{1}{6}\kappa^3 - \kappa^2 + \frac{7}{12}\kappa$  multiplications.
- (5) the computation of the matrix product  $L_{ii} \mathbf{e}_i$  requires  $\frac{1}{2}\kappa(\kappa+1)$  additions and multiplications.
- (6) the addition of  $(\mathbf{m}_i + C_{ii} C_{ii}^{-1} (\mathbf{x}_I - \mathbf{m}_I))$  and  $(L_{ii} \mathbf{e}_i)$  requires  $\kappa$  additions.

The total number of computations in SGGS can be estimated as follows.

$$\begin{aligned}
N_{\text{add}}(\text{SGGS}) &\approx \frac{K}{\kappa} \left[ (2\beta-1)\alpha v + \frac{1}{3}v^3 - \frac{1}{2}v^2 + \frac{11}{12}v + \frac{1}{2}v(v+1)(\kappa+1) + \kappa v + \kappa^2 v + \kappa^2 + v \right. \\
&\quad \left. + \frac{1}{6}\kappa^3 - \frac{1}{2}\kappa^2 + \frac{1}{12}\kappa + \frac{1}{2}\kappa(\kappa+1) + \kappa \right] \\
&\approx \frac{K}{\kappa} \left[ \frac{1}{3}v^3 - \frac{1}{2}v^2 + \frac{1}{2}\kappa v^2 + \frac{1}{2}\kappa v + \kappa^2 v + \frac{1}{2}\kappa^2 + \frac{1}{6}\kappa^3 \right] \\
&= \frac{K}{\kappa} \left[ \frac{1}{6}(\kappa+v)^3 + \frac{1}{6}v^3 + \frac{1}{2}\kappa^2 v - \frac{1}{2}v^2 + \frac{1}{2}\kappa v + \frac{1}{2}\kappa^2 \right] \\
&= \Theta\left(\frac{K}{\kappa}(\kappa+v)^3\right)
\end{aligned}$$

$$\begin{aligned}
N_{\text{mul}}(\text{SGGS}) &\approx \frac{K}{\kappa} \left[ (\beta+1)\alpha v + \frac{1}{3}v^3 - \frac{1}{2}v^2 + \frac{11}{12}v + \frac{1}{2}v(v+1)(\kappa+1) + \kappa v + \kappa^2 v \right. \\
&\quad \left. + \frac{1}{6}\kappa^3 - \kappa^2 + \frac{7}{12}\kappa + \frac{1}{2}\kappa(\kappa+1) \right] \\
&\approx \frac{K}{\kappa} \left[ \frac{1}{3}v^3 + \frac{1}{2}\kappa v^2 + \frac{1}{2}\kappa v + \kappa^2 v + \frac{1}{6}\kappa^3 - \frac{1}{2}\kappa^2 \right] \\
&= \frac{K}{\kappa} \left[ \frac{1}{6}(\kappa+v)^3 + \frac{1}{6}v^3 + \frac{1}{2}\kappa^2 v + \frac{1}{2}\kappa v - \frac{1}{2}\kappa^2 \right] \\
&= \Theta\left(\frac{K}{\kappa}(\kappa+v)^3\right)
\end{aligned}$$

where  $\frac{K}{\kappa}$  indicates the number of groups. Since

$$\frac{K}{6\kappa}(\kappa+v)^3 \leq N_{\text{add}}(\text{SGGS}) \leq \frac{K}{3\kappa}(\kappa+v)^3$$

and

$$\frac{K}{6\kappa}(\kappa+v)^3 \leq N_{\text{mul}}(\text{SGGS}) \leq \frac{K}{3\kappa}(\kappa+v)^3$$

one may estimate  $N_{\text{add}}(\text{SGGS})$  and  $N_{\text{mul}}(\text{SGGS})$  by  $\alpha_{\text{add}}\frac{K}{\kappa}(\kappa+v)^3$  and  $\alpha_{\text{mul}}\frac{K}{\kappa}(\kappa+v)^3$ , where the constants  $\alpha_{\text{add}}$  and  $\alpha_{\text{mul}}$  are between  $\frac{1}{6}$  and  $\frac{1}{3}$ :  $\frac{1}{6} \leq \alpha_{\text{add}}, \alpha_{\text{mul}} \leq \frac{1}{3}$ . Furthermore, assuming that the cost to perform an addition is  $a_{\text{add}}$  and the cost of an multiplication is  $a_{\text{mul}}$ , the total cost of all total arithmetic operations can be estimated as the following,

$$N_{\text{total}}(\text{SGGS}) = N_{\text{add}}(\text{SGGS}) + N_{\text{mul}}(\text{SGGS}) \approx (\alpha_{\text{add}}a_{\text{add}} + \alpha_{\text{mul}}a_{\text{mul}})\frac{K}{\kappa}(\kappa+v)^3 = b\frac{K}{\kappa}(\kappa+v)^3$$

where  $b = \alpha_{\text{add}}a_{\text{add}} + \alpha_{\text{mul}}a_{\text{mul}}$ .

Note that when  $\kappa=1$ , the computation of SGGS is  $\Theta(K(1+v)^3) = \Theta(Kv^3)$ . This is consistent with the computation of SGS since the 1-SGGS is but SGS. When  $\kappa=K$ ,

implying  $v=n$ , the computation is  $\Theta((n+K)^3)$ , this is consistent with the computation of the LU decomposition algorithm since the K-SGGS is but the LU decomposition algorithm.

### 5.3.4 Optimal SGGS in Terms of Group Size

Equation 5.20 indicates that the computing time is determined by the upper bound  $v$  and the group size  $\kappa$ . In practice, it is interesting to discuss the optimal group size  $\kappa$  for a given upper bound  $v$ , with regard to computations. The derivative of  $N_{\text{total}}(\text{SGGS})$  is given by

$$\frac{d}{d\kappa}N_{\text{total}}(\text{SGGS}) \approx \frac{d}{d\kappa}\left[b\frac{K}{\kappa}(\kappa+v)^3\right] = \frac{bK(\kappa+v)^2(2v-\kappa)}{\kappa^2} \quad (5.21)$$

Formula 5.21 indicates that the computing time decreases when the group size,  $\kappa$ , increases from 1 to  $0.5v$ , then, the computing time increases when  $\kappa$  increases after  $0.5v$ . Therefore, the optimal SGGS is the  $0.5v$ -SGGS.

If we substitute  $\kappa$  with  $0.5v$ , the arithmetic operations of the  $0.5v$ -SGGS can be approximated as follows,

$$\begin{aligned} N_{\text{add}}(0.5v\text{-SGGS}) &\approx \frac{2K}{v}\left[\frac{1}{6}\left(\frac{3}{2}v\right)^3 + \frac{1}{6}v^3 + \frac{1}{8}v^3 - \frac{1}{2}v^2 + \frac{3}{4}v^2 + \frac{1}{8}v^2\right] \\ &= K\left(\frac{41}{24}v^2 - \frac{9}{8}v\right) \\ N_{\text{mul}}(0.5v\text{-SGGS}) &\approx \frac{2K}{v}\left[\frac{1}{6}\left(\frac{3}{2}v\right)^3 + \frac{1}{6}v^3 + \frac{1}{8}v^3 + \frac{3}{4}v^2 - \frac{1}{8}v^2\right] \\ &= K\left(\frac{41}{24}v^2 + \frac{5}{4}v\right) \\ &\approx K\left(\frac{1}{3}v^3 + \frac{1}{2}v^2\right) \end{aligned}$$

It is interesting to compare the  $0.5v$ -SGGS and SGS in terms of arithmetical operations. The ratio of additions of these two algorithms is approximated by

$$\frac{N_{\text{add}}(0.5v\text{-SGGS})}{N_{\text{add}}(\text{SGS})} \approx \frac{\frac{41}{24}v^2 - \frac{9}{8}v}{\frac{1}{3}v^3 - \frac{1}{2}v^2} = \frac{41v - 27}{8v^2 - 12v}$$

and the ratio of multiplications is approximated by

$$\frac{N_{\text{mul}}(0.5v\text{-SGGS})}{N_{\text{mul}}(\text{SGS})} \approx \frac{\frac{41}{24}v^2 + \frac{5}{4}v}{\frac{1}{3}v^3 + \frac{1}{2}v^2} = \frac{41v + 30}{8v^2 + 12v}$$

Figure 5.2 shows these ratios vs. the neighborhood size  $v$ . The ratio of additions is very similar to that of multiplications, and both indicate that the larger the neighborhood size chosen in the sequential simulation process, the better the  $0.5v$ -SGGS as opposed to SGS. The  $0.5v$ -SGGS is roughly 2 times faster than SGS if  $v = 10$ , and roughly 10 times faster than SGS when  $v$  reaches 50.

Note that the SEA causes a smaller error in the  $0.5v$ -SGGS than in SGS. As will be mentioned later in Section 5.4, the larger neighborhood size, the smaller the error caused by the SEA. In SGS, the neighborhood size is not more than  $v$ ; while in SGGS, the neighborhood size of the first node in a group is  $v$ , but the size of the second node becomes  $v+1$ , then  $v+2$ , ..., and the last one is  $v+\kappa-1$ . This indicates that the  $0.5v$ -SGGS is preferable to SGS not only in computing time, but also in precision .

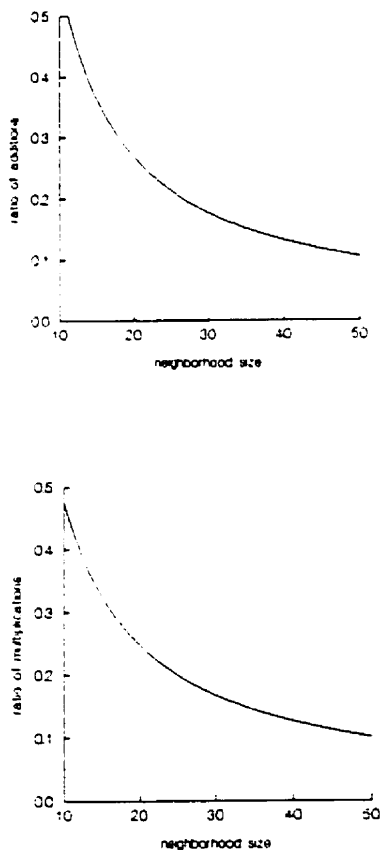


Figure 5.2 The arithmetic operation ratios between the  $0.5v$ -SGGS and SGS vs. neighborhood size.

### 5.3.5 Implementation Process of SGGS

The implementation of SGGS proceeds as follows:

1. Define an external path that visits each group in the grid, and an internal path that visits all nodes in each group;
2. Find a neighborhood for the current group to be simulated;
3. Calculate the posterior mean vector and the posterior covariance matrix of the current group by Equation 5.18 and 5.19;
4. Generate the simulated values of the current group by Equation 5.20;
5. Add the simulated values of the current group into the data set;
6. Proceeds to the next group until all groups are simulated.

An important characteristic of SGGS is that it uses two paths to visit all grid nodes: an internal path and an external path. A sequential path in the sequential simulation algorithms has the great advantage of saving time, since the configuration of simulated values selected in the neighborhood can be fixed so that no searching time is required, and its covariance matrix will be invariant for most nodes. However, a sequential path generates anisotropic artifacts, and this leads to a random path solution in SGS, at the cost of computing time (e.g., Isaaks, 1991).

Fortunately, a proper internal path may provide a way to successfully reduce the amount of artifacts caused by a sequential external path. One option is the inverse-direction path, illustrated by Figure 5.3. Also, one may choose several random paths for the internal path design to reduce the number of artifacts. For example, we design 10 unique random paths. During the sequential process the internal path of each group is randomly chosen from these 10 paths. The reduction of artifacts is based on both the group size and the number of random paths. The larger the group size and the more random paths, the greater the reduction of artifacts.

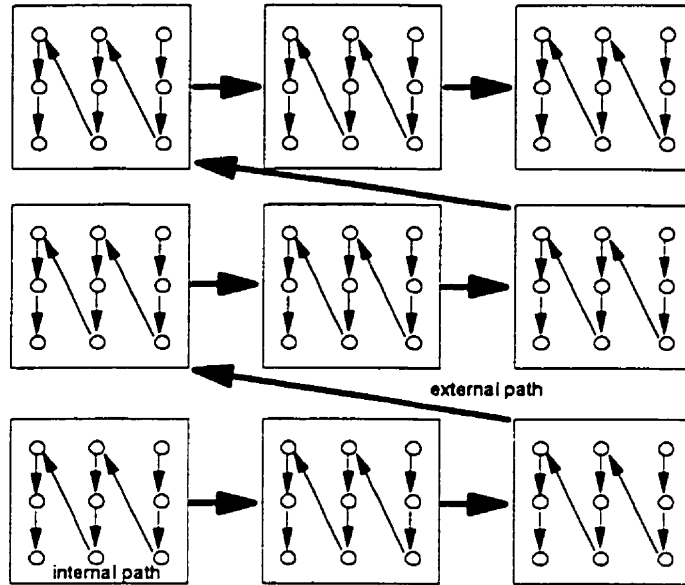


Figure 5.3 An inverse-direction combination of an internal path and an external path.

### 5.3.6 The SEA Loss

The computing time of the 0.5v-SGGS increases quadratically with the neighborhood size, indicating that a smaller neighborhood size is always preferred in terms of computing time. On the other hand, however, a smaller neighborhood size will cause a larger precision loss, therefore a larger neighborhood size is favorable in accounting for precision requirement. Therefore, a good sequential simulation should balance the precision requirement and the computing time. To measure the precision loss caused by the SEA, the following definition is useful.

**Definition 5.1** the SEA loss at a node  $\mathbf{u}_i$  can be defined as the mean square difference between the simulated value generated by the information in the neighborhood and the simulated value generated by all information,

$$\rho[x(\mathbf{u}_i) | (nn_i), (n_T)] = \frac{1}{2} E \{ x(\mathbf{u}_i | (nn_i)) - x(\mathbf{u}_i | (n_T)) \}^2 \quad (5.22)$$

In order to simplify Equation 5.22, we first introduce the following property of posterior covariances.

**Property 5.1.** The covariance of  $z(u_i)$  and  $z(u_j)$  posterior to  $(k)$ ,  $C_{ij,k} = \text{cov}[z(u_i), z(u_j) | (k)]$ , equals to zero if (i) one of  $z(u_i)$ ,  $z(u_j)$  has no correlation with the other and with the information  $(k)$ , or (ii)  $z(u_i) \subseteq (k)$  or  $z(u_j) \subseteq (k)$ .

Proof.

(i) Suppose  $z(u_i)$  has no correlation with  $z(u_j)$  and with the information  $(k)$ , then

$$C_{ij} = C_{kj} = 0$$

this leads to

$$C_{ij,k} = C_{ij} - C_{ik} C_{kk}^{-1} C_{kj} = 0 - 0 C_{kk}^{-1} C_{kj} = 0$$

(ii) Assume  $z(u_i) \subseteq (k)$ , then vector

$$C_{ik} = [\text{Cov}(z(u_i), z(u_1)), \dots, \text{Cov}(z(u_i), z(u_i)), \dots, \text{Cov}(z(u_i), z(u_k))]$$

is but a row of the covariance matrix of  $(k)$ ,  $C_{kk}$ , which entails

$$C_{ik} C_{kk}^{-1} = (0, \dots, 0, 1, 0, \dots, 0)$$

this is a row with all zeros except the  $i$ th element being one. Consequently,

$$C_{ik} C_{kk}^{-1} C_{kj} = C_{ij}$$

then the posterior covariance

$$C_{ij,k} = C_{ij} - C_{ik} C_{kk}^{-1} C_{kj} = 0$$

Therefore the above property is true.

The SEA loss can be further developed as follows,

$$\begin{aligned} \rho[x(u_i) | (nn_i), (n_i)] &= \frac{1}{2} E\{[x(u_i) | (nn_i) - x(u_i) | (n_i)]^2\} \\ &= \frac{1}{2} E\{[E\{x(u_i) | (nn_i)\} + \sqrt{\text{var}(x(u_i) | (nn_i))} \cdot e_i - E\{x(u_i) | (n_i)\} - \sqrt{\text{var}(x(u_i) | (n_i))} \cdot e_i]^2\} \\ &= \frac{1}{2} E\{[E\{x(u_i) | (nn_i)\} - E\{x(u_i) | (n_i)\}]^2 + \frac{1}{2} [\sqrt{\text{var}(x(u_i) | (nn_i))} - \sqrt{\text{var}(x(u_i) | (n_i))}]^2\} \end{aligned}$$

Since

$$\begin{aligned} E\{[E\{x(u_i) | (nn_i)\} - E\{x(u_i) | (n_i)\}]^2\} &= E\{[\mu_i + C_{ii} C_{ii}^{-1} (x_i - \mu_i) - \mu_i - C_{ii} C_{ii}^{-1} (x_i - \mu_i)]^2\} \\ &= C_{ii} C_{ii}^{-1} C_{ii} + C_{ii} C_{ii}^{-1} C_{ii} - 2 C_{ii} C_{ii}^{-1} C_{ii} C_{ii}^{-1} C_{ii} \\ &= C_{ii} C_{ii}^{-1} C_{ii} - C_{ii} C_{ii}^{-1} C_{ii} + 2(C_{ii} C_{ii}^{-1} C_{ii} - C_{ii} C_{ii}^{-1} C_{ii} C_{ii}^{-1} C_{ii}) \\ &= \text{var}[x(u_i) | (nn_i)] - \text{var}[x(u_i) | (n_i)] + 2(C_{ii} C_{ii}^{-1} C_{ii,i}) \end{aligned}$$

where  $C_{ii,i}$  denotes a vector of posterior covariances. Note that  $(nn_i) \subseteq (n_i)$ , according to Property 5.1,  $C_{ii,i} = 0$ . This entails

$$E\{[E\{x(u_i) | (nn_i)\} - E\{x(u_i) | (n_i)\}]^2\} = \text{var}[x(u_i) | (nn_i)] - \text{var}[x(u_i) | (n_i)] \quad (5.23)$$

and

$$\begin{aligned}\rho[x(\mathbf{u}_i) | (nn_i), (n_i)] &= \frac{1}{2} \{ (\text{var}[x(\mathbf{u}_i) | (nn_i)] - \text{var}[x(\mathbf{u}_i) | (n_i)]) \\ &\quad + (\sqrt{\text{var}[x(\mathbf{u}_i) | (nn_i)]} - \sqrt{\text{var}[x(\mathbf{u}_i) | (n_i)]})^2 \} \\ &= \text{var}[x(\mathbf{u}_i) | (nn_i)] (1.0 - \sqrt{\text{var}[x(\mathbf{u}_i) | (n_i)] / \text{var}[x(\mathbf{u}_i) | (nn_i)]}) \quad (5.24)\end{aligned}$$

Equation 5.24 indicates that the SEA loss is only determined by two posterior variances  $\text{var}[x(\mathbf{u}_i) | (nn_i)]$  and  $\text{var}[x(\mathbf{u}_i) | (n_i)]$ . Furthermore the SEA loss has the following properties:

1. The SEA loss is positive:

$$\rho[x(\mathbf{u}_i) | (nn_i), (n_i)] \geq 0$$

2. The SEA loss is monotonic decreasing with regard to increasing data in the neighborhood:

$$\begin{aligned}\rho[x(\mathbf{u}_i) | (nn_{i+1}), (n_i)] &= \frac{1}{2} \{ (\text{var}[x(\mathbf{u}_i) | (nn_{i+1})] - \text{var}[x(\mathbf{u}_i) | (n_i)]) \\ &\quad + (\sqrt{\text{var}[x(\mathbf{u}_i) | (nn_{i+1})]} - \sqrt{\text{var}[x(\mathbf{u}_i) | (n_i)]})^2 \} \\ &\leq \frac{1}{2} \{ (\text{var}[x(\mathbf{u}_i) | (nn_i)] - \text{var}[x(\mathbf{u}_i) | (n_i)]) \\ &\quad + (\sqrt{\text{var}[x(\mathbf{u}_i) | (nn_i)]} - \sqrt{\text{var}[x(\mathbf{u}_i) | (n_i)]})^2 \} \\ &= \rho[x(\mathbf{u}_i) | (nn_i), (n_i)]\end{aligned}$$

The SEA loss will be zero when the neighborhood  $(nn_i)$  expands to include all information  $(n_i)$ ,

$$\rho[x(\mathbf{u}_i) | (n_i), (n_i)] = 0$$

3. The SEA loss is monotonic increasing with regard to increasing overall information:

$$\begin{aligned}\rho[x(\mathbf{u}_i) | (nn_i), (n_{i+1})] &= \frac{1}{2} \{ (\text{var}[x(\mathbf{u}_i) | (nn_i)] - \text{var}[x(\mathbf{u}_i) | (n_{i+1})]) \\ &\quad + (\sqrt{\text{var}[x(\mathbf{u}_i) | (nn_i)]} - \sqrt{\text{var}[x(\mathbf{u}_i) | (n_{i+1})]})^2 \} \\ &\geq \frac{1}{2} \{ (\text{var}[x(\mathbf{u}_i) | (nn_i)] - \text{var}[x(\mathbf{u}_i) | (n_i)]) \\ &\quad + (\sqrt{\text{var}[x(\mathbf{u}_i) | (nn_i)]} - \sqrt{\text{var}[x(\mathbf{u}_i) | (n_i)]})^2 \} \\ &= \rho[x(\mathbf{u}_i) | (nn_i), (n_i)]\end{aligned}$$

- (5) The SEA loss is bounded between 0 and  $\text{var}[x(\mathbf{u}_i) | (nn_i)]$ :

$$0 \leq \rho[x(\mathbf{u}_i) | (nn_i), (n_i)] \leq \text{var}[x(\mathbf{u}_i) | (nn_i)]$$

It might be more meaningful to consider the following relative SEA loss:

$$\begin{aligned}R[x(\mathbf{u}_i) | (nn_i), (n_i)] &= \rho[x(\mathbf{u}_i) | (nn_i), (n_i)] / \text{var}[x(\mathbf{u}_i) | (nn_i)] \\ &= 1.0 - \sqrt{\text{var}[x(\mathbf{u}_i) | (n_i)] / \text{var}[x(\mathbf{u}_i) | (nn_i)]} \quad (5.25)\end{aligned}$$

The RSEA loss is within the interval  $[0, 1]$ . The information behind the RSEA loss is straightforward: decreasing of the RSEA loss is directly associated with decreasing of the difference between two posterior variances, and the RSEA loss reaches zero when these

posterior variances become identical. An advantage of the RSEA loss is that it is only affected by the grid, the range, and the type of the covariance model, without any effect from the sill.

After the definition of the RSEA loss, our next concern is to assess it in different grid designs using different covariance models.

### 5.3.6.1 Assessment of the RSEA loss

This section concentrates on the assessment of the upper bound of the SEA loss for a given grid ratio  $l/a$  ( $a$  is the range and  $l$  is the lag of the grid) and a given covariance model. Two popular covariance models are discussed: the spherical model and exponential model. The discussion of the Gaussian model will be mentioned at the end of this section, as a counterpart example.

The RSEA loss for a given grid ratio reaches its upper bound when  $\text{var}[x(\mathbf{u}_i) | (n_{\mathbf{t}})]$  reaches its lower bound and  $\text{var}[x(\mathbf{u}_i) | (n_{\mathbf{t}})]$  reaches its upper bound simultaneously. The lower bound of  $\text{var}[x(\mathbf{u}_i) | (n_{\mathbf{t}})]$  is given by

$$\min_{n_{\mathbf{t}}} \text{var}[x(\mathbf{u}_i) | (n_{\mathbf{t}})] = \lim_{n_{\mathbf{t}} \rightarrow \infty} \text{var}[x(\mathbf{u}_i) | (n_{\mathbf{t}})] = \text{var}[x(\mathbf{u}_i) | (\infty)]$$

and the upper bound of  $\text{var}[x(\mathbf{u}_i) | (n_{\mathbf{t}})]$  is given by

$$\max_{n_{\mathbf{t}}} \text{var}[x(\mathbf{u}_i) | (n_{\mathbf{t}})] = \lim_{n_{\mathbf{t}} \rightarrow 1} \text{var}[x(\mathbf{u}_i) | (n_{\mathbf{t}})] = \text{var}[x(\mathbf{u}_i) | (1)]$$

where  $\text{var}[x(\mathbf{u}_i) | (\infty)]$  denotes the variance posterior to the information on the whole grid and  $\text{var}[x(\mathbf{u}_i) | (1)]$  denotes the variance posterior to the closest datum. One may get

$$R[x(\mathbf{u}_i) | (n_{\mathbf{t}}), (n_{\mathbf{t}})] \leq 1.0 - \sqrt{\text{var}[x(\mathbf{u}_i) | (\infty)] / \text{var}[x(\mathbf{u}_i) | (1)]}$$

$\text{var}[x(\mathbf{u}_i) | (\infty)]$  converges very fast for a given grid design, that is, for a given grid ratio,

$$\text{var}[x(\mathbf{u}_i) | (\infty)] \approx \text{var}[x(\mathbf{u}_i) | (n_{\mathbf{t}})]$$

where  $(n_{\mathbf{t}})$  is a neighborhood of considerably small size ( $n_{\mathbf{t}} < 50$ ). This can be demonstrated by the following configuration design:  $\text{var}[x(\mathbf{u}_i) | (n_{\mathbf{t}})]$  is calculated sequentially by considering the 8 closest data locations around  $\mathbf{u}_i$  (see Figure 5.4(a)), then the 24 closest locations (see Figure 5.4(b)), then the 48 closest locations (see Figure 5.4(c)), etc.. The results of  $\text{var}[x(\mathbf{u}_i) | (n_{\mathbf{t}})]$  for both the spherical model and exponential model are shown in Figure 5.5 and 5.6, indicating that  $\text{var}[x(\mathbf{u}_i) | (\infty)]$  can be approximated sufficiently by considering only 48 closest locations around  $\mathbf{u}_i$ ,

$$\text{var}[x(\mathbf{u}_i) | (\infty)] \approx \text{var}[x(\mathbf{u}_i) | (48)]$$

On the other hand,  $\text{var}[x(\mathbf{u}_i) | (1)]$  is given by

$$\text{var}[x(\mathbf{u}_i) | (1)] = C(0) - C(h)^2/C(0)$$

where  $h$  denotes the distance of the closest datum. Figure 5.7 and 5.8 show the lower bounds of the RSEA loss of the exponential model and spherical model with the grid ratio changing from 0.001 to 0.5, implying (i) the upper bound of the RSEA loss is decreasing when the grid ratio is increasing, and (ii) the upper bound is between 0.0 and 0.42.

### 5.3.6.2 Optimal size of neighborhood with required RSEA loss

The RSEA loss of both the exponential model and the spherical model is, in practice, much smaller than its upper bound, this makes SGGS appropriate and reliable. To show practical variations of the RSEA loss, the data configuration and the neighborhood are designed as follows. Randomly pick up 120 nodes from a  $21 \times 21$  grid around the node to be simulated, these nodes construct the configuration of the information, thus the simulated node ratio =  $\frac{\text{simulated nodes}}{\text{all nodes}} \approx \frac{1}{4}$ . Partition the area into 4 sub-areas, and select the closest node in each sub-area to construct a 4-location neighborhood, then calculate the RSEA loss. Next choose the two closest nodes in each sub-area to construct an 8-location neighborhood, again calculate the RSEA loss. As the neighborhood is continually extended, the variation of the RSEA loss is apparent. This process can be repeated many times to get a reliable evaluation of the RSEA loss.

Figure 5.9 shows the results of the RSEA loss for the exponential model with  $1/a = 0.01, 0.05, \text{ and } 0.1$  with 50 repetitions. Based on these results, the optimal size of the neighborhood of the exponential model with two RSEA loss requirements (5% and 1%) is shown in Table 5.1. In general the optimal size decreases when the grid ratio increases. When the grid ratio larger than 0.1, under the 5% RSEA loss requirement it is enough to pick up only 1 datum in each sub-area to construct a 4 point data neighborhood.

Table 5.1 Optimal size of the neighborhood for the exponential model.

grid ratio ( $1/a$ )	optimal size (the RSEA loss < 5%)	optimal size (the RSEA loss < 1%)
$\leq 0.01$	2x4	5x4
$> 0.01 \ \& \ \leq 0.1$	2x4	4x4
$> 0.1$	1x4	3x4

The RSEA loss does not vary monotonically for the spherical model, this is demonstrated in Figure 5.10, 5.11, and 5.12. It is interesting to note that the RSEA loss is very small and roughly invariant when the grid ratio is not more than 0.05, but it increases a considerable amount when the grid ratio is between 0.07 and 0.25, then it decreases rapidly when the grid ratio is over 0.25. The optimal size of the neighborhood with respect to different grid ratios is given in Table 5.2.

Table 5.2 Optimal size of the neighborhood for the spherical model.

grid ratio ( $l/a$ )	optimal size (the RSEA loss < 5%)	optimal size (the RSEA loss < 1%)
$\leq 0.07$	2x4	6x4
$> 0.07 \ \& \ \leq 0.17$	5x4	not available
$> 0.17 \ \& \ \leq 0.25$	5x4	9x4
$> 0.25$	2x4	5x4

Both the exponential and the spherical model demonstrate the presence of the screen effect. This effect is sufficient that a small neighborhood can fulfill the 5% RSEA loss requirement, thereby ensuring the success of the SGGS implementation.

Unfortunately, the success of SGGS for the exponential and spherical models does not indicate that it is applicable for any covariance model, and a counterpart example is the Gaussian model. Figure 5.13 shows the RSEA loss of the Gaussian model with the grid ratio = 0.15, 0.20, and 0.25, indicating that the RSEA loss increases when the grid ratio decreases. When the grid ratio is less than 0.25, the RSEA loss is fairly high ( $\gg 5\%$ ), this infers that SGGS is much less effective for the Gaussian model in most applications.

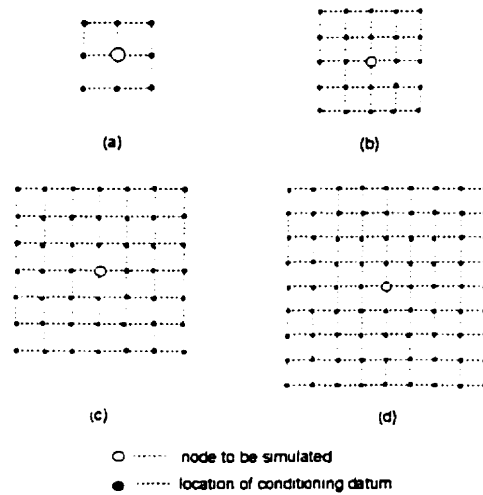


Figure 5.4 Four neighborhoods with regular grid: 8, 24, 48, and 80.

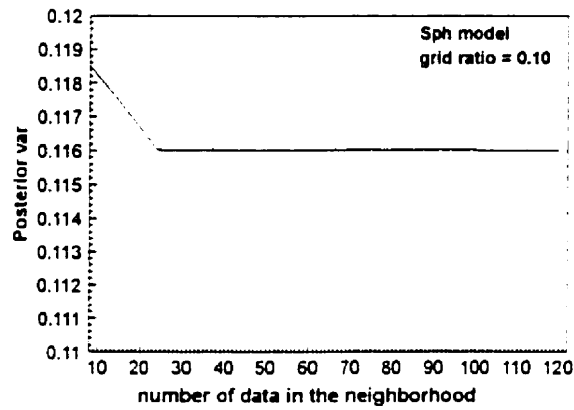


Figure 5.5 Convergence of posterior variance of the spherical model, the grid ratio = 0.1.

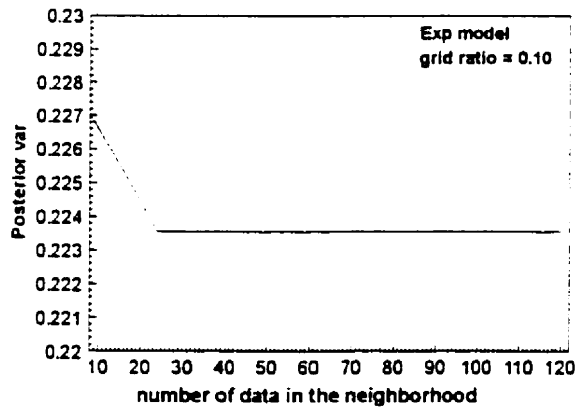


Figure 5.6 Convergence of posterior variance of the exponential model, the grid ratio=0.1.

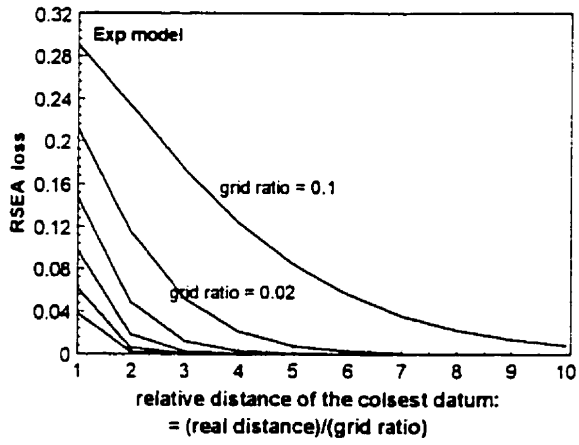
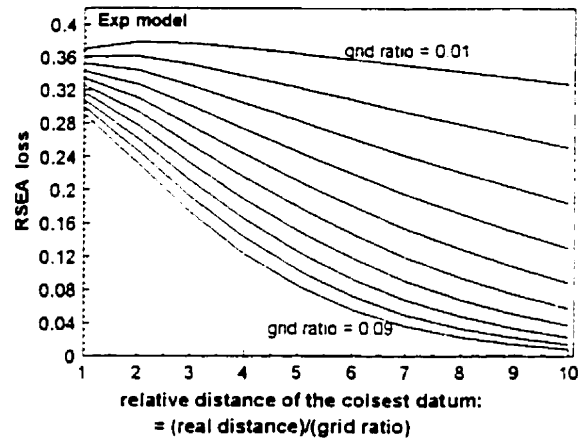
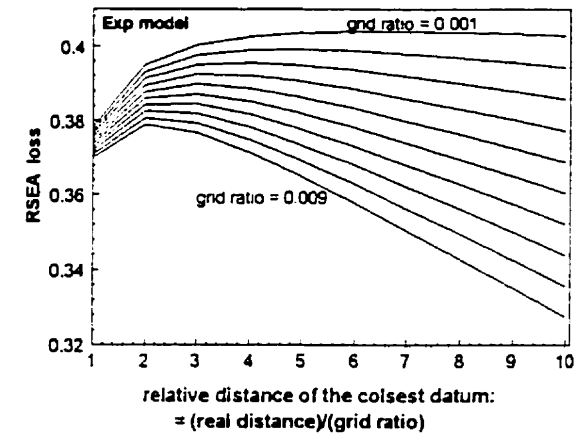


Figure 5.7 The upper bound of the RSEA loss of the exponential model with different grid ratios and relative closest distances (=distance/grid-ratio).

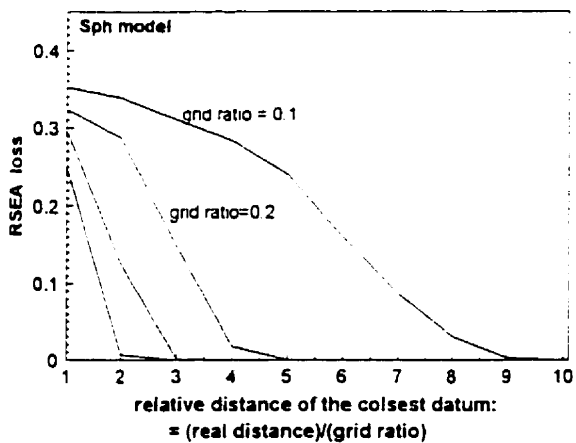
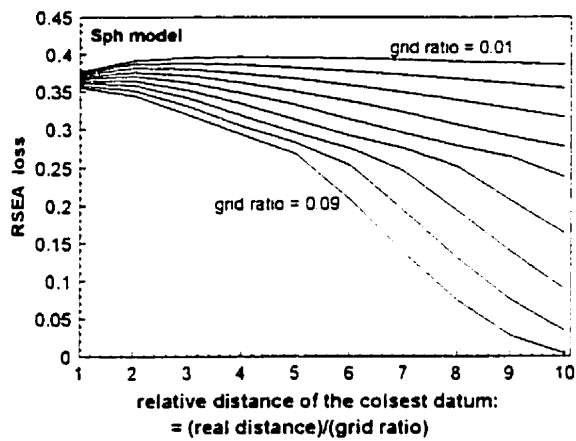
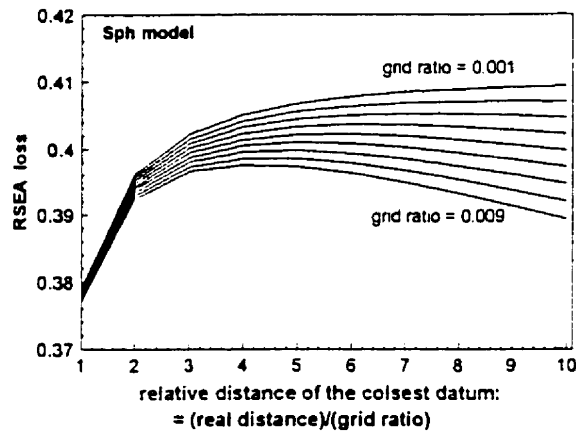


Figure 5.8 Upper bound of the RSEA loss of the spherical model with different grid ratios and relative closest distances (=distance/grid-ratio).

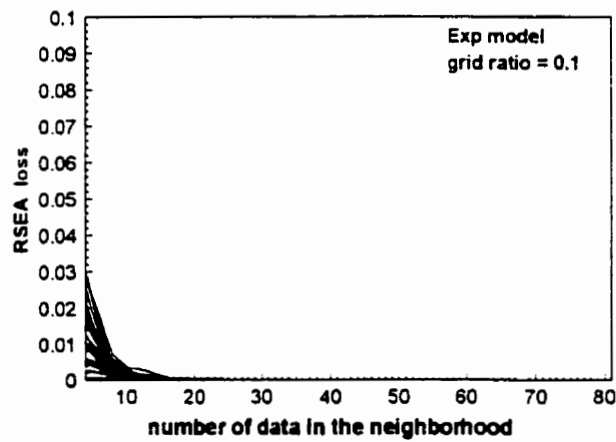
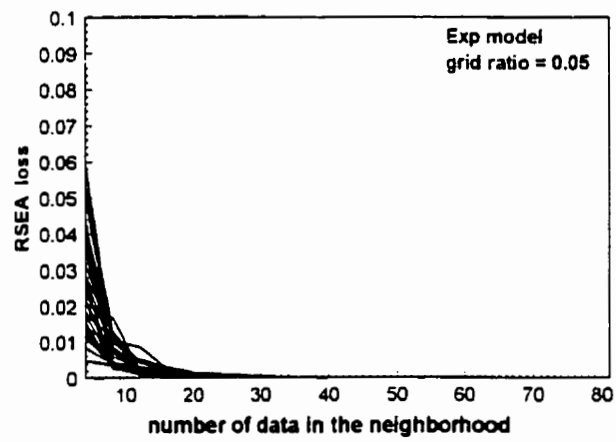
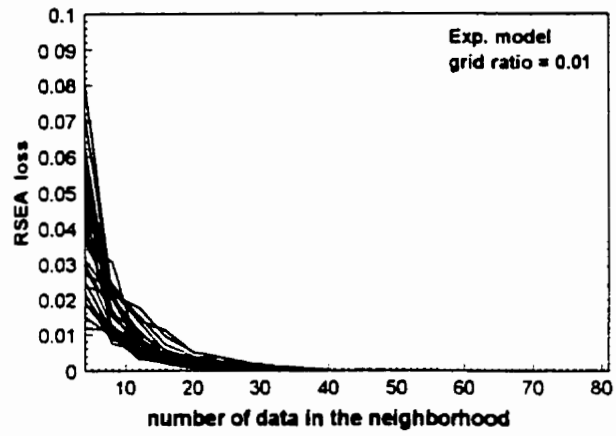


Figure 5.9 The RSEA loss of exponential model for grid ratio=0.01, 0.05, 0.10.  
120 'real' data are randomly distributed in a grid of  $21 \times 21$ .

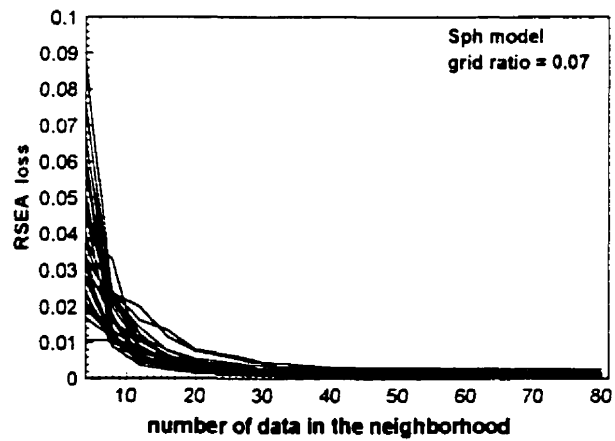
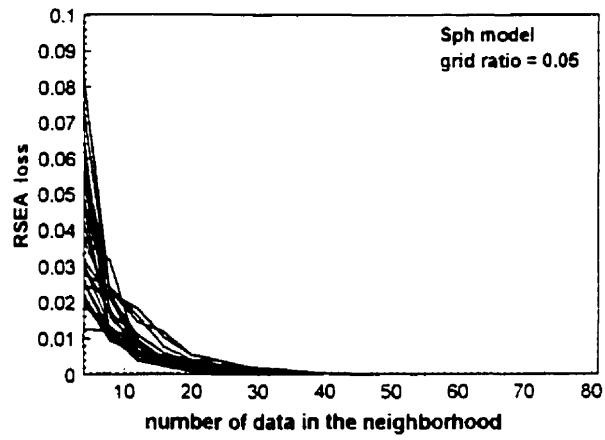
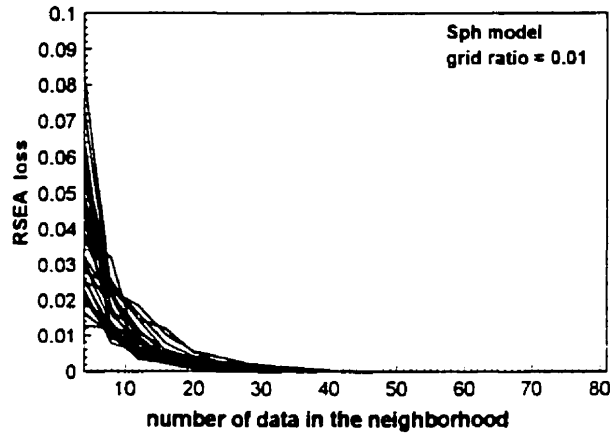


Figure 5.10 The RSEA loss of spherical model for grid ratio=0.01, 0.05, 0.07. 120 'real' data are randomly distributed in a grid of  $21 \times 21$ .

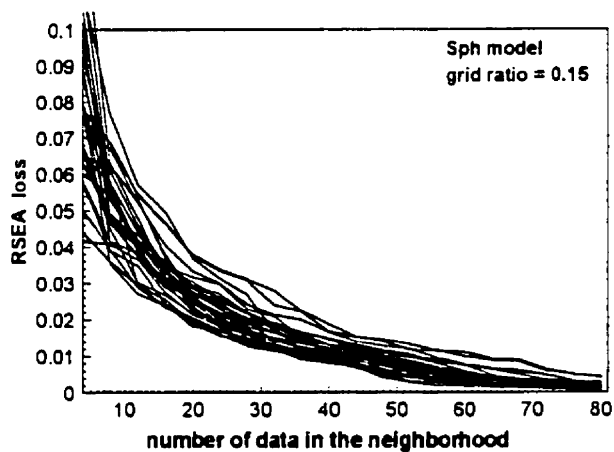
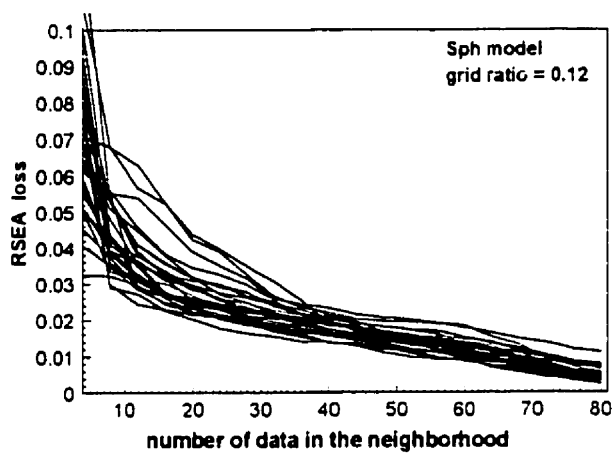
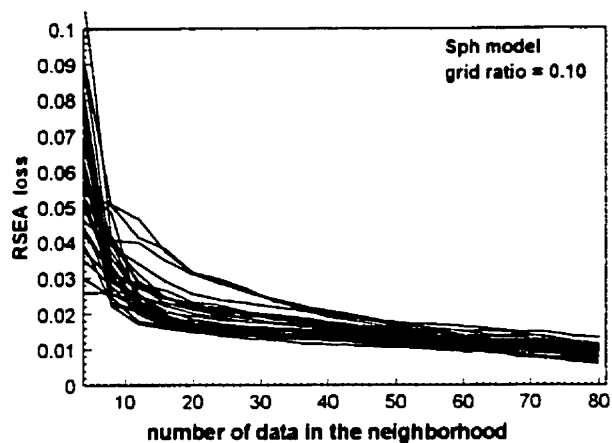


Figure 5.11 The RSEA loss of spherical model for grid ratio=0.10, 0.12, 0.15. 120 'real' data are randomly distributed in a grid of  $21 \times 21$ .

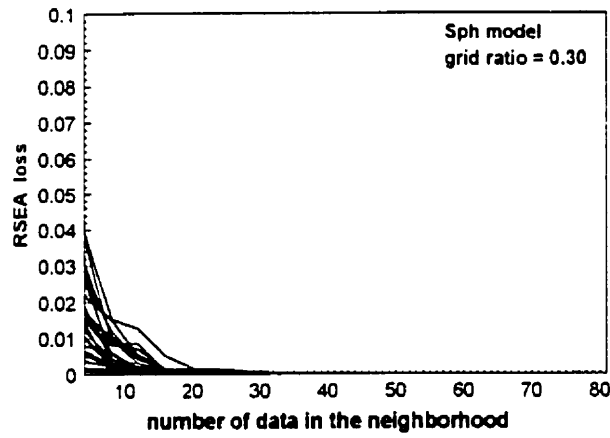
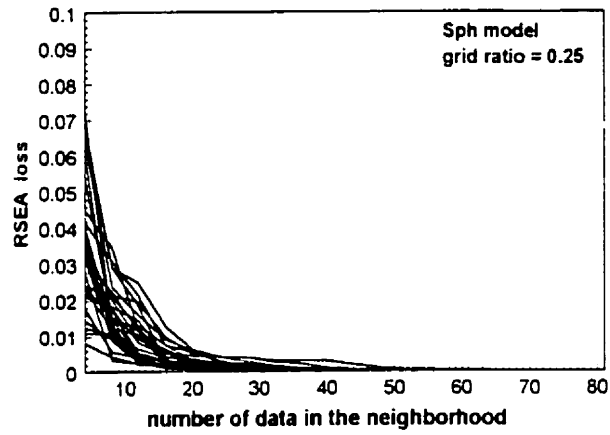
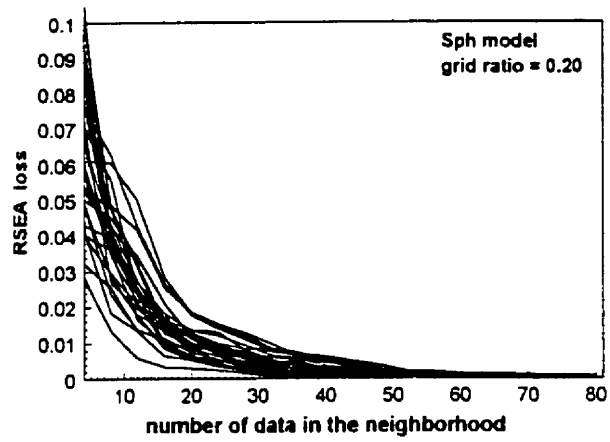


Figure 5.12 The RSEA loss of spherical model for grid ratio=0.20, 0.25, 0.30. 120 'real' data are randomly distributed in a grid of 21×21.

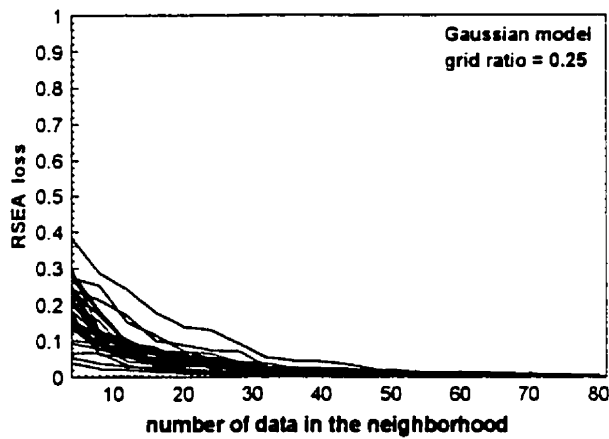
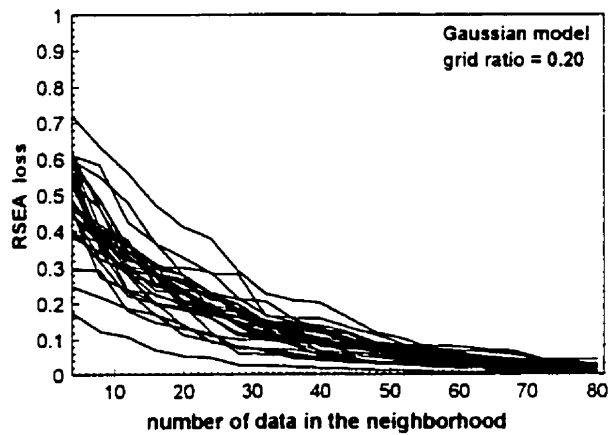
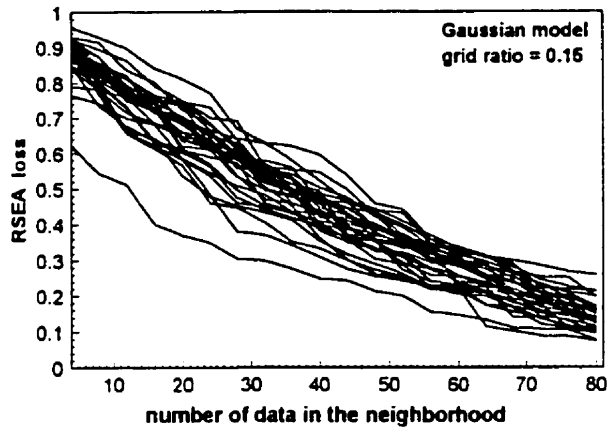


Figure 5.13 The RSEA loss of Gaussian model for grid ratio=0.15, 0.20, 0.25. 120 'real' data are randomly distributed in a grid of  $21 \times 21$ .

## **5.4 The Simulated Annealing Technique Honoring Experimental Variograms**

### **5.4.1 Problem Definition**

Covariance/variogram model fitting is an important step for all current simulation techniques. The fitted covariance/variogram model is assumed to characterize the properties of the second-order moment presented in the experimental variograms of the conditioning data. In practice, covariance/variogram model fitting is a time-consuming process which involves a great number of modifications, such as anisotropy recognition, nested structure identification, model type selection, and the adjustment of sills and ranges. Moreover, the model candidates must be constrained by the positive definite requirement, regardless of whether this hinders their ability to properly characterize the space-time continuity.

Another negative impact of covariance/variogram model fitting is that, for natural processes, the variations of the second-order moment are often artificially smoothed. This variation reduction of the second-order moment more or less simplifies the nature of space-time continuity. Therefore, it is argued that instead of fitting experimental covariances/variograms with a model, one would consider generating simulations which directly reproduce experimental covariances/variograms. The simulated images with reproduced experimental covariances/variograms mimic more faithfully the nature of physical processes than those generated by the algorithms commemorating covariance/variogram models.

Though this idea might be attractive, it is impractical for most simulation techniques, due to the requirement of positive covariance matrices. Fortunately, the development of the simulated annealing method provides a means to implement the experimental covariance/variogram reproduction in simulated images.

The simulated annealing method generates the required simulations through an objective function design. Given an initial image, the annealing method swaps values at different nodes to minimize the objective function, instead of regenerating values at nodes

directed by specific rules, as do most simulation techniques. Therefore, the requirement of positive covariance matrices becomes unnecessary.

#### 5.4.2 Simulated Annealing Techniques

In the 'annealing' approach to stochastic simulation there is no explicit random function model. Rather, the creation of a simulated realization is formulated as an optimization problem to be solved with a stochastic relaxation or 'annealing' technique. An objective function is needed to implement some practical requirements of the desired simulation, which is a measure of the difference between the desired spatial characteristics and those of the candidate realization. The essential feature of annealing methods is to iteratively perturb the candidate realization and then to use a decision rule to accept or reject the perturbation. The decision rule is based on how much the perturbation has brought the candidate realization closer to having the desired properties. One possible decision rule is based on an analogy with the metallurgical process of annealing, hence the name simulated annealing (e.g., Kirkpatrick, et al., 1983; Geman and Geman, 1984).

Simulated annealing is a prescription for whether or not to accept a given perturbation. The acceptance probability distribution is given by

$$P\{\text{accept}\} = \begin{cases} 1 & O_{\text{new}} \leq O_{\text{old}} \\ e^{-\frac{O_{\text{old}} - O_{\text{new}}}{p}} & \text{otherwise} \end{cases} \quad (5.26)$$

where  $O_{\text{old}}$  denotes the previous value of the objective function,  $O_{\text{new}}$  denotes the value of the objective function associated with the current perturbation, and the parameter  $p$  is analogous to the 'temperature' in annealing. The higher the 'temperature', the more likely an unfavorable perturbation will be accepted.

The virtues of simulated annealing techniques are as follows: (i) they are model-free, that is, the implicit S/TRF model can be Gaussian or non-Gaussian, homogeneous or non-homogeneous. Moreover, there is a potential for simulated annealing to generate conditional simulations directly based on experimental data without models, such as the histogram, the experimental variogram, and so on; (ii) multiple-point statistics, which has the potential to generate conditional simulation by accounting for geometrical structures of spatiotemporal variations, (iii) it could be used to implement other relevant requirements for the simulated realization.

### 5.4.3 Experimental Variogram Reproduction

The experimental variograms of the conditioning data can be reproduced through the proper design of the objective function, which might be defined as the square difference between the variograms of the current image,  $\gamma^*(\mathbf{h}, \tau)$ , and the experimental variograms of the conditioning data,  $\gamma^*(\mathbf{h}, \tau)$ ,

$$O = \sum_{\mathbf{h}, \tau} \frac{[\gamma^*(\mathbf{h}, \tau) - \gamma^*(\mathbf{h}, \tau)]^2}{\gamma^*(\mathbf{h}, \tau)^2} \quad (5.27)$$

Rather than a variogram model which is continuous with any space lags and time intervals, the experimental variograms of the conditioning data are always discretely calculated. To generate experimental covariances between any space lags and time intervals, a multivariate interpolation is needed. Suppose an experimental variogram is denoted as  $\gamma^*(h, \theta, \tau)$ , where  $h$  is the space absolute distance with  $h_1 \leq h < h_2$ ,  $\theta$  is the direction in space with  $\theta_1 \leq \theta < \theta_2$ , and  $\tau$  is the time interval with  $\tau_1 \leq \tau < \tau_2$ . Then the required interpolation is given by

$$\begin{aligned} \gamma^*(h, \theta, \tau) \approx & \frac{1}{(h_1 - h_2)(\theta_1 - \theta_2)(\tau_1 - \tau_2)} [-(h - h_1)(\theta - \theta_1)(\tau - \tau_1)\gamma^*(h_2, \theta_2, \tau_2) \\ & + (h - h_1)(\theta - \theta_1)(\tau - \tau_2)\gamma^*(h_2, \theta_2, \tau_1) + (h - h_1)(\theta - \theta_2)(\tau - \tau_1)\gamma^*(h_2, \theta_1, \tau_2) \\ & - (h - h_1)(\theta - \theta_2)(\tau - \tau_2)\gamma^*(h_2, \theta_1, \tau_1) + (h - h_2)(\theta - \theta_1)(\tau - \tau_1)\gamma^*(h_1, \theta_2, \tau_2) \\ & - (h - h_2)(\theta - \theta_1)(\tau - \tau_2)\gamma^*(h_1, \theta_2, \tau_1) - (h - h_2)(\theta - \theta_2)(\tau - \tau_1)\gamma^*(h_1, \theta_1, \tau_2) \\ & + (h - h_2)(\theta - \theta_2)(\tau - \tau_2)\gamma^*(h_1, \theta_1, \tau_1)] \end{aligned} \quad (5.28)$$

where  $\gamma^*(h_i, \theta_i, \tau_i)$ ,  $i = 1$  to  $2$ , are known experimental variograms of the conditioning data.

### 5.4.4 The Implementation Procedure

The implementation procedure of the required simulation can be represented as follows. First, an initial simulation is generated by assigning each node a value at random from the desired distribution. This initial simulation is sequentially modified by swapping the values in pairs of nodes not involving a conditioning datum. A swap is accepted if the objective function is lowered. Not all swaps which raise the objective function are rejected; the success of the method depends on a slow cooling of the simulation controlled by a 'temperature' function which decreases with time. The higher the 'temperature', the greater the probability that an unfavorable swap will be accepted. The simulation is completed when the simulation is 'frozen', in other words, when further swaps do not lower the objective function or when a specified minimum objective function is reached.

The following parameters determine the computing time of this method:

$p_0$ : the initial 'temperature'. Usually  $p_0$  is designed to be high. The default  $p_0$  is 1.0.

$\lambda$ : the reduction factor,  $0 < \lambda < 1$ . It is used to lower the temperature whenever enough perturbations have been accepted or too many perturbations have been tried.

$K_{\max}$ : the maximum number of attempted perturbations at any one temperature. The temperature is multiplied by  $\lambda$  whenever  $K_{\max}$  is reached (on the order of 100 times the number of nodes).

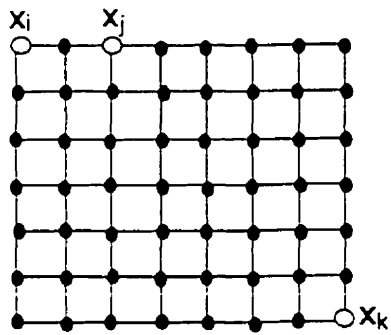
$K_{\text{accept}}$ : the acceptance target. After  $K_{\text{accept}}$  perturbations are accepted, the temperature is multiplied by  $\lambda$  (on the order of 10 times the number of nodes).

$S$ : the stop number. When  $K_{\max}$  is reached  $S$  times the process is stopped (set at 2 or 3).

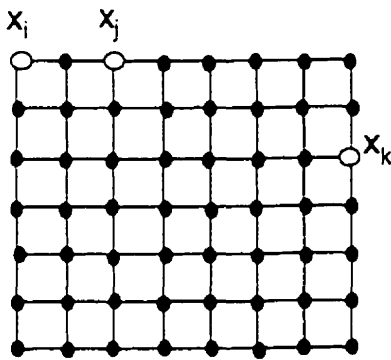
$N_{\text{cov}}$ : the number of experimental variograms involved in each objective function updating.  $N_{\text{cov}}$  determines the number of experimental variograms (related to space lags and directions, and time intervals) that are to be reproduced. In practice,  $N_{\text{cov}}$  indicates the neighborhood size associated with each swap: all variograms between one swapped value and other values in its neighborhood will be updated.

Usually no screen effect approximations exist in the simulated annealing process, therefore,  $N_{\text{cov}}$  is crucial for the required experimental variogram reproduction and for the computing time as well. In practice, the grid lag is smaller than the unit lag of the experimental variogram calculation, therefore  $N_{\text{cov}}$  might be relatively large in spatiotemporal simulations. For example, if the grid lag is half of the unit lag of the experimental variograms, to reproduce experimental covariances for 5 lags in  $R^2 \times T$ , there must be around  $(2 \times 10)^3$  experimental variogram updating required in each objective function updating; if the grid lag is  $\frac{1}{5}$  of the unit lag, then each objective function updating requires around  $(2 \times 5 \times 5)^3 = 125000$  experimental variogram updating.

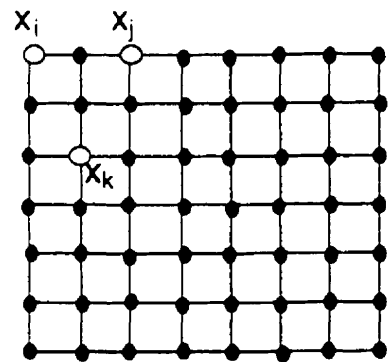
When a swap is considered, the variograms of the current image are updated rather than recalculated. Suppose two values  $x_i$  and  $x_j$  are potentially swapped, as an example. For another value  $x_k$ , there are three conditions for variogram updating, shown in Figure 5.14: (a) no variograms involving  $x_k$  will be updated since  $x_k$  is far away from both  $x_i$  and  $x_j$ ; (b) only the variogram between  $x_j$  and  $x_k$  needs to be updated since  $x_k$  is far from  $x_i$ , and (c) two variograms need to be updated: one between  $x_j$  and  $x_k$  and another between  $x_i$  and  $x_k$ .



(a)



(b)



(c)

Figure 5.14 Three conditions in the swap between  $x_i$  and  $x_j$ : (a) variogram updating does not involve  $x_k$  since it is far away from both  $x_i$  and  $x_j$ ; (b) only the variogram between  $x_j$  and  $x_k$  needs to be updated since  $x_k$  is far from  $x_i$ , and (c) two variograms need to be updated: one between  $x_j$  and  $x_k$  and another between  $x_i$  and  $x_k$ .

The updating in condition (b) is given by

$$\dot{\gamma}_{\text{new}}(h_{jk}, \theta_{jk}, \tau_{jk}) = \dot{\gamma}_{\text{old}}(h_{jk}, \theta_{jk}, \tau_{jk}) + \frac{1}{2N(h_{jk}, \theta_{jk}, \tau_{jk})} [(x_k - x_i)^2 - (x_k - x_j)^2] \quad (5.29)$$

where  $(h_{jk}, \theta_{jk}, \tau_{jk})$  denotes the space-time difference associated with  $x_j, x_k$ , characterized by the spatial absolute distance  $h_{jk}$ , the spatial orientation  $\theta_{jk}$ , and the time interval  $\tau_{jk}$ .

For condition (c), in addition to Equation 5.31, the updating is as follows,

$$\dot{\gamma}_{\text{new}}(h_{ik}, \theta_{ik}, \tau_{ik}) = \dot{\gamma}_{\text{old}}(h_{ik}, \theta_{ik}, \tau_{ik}) + \frac{1}{2N(h_{ik}, \theta_{ik}, \tau_{ik})} [(x_k - x_j)^2 - (x_k - x_i)^2] \quad (5.30)$$

### 5.4.3 An Improvement of Implementation

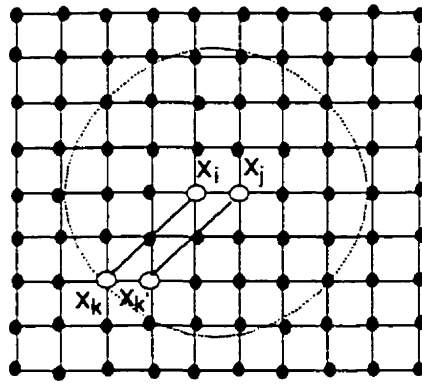
Though the above updating make the implementation faster than recalculation, the computing time is still huge due to the great amount of variogram updating involved in updating each objective function. More effects are needed to speed up the simulation process. The following implementation is one way to do so.

In practice, the pair of two swapped values,  $x_i$  and  $x_j$ , are close to each other. Suppose there are  $p$  variograms involving  $x_i$  and  $q$  variograms involving  $x_j$  to be updated. Denote these variograms by  $(\gamma_{i1}, \dots, \gamma_{ip})$  and by  $(\gamma_{j1}, \dots, \gamma_{jq})$ . When  $x_i$  and  $x_j$  are not close to the edges of the simulation grid, as shown in Figure 5.15(a), then  $p = q$ , that is, for each variogram involving  $x_i, \gamma_{ik}$ , there exists a variogram involving  $x_j, \gamma_{jk}$ , whose space-time difference is the same as that of  $\gamma_{ik}$ :  $(h_{ik}, \theta_{ik}, \tau_{ik}) = (h_{jk}, \theta_{jk}, \tau_{jk})$ . If  $x_i$  and  $x_j$  are close to the edges of the simulation grid as shown in Figure 5.15(b), for most variograms involving  $x_i$ , there still exists corresponding variograms involving  $x_j$  such that their space-time differences are identical.

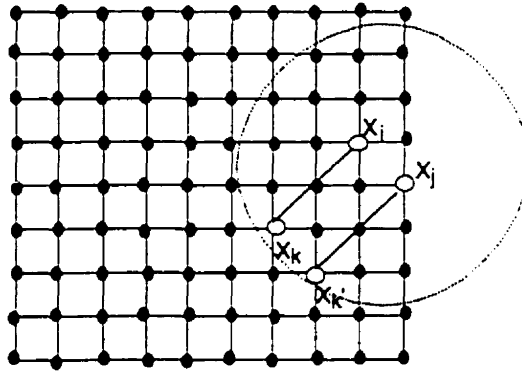
Now, let the space-time difference between  $x_i$  and  $x_k$  be identical to that between  $x_j$  and  $x_k$ , which is represented by  $(h, \theta, \tau)$ . Then instead of two variogram updating in the current implementation,  $\gamma_{ik}$  and  $\gamma_{jk}$ , one may consider the following simplified formula,

$$\begin{aligned} \dot{\gamma}_{\text{new}}(h, \theta, \tau) &= \dot{\gamma}_{\text{old}}(h, \theta, \tau) + \frac{1}{2N(h, \theta, \tau)} [(x_k - x_i)^2 - (x_k - x_j)^2 + (x_k - x_j)^2 - (x_k - x_i)^2] \\ &= \dot{\gamma}_{\text{old}}(h, \theta, \tau) + \frac{1}{2N(h, \theta, \tau)} 2(x_i - x_j)(x_k - x_k) \end{aligned} \quad (5.31)$$

In fact, this implementation saves more than half of updating time.



(a)



(b)

Figure 5.15 The swap between  $x_i$  and  $x_j$ . For one variogram updating between  $x_i$  and  $x_k$ , there usually exists another variogram updating  $x_j$  and  $x'_k$ , such that their space-time differences are identical. (a)  $x_i$  and  $x_j$  are not close to the edges of the grid, and (b)  $x_i$  and  $x_j$  are close to the edges. The dot line implies the neighborhood of the swap.

## 5.5 Summary

Both SGGS and the simulated annealing technique can be applied to generate realizations of spatiotemporal processes. An advantage of these techniques for spatiotemporal conditional simulations is that their implementation does not explicitly involve the joint space-time measure which is often a topic of argument.

SGGS is a series of sequential Gaussian simulation algorithms including the current SGS and LU decomposition algorithm. Among them, the best is the  $0.5\nu$ -SGGS, where  $\nu$  indicates the neighborhood size. For instance, the  $0.5\nu$ -SGGS with  $\nu$  being 50 is roughly 10 times faster to calculate than the current SGS.

The SGGS error caused by the SEA can be characterized by the SEA loss defined as the mean square difference between the simulated value posterior to the information in the neighborhood and the simulated value posterior to all information. The SEA loss is fully determined by the posterior variances, monotonic increasing with the whole information and monotonic decreasing with the information in the neighborhood. The result shows that both the exponential model and the spherical model can match the 5% RSEA loss requirement for any grid design with a considerably small neighborhood. However, a Gaussian model has a fairly high SEA loss in most applications.

It is worth noting that the SGGS technique can be easily expanded to the Gaussian joint simulation with the same strategy. However, a detailed discussion of this expansion is beyond the scope of this thesis.

Also, the SEA loss is a very useful tool for sequential joint simulation techniques to evaluate the error generated by ignoring further information. Also indicated in this discussion are the potential problems associated with sequential simulation techniques if the covariance model is neither an exponential model nor a spherical model. A good strategy is to evaluate its SEA loss and estimate the optimal size with an acceptable loss before implementing the simulation.

The simulated annealing technique honoring experimental variograms provides a way of generating realizations of spatiotemporal processes without the covariance/variogram model fitting, which is prerequisite for other simulation algorithms. This saves a great amount of computations in model identification and avoids possibly complicated derivation of positive definite property of model candidates. Furthermore, the simulated images honoring experimental covariances/variograms mimic more faithfully the nature of physical processes than that generated by the simulation algorithms honoring covariance/variogram models.

The computing time of the simulated annealing algorithm honoring experimental variogram reproduction is crucial to generate satisfactory realizations of spatiotemporal processes. In practice the current implementation can only reproduce a small part of experimental variograms of conditioning data due to the huge number of computations associated with experimental variogram reproduction. Further improvements of computing time needs to be made to obtain ideal images.

## Chapter 6

# Space-Time Modelling of the Pressure System in a Carbonate Reservoir

### 6.1 Introduction

Reservoir pressure is a key parameter in predicting reservoir performance, guiding reservoir management decisions and developing operating strategies. During the production life of a reservoir, pressure is monitored at various wells and the results are used to address reservoir management problems. For instance, reservoir performances are checked against flow simulation predictions, changes in patterns of pressure gradients are evaluated, and pressure build-ups or drops are examined. Injection and production operations may then be adjusted to improve production performance. Optimization of the pressure monitoring process is an essential element of reservoir management.

A pressure monitoring scheme should address the question of which wells and how often they should be sampled to adequately monitor both local and global pressure changes. The development of such a scheme should account for distinct physical, engineering and economic characteristics. The distribution of reservoir pressure is a joint function of spatial geological heterogeneity and temporal production characteristics. Economic considerations of the monitoring scheme relate to the lack of production in a shut-in well for the period of pressure transient testing.

In addition, one of the most important goals of reservoir management is to predict future production rates. Over the years, engineers have developed several methods to achieve this goal. These methods, ranging from simple decline curve analysis techniques to sophisticated multidimensional and multiflow reservoir simulators, involve a process of parameter modifications to let the calculated production rates match the real rates. This process is referred to as history matching (e.g., Dake, 1978; Aziz, 1979). The reservoir pressure history match is requisite to history matching, which includes the match of local average pressures as well as the match of pressure distribution in the reservoir at different times. An adequate space-time mapping of the reservoir pressure during a past period, therefore, provides a basis for history matching. The space-time mapping of the reservoir pressure will contribute to an understanding of the evolution of the reservoir pressure,

reveal the potential gradients that are controlling fluid movement in the reservoir, and allow the inference of a pressure distribution in parts of the reservoir or parts of the production period where or when there are no data.

In this chapter, a case study is presented which is based on the shut-in pressure measurements of a carbonate reservoir. The space-time continuity of the reservoir pressure is investigated using spatiotemporal experimental variograms. The space-time mapping of the pressure is estimated using S/T block OK. The pressure monitoring scheme is analyzed based on multiple conditional simulations of the reservoir pressure in order to estimate local changes of the reservoir pressure adequately.

## 6.2 Statistics of Pressure Measurements

A total of 644 pressure measurements were collected from 145 wells in the carbonate reservoir, 576 of them from 116 production wells and the others from 29 injection wells. The wells are irregularly located in the study area, as shown in Figure 6.1, and pressure data were irregularly collected from 1986 up to 1993.

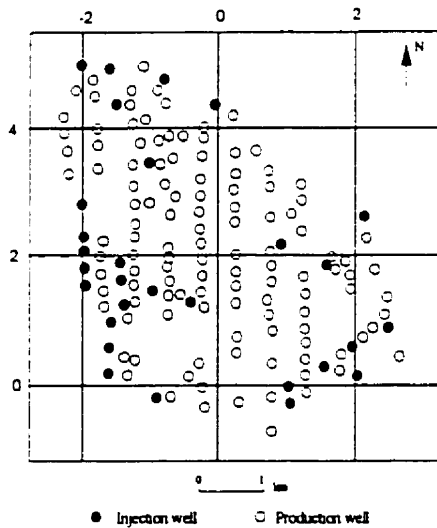


Figure 6.1 The well locations in the study area.

The histogram of pressure measurements of production wells, illustrated in Figure 6.2, approximately shows a normal distribution shape. However, the histogram of pressure measurements of injection wells, illustrated in Figure 6.3, shows a somewhat negatively

skewed distribution. Thus, it may be reasonable to consider that the pressure data of production wells and injection wells come from different populations. The pressure data of injection wells were then excluded from the original data set and the investigation was concentrated on the pressure system of production wells.

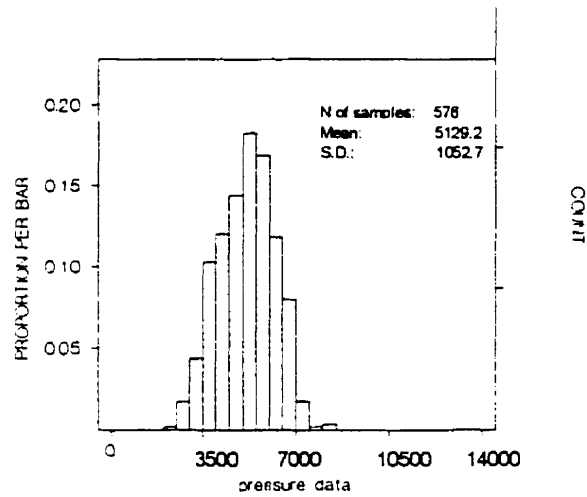


Figure 6. 2 Histogram of the pressure data from production wells.

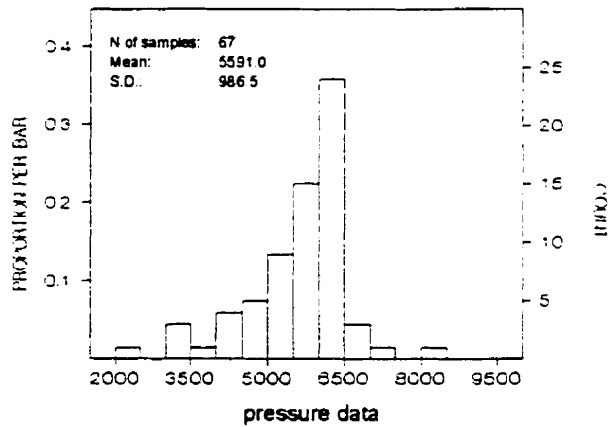


Figure 6.3 Histogram of the pressure data from injection wells.

### 6.3 Spatiotemporal Continuity Characterization of the Reservoir Pressure

The spatiotemporal continuity of the pressure data was investigated using spatiotemporal experimental variograms computed in the N-S, NE 45°, E-W, and SE 45° directions, with a space lag of 0.2(km) and a time interval of 1(month). The directional tolerance, space-lag tolerance, and time-interval tolerance are respectively 45°, 0.1(km), and 0.5(month). These variograms are shown in Figure 6.4, 6.5, 6.6, and 6.7. The characteristics of the experimental variograms are:

- (1) the behaviors at the origin show a good continuity, indicating that no nugget effect existed for the spatiotemporal continuity;
- (2) the spatial anisotropy, involving different ranges in the four directions, is apparent. More precisely, the range is around 0.66 km in the E-W direction, around 0.52 km in the NE 45° direction, around 0.33 km in the N-S direction, and around 0.52 km in the SE 45° direction. These four space ranges, denoted by  $a_1$ ,  $a_2$ ,  $a_3$ , and  $a_4$ , form an elliptical-shaped directional graph, which is shown in Figure 6.8. Note that sills in four directions are all around  $8 \cdot 10^5$ , implying the presence of geometric anisotropy in the data set.

Based on these characteristics, the space-time continuity of the reservoir pressure was assumed that the pressure data show a homogeneous spatiotemporal continuity with distinct geometric anisotropy, which could be modeled by a joint distance variogram function. The geometric anisotropy demonstrates that the long axis of the ellipse is along the E-W direction, with a ratio of 2.0. The fitted spatiotemporal variogram model is given by

$$\gamma(h, \tau) = 8 \times 10^5 \times \{1 - \exp[-((\frac{h_1}{0.22})^2 + (\frac{\tau}{18.3})^2)^{1/2}]\} \quad (6.1)$$

and the reduced space distance  $h_1$  is given by

$$h_1 = \sqrt{h_x^2 + 2^2 h_y^2} \quad (6.2)$$

where  $h_x$  denotes the distance in the E-W direction while  $h_y$  denotes the distance in the N-S direction. This model indicates a spatial range of  $0.11 \times 3$  km in the N-S direction and a spatial range of  $0.22 \times 3$  km in the E-W direction. Also, Equation 6.1 indicates a time range of  $183 \times 3$  days, or 1.5 years. Figure 6.9 shows the fitted model, which is comparable with the experimental variograms in the E-W direction shown in Figure 6.4.

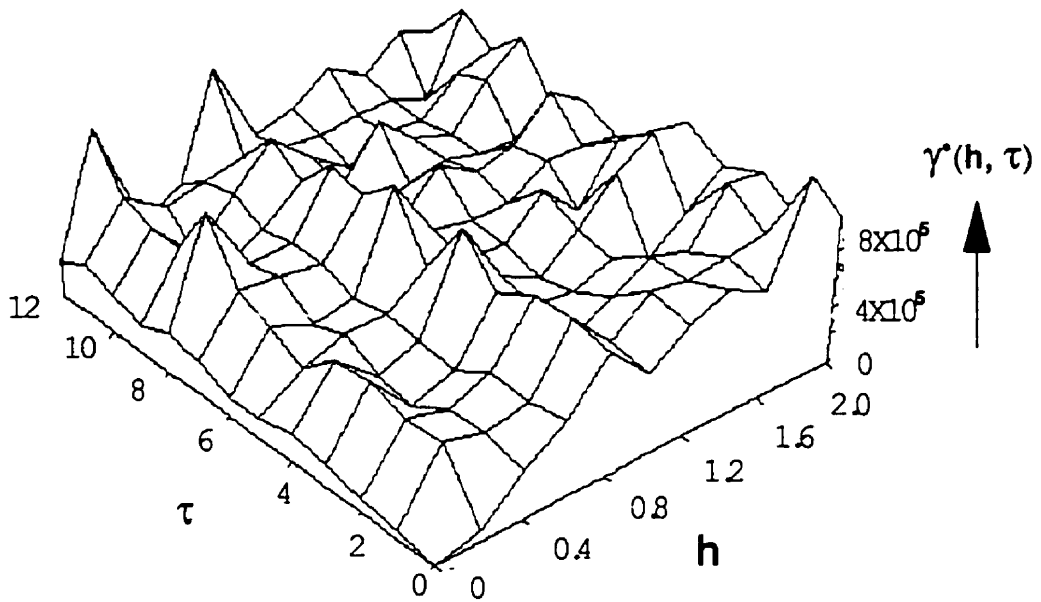


Figure 6.4 Spatiotemporal experimental variogram of pressure data in the E-W direction, the unit of space lag is kilometer and the unit of time interval is month.

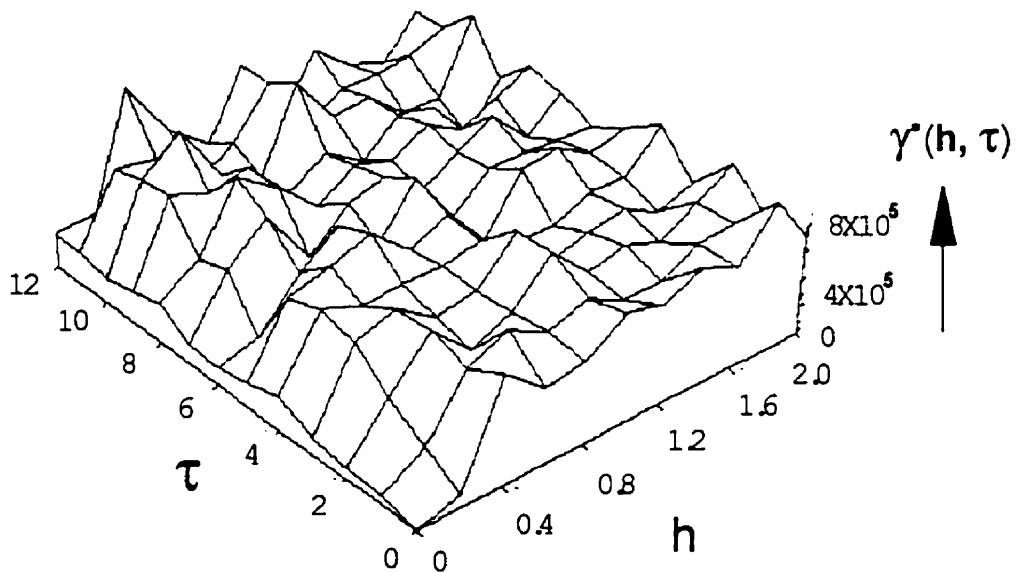


Figure 6.5 Spatiotemporal experimental variogram of pressure data in the NE 45° direction, the unit of space lag is kilometer and the unit of time interval is month.

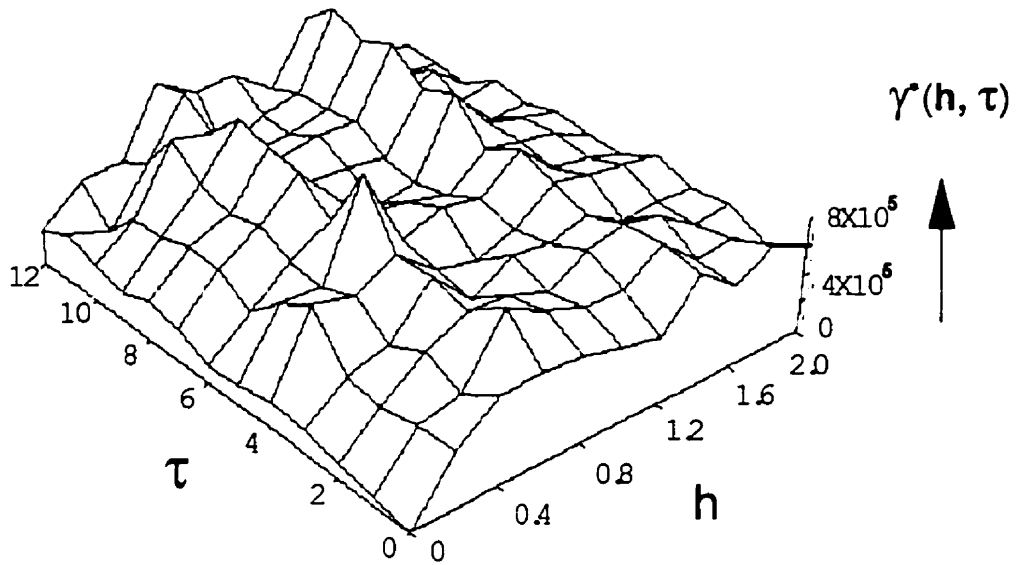


Figure 6.6 Spatiotemporal experimental variogram of pressure data in the N-S direction, the unit of space lag is kilometer and the unit of time interval is month.

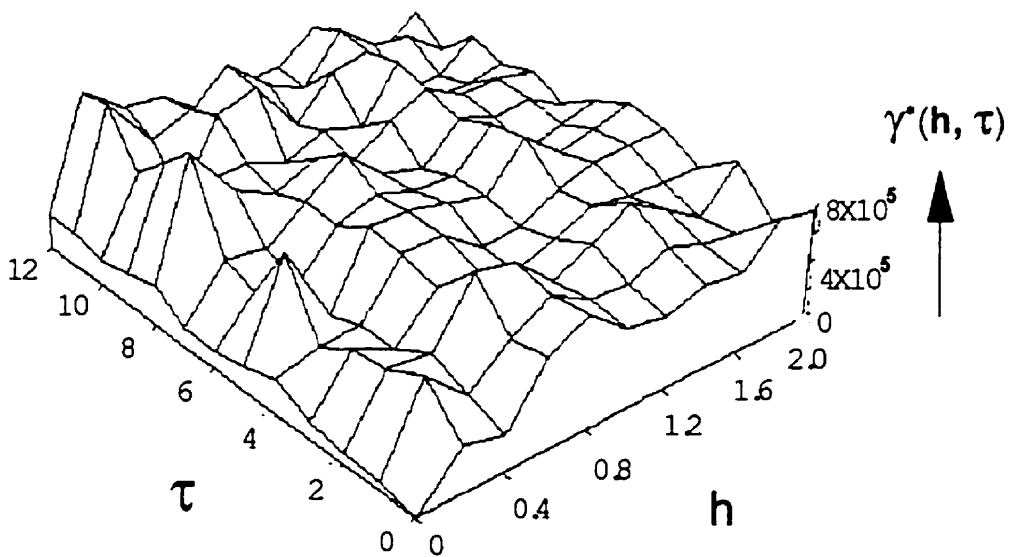


Figure 6.7 Spatiotemporal experimental variogram of pressure data in the SW  $45^\circ$  direction, the unit of space lag is kilometer and the unit of time interval is month.

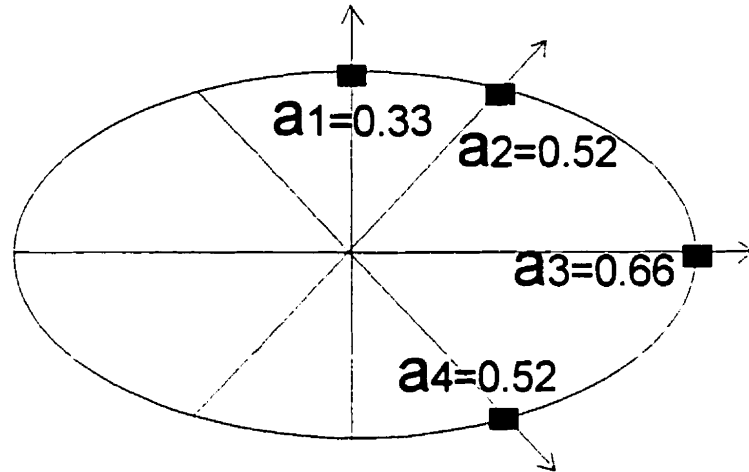


Figure 6.8 The elliptical-shaped directional graph.  $a_1$ ,  $a_2$ ,  $a_3$ , and  $a_4$  denote four space ranges in the N-S direction, NE 45° direction, E-W direction, and SE 45° direction, respectively.

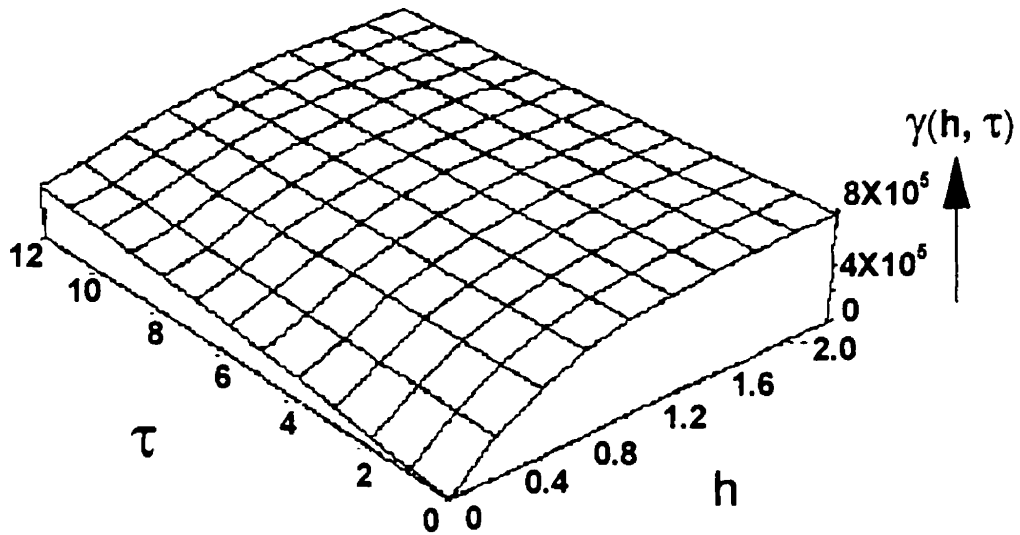


Figure 6.9 The spatiotemporal variogram model of the reservoir pressure. The space distance here is the reduced distance  $h_1$  given in Equation 6.2. This model is comparable with the experimental variograms in the E-W direction shown in Figure 6.4.

## 6.4 Space-Time Mapping of the Reservoir Pressure

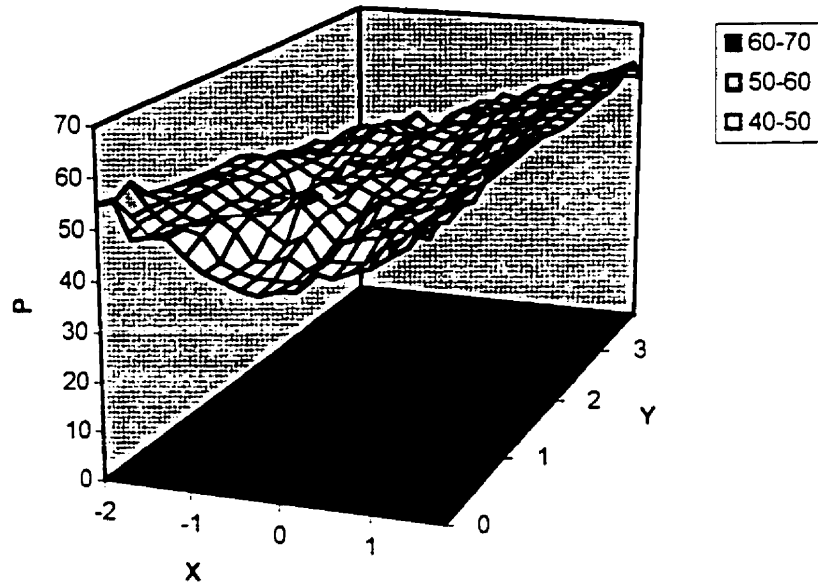
The space-time mapping of the reservoir pressure, in this context, was computed using S/T block OK, developed in Section 4.3, with the spatiotemporal variogram model given by Equation 6.1.

The space-time mapping of the reservoir pressure was computed in an area of 16 km<sup>2</sup> during 1989-1992. The total number of space-time gridblocks to be estimated is  $20 \times 20 \times 16 = 6400$ , each gridblock has a size of  $0.2(\text{km}) \times 0.2(\text{km}) \times 3(\text{month})$ . The block discretion is  $4 \times 4 \times 3$ . The quadrant search was applied for the neighborhood determination at each space-time gridblock to be estimated, each quadrant has not more than 8 data. Note that the quadrant search implies the quadrant spatial partition of the neighborhood, and the neighborhood partition in time was not considered in order to ensure enough data for kriging operations. The space-time mapping from the first quarter of 1989 up to the fourth quarter of 1992 are shown from Figure 6.10 up to 6.17.

The result of spatiotemporal mapping of reservoir pressure shows the following properties:

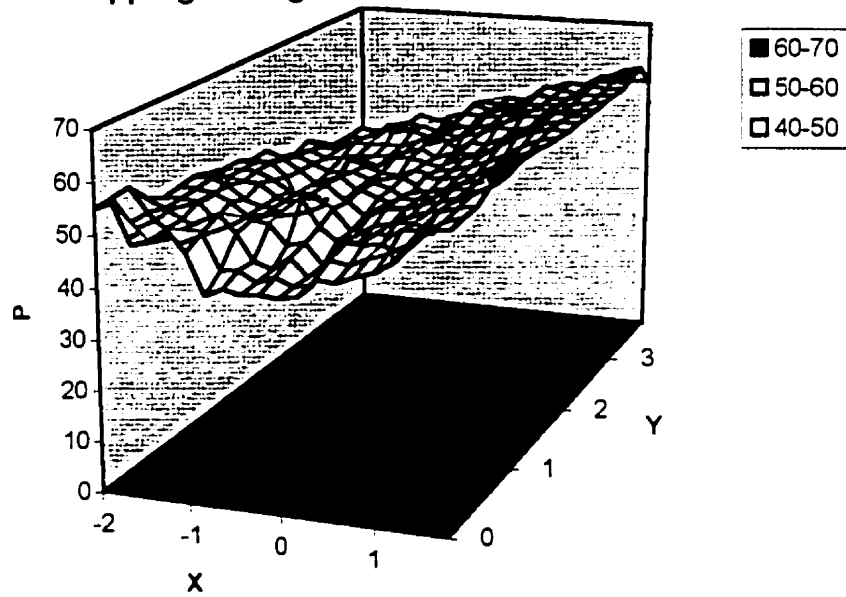
- (1) In the maps of 1989, high pressure zones ( $> 60$ ) are around the northeast, and a few are around the southwestern corner. The low pressure zones ( $< 50$ ) spreads from southeast to northwest, where the production wells are located in.
- (2) The gradient of the pressure tends to decrease with time passing. This can be seen from the maps of 1989 and 1990, where both the high pressure zones and the low pressure zones are gradually reducing from the first quarter of 1989 up to the last quarter of 1990, since then these zones are only scattered in the center. From 1991 to 1992, the high pressure zones and low pressure zones tend to disappear, leading to significant reduction of pressure gradients in most areas.

### Pressure Mapping During the First Quarter of 1989



(a)

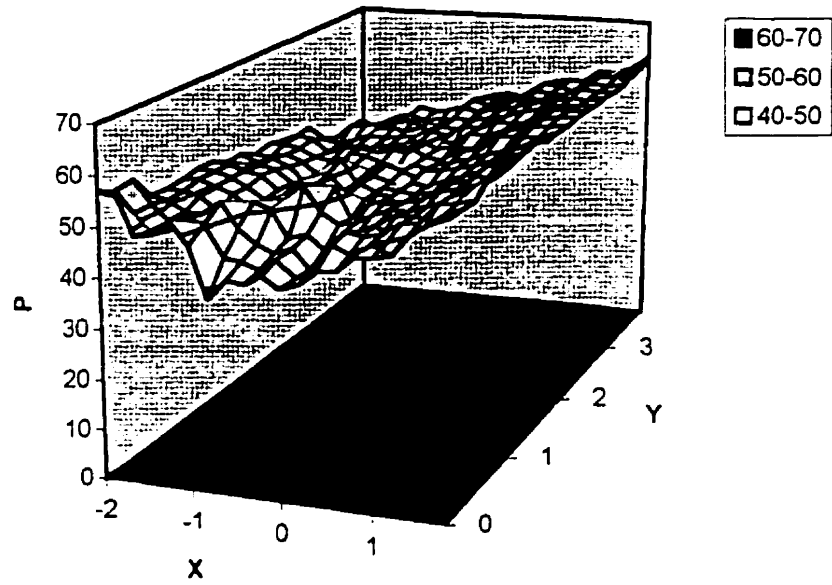
### Pressure Mapping During the Second Quarter of 1989



(b)

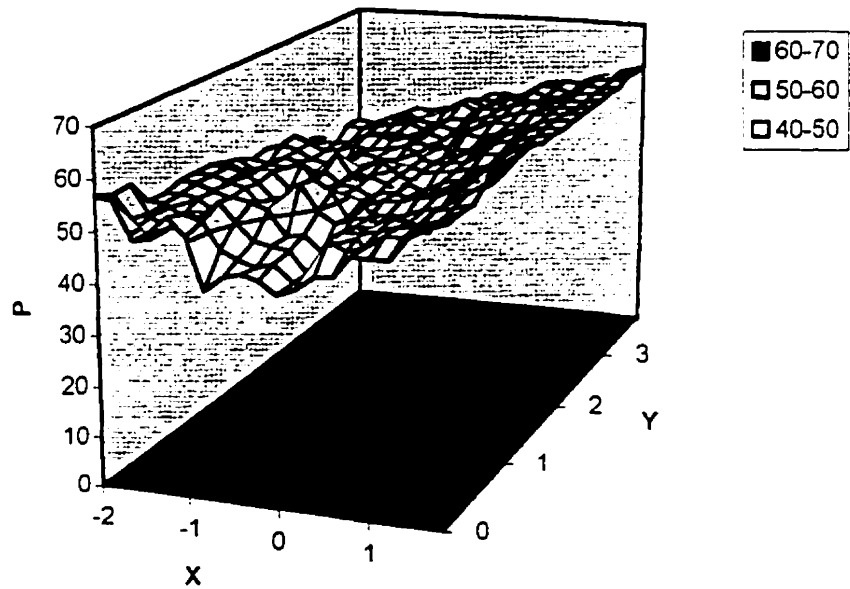
Figure 6.10 Space-Time mapping of reservoir pressure in (a) the first quarter of 1989, and (b) the second quarter of 1989.

### Pressure Mapping During the Third Quarter of 1989



(a)

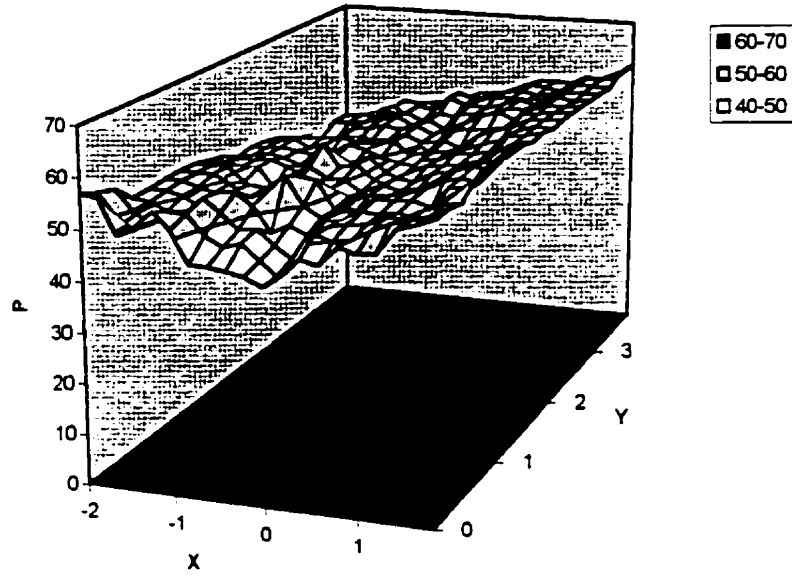
### Pressure Mapping During the Fourth Quarter of 1989



(b)

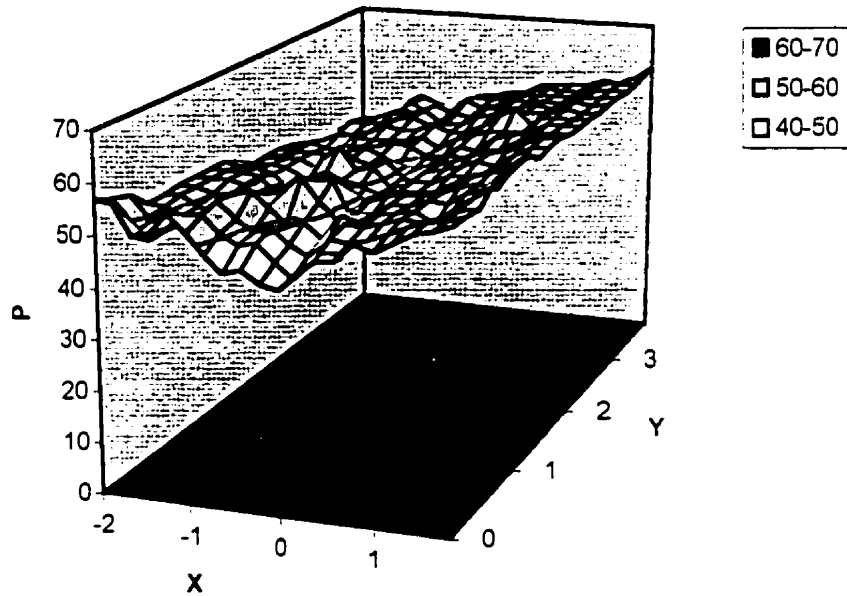
Figure 6.11 Space-Time mapping of reservoir pressure in (a) the third quarter of 1989, and (b) the fourth quarter of 1989.

Pressure Mapping During the First Quarter of 1990



(a)

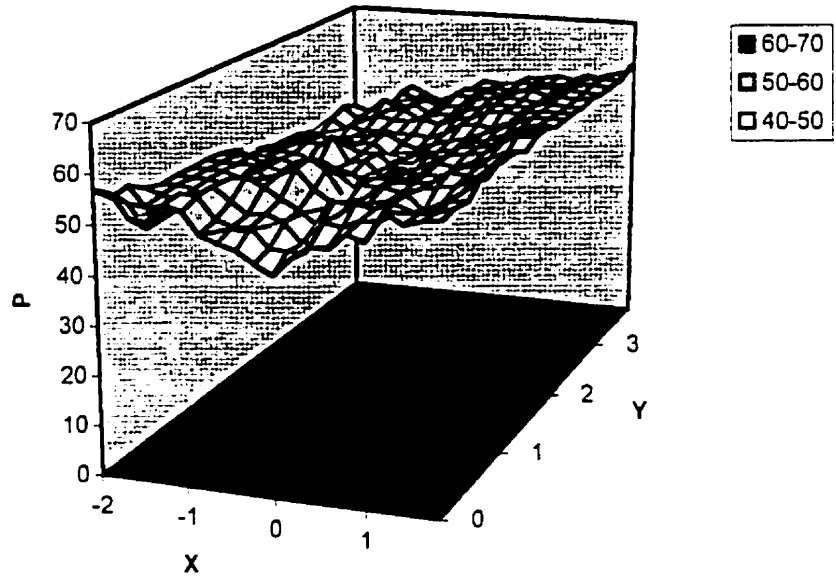
Pressure Mapping During the Second Quarter of 1990



(b)

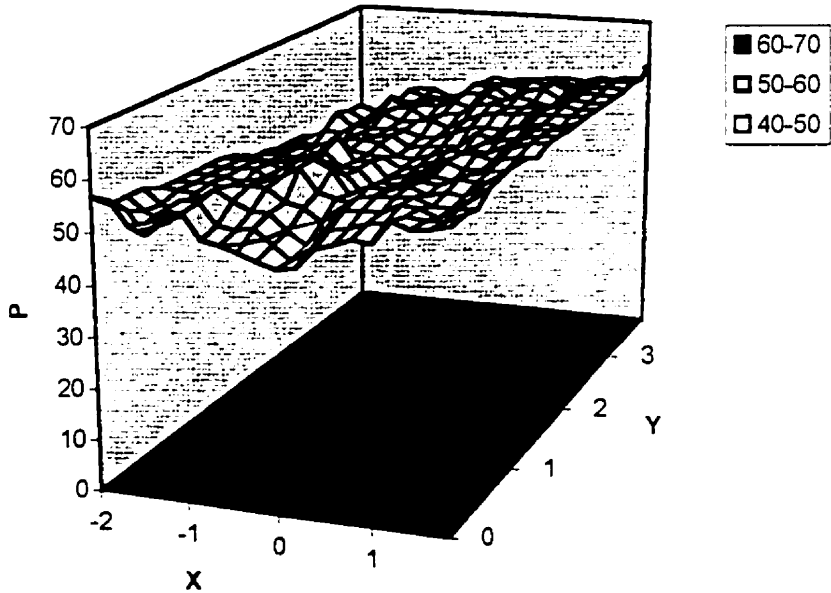
Figure 6.12 Space-Time mapping of reservoir pressure in (a) the first quarter of 1990, and (b) the second quarter of 1990.

### Pressure Mapping During the Third Quarter of 1990



(a)

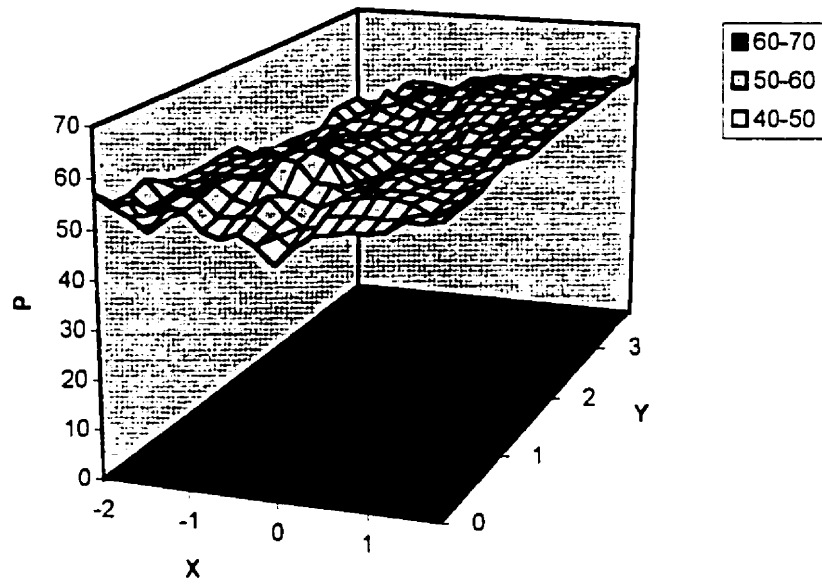
### Pressure Mapping During the Fourth Quarter of 1990



(b)

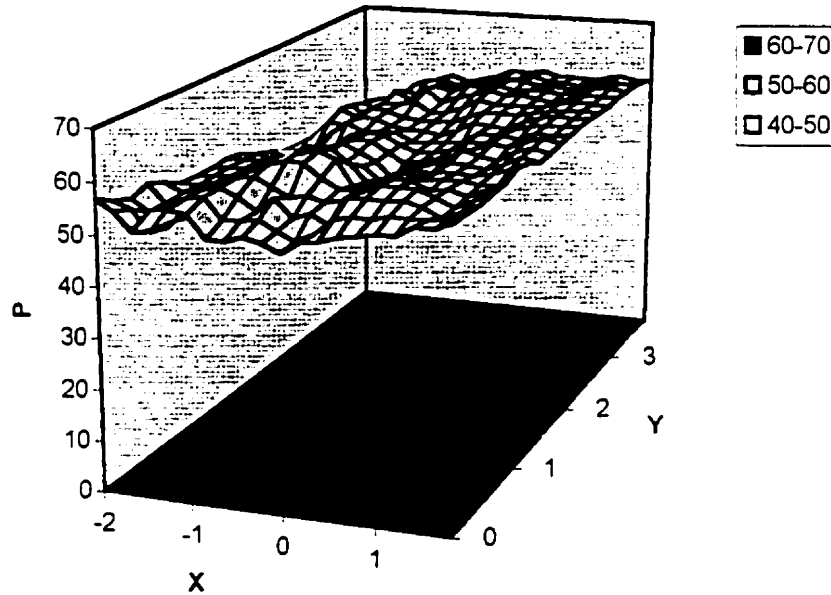
Figure 6.13 Space-Time mapping of reservoir pressure in (a) the third quarter of 1990, and (b) the fourth quarter of 1990.

### Pressure Mapping During the First Quarter of 1991



(a)

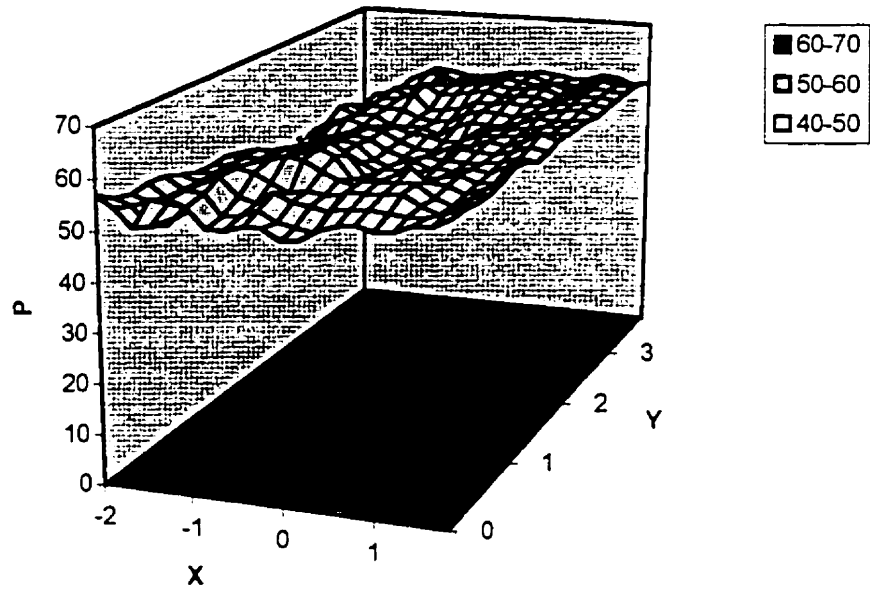
### Pressure Mapping During the Second Quarter of 1991



(b)

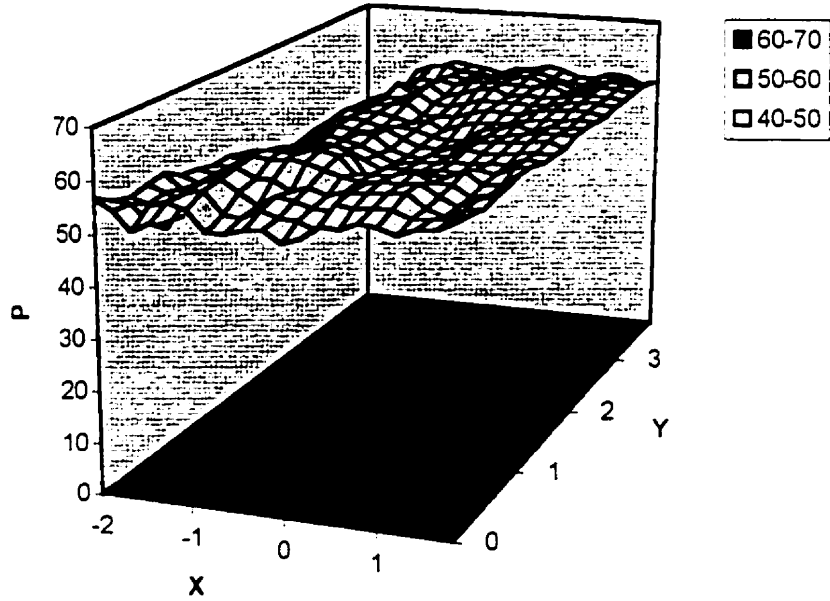
Figure 6.14 Space-Time mapping of reservoir pressure in (a) the first quarter of 1991, and (b) the second quarter of 1991.

### Pressure Mapping During the Third Quarter of 1991



(a)

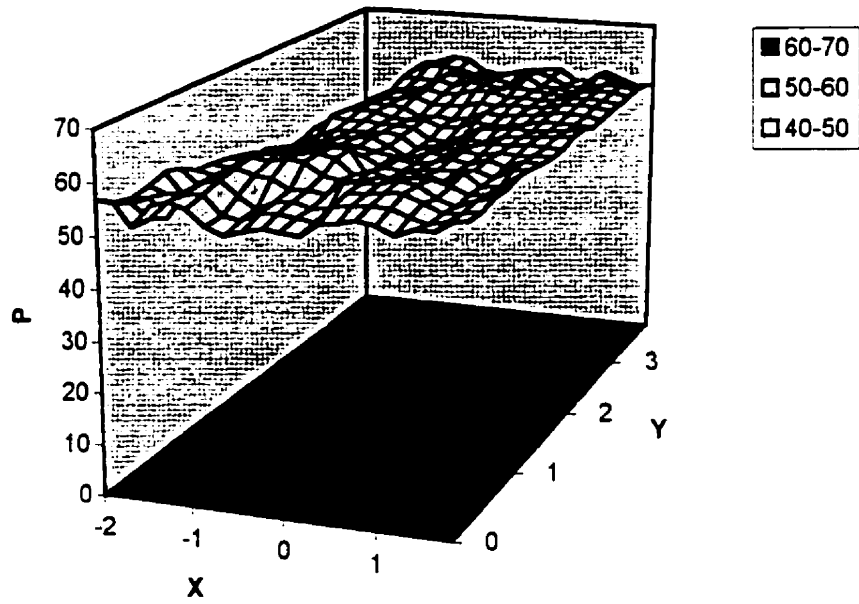
### Pressure Mapping During the Fourth Quarter of 1991



(b)

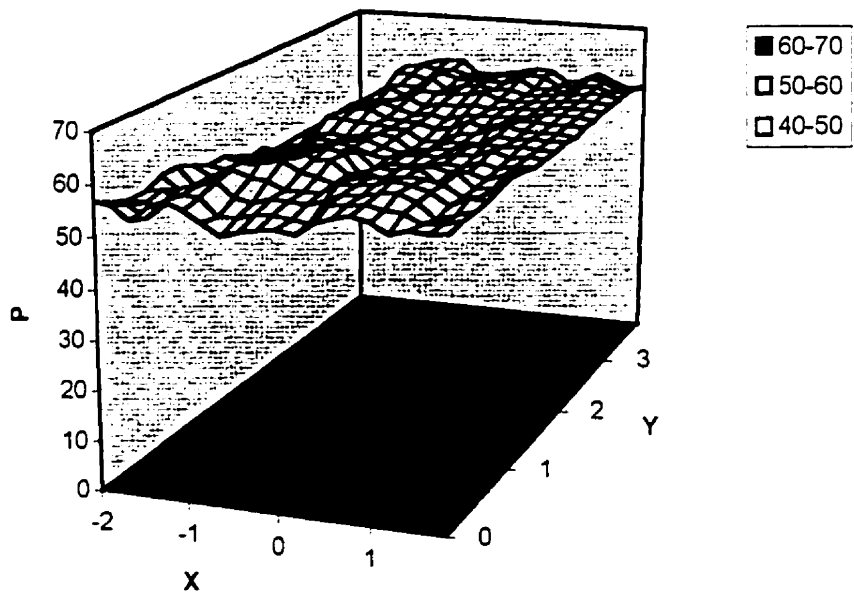
Figure 6.15 Space-Time mapping of reservoir pressure in (a) the third quarter of 1991, and (b) the fourth quarter of 1991.

### Pressure Mapping During the First Quarter of 1992



(a)

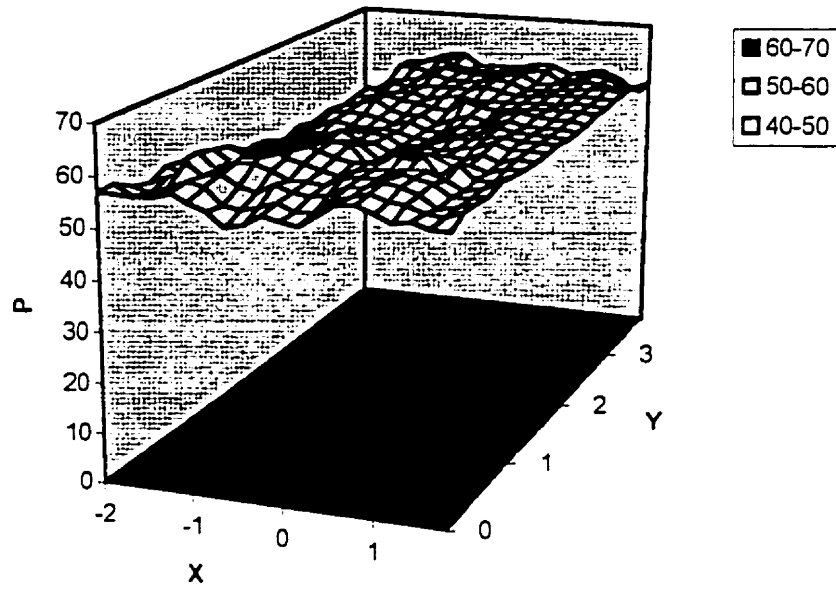
### Pressure Mapping During the Second Quarter of 1992



(b)

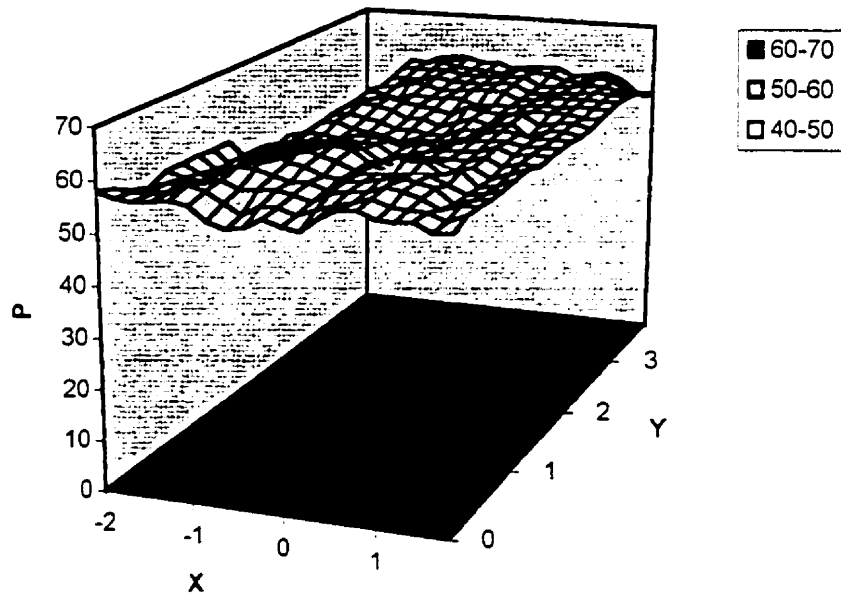
Figure 6.16 Space-Time mapping of reservoir pressure in (a) the first quarter of 1992, and (b) the second quarter of 1992.

### Pressure Mapping During the Third Quarter of 1992



(a)

### Pressure Mapping During the Fourth Quarter of 1992



(b)

Figure 6.17 Space-Time mapping of reservoir pressure in (a) the third quarter of 1992, and (b) the fourth quarter of 1992.

## 6.5 Conditional Simulations of the Reservoir Pressure

The conditional simulations of the reservoir pressure for the year of 1990 were generated by using the SGGs technique developed in Section 5.3. The simulation grid was designed to have  $200 \times 200 \times 12 = 480000$  nodes, with a space-time spacing of  $0.02(\text{km}) \times 0.02(\text{km}) \times 1(\text{month})$ . The selection of such space-time spacing is based on the spatiotemporal correlation structure and the requirement of sampling scheme discussed after this section. The quadrant search was applied for the neighborhood determination of each node to be simulated, and each quadrant has an upper bounds of 8 data, implying that the neighborhood size  $v = 4 \times 8 = 32$  data. The group size of SGGs was designed to be  $4 \times 4 = 16$ , which indicates that the  $0.5v$ -SGGS was adopted to save computing time.

The 576 conditioning data are mentioned in Section 6.1, with the histogram shown in Figure 6.2 and the joint-distance variogram model expressed by Equation 6.1. In view of the histogram of the conditioning data, it was decided to use a single population Gaussian S/TRF model for the conditional simulations of the reservoir pressure, with the spatiotemporal covariance model corresponding to the variogram model given by Equation 6.1.

Histograms of two conditional simulations of the reservoir pressure are shown in Figure 6.18. In comparison with Figure 6.2, it is apparent that the normal distribution shape and statistics of the pressure data are reproduced in conditional simulations by SGGs. Their corresponding experimental variograms are shown in Figure 6.19 and 6.20, which indicates that the characteristics of the space-time continuity of the pressure data were also reproduced in the conditional simulations. Note that these experimental variograms are fairly smooth due to that hundreds of thousands pairs are involved in each experimental variogram calculation, which leads to a strong smooth effect.

Figure 6.21, 6.22, 6.23, and 6.24 show two conditional simulations of the reservoir pressure during 1990, each have 4 time slices (January, April, July, and October). The anisotropy feature of the reservoir pressure was also reproduced in the conditional simulations of the reservoir pressure, showing that the continuity of the conditional simulation in the E-W direction was longer than that in the N-S direction.

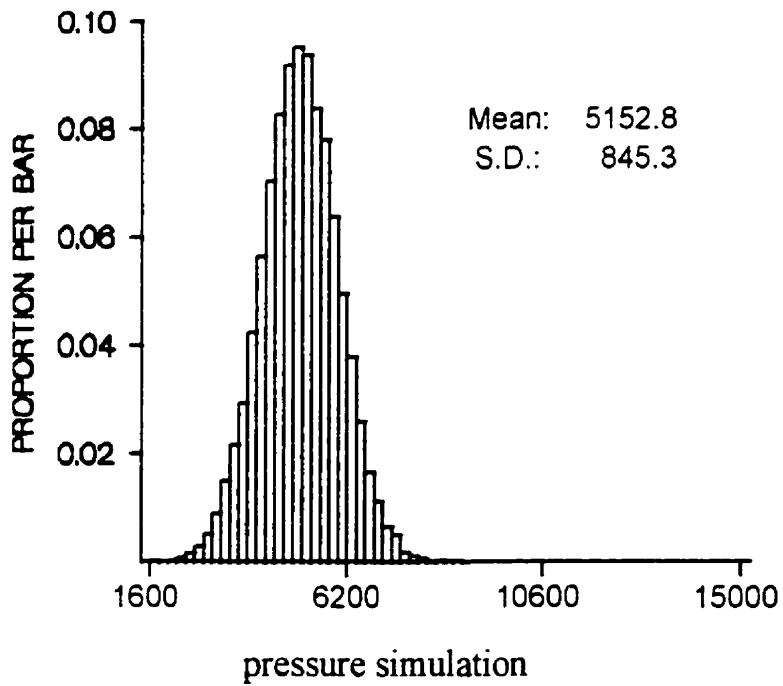
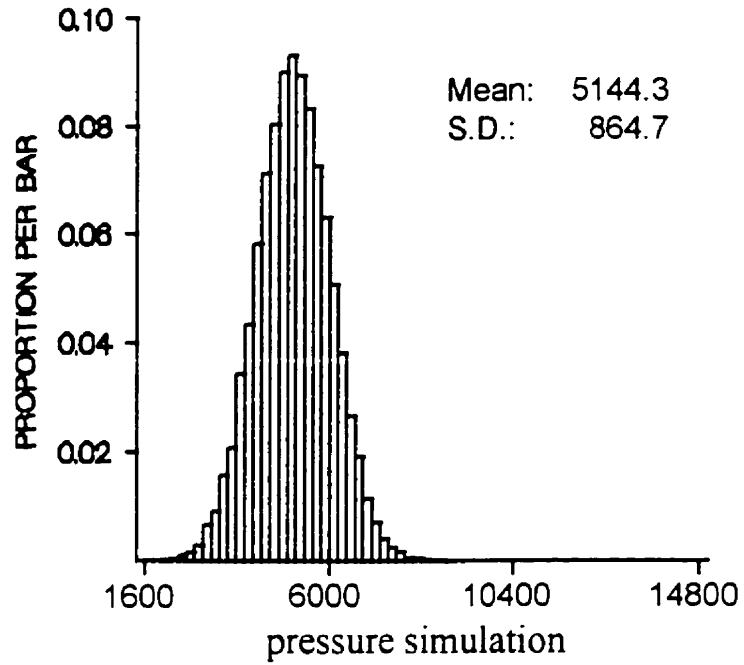


Figure 6.18 Histograms of two conditional simulations of the reservoir pressure generated by SGGS.

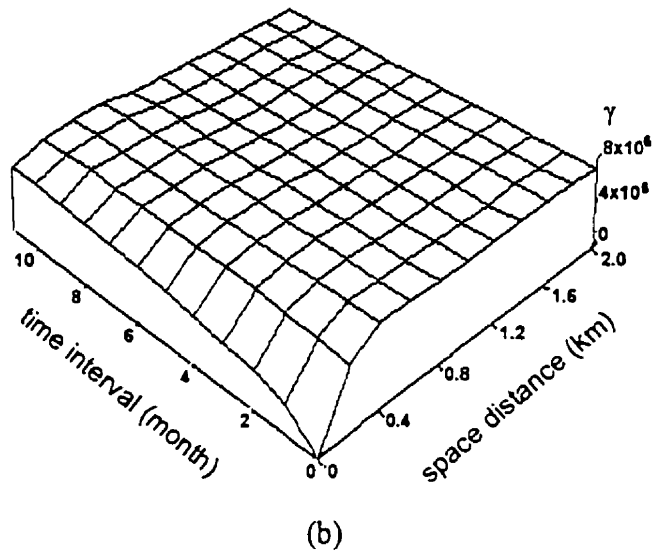
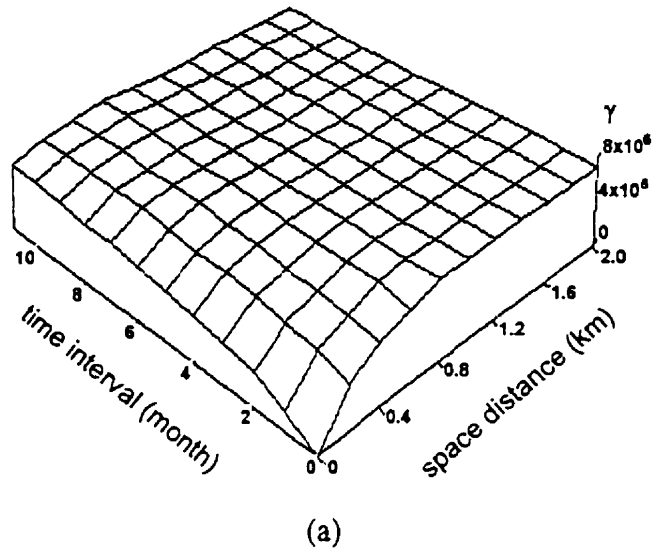


Figure 6.19 Experimental variograms of one conditional simulation of the reservoir pressure generated by SGGS. (a) variograms in the E-W direction, (b) variograms in the N-S direction.

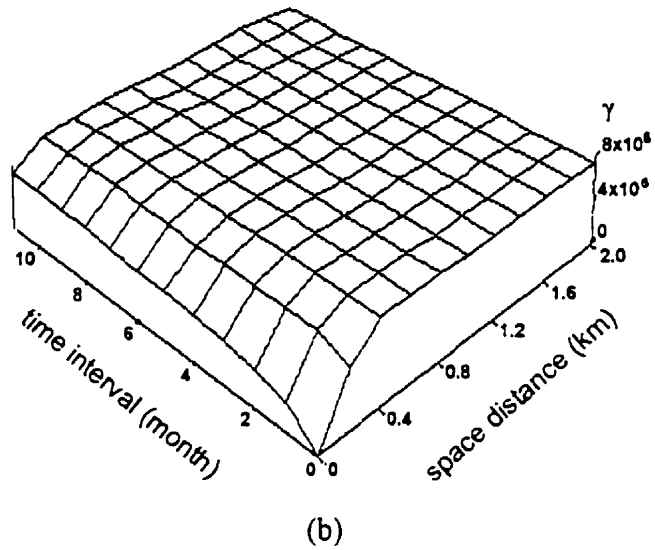
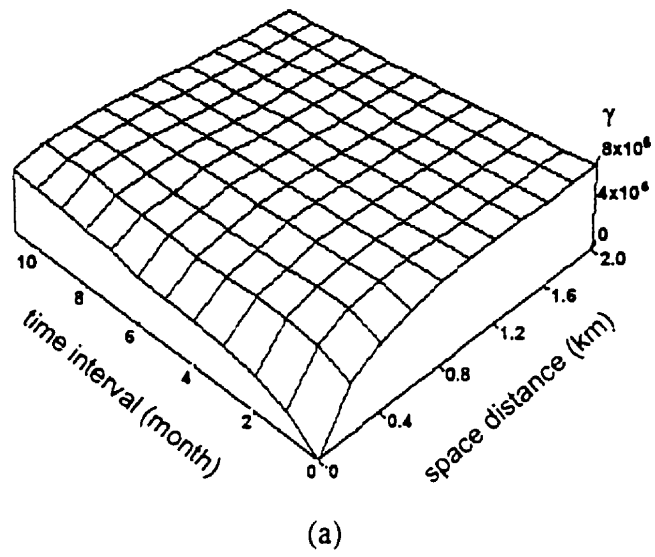
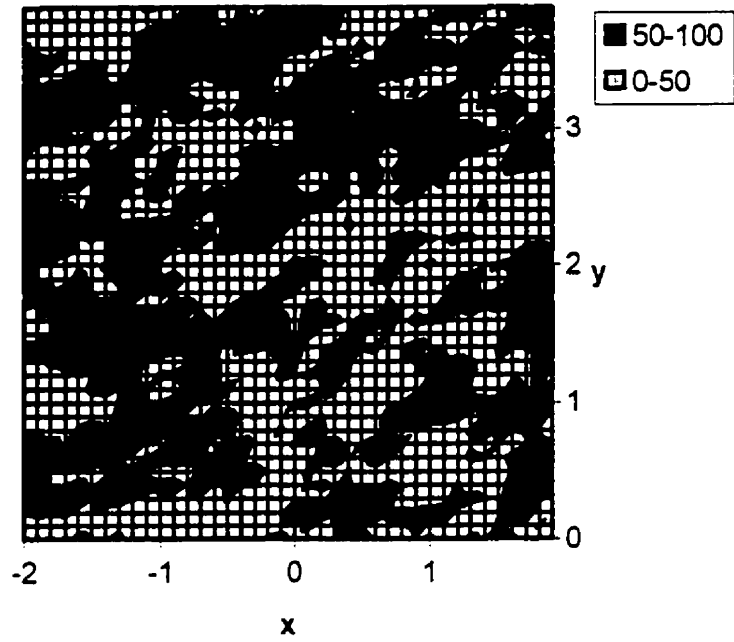


Figure 6.20 Experimental variograms of one conditional simulation of the reservoir pressure generated by SGGs. (a) variograms in the E-W direction, (b) variograms in the N-S direction.

### Pressure simulation at Jan. 90



### Pressure simulation at April 90

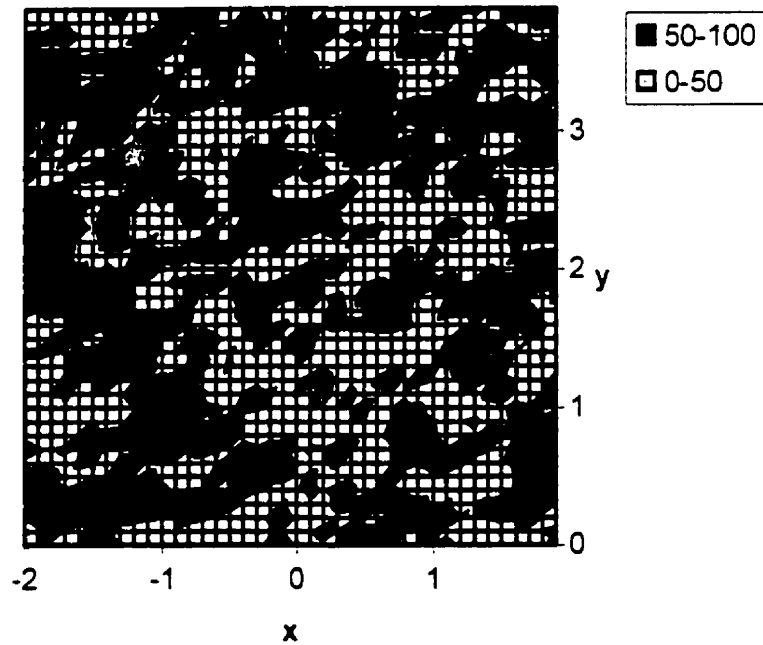
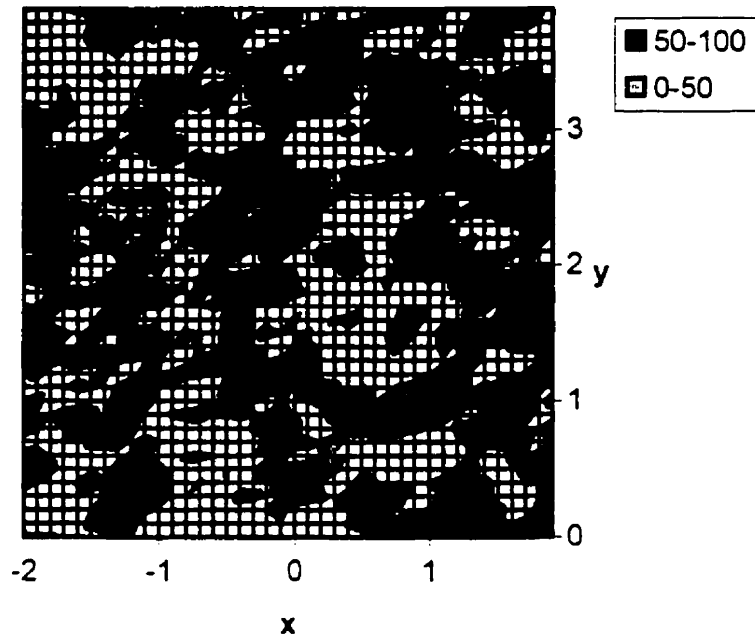


Figure 6.21 Conditional simulations of the reservoir pressure using SGGs at two time slices: January 1990 and April 1990.

### Pressure simulation at July 90



### Pressure simulation at Oct. 90

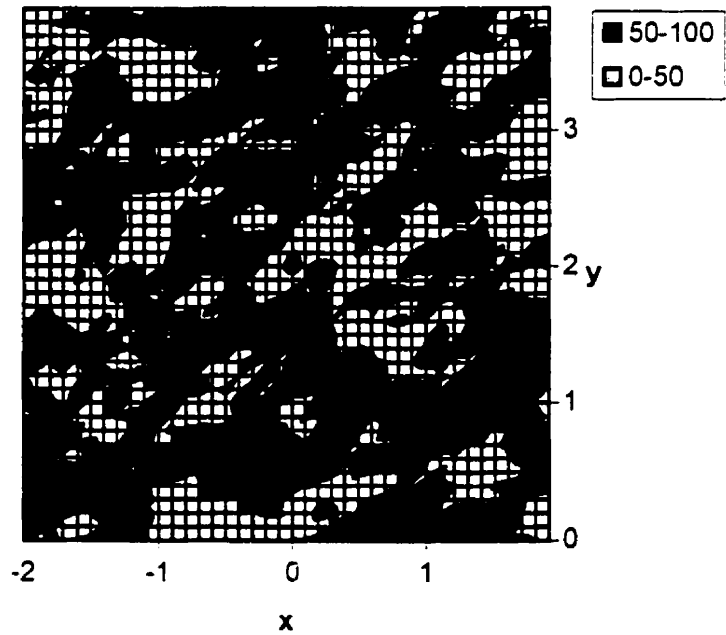
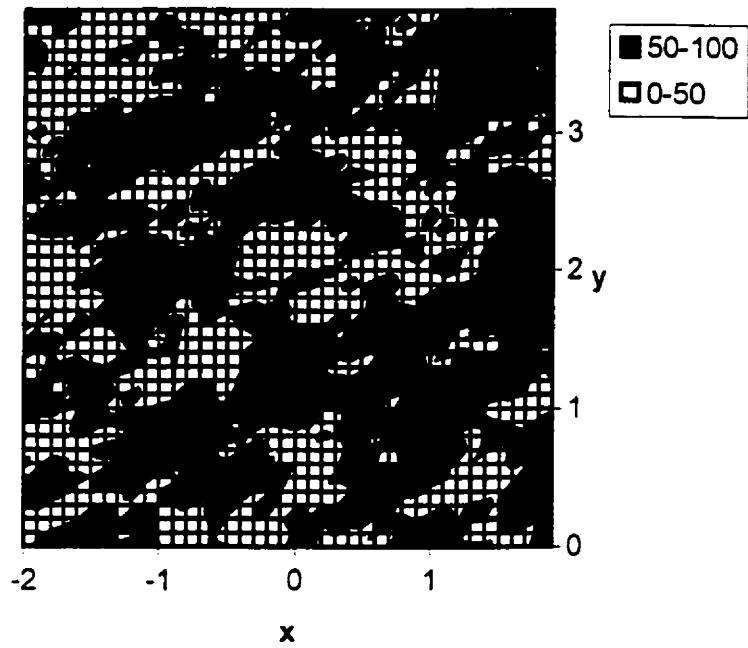


Figure 6.22 Conditional simulations of the reservoir pressure using SGGS at two time slices: July 1990 and October 1990.

### Pressure simulation at Jan. 90



### Pressure simulation at April 90

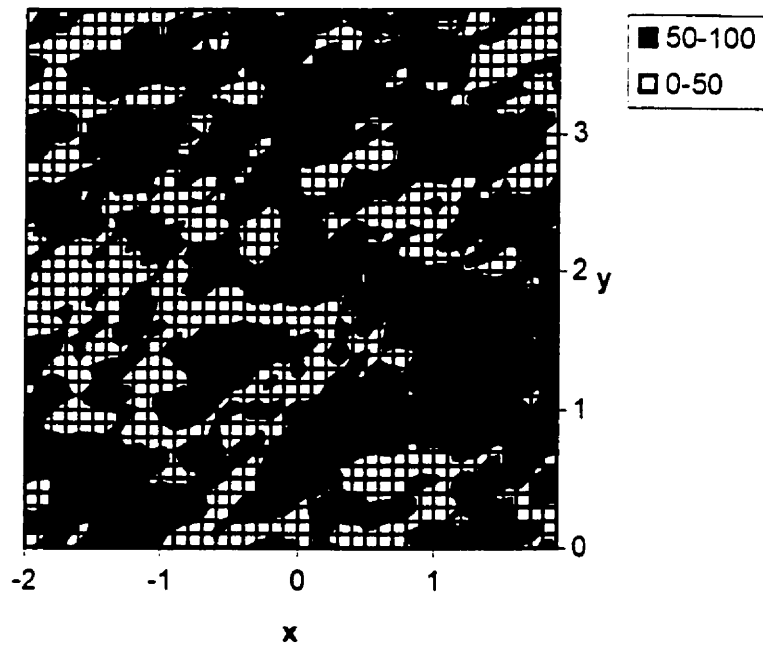
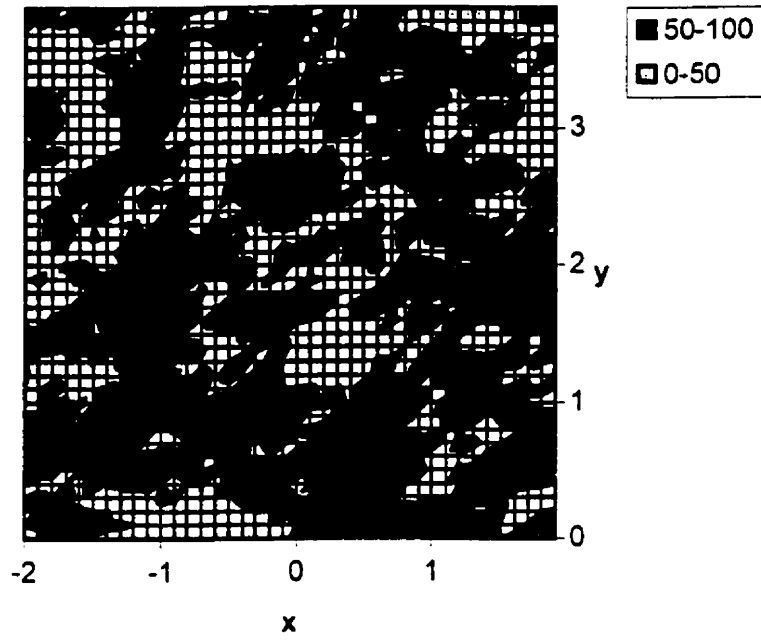


Figure 6.23 Conditional simulations of the reservoir pressure using SGGS at two time slices: January 1990 and April 1990.

### Pressure simulation at July 90



### Pressure simulation at Oct. 90

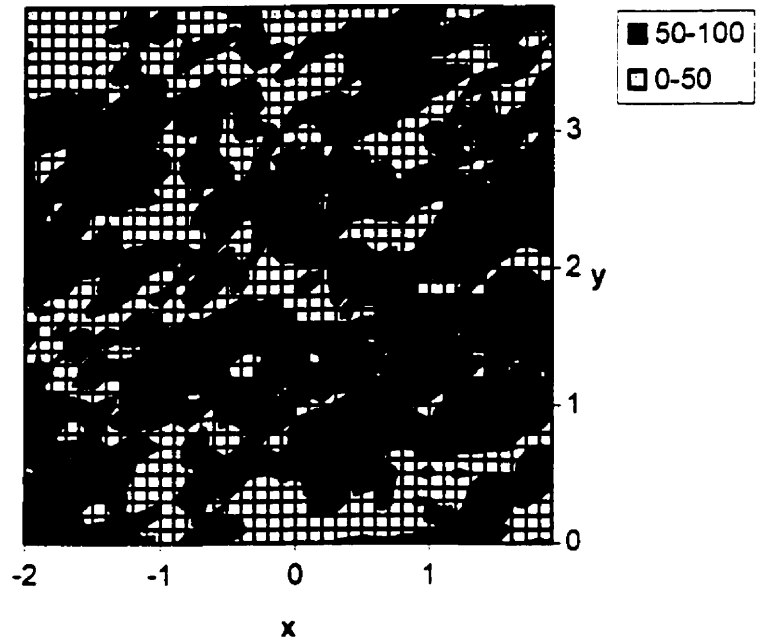


Figure 6.24 Conditional simulations of the reservoir pressure using SGGS at two time slices: July 1990 and October 1990.

## 6.6 Pressure Monitoring Scheme

The goal of pressure monitoring scheme is to construct an appropriate monitoring grid which may estimate local pressure changes in a given period of time adequately for reservoir management and history matching. Therefore, the investigation of monitoring scheme requires space-time sampling design accounting for local averages of pressure to minimize the error level of monitoring in terms of local changes.

In the geostatistical literature, this investigation can be traditionally carried out using average local kriging variance as the sampling criterion (e.g., Barnes, 1988). The local kriging variance indicates the estimation error associated with the neighborhood configuration, hence, the sampling design asking for minimization of average local kriging variance might provide a solution for monitoring scheme. However, this sampling investigation has a drawback that the local variation of interest is disregarded. In practice the estimation error is caused by both the configuration of samples in the neighborhood and values of samples. As an example, Figure 6.25 shows two neighborhoods used to estimate the blocks indicated by squares. Their configurations are the same, but the local variations are different: the local variation in (a) is smaller than that in (b). The estimation error in (a) is hopefully smaller than that in (b). The difference of estimation errors between these neighborhoods indicates the difference of estimation error caused by the local variations which cannot be indicated by local kriging variance.

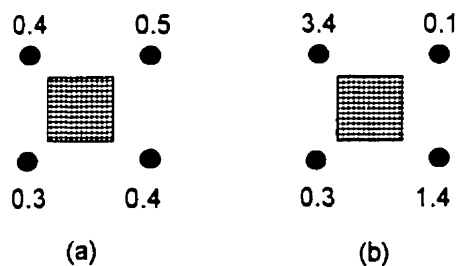


Figure 6.25 Two neighborhoods used to estimate the blocks indicated by the squares. Their configurations are the same, but the local variations are different: the variation in (a) is smaller than that in (b).

Fortunately, the sampling design concerning both the local configuration and variation of samples was introduced by using conditional simulations (e.g., Englund and Heravi, 1993). Conditional simulation mimics both the correlation structure and local variations of

interest. Based on conditional simulation results, the sampling design regarding local variations can be carried out using a criterion accounting for local estimation errors. The crucial point of sampling investigation using conditional simulation is that it not only accounts for local estimation error caused by both local configuration and local variation of samples, but also is capable of showing the uncertainty associated with local estimation errors.

In practice there are three types of sampling scheme (e.g., Bras and Rodriguez, 1985): (i) systematic sampling scheme where the sampling is performed with a regular grid, (ii) stratified-random sampling scheme where samples are picked up randomly in gridblocks, but these gridblocks are regularly distributed, and (iii) simple-random sampling scheme where the sampling is performed randomly in the entire area. Stratified-random sampling scheme is most widely used in geoscience applications, which will be adopted in the study of sampling scheme in this chapter and in Chapter 7. Stratified-random sampling scheme is defined by the sampling spacing. Once the sampling spacing is determined, the size of gridblock is fixed, and the sampling is performed by randomly choosing one sample site in each gridblock.

In this section, the investigation of pressure monitoring scheme is carried out based on spatiotemporal conditional simulations of the reservoir pressure. The spatiotemporal conditional simulations of the reservoir pressure are generated by using SGGS. The sampling criterion regarding local changes of pressure is defined in terms of average local estimation error. The uncertainty associated with average local estimation error of a given sampling grid is also investigated based on multiple conditional simulations of the reservoir pressure.

### 6.6.1 Implementation Steps

The sampling investigation of the reservoir pressure was implemented as follows:

1. define a sampling criterion accounting for local estimation errors. This criterion can be defined in terms of average local estimation error. The average local estimation error (ALEE) can be defined as follows,

$$\delta_{ALEE} = \frac{1}{n_e} \sum_{i=1}^{n_e} (x_i - x_i^*)^2 / C(\mathbf{0}, \mathbf{0}) \quad (6.1)$$

where  $x_i$  denotes the 'true' pressure of a gridblock defined as the average pressure of the gridblock,  $x_i^*$  denotes the estimated pressure of the gridblock,  $n_e$  denotes the number of gridblocks to be estimated, and  $C(0,0)$  is the variance of the simulation model. Generally  $\delta_{ALEE} \in [0, 1]$ .

2. define a simulation grid and a division of the space-time domain. The number of simulated nodes must be much larger than the number of space-time gridblocks.
3. generate a realization of the reservoir pressure on the simulation grid.
4. define a sampling grid.
5. calculate 'true' pressures of gridblocks.
6. sample pressures from simulated pressures with the given sampling grid, use these samples to estimate pressures of gridblocks.
7. compute the average local estimation error given by Equation 6.3.
8. repeat Step 4-7 to obtain average local estimation errors of different sampling grids.
9. repeat Step 3-8 to obtain uncertainties associated with average local estimation errors of different sampling grids.

### 6.6.2 Computations and Results

The sampling investigation of the reservoir pressure was performed for the year of 1990. The reservoir during 1990 was divided into 1080 space-time gridblocks, each has a size of  $0.32(\text{km}) \times 0.32(\text{km}) \times 3(\text{month})$ . The 'true' pressure of a gridblock is defined as the average pressure of  $16 \times 16 \times 3$  pressure values in this gridblock.

The sampling grid was initially set with a space-time spacing of  $0.2(\text{km}) \times 0.2(\text{km}) \times 3(\text{month})$ , the average local estimation error given by Equation 6.3 was calculated. Then the spatial spacing was increased 0.04 km each time, until it reached 0.68 km. the spatial spacings beyond 0.68 km were not considered since they are out of the range of the correlation structure. After the spatial spacing reaches 0.68 km, it was reset to 0.2 km, and the time spacing was increased one month each time. This process keeps running until the spatial spacing reached 0.68 km and the time spacing reached five months simultaneously, the average local estimation errors associated with different sampling spacings were obtained. This procedure was repeated 40 times to demonstrate the uncertainty of average local estimation errors associated with different sampling spacings.

Figure 6.26 shows average local estimation errors vs. spatial spacing for three time spacings: 3 months, 4 months, and 5 months. The thick lines indicate the means of average

local estimation errors. The differences of these three thick lines are fairly small. The mean of average local estimation errors tends to be minimum when the spatial spacing is around 0.32 km. After 0.32 km the mean of average local estimation error is increased almost linearly with the spatial spacing.

To verify these observations, conditional simulations during 1991 were generated, and similar sampling scheme was performed with different sampling grids. Figure 6.27 shows the result of average local estimation errors vs. spatial spacing. In comparison with Figure 6.26, their difference is considerably small, which implies that the impact of time spacing on the average local estimation error is fairly small. and the optimal spatial spacing is around 0.32 km.

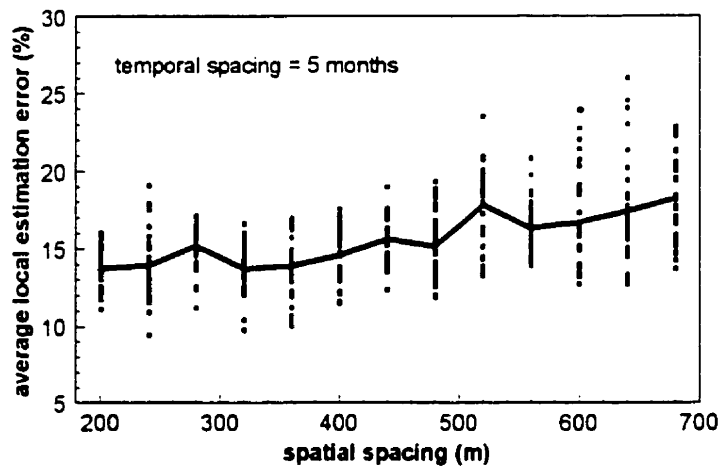
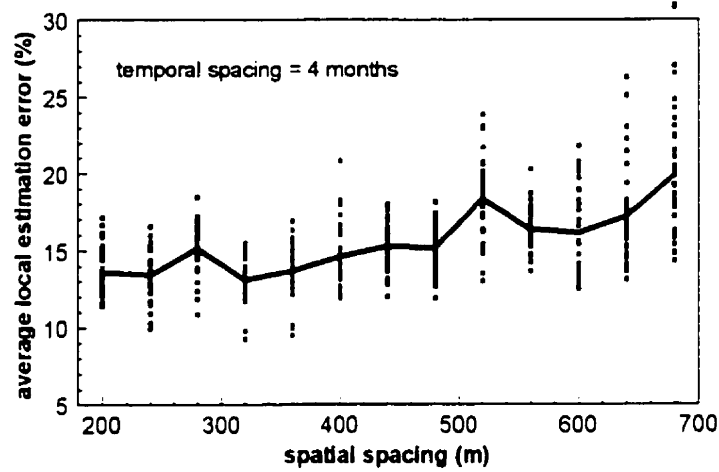
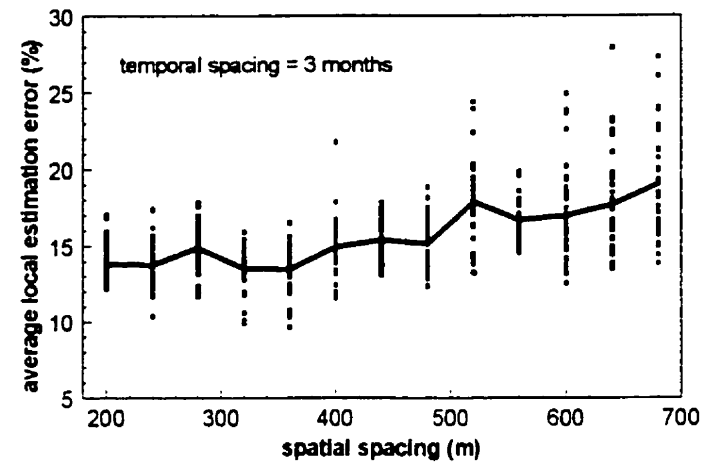


Figure 6.26 Average local estimation error vs. spatial spacing for three time spacing for 1990: 2 months, 3 months, and 4 months. The thick line indicates the means.

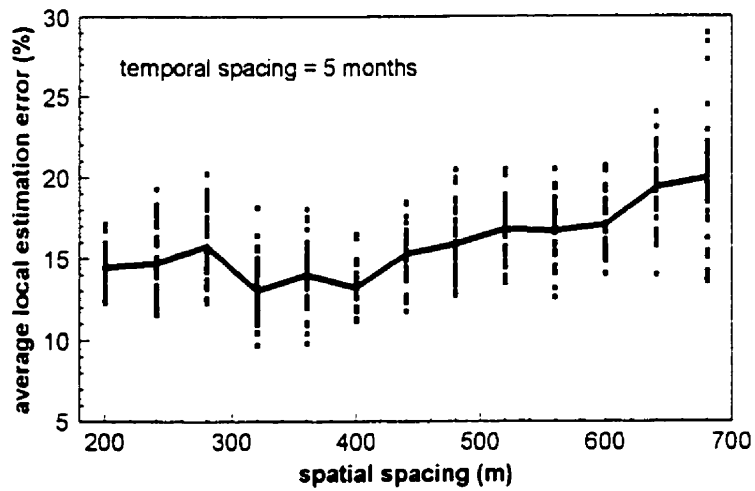
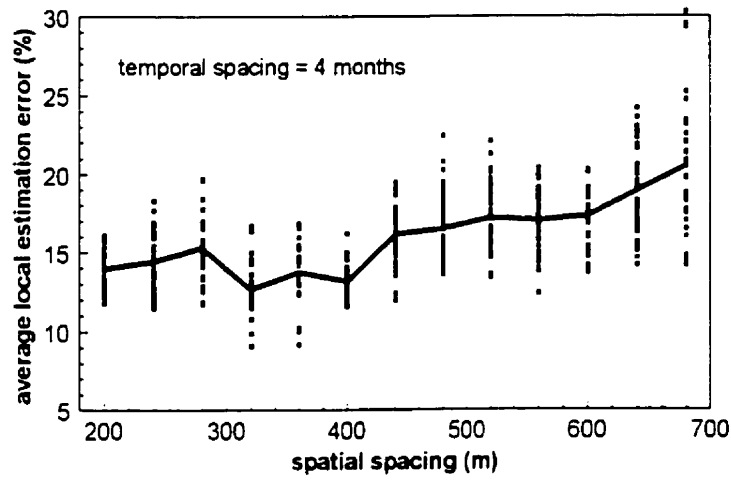
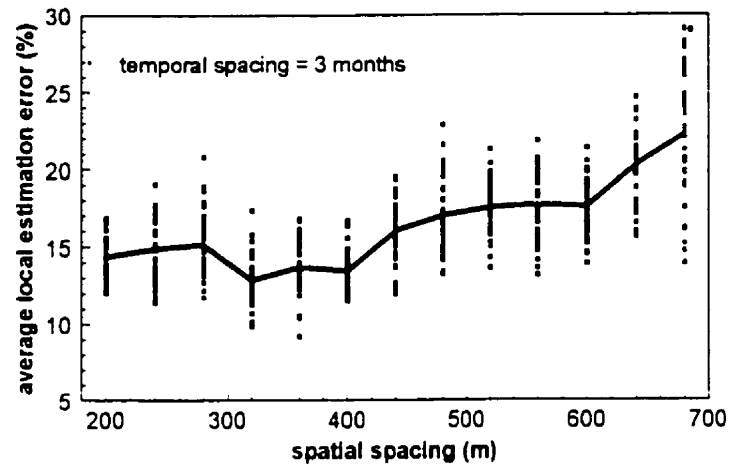


Figure 6.27 Average local estimation error vs. spatial spacing for three time spacing for 1991: 2 months, 3 months, and 4 months. The thick line indicates the means.

## 6.7 Summary

This chapter presents the space-time modelling of reservoir pressure systems in a carbonate reservoir. The reservoir pressure was viewed as a spatiotemporal process, and its variation was characterized, estimated and simulated with the means of S/TRF proposed in previous chapters.

The space-time modelling of the reservoir pressure system was concentrated on the pressure data in production wells, since the pressure data in injection wells are likely to be different from that in production wells in terms of population distributions. The distribution of the reservoir pressure was assumed to be normal based on its histogram, and the space-time continuity was supposed to be stationary with a geometric anisotropy structure. A joint-distance exponent function was adopted as the spatiotemporal variogram model.

The space-time mapping of the reservoir pressure from the first quarter of 1989 up to the last quarter of 1992 was performed by using S/T block OK techniques. The results show that the gradient of the reservoir pressure tends to decrease with time passing, and high/low pressure bands likely spread from north to south, which is consistent with the space-time continuity characteristics of the reservoir pressure mentioned previously.

The monitoring scheme of the reservoir pressure system was analyzed based on spatiotemporal conditional simulations of the reservoir pressure. The goal of the monitoring scheme is to monitor local changes of the reservoir pressure adequately, therefore, average local estimation error is adopted to evaluate different sampling grids. The conditional simulations of the reservoir pressure was generated by using SGGS. Average local estimation errors and associated uncertainties of different sampling grids were computed based on multiple conditional simulations of the reservoir pressure. The result shows that (i) the impact of time spacing on the average local estimation error is not significant, and (ii) the optimal spatial spacing is approximately 0.32 km.

## Chapter 7

### Space-Time Modelling of Springwater Contents

#### 7.1 Introduction

The deterioration of groundwater quality is an increasingly critical situation throughout the world. This concern has given rise to regulations that require extensive groundwater monitoring to detect, at the earliest possible time, the release of contaminants from natural sources, resource extraction and other man-made sources. Groundwater contamination can be monitored by analyzing well and spring water for a series of dissolved ion species. Groundwater quality data sets can then be used to model changes in the composition of groundwater and outline potential zones of contamination. Groundwater contents vary in space and in time simultaneously depending on such factors as the geological environments of aquifers, human activities, and climate conditions. The spatiotemporal variability of groundwater contents can therefore be modelled based on the framework of S/T RF.

This study will attempt to utilize the techniques of spatiotemporal processes developed in previous chapters to model spatiotemporal variability of groundwater contents, based on the springwater data from a Belgian study. The study area is the Dyle watershed, located in the Dyle River basin, 30 km southeast of Brussels (Belgium). This area is made up of a Paleozoic basement overlaid unconformably by a thick horizontal layer (30-50 m thick) of Tertiary sand of Bruxellian age (Legrand, 1968). The Bruxellian sand layer forms the main part of the aquifer. The main Bruxellian aquifer behaves like an unconfined porosity aquifer recharged by rainwater over its whole surface and drained by valleys.

From 1974 to 1983, spring waters were repeatedly analyzed upstream in the Dyle River basin. In 1975, Goovaerts, Sonnet and Navarre (1993) used factorial kriging analysis to analyze a data set of 11 ions. Principal component analysis was performed to determine three principal component groups. The first group was alkaline, containing Ca, Sr, and EC, and was likely influenced by the geological characteristics of the aquifer. The second group seemed to contain properties influenced by the geology and/or human activities. It contained Mg, Cl, and SO<sub>4</sub>. The third group contained Na, NO<sub>3</sub>, and K, which are highly influenced by human activities. The experimental variograms of the three groups show two

scales of spatial variation: the first one is modelled with a range of 1 km and the second one is modelled with a range of 9 km. The cokriged maps of the three groups were computed to demonstrate the spatial variability of these groups.

In the present study, the data of three ions (Ca, Cl, and  $\text{NO}_3$ ) from 68 springs for six years (1975, 1979, 1980, 1981, 1982, 1983) were used to show the space-time variability of springwater contents. Each spring was sampled once every year, indicating that a total of 408 data are available for each ion. The locations of springs are shown in Figure 7.1. The characteristics of space-time continuity of springwater contents were investigated by spatiotemporal experimental variograms. The space-time mapping of springwater contents was performed for four years (from 1979 to 1982) to show the space-time variability of springwater contents. Finally, the sampling design was analyzed based on conditional simulations of springwater contents.

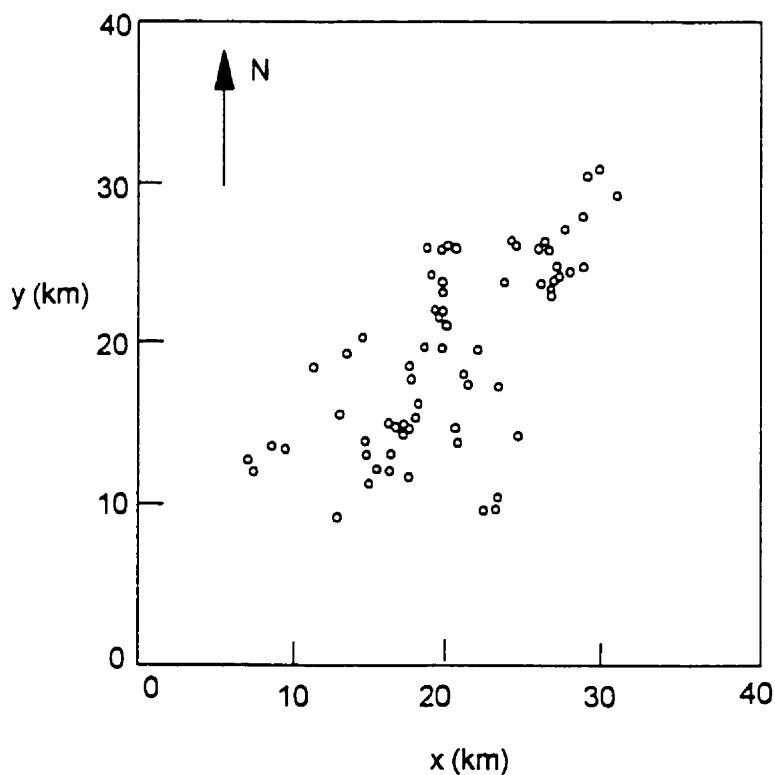


Figure 7.1 Locations of 68 springs.

## 7.2 Statistics and Space-Time Continuity of Spring Data

The histograms of Ca, Cl, and  $\text{NO}_3$  concentrations are illustrated in Figures 7.2, 7.3, and 7.4. The Cl and  $\text{NO}_3$  histograms each show a roughly normal distribution shape, while the Ca histogram demonstrates a two-peaked shape. Their four space-directional experimental variograms and space-omnidirectional experimental variograms are shown in Figures 7.5, 7.6, and 7.8. The experimental variograms of Ca concentrations show a presence of space-anisotropy structure: the range in the E-W direction is longer than that in the N-S direction. In general, experimental variograms of Ca, Cl, and  $\text{NO}_3$  concentrations show fairly large fluctuations. The space-anisotropy structure and the large fluctuations of the experimental variograms may be caused by the presence of space-time trends due to zonal variations of geological environments and periodical alternations of climate and human activities. The presence of space-time trends was identified and the types of trend models were recognized in sections below.

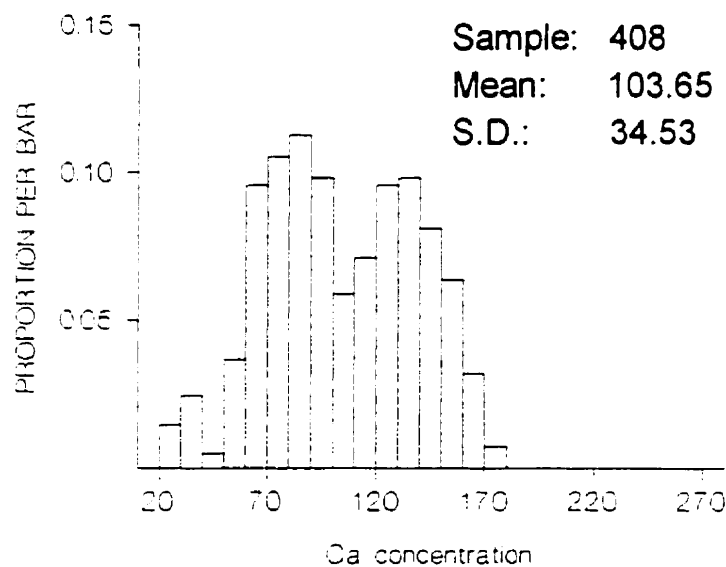


Figure 7.2 The histogram of Ca concentrations.

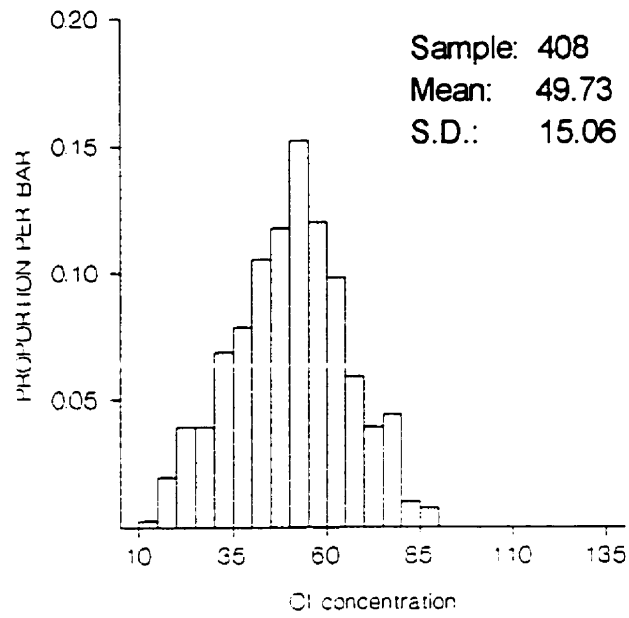


Figure 7.3 The histogram of Cl concentrations.

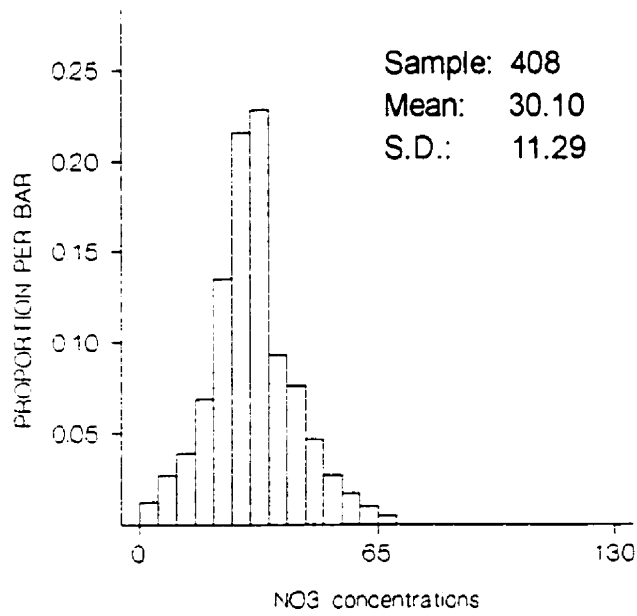
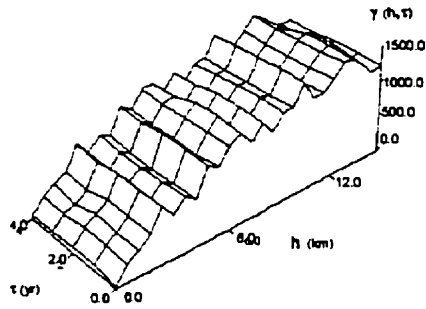


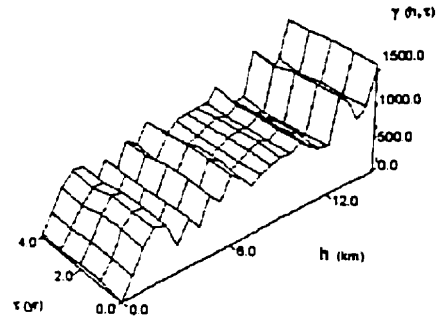
Figure 7.4 The histogram of NO<sub>3</sub> concentrations.

Ca original simivariograms in 0 degree



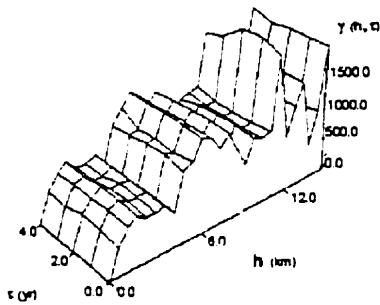
(a)

Ca original simivariograms in 45 degree



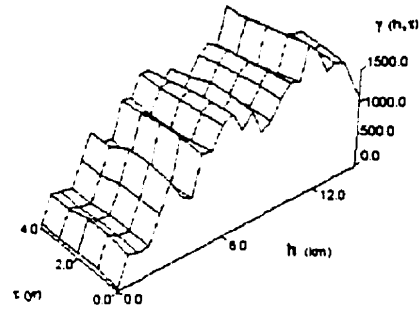
(b)

Ca original simivariograms in 90 degree



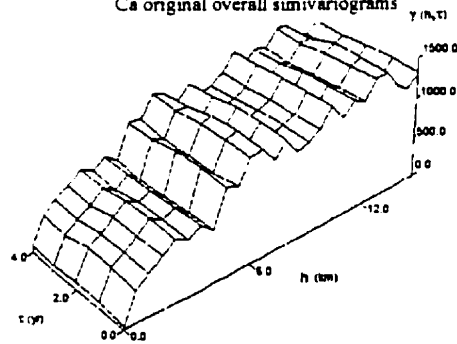
(c)

Ca original simivariograms in 135 degree



(d)

Ca original overall simivariograms



(e)

Figure 7.5 Experimental variograms of Ca concentrations. (a) variograms in the E-W direction, (b) variograms in the NE 45 direction, (c) variograms in the N-S direction, (d) variograms in the NW 45 direction, and (e) omnidirectional variograms .

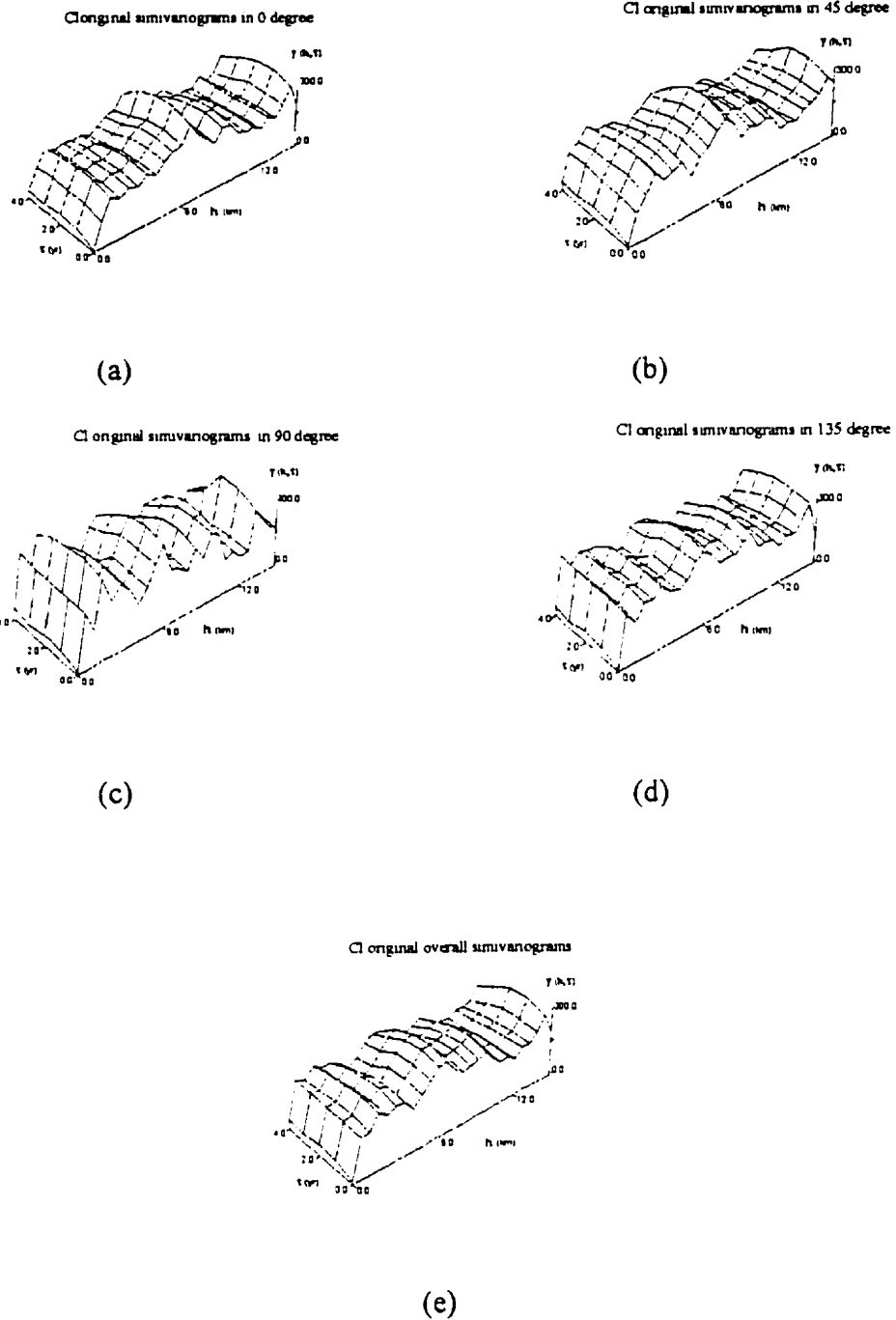


Figure 7.6 Experimental variograms of Cl concentrations. (a) variograms in the E-W direction, (b) variograms in the NE 45 direction, (c) variograms in the N-S direction, (d) variograms in the NW 45 direction, and (e) omnidirectional variograms .

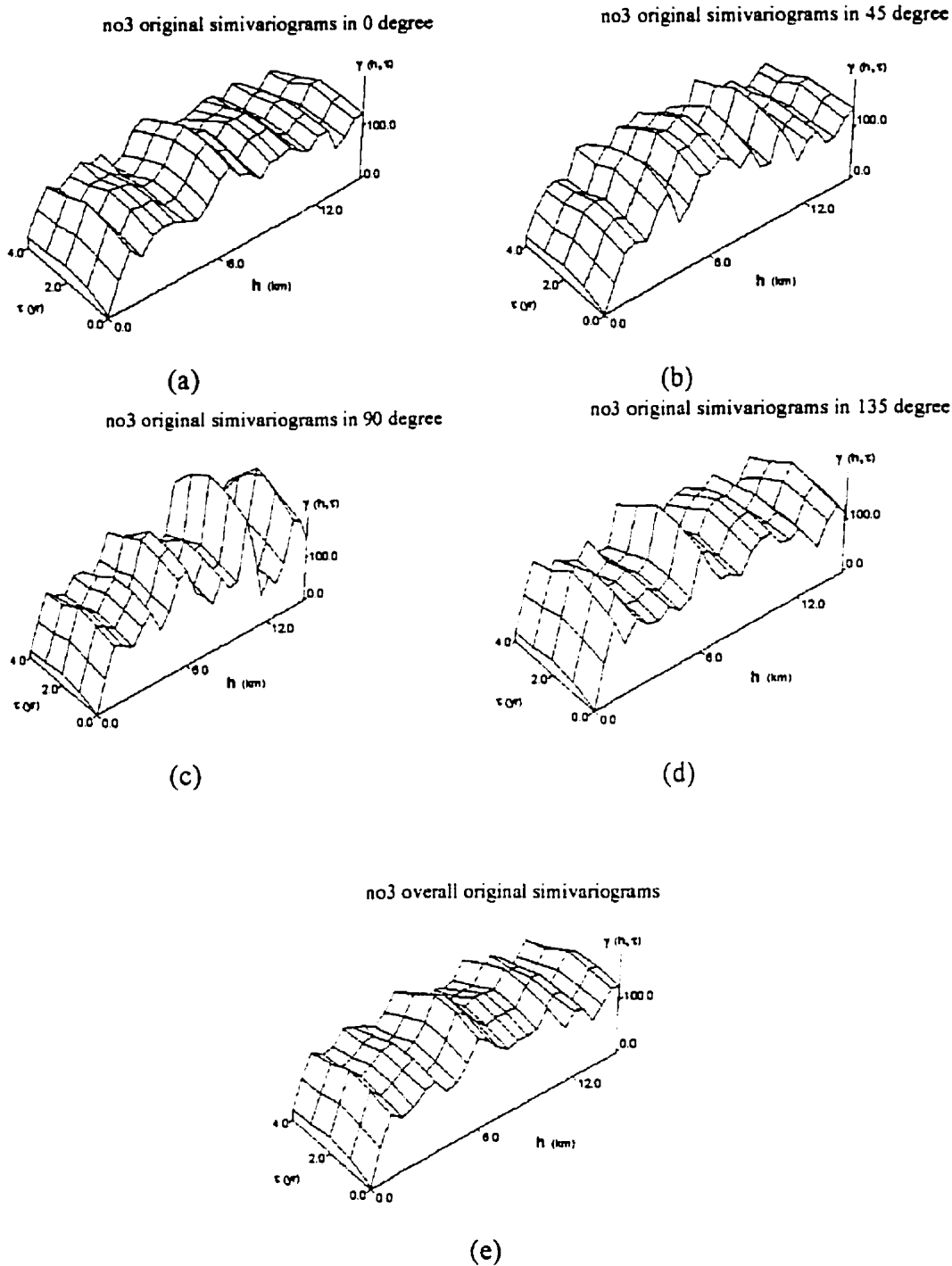


Figure 7.7 Experimental variograms of  $\text{NO}_3$  concentrations. (a) variograms in the E-W direction, (b) variograms in the NE 45 direction, (c) variograms in the N-S direction, (d) variograms in the NW 45 direction, and (e) omnidirectional variograms .

### 7.3 Recognition of a Space-Time Trend

The presence of the space-time trend was investigated using trend-surface analysis with 16 trend models and 4 criteria in four subareas. Trend-surface analysis is one of the most powerful tools used for trend recognition (e.g., Davis, 1973; Agterberg, 1974). Once the space-time trend was recognized, the residuals of springwater contents could be computed, and the correlation structures of these residuals could be obtained (e.g., Matheron, 1971; David, 1977). The partition of four subareas was based on the distribution of high/low value bands in the study area. The 16 trend models were constructed by different combinations of spatial components (indicated by  $\xi$ ) and temporal components (indicated by  $\zeta$ ), see Table 4.1. Average absolute error, average square error, average error, and coefficient of determination were calculated for each trend model.

Coefficient of determination is one of the most important measures of the adequacy of regression/trend models (e.g., Gunst and Mason, 1980), which is defined as follows,

$$r^2 = \frac{\sum_{i=1}^N (\hat{Z}_i - \bar{Z})^2}{\sum_{i=1}^N (Z_i - \bar{Z})^2}$$

where  $Z_i$  ( $i=1$  to  $N$ ) denote values of the interest,  $\hat{Z}_i$  ( $i=1$  to  $N$ ) denote values of the trend function, and  $\bar{Z}$  denotes the average.  $r^2 \in [0, 1]$ . Generally an appropriate trend model is associated with a large value of coefficient of determination.

The determination of harmonic trends involves choosing spatial and temporal periods. The spatial and temporal periods were selected by trial and error with regard to coefficient of determination. The results showed that the spatial periods of Ca, Cl, and  $\text{NO}_3$  concentrations are respectively around 4.0, 4.2, and 4.0 kilometers, and the temporal period of Ca, Cl, and  $\text{NO}_3$  concentrations are all around 3 years.

The average results of trend-surface analysis for Ca, Cl, and  $\text{NO}_3$  concentrations in four subareas are shown in Tables 7.1, 7.2, and 7.3. The trend model that was linear plus harmonic in space ( $\xi=1+i$ ) and linear in time ( $\zeta=1$ ) obtained large values of coefficient of determination for all of these ion concentrations. Therefore, this type of trend model is chosen and its adequacy is further investigated based on the residuals.

## 7.4 Statistics and Space-Time Continuity of Ion Residuals

The following definition of the residual of a S/TRF  $X(s, t)$  can be obtained from Equation 1.10,

$$\hat{Y}(s, t) = X(s, t) - \hat{m}(s, t) = [m(s, t) - \hat{m}(s, t)] + Y(s, t)$$

where  $\hat{m}(s, t)$  indicates the chosen trend model. The residual  $\hat{Y}(s, t)$  is actually an estimate of  $Y(s, t)$  assumed to be stationary with a mean of zero. Therefore, if the chosen trend model,  $\hat{m}(s, t)$ , is an appropriate estimate of the trend,  $m(s, t)$ , then the difference,  $[m(s, t) - \hat{m}(s, t)]$ , should be sufficiently small, indicating that the residual  $\hat{Y}(s, t)$  should also be stationary with a mean of zero. In addition, there should be no distinct anisotropy in correlation structures of the residuals (e.g., Neuman and Jacobson, 1984).

Figures 7.8, 7.9, and 7.10 show the histograms of Ca, Cl, and  $\text{NO}_3$  residuals. They all approximately show normal distributions with a mean of zero. In comparison with Figure 7.2, the two-peaked shape presented in the histogram of Ca concentrations disappeared in the histogram of Ca residuals. The four directional (E-W, NE 45, N-S, and NW 45) and omnidirectional experimental variograms of Ca, Cl, and  $\text{NO}_3$  residuals were calculated with a space lag of 0.2 kilometer and a time interval of 1.0 year. The directional tolerance, space-lag tolerance, and time-interval tolerance were respectively set to be  $45^\circ$ , 0.1 kilometer, and 0.5 year. These experimental variograms are illustrated in Figures 7.11, 7.12, and 7.13. These pictures show fairly stable structures of the space-time continuity. All of these residuals show space-isotropic structures in their experimental variograms. These improved illustrations of the space-time continuity and distribution of residuals imply the adequacy of trend models given in Table 7.4, 7.5, and 7.6.

The space-omnidirectional experimental variograms of Ca residuals were fitted by the following joint-distance spherical model (shown in Figure 7.12(f)):

$$\gamma(h, \tau) = 13.13 + 250.0 \cdot \text{sph}\left(\sqrt{\left(\frac{h}{0.72}\right)^2 + \left(\frac{\tau}{10}\right)^2}\right) \quad (7.1)$$

where  $\text{sph}(\cdot)$  stands for a standard spherical function with a range of 1.

The space-omnidirectional experimental variograms of Cl residuals were also fitted by a joint-distance spherical model (shown in Figure 7.13(f)):

$$\gamma(h, \tau) = 7.25 + 74.0 \cdot \text{sph}\left(\sqrt{\left(\frac{h}{0.72}\right)^2 + \left(\frac{\tau}{7.0}\right)^2}\right) \quad (7.2)$$

The space-omnidirectional experimental variograms of NO<sub>3</sub> residuals were fitted by a separable exponential model (shown in Figure 7.13(f)):

$$\gamma(h, \tau) = 2.98 + 41.5 \cdot \exp\left(-\frac{h}{0.3}\right) \exp\left(-\frac{\tau}{2.0}\right) \quad (7.3)$$

Table 7.1 The average results of trend-surface analysis for Ca concentrations.

Spatial period = 4.0 and temporal period = 3.0

trend model	average absolute error	average square error	average error	coefficient of determination
$\xi = 0 / \zeta = 1$	24.943	957.541	-0.00000221	.0063
$\xi = 0 / \zeta = 2$	24.831	952.961	-0.00004422	.0139
$\xi = 1 / \zeta = 0$	18.059	583.443	.00000004	.2545
$\xi = 1 / \zeta = 1$	17.991	579.113	.00000214	.2609
$\xi = 1 / \zeta = 2$	17.962	574.534	.00000640	.2685
$\xi = 2 / \zeta = 0$	15.999	468.741	.00000760	.3783
$\xi = 2 / \zeta = 1$	15.923	464.413	-0.00004929	.3847
$\xi = 2 / \zeta = 2$	15.889	453.404	-0.00002228	.4005
$\xi = 0 / \zeta = i$	24.847	951.451	.00000035	.0145
$\xi = 1 / \zeta = i$	17.862	567.982	.00000340	.2754
$\xi = i / \zeta = 0$	21.671	767.480	-0.00000133	.1559
$\xi = i / \zeta = 1$	16.199	466.690	.00000087	.4617
$\xi = i / \zeta = i$	24.572	933.461	-0.00000056	.0285
$\xi = 1+i / \zeta = 0$	16.520	494.140	.00000014	.3484
$\xi = 1+i / \zeta = 1$	11.164	238.481	.00001198	.6343
$\xi = 1+i / \zeta = i$	17.703	559.604	-0.00000321	.2809

Table 7.2 The average results of trend-surface analysis for Cl concentrations.  
 Spatial period = 4.2 and temporal period = 3.0

trend model	average absolute error	average square error	average error	coefficient of determination
$\xi = 0 / \zeta = 1$	11.679	220.704	-.00000145	.0247
$\xi = 0 / \zeta = 2$	11.648	219.929	.00000726	.0290
$\xi = 1 / \zeta = 0$	10.900	188.841	.00000231	.1809
$\xi = 1 / \zeta = 1$	10.733	183.622	-.00000049	.2057
$\xi = 1 / \zeta = 2$	10.683	182.846	.00000757	.2100
$\xi = 2 / \zeta = 0$	9.101	138.588	-.00001974	.3876
$\xi = 2 / \zeta = 1$	8.828	133.368	.00003704	.4123
$\xi = 2 / \zeta = 2$	8.748	131.116	.00001034	.4231
$\xi = 0 / \zeta = i$	11.622	219.702	-.00000036	.0307
$\xi = 1 / \zeta = i$	10.533	178.386	.00000059	.2292
$\xi = i / \zeta = 0$	11.424	211.254	.00000070	.0584
$\xi = i / \zeta = 1$	7.808	106.367	.00000037	.5104
$\xi = i / \zeta = i$	11.796	219.028	-.00000001	.0281
$\xi = 1+i / \zeta = 0$	10.315	174.096	.00000193	.2403
$\xi = 1+i / \zeta = 1$	6.542	74.147	-.00000966	.6661
$\xi = 1+i / \zeta = i$	10.633	182.867	.00000023	.2063

Table 7.3 The average results of trend-surface analysis for NO<sub>3</sub> concentrations.  
 Spatial period = 4.0 and temporal period = 3.0

trend model	average absolute error	average square error	average error	coefficient of determination
$\xi = 0 / \zeta = 1$	8.436	127.397	.00000035	.0231
$\xi = 0 / \zeta = 2$	8.293	124.276	-.00000559	.0516
$\xi = 1 / \zeta = 0$	7.901	107.738	-.00000006	.1667
$\xi = 1 / \zeta = 1$	7.789	105.012	.00000096	.1899
$\xi = 1 / \zeta = 2$	7.660	101.890	.00000593	.2184
$\xi = 2 / \zeta = 0$	7.251	83.306	.00002093	.3304
$\xi = 2 / \zeta = 1$	7.122	80.579	-.00000799	.3535
$\xi = 2 / \zeta = 2$	6.936	76.875	-.00002518	.3871
$\xi = 0 / \zeta = i$	8.357	125.140	-.00000081	.0439
$\xi = 1 / \zeta = i$	7.551	97.714	.00000145	.2531
$\xi = 2 / \zeta = i$	8.249	110.703	-.00000019	.1317
$\xi = i / \zeta = 0$	5.542	48.530	-.00000003	.5742
$\xi = i / \zeta = 1$	8.470	128.254	.00000005	.0128
$\xi = i / \zeta = i$	7.504	94.344	.00000005	.2578
$\xi = 1+i / \zeta = 0$	7.504	94.344	.00000005	.2578
$\xi = 1+i / \zeta = 1$	4.978	41.534	-.00001967	.6265
$\xi = 1+i / \zeta = i$	7.824	105.721	.00000032	.1809

Table 7.4 The coefficients of trend models for Ca concentrations. Spatial period = 4.0.

Terms	Coefficients			
	Subarea 1	Subarea 2	Subarea 3	Subarea 4
1	-398.79626	302.25021	1874.58632	580.06381
sinxsiny	-27.86769	23.45691	5.66300	7.07465
sinxcosy	-21.94068	33.69272	-7.90850	8.91022
cosxsiny	2.86373	1.38780	19.44422	-32.35837
cosxcosy	17.94947	27.09568	-15.08979	-15.06449
x	31.96374	-7.57923	-135.55691	-26.33426
y	2.77919	-5.43775	31.67979	9.04106
t	7.55964	-7.46086	-22.68417	-5.11834
tsinxsiny	.22724	.33661	.16236	-.10872
tsinxcosy	-.32940	.22874	.12255	.07076
tcosxsiny	-.46521	.15306	-.06551	-.11483
tcosxcosy	.22879	-.00087	-.05824	.09079
xt	-.54492	.34294	1.73524	.27718
yt	-.00970	.06615	-.42142	-.07785

Table 7.5 The coefficients of trend models for Cl concentrations. Spatial period = 4.2.

Terms	Coefficients			
	Subarea 1	Subarea 2	Subarea 3	Subarea 4
1	-112.00518	-63.17836	586.22471	536.81793
sinxsiny	2.07095	3.59487	24.31402	1.28652
sinxcosy	35.37537	10.63452	-11.38405	-10.97134
cosxsiny	-1.90274	-15.28992	-17.77876	-20.81482
cosxcosy	7.66108	11.93763	4.69861	-3.07201
x	13.67018	-4.38449	-53.50940	-24.73183
y	-5.00613	5.23969	20.46250	6.05729
t	3.02683	-1.60488	-7.05936	-5.63734
tsinxsiny	-.09512	-.07059	-.21906	.01349
tsinxcosy	.25492	.00068	.27136	.09082
tcosxsiny	.16508	.02191	-.19702	-.10498
tcosxcosy	.14932	-.12683	.13263	-.01334
xt	-.19088	.20607	.65101	.29269
yt	.00704	-.06771	-.21731	-.07580

Table 7.6 The coefficients of trend models for NO<sub>3</sub> concentrations. Spatial period = 4.0.

Terms	Coefficients			
	Subarea 1	Subarea 2	Subarea 3	Subarea 4
1	36.16709	1388.28317	-77.37017	91.21171
sinxsiny	14.66309	6.93164	5.94253	1.73782
sinxcosy	-11.24191	11.39687	-13.22187	-2.95470
cosxsiny	28.48949	2.38497	-9.09622	1.61511
cosxcosy	3.58883	1.56553	14.53264	-2.84192
x	3.17122	-9.25165	4.85633	-11.85963
y	-5.72212	-11.34528	1.84959	4.91687
t	-.37057	-16.95049	-2.19038	-2.30121
tsinxsiny	-.27221	-.08980	-.10192	.06021
tsinxcosy	-.00568	.16165	.12205	.01690
tcosxsiny	-.06222	-.12204	-.10081	.00007
tcosxcosy	.45124	.16563	-.25864	.08260
xt	-.02094	.74913	.19562	.15677
yt	.07927	.13082	-.07948	-.06043

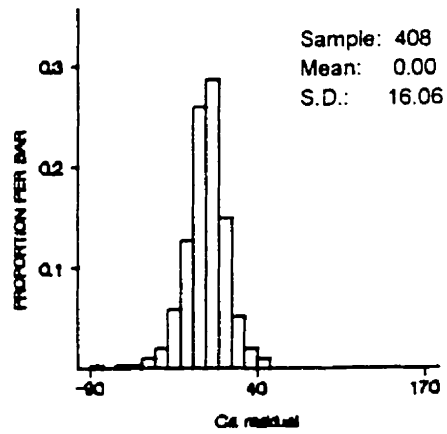


Figure 7.8 The histogram of Ca residuals.

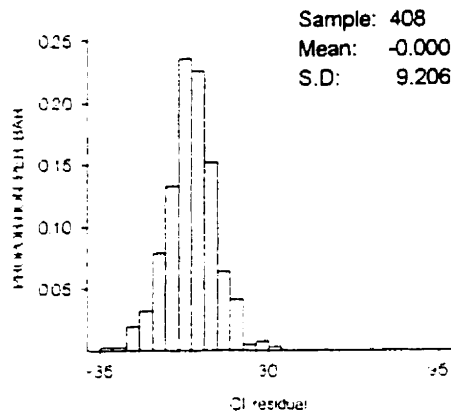


Figure 7.9 The histogram of Cl residuals.

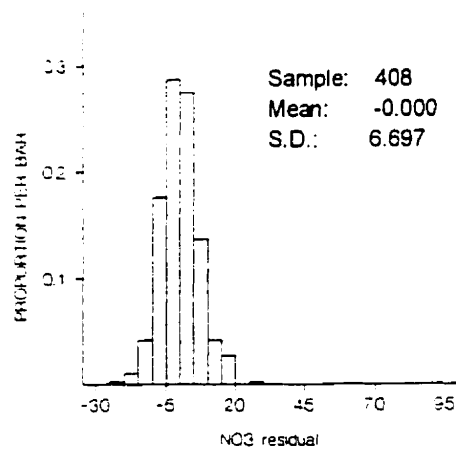
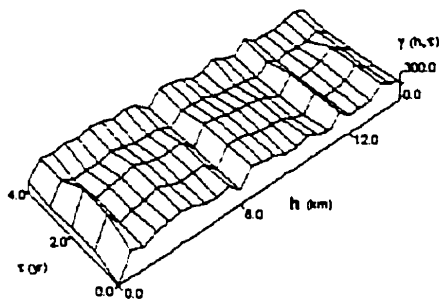


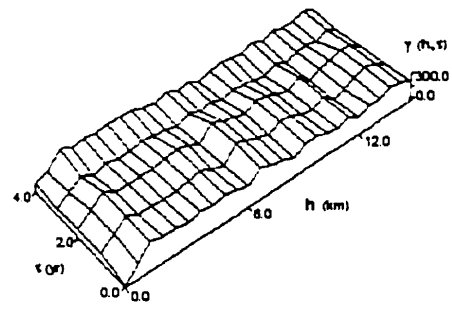
Figure 7.10 The histogram of NO<sub>3</sub> residuals.

Ca residual simivariograms in 0 degree



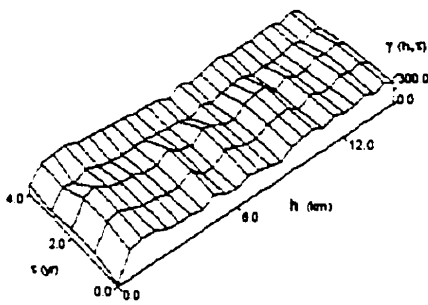
(a)

Ca residual simivariograms in 45 degree



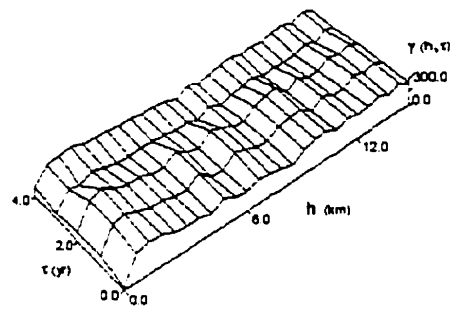
(b)

Ca residual simivariograms in 90 degree



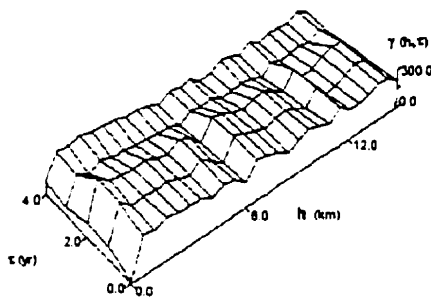
(c)

Ca residual simivariograms in 135 degree



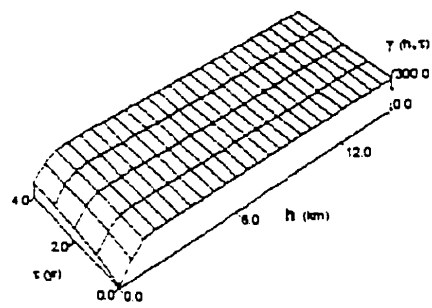
(d)

Ca residual overall simivariograms



(e)

Ca simivariogram model



(f)

Figure 7.11 Experimental variograms of Ca residuals. (a) variograms in the E-W direction, (b) variograms in the NE 45 direction, (c) variograms in the N-S direction, (d) variograms in the NW 45 direction, (e) omnidirectional variograms, and (f) the fitted variogram model.

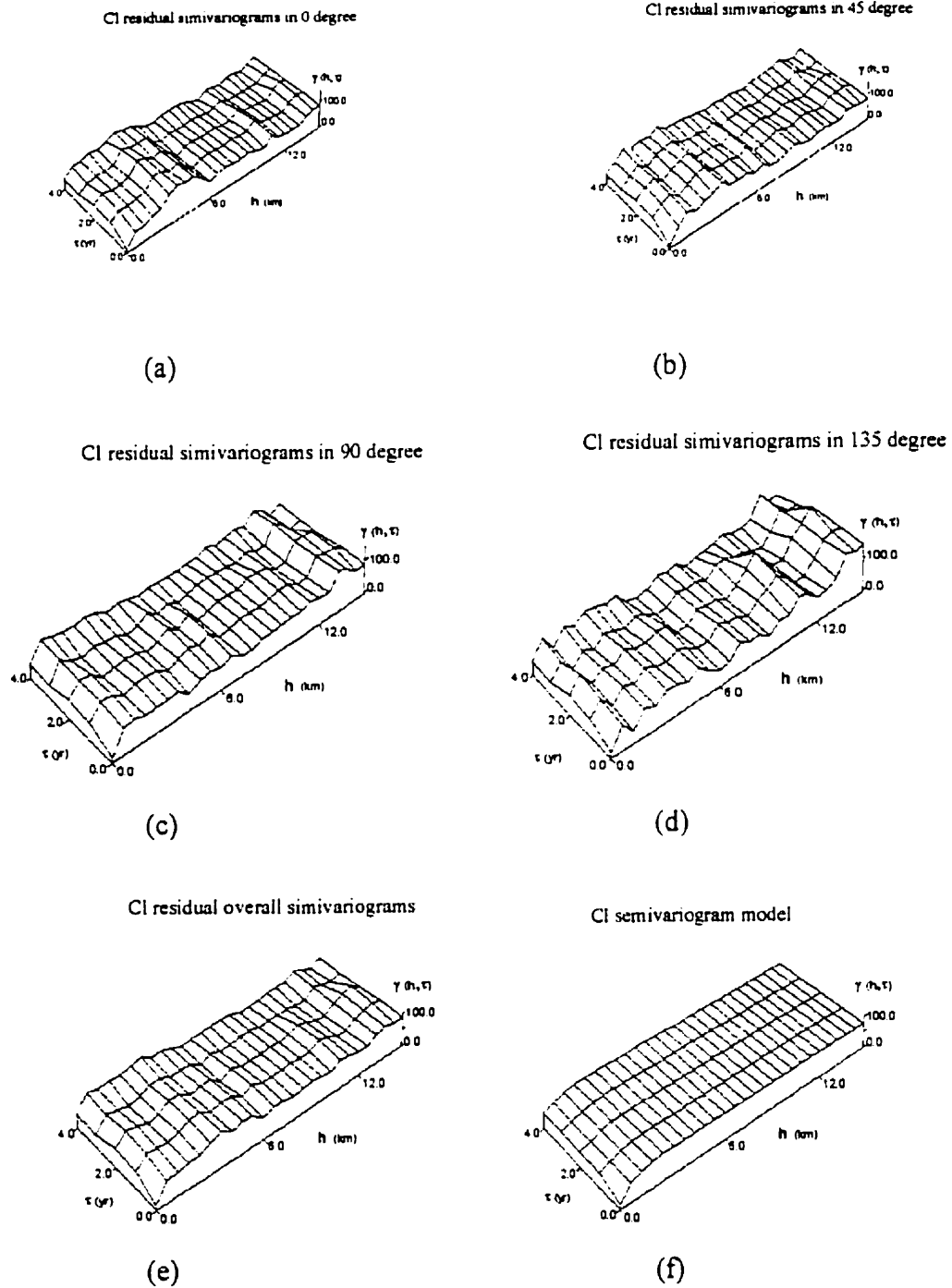
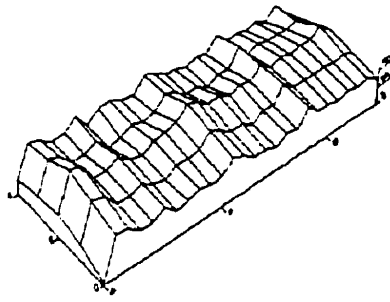


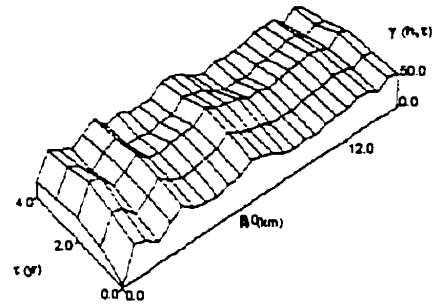
Figure 7.12 Experimental variograms of CI residuals. (a) variograms in the E-W direction, (b) variograms in the NE 45 direction, (c) variograms in the N-S direction, (d) variograms in the NW 45 direction, (e) omnidirectional variograms, and (f) the fitted variogram model.

no3 residual simivariograms in 0 degree



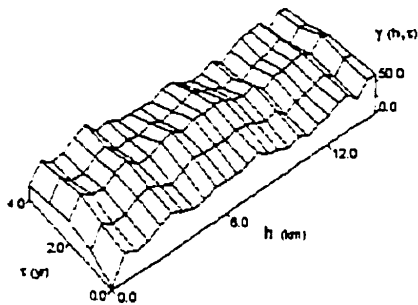
(a)

no3 residual simivariograms in 45 degree



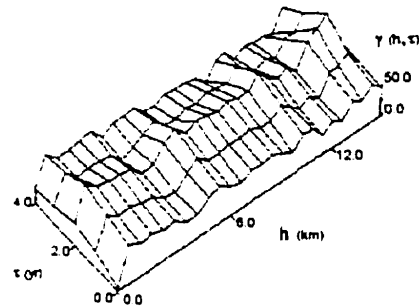
(b)

no3 residual simivariograms in 90 degree



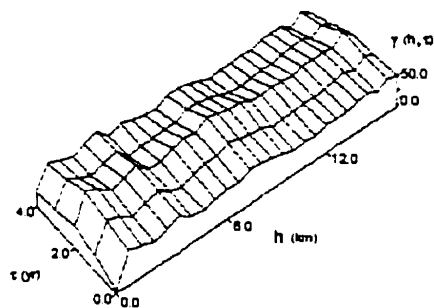
(c)

no3 residual simivariograms in 135 degree



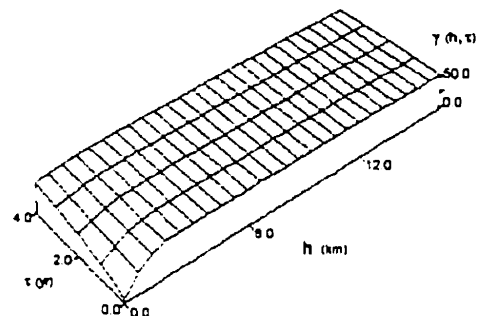
(d)

no3 overall residual simivariograms



(e)

no3 simivariogram model



(f)

Figure 7.13 Experimental variograms of  $\text{NO}_3$  residuals. (a) variograms in the E-W direction, (b) variograms in the NE 45 direction, (c) variograms in the N-S direction, (d) variograms in the NW 45 direction, (e) omnidirectional variograms, and (f) the fitted variogram model.

## 7.5 Space-Time Mapping of Springwater Contents

### 7.5.1 Different Trend Models in Subareas

A question may arise for UK system when different trend models are specified in subareas. Figure 7.14 shows that the location to be estimated has a neighborhood including data points from other subareas. Assume that the trend is represented by different coefficients in subareas,

$$m(s, t) = \sum_{j=1}^L \alpha_j f_j(s, t), (s, t) \in \text{Subarea}_i$$

as a result, the unbiased condition of the UK system is changed into the following,

$$\sum_{i=1}^L [\alpha_{l_0} f_l(s_0, t_0) - \sum_{i=1}^N \lambda_i \alpha_{li} f_l(s_i, t_i)] = 0$$

or

$$\sum_{i=1}^N \lambda_i \frac{\alpha_{li}}{\alpha_{l_0}} f_l(s_i, t_i) = f_l(s_0, t_0), l = 1 \text{ to } L.$$

Note that this condition becomes the common unbiased condition when  $\alpha_{li} = \alpha_{l_0}$ ,  $i = 1$  to  $N$ .

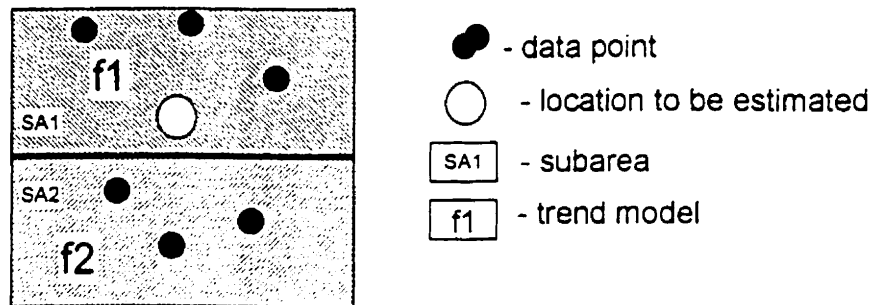


Figure 7.14 A neighborhood configuration. The data points in the neighborhood come from different subareas, and the trend function at the location to be estimated is different from that of some data points.

In practice, however, this problem can be solved simply by constraining neighborhood in the same subarea. More often, most boundaries used to split the area into subareas are man-made for convenience. It is reasonable to assume that in any small neighborhood the trend model is invariant, so that the common UK technique can be used without modifications. This assumption is applied in the following sections.

## 7.5.2 Mapping Results

The space-time mapping of Ca, Cl, and NO<sub>3</sub> concentrations was performed by S/T block UK technique developed in Section 4.4, using the following kriging plan.

- Block discretion = 4×4×3.
- Search radius = 5 km/year.
- Octant search (8 data per octant).
- Use of the trend form ( $\xi=1+i/\zeta=1$ ).
- Use of the variogram function defined by Equation 6.1.

Figure 7.15 shows the space-time mapping of Ca concentrations from 1980 to 1982. The north-south central area of low values corresponds to the valley of the Dyle River, the high values are mostly observed in the northeast part and the southwest corner of the maps.

Figure 7.16 shows the space-time mapping of Cl concentrations from 1980 to 1982. High values are mostly observed in the east-central part of the maps. With a close look at the south part of maps, the high-value band tends to expand with passing time.

Figure 7.17 demonstrates the space-time mapping of NO<sub>3</sub> concentrations from 1980 to 1982. High values are mostly observed in the south of the maps. The high-value band in the central part tends to expand with passing time.

The result of Ca mapping is compatible with the cokriging result of the first group from Goovaerts' work, while the Cl mapping and NO<sub>3</sub> mapping are fairly consistent with that of the second and third group, respectively. This is reasonable since the first group contains Ca, the second group contains Cl, and the third group contains NO<sub>3</sub>.

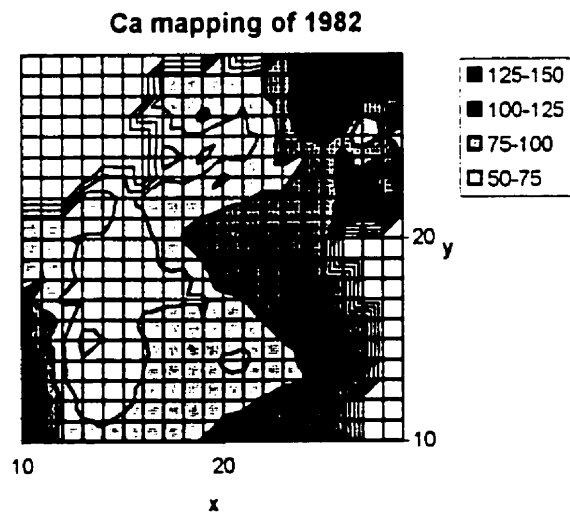
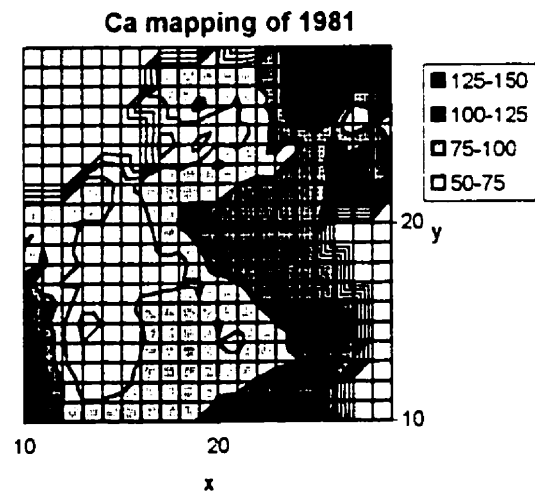
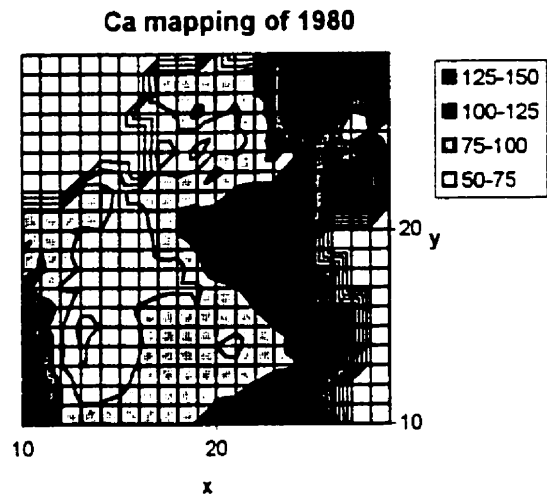


Figure 7.15 Space-Time mapping of Ca concentrations from 1980 to 1982.

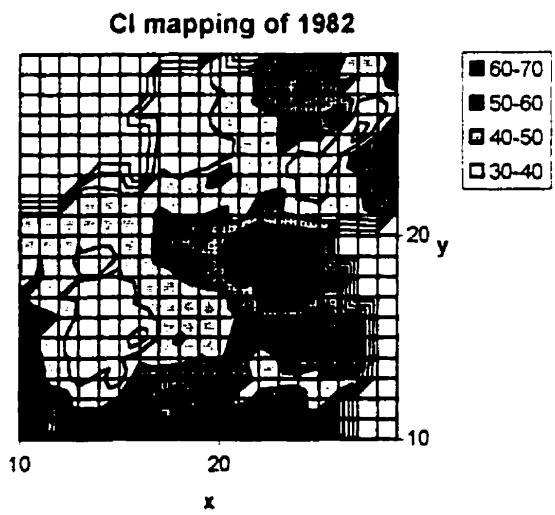
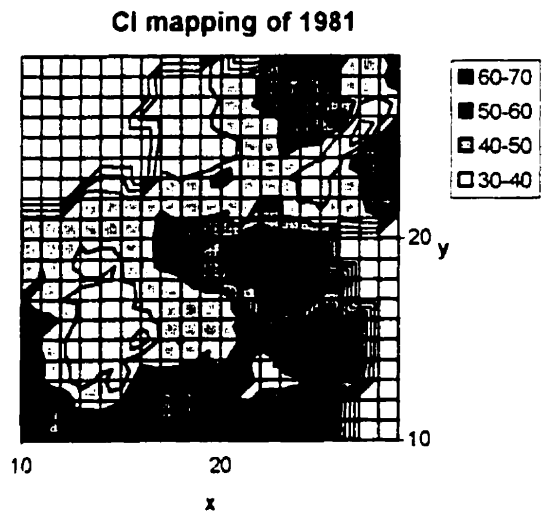
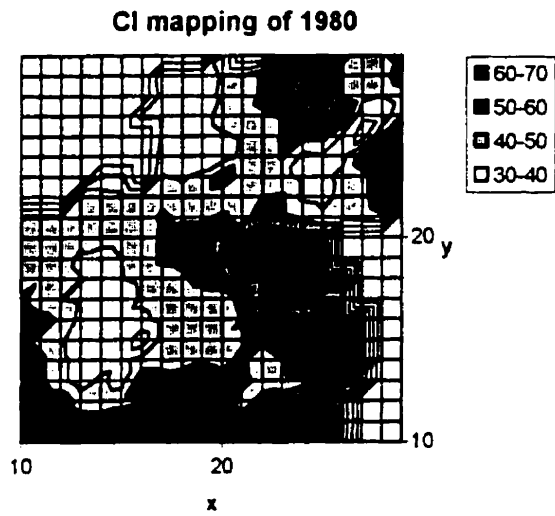


Figure 7.16 Space-Time mapping of CI concentrations from 1980 to 1982.

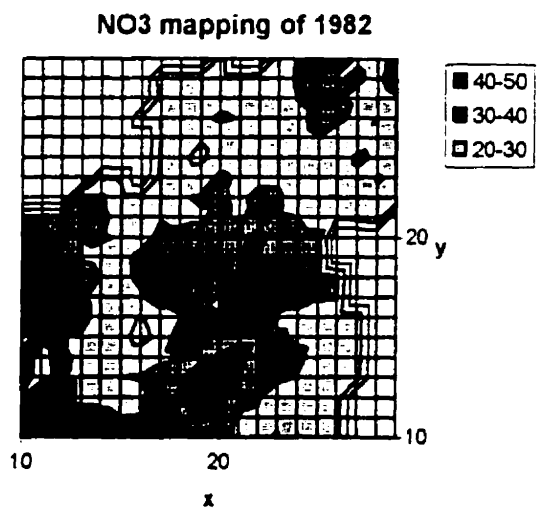
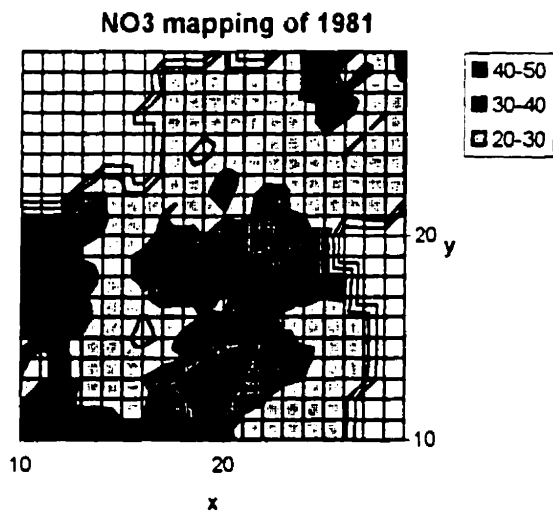
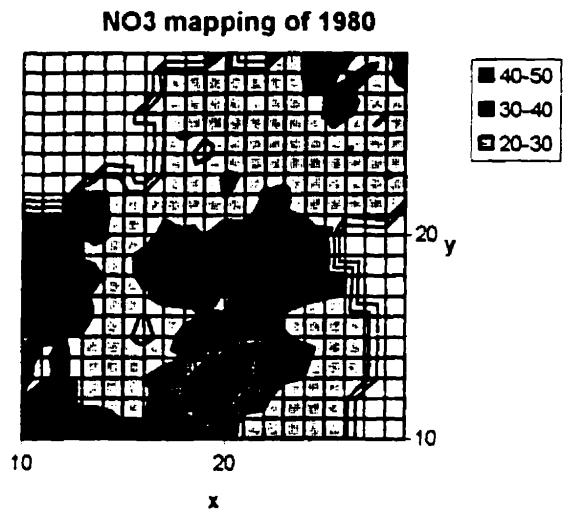


Figure 7.17 Space-Time mapping of NO<sub>3</sub> concentrations from 1980 to 1982.

## 7.6 Conditional Simulations of Ca Residuals

Conditional simulations of Ca residuals were generated by using both SGGS and the simulated annealing technique honoring experimental variograms. The simulation grid was designed to have  $100 \times 100 \times 5 = 50000$  nodes, with a spacing of  $0.2(\text{km}) \times 0.2(\text{km}) \times 1(\text{year})$ . A total of 408 conditioning data were used for the conditional simulation of Ca residuals.

### 7.6.1 Conditional Simulations of Ca Residuals Using SGGS

Conditional simulations of Ca residuals were first generated by using SGGS. The quadrant search was applied for the neighborhood determination, each quadrant having 8 data, which gives a neighborhood size of  $v = 4 \times 8 = 32$  data. The group size of SGGS was designed to be  $4 \times 4 = 16$ , therefore the  $0.5v$ -SGGS was adopted.

Figure 7.18 shows histograms of two conditional simulations of Ca residuals. The corresponding variograms are shown in Figure 7.19. The sample variograms of two conditional simulations are fairly smooth since hundreds of thousands of pairs were involved in each variogram calculation and that resulted in smooth effect. As a result, the difference between the variograms of these simulations is indistinct. In comparison with the histogram and variogram model of Ca residuals shown in Figure 7.8 and 7.11, these conditional simulations reproduced the first and second-order moments of Ca residuals.

Figure 7.20 and 7.21 show the two simulations of Ca residuals using SGGS. Each simulation has three time slices (1980, 1981, 1982). Note that a sequential external path along the E-W direction with an inverse-direction internal path was adopted in the implementation, and the results show that there are no distinct artifacts in the E-W direction (x axis).

Figure 7.22 and 7.23 show the two simulations of Ca concentrations corresponding to residuals shown in Figure 7.20 and 7.21. Each simulation has three time slices (1980, 1981, 1982). Though there are some local changes between these two simulations, the regional bands of high and low values honor the same structure of Ca mapping shown in Figure 7.15 because of the trend.

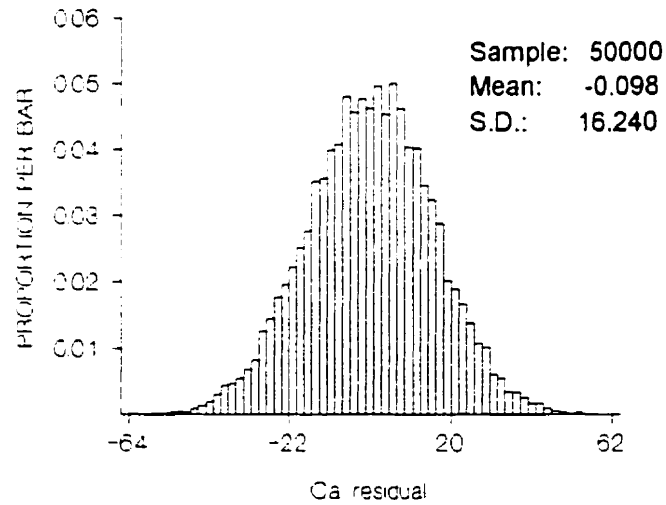
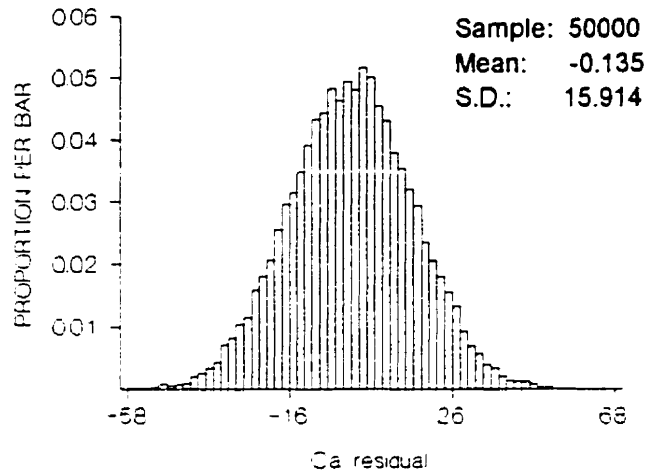


Figure 7.18 Histograms of two conditional simulations of Ca residuals generated by SGGS.

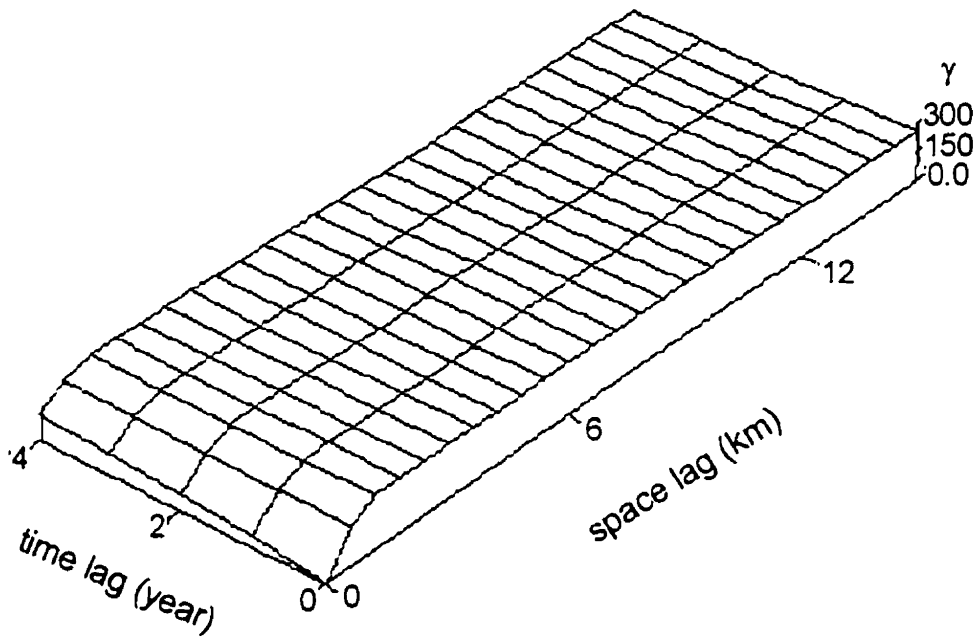
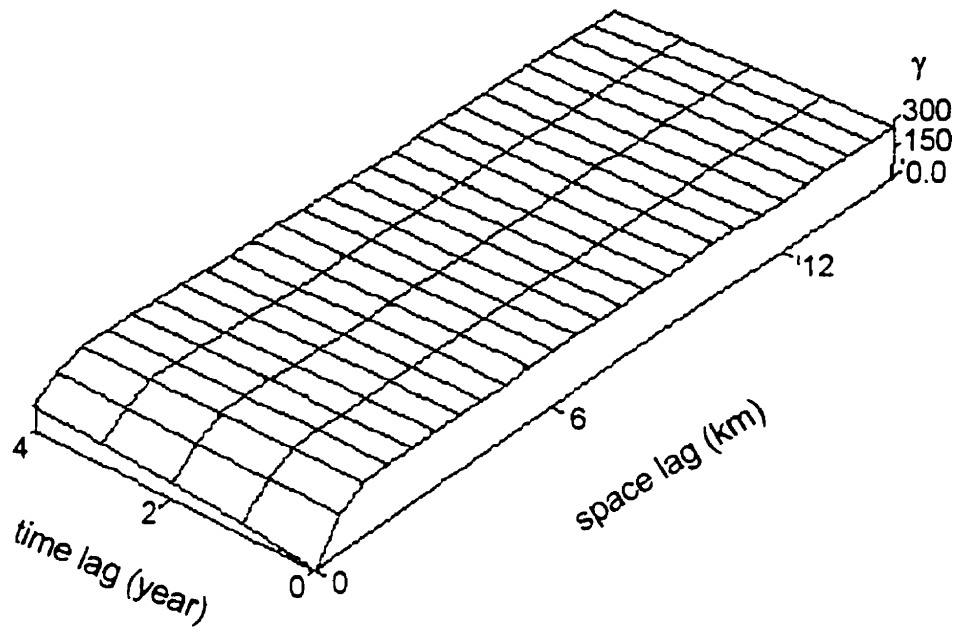
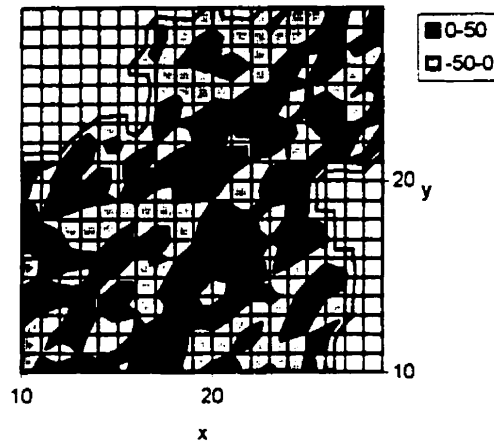
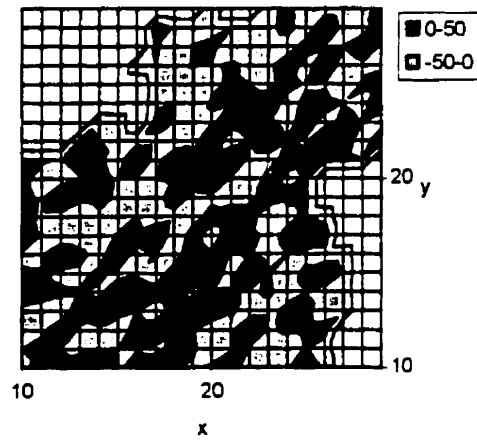


Figure 7.19 Omnidirectional variograms of two conditional simulations of Ca residuals generated by SGGs.

Simulation of Ca residual at 1980



Simulation of Ca residual at 1981



Simulation of Ca residual at 1982

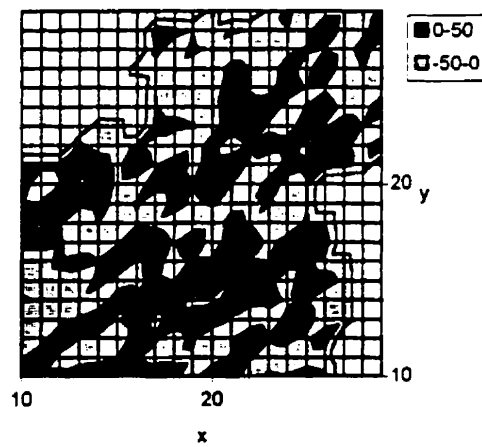
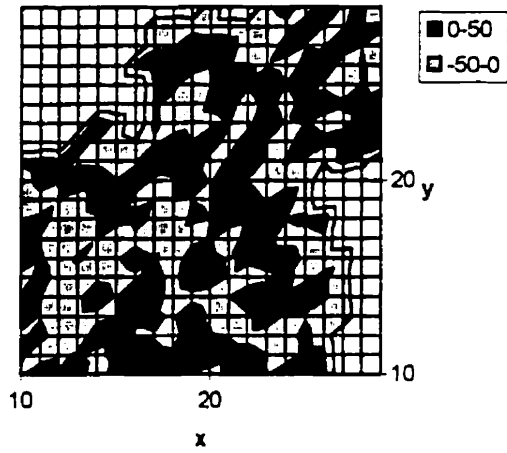
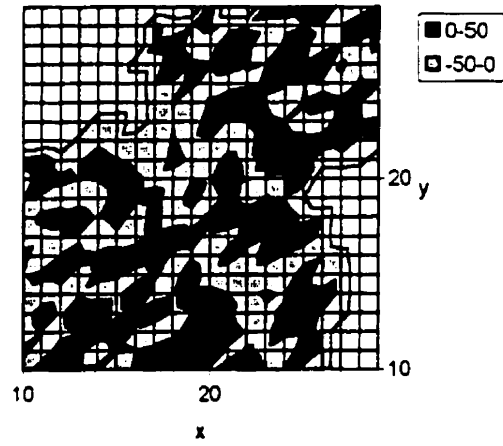


Figure 7.20 A conditional simulation of Ca residuals at three time slices (1980, 1981, 1982) generated by using SGGs.

Simulation of Ca residual at 1980



Simulation of Ca residual at 1981



Simulation of Ca residual at 1982

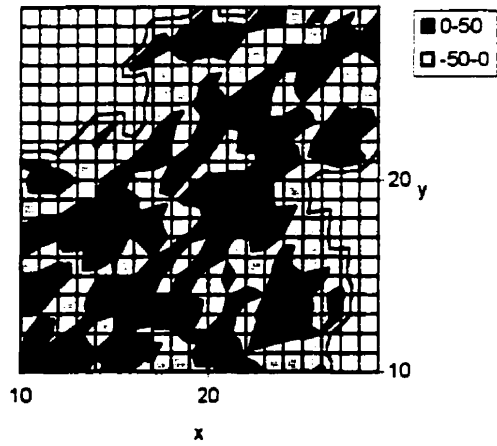


Figure 7.21 A conditional simulation of Ca residuals at three time slices (1980, 1981, 1982) generated by using SGGs.

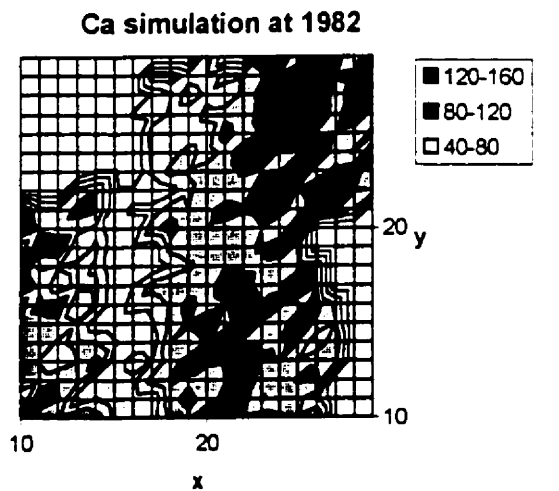
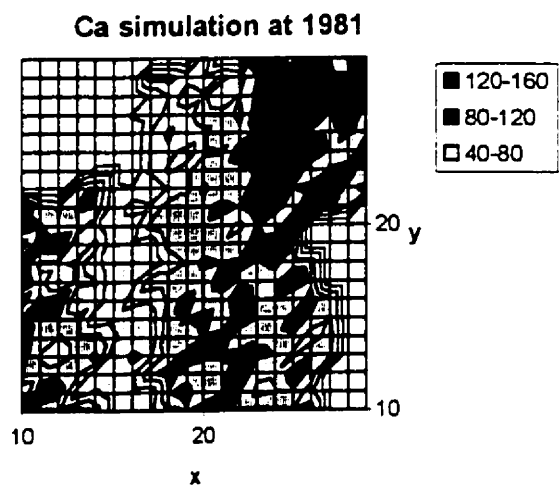
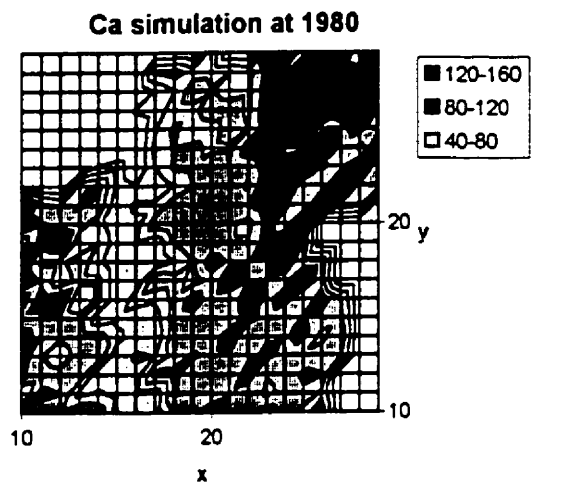


Figure 7.22 A conditional simulation of Ca concentrations at three time slices (1980, 1981, 1982).

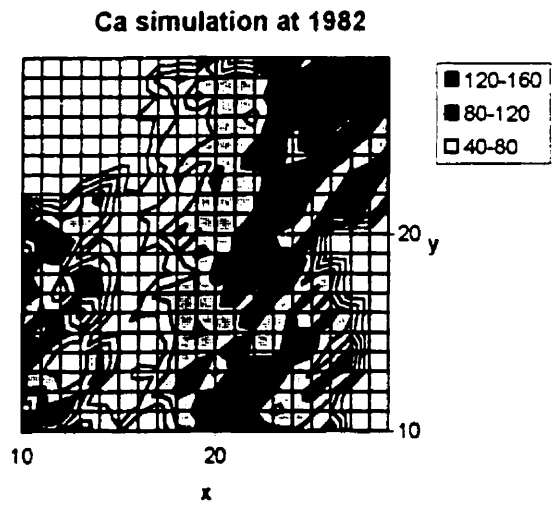
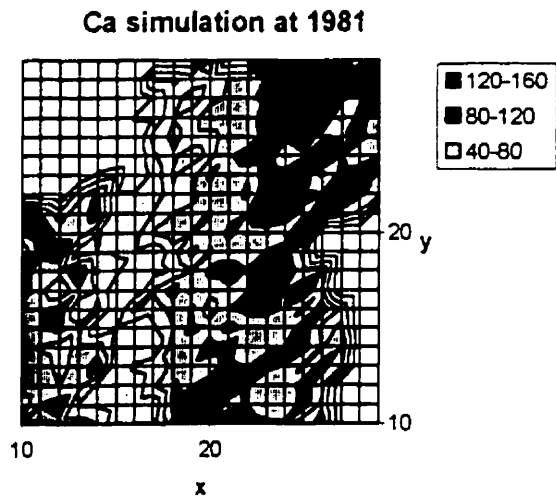
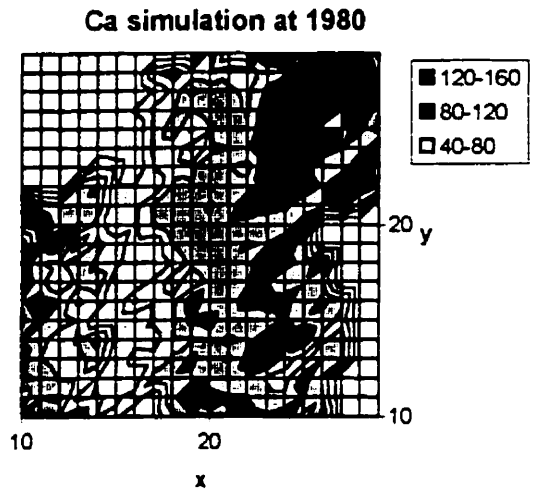


Figure 7.23 A conditional simulation of Ca concentrations at three time slices (1980, 1981, 1982).

## 7.6.2 Conditional Simulations of Ca Residuals Using Simulated Annealing

The conditional simulations were also generated using simulated annealing to examine the impact of experimental variogram reproduction of Ca residuals. The space-omnidirectional experimental variograms were used to construct the objective function.

The implementation parameters of the simulated annealing algorithm were set as follows:

- $\rho_0$ : the initial 'temperature' was set to 1.0.
- $\lambda$ : the reduction factor was set to 0.1.
- $K_{\max}$ : the maximum number of attempted perturbations was set to 600,000.
- $K_{\text{accept}}$ : the acceptance target was set to 60,000.
- S: the stop number was set to 3.
- $\Delta O$ : the low objective function indicating convergence was set to 0.02.
- $N_{\text{cov}}$ : the number of nodes in neighborhood, to be taken into account in the objective function updating of each swap, was set to 600.

The parameter  $N_{\text{cov}}$  determines the number of experimental variograms to be reproduced through implementation. Since the simulation lag is usually smaller than that involved in experimental variogram calculation (in the case study the simulation lag is 0.2 km while the space lag involved in experimental variogram calculation is 0.6 km), a large  $N_{\text{cov}}$  is needed for the reproduction of whole experimental variograms. For instance, to reproduce a total of 130 experimental variogram values of Ca residuals,  $N_{\text{cov}}$  has to be set to at least  $(0.6 \times 25 / 0.2)^2 \times 5 = 28125$ , which will claim colossal amount of computing time. Consequently, a  $N_{\text{cov}}$  of 600 implies that only a small portion of experimental variograms of Ca residuals can be reproduced. Fortunately, this portion includes the experimental variograms associated with nearest nodes which are most significant in experimental variogram reproduction.

Figure 7.24 shows the histograms of two conditional simulations of Ca residuals. They are quite close to the histogram of Ca residuals shown in Figure 7.8. Figure 7.25(a) shows the portion of experimental variograms of Ca residuals required to be reproduced in the simulations ( $\gamma^*(h, \tau)$  with  $h \leq 2(\text{km})$  and  $\tau \leq 2(\text{year})$ ), (b) and (c) show the portions of the

corresponding experimental variograms of the two conditional simulations. The similarity of these pictures indicates that these conditional simulations reproduced adequately the structure of experimental variograms.

Figure 7.26 and 7.27 show the two conditional simulations of Ca residuals by using the simulated annealing, and the corresponding simulations of Ca concentrations are shown in Figure 7.28 and 7.29. Similarly to the results by using the SGGS shown in Figure 7.22 and 7.23, the regional distribution of high/low value bands remains unchanged due to the impact of the trend.

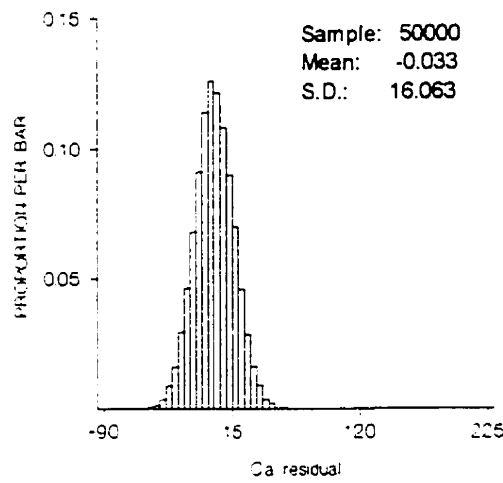
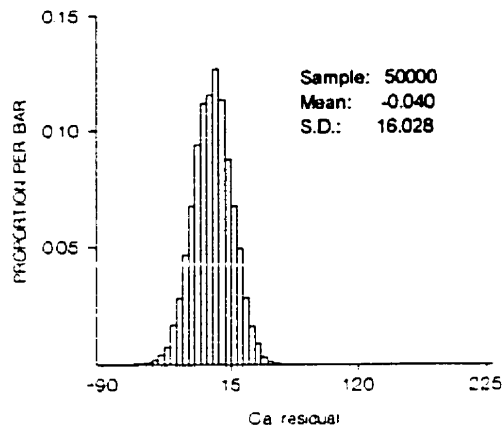
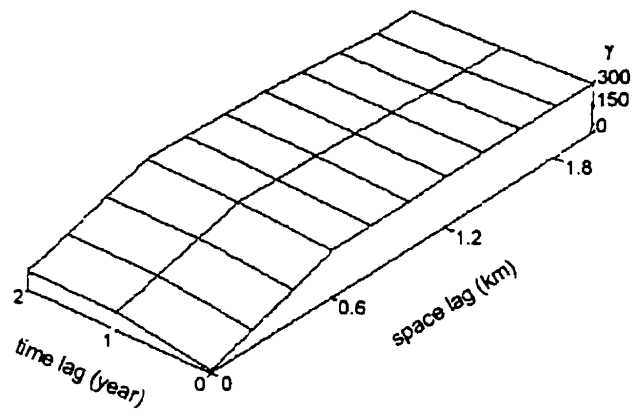
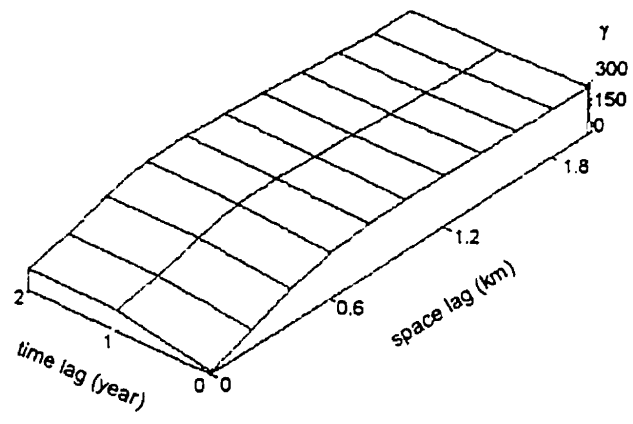


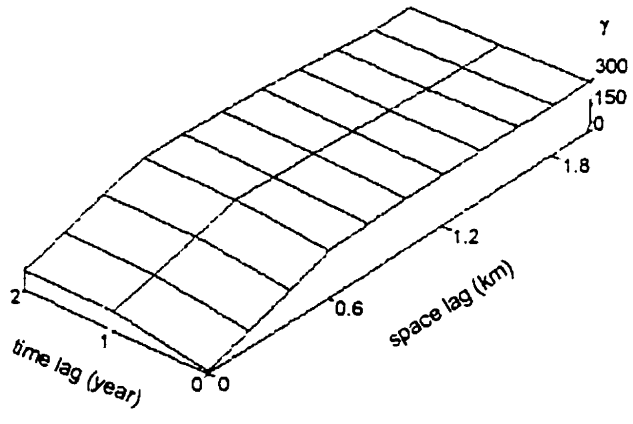
Figure 7.24 Histograms of two conditional simulations of Ca residuals generated by the simulated annealing.



(a)



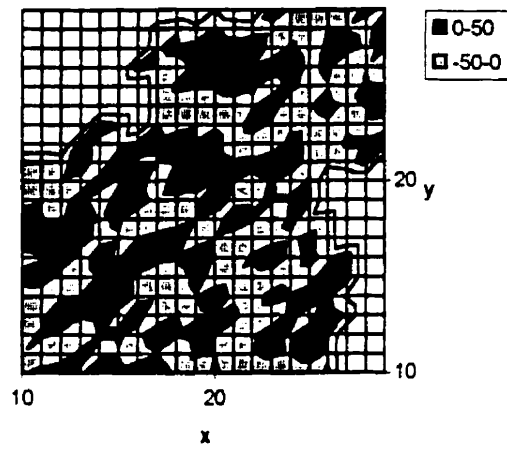
(b)



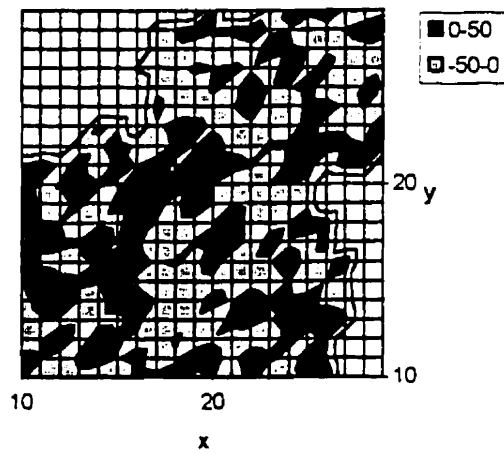
(c)

Figure 7.25 Space-Omnidirectional variograms of Ca residuals are shown in (a), and space-omnidirectional variograms of two conditional simulations of Ca residuals are shown in (b) and (c).

**Simulation of Ca residual at 1980**



**Simulation of Ca residual at 1981**



**Simulation of Ca residual at 1982**

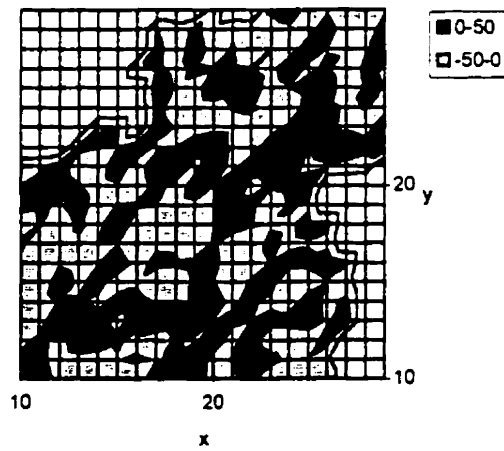
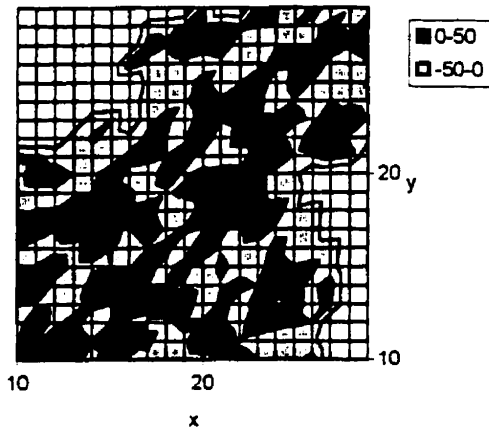
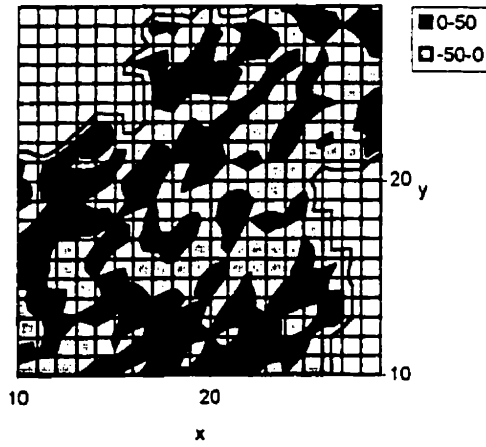


Figure 7.26 A conditional simulation of Ca residuals at three time slices (1980, 1981, 1982) generated by using the simulated annealing.

**Simulation of Ca residual at 1980**



**Simulation of Ca residual at 1981**



**Simulation of Ca residual at 1982**

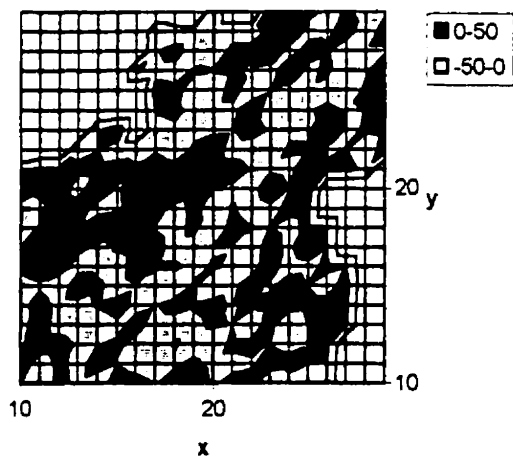


Figure 7.27 A conditional simulation of Ca residuals at three time slices (1980, 1981, 1982) generated by using the simulated annealing.

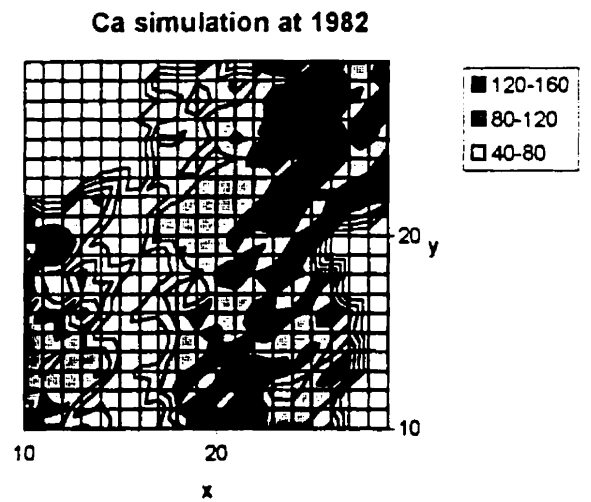
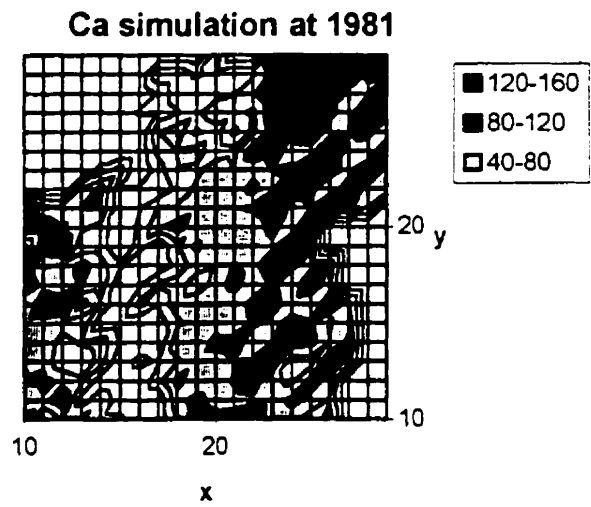
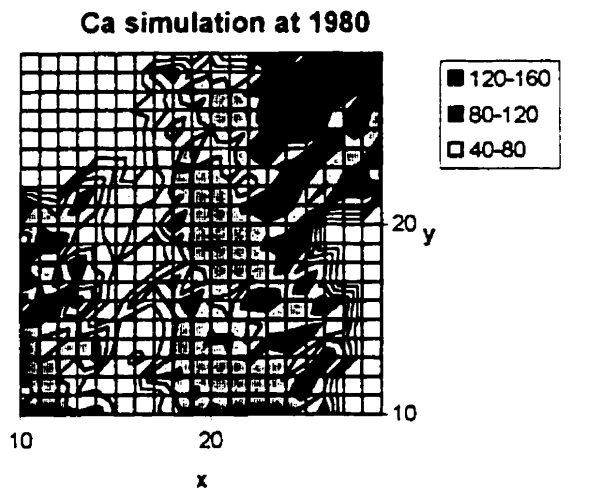


Figure 7.28 A conditional simulation of Ca concentrations at three time slices (1980, 1981, 1982).

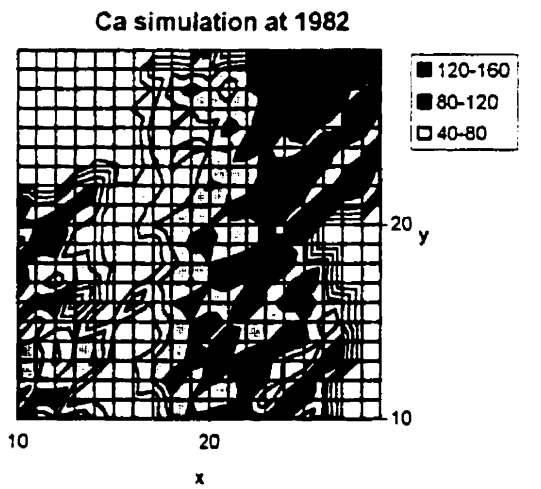
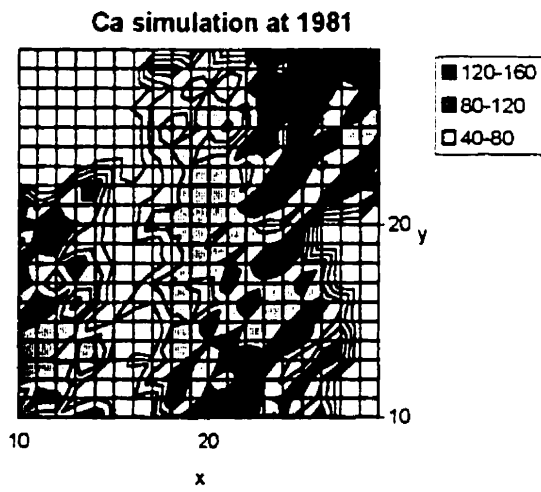
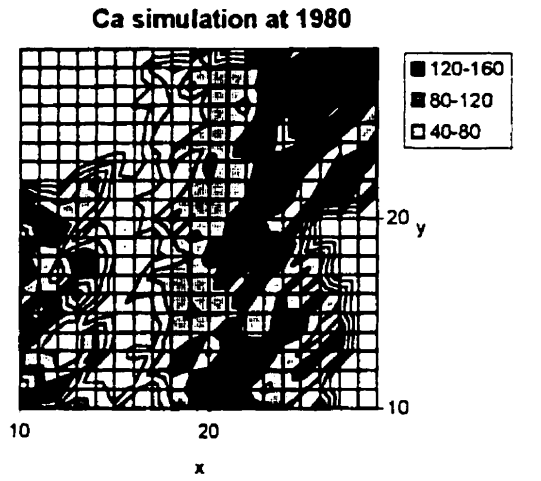


Figure 7.29 A conditional simulation of Ca concentrations at three time slices (1980, 1981, 1982).

## 7.7 Monitoring Scheme of Ca Concentrations

This section will concentrate on the groundwater monitoring scheme with reference to Ca concentrations, in order to show the impact of the sampling grid on average local estimation errors and associated uncertainties. The sampling criterion and control parameters are mentioned in Section 6.5.1, and the implementation procedure is similar to that discussed in Section 6.5.2. Since Ca concentrations are considered to be nonstationary, and are assumed to have the space-time trends given in Tables 7.4, their conditional simulations are generated by combining the space-time trend with realizations of residuals. The conditional simulations of Ca residuals were generated first by using the SGGS, and then by using the simulated annealing algorithm honoring experimental variograms. The size of the space-time gridblock to be estimated is chosen to be  $1.0(\text{km}) \times 1.0(\text{km}) \times 1(\text{year})$ . The selection of gridblock size is based on the average spacing of springwater data as well as the correlation structure of Ca concentrations. Consequently a total of  $20 \times 20 \times 5 = 2000$  gridblocks were estimated.

The sampling grid was initially set with a spacing of  $0.6(\text{km}) \times 0.6(\text{km}) \times 1(\text{year})$ , then the spacing was expanded to  $0.8(\text{km}) \times 0.8(\text{km}) \times 1(\text{year})$ ,  $1(\text{km}) \times 1(\text{km}) \times 1(\text{year})$ , and so on. By continuing this process of expanding the spatial spacing ultimately to 3.0 km, a variation curve of average local estimation error vs. spatial spacing was obtained. This procedure was repeated 40 times, in order to demonstrate the uncertainty associated with average local estimation errors.

### 7.7.1 Sampling Results

Based on the simulations of Ca concentrations using the SGGS, the variation of average local estimation error was calculated, which is shown in Figure 7.30. The average local estimation error is flat when the spatial spacing is from 0.6 km to 1.0 km, and then it increases quickly when the spacing is from 1.0 km to 1.4 km. The estimation error keeps flat again when the spacing is from 1.4 km to 2.6 km, finally it increases quickly after 2.6 km.

The sampling investigation was also performed with the simulations using the simulated annealing, and the average local estimation error vs. spatial spacing is shown in Figure 7.31. In comparison with Figure 7.30, they are highly similar to each other. These results suggest that the optimal spatial spacing is approximately 1.0 km. Note that the average

estimation error is fairly high (20%-50%) compared with the result shown in Figure 6.28 (<20%), this is true because Ca concentrations are treated to be nonstationary while the reservoir pressure is treated to be stationary. In general the local estimation error of a nonstationary process is larger than that of a stationary process.

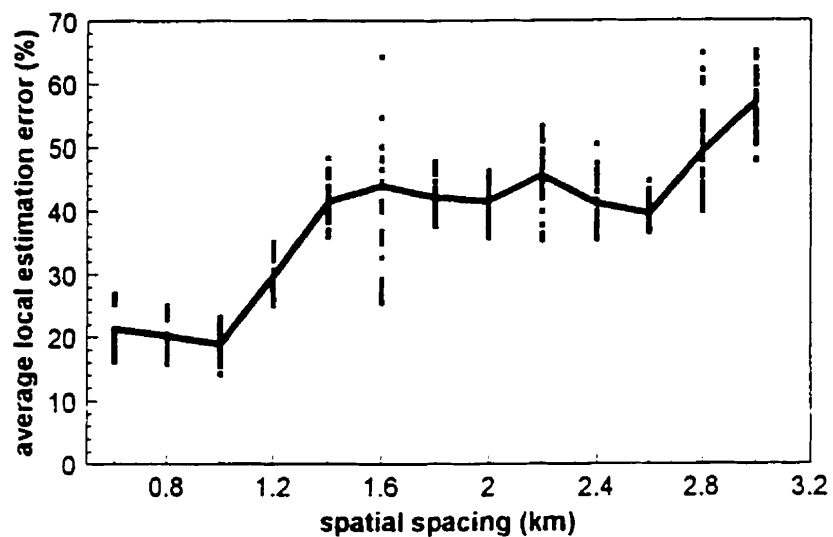


Figure 7.30 Average local estimation error vs. spatial spacing. The thick line indicates the means. The conditional simulations of Ca residuals were generated by the SGGS.

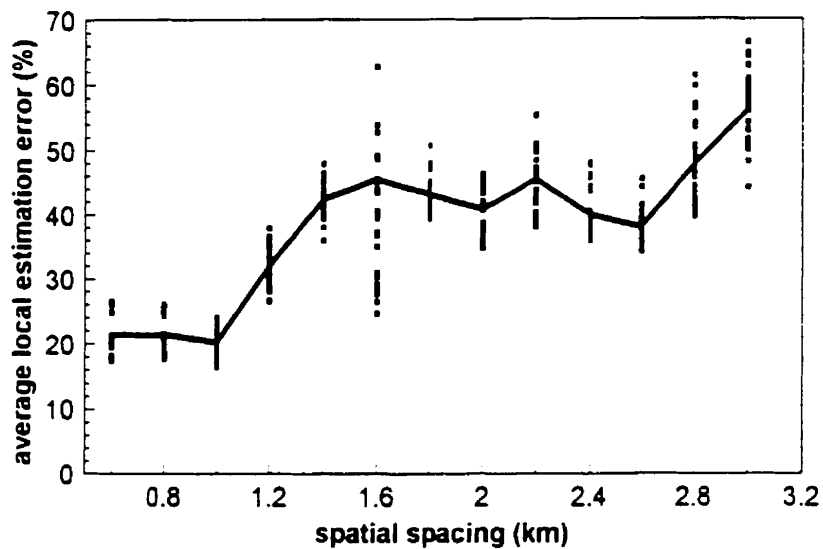


Figure 7.31 Average local estimation errors vs. spatial spacing. The conditional simulations of Ca residuals were generated by the simulated annealing.

## 7.8 Summary

In the present study, the space-time modelling of springwater contents was performed using the data from a study of spring water in the Dyle watershed. Under the framework of S/TRF modelling, space-time continuity characterizations, space-time estimations, space-time conditional simulations, and space-time monitoring scheme of springwater contents were accomplished. Due to the nonstationary properties of spring contaminants, the proposed methodology is a decomposition-combination process: first, decompose spring contaminants into trend components and residual components by trend-surface analysis; then, study residual components with space-time continuity characterization tools to obtain space-time variogram models and required conditional simulations of residuals; finally, use trend models and variogram models to estimate variations of springwater contents, and combine trend components with residual simulations to construct simulations of springwater contents for sampling investigation.

The space-time trend of springwater contents was recognized by using trend-surface analysis, leading to residuals with isotropic structures of space-time continuity. The space-time mapping of springwater contents was performed by using S/T block UK, and the results were compatible with previous work in this area.

The conditional simulation of Ca concentrations were generated by combining the trend with the simulation of Ca residuals. Because of the presence of a trend, the randomness of simulations of Ca concentrations is greatly lowered compared with that of Ca residuals, which can be seen in Figure 7.22 and 7.23, or in Figure 7.28 and 7.29. The main property of simulations of Ca concentrations is the combination of the randomness owned in simulations of Ca residuals and the determination owned in the trend. The monitoring scheme was investigated using conditional simulations of Ca concentrations, and the result suggests that the optimal spatial spacing is approximately one kilometer.

The simulated annealing algorithm honoring experimental variograms provides a means to generate conditional simulations that incorporate the natural properties of spatiotemporal processes. Furthermore, it suggests the possibility that the continuity characterization step may no longer be prerequisite for conditional simulations. However, the case study shows that the long running time of the implementation process greatly

constrains its capacity for large-scale spatiotemporal simulations. For example, if one wants to obtain a denser simulation, which shortens the simulation spacing from 0.2 km to 0.1 km in the case study, then the maximum number of attempted perturbations and the acceptance target have to increase four times, and the number of experimental variograms involved in each objective function updating also has to increase four times to ensure the reproduction of the same required variograms. This implies that the running time will increase by 16 times. Therefore, future research associated with this algorithm should focus on the reduction of running time, in order to make it applicable for large-scale spatiotemporal simulations.

## Chapter 8

### Conclusions and Recommendations

This chapter summarizes the project results and outlines how the initial objectives have been reached. Recommendations for further work are finally highlighted.

#### 8.1 Conclusions

According to the specific objectives addressed in Chapter 1, the systematic analysis of spatiotemporal processes was studied with regard to three aspects: the space-time continuity characterization, the space-time estimation, and the space-time simulation. For the space-time characterization, spatiotemporal experimental variograms were displayed with recognition of different space and time measures to show the nature of space-time continuity of spatiotemporal processes. Features of the space-time continuity were summarized in terms of both traditional hypotheses such as homogeneity, anisotropy, and regularity, and special hypotheses for space-time continuity such as separability. The permissibility criteria of space-time covariance models were proposed and two popular types of covariance models were discussed: separable models and joint-distance models. A general form of spatiotemporal covariance functions was also addressed.

The estimation of spatiotemporal processes was developed in terms of space-time kriging techniques. The singularity analysis of simple/ordinary space-time kriging techniques was carried out showing that any strictly positive definite covariance model ensures a unique solution to simple/ordinary space-time kriging systems. The criteria of strictly positive definite functions were consequently proposed. The singularity analysis of universal space-time kriging techniques was emphasized in the form of space-time trends and data configuration. Finally, the tensorial invariance of universal spatiotemporal kriging systems was investigated in terms of the space-time trend.

The conditional simulation techniques of spatiotemporal processes were developed in terms of SGGS and the simulated annealing honoring experimental variograms. The SGGS is actually a series of sequential simulation algorithms associated with different group sizes, including SGS and LUD. The optimal algorithm is the  $0.5v$ -SGGS whose group size is around half of the neighborhood size  $v$ , and its running time is practically 2-7 times faster than the current SGS depending on the neighborhood size. The simulation

error caused by ignoring farther information during the SGGs process was characterized by the SEA loss and investigated with popular covariance models using different simulation grids. The optimal neighborhood sizes with acceptable SEA loss were provided. The simulated annealing algorithm with experimental variogram reproduction was proposed, with an emphasis on the interpolation of experimental variograms and the improvement of the implementation process as well. This provides a way of generating realizations of spatiotemporal processes without covariance/variogram model fitting, which is prerequisite for other simulation algorithms.

The techniques of S/TRF modelling were used first for modelling the pressure system in a carbonate reservoir. The quantification of continuity patterns in terms of spatiotemporal variograms was used to subsequently estimate and conditionally simulate the reservoir pressure. Finally, groundwater monitoring in terms of spatiotemporal processes was investigated using springwater data in the Dyle watershed. The space-time trends of three contaminants were recognized through trend-surface analysis. The estimation of spring contaminants was performed using the space-time block UK. The sampling grid of groundwater monitoring was investigated in terms of Ca concentrations. The results of these case studies as well as the theory suggest that the techniques of S/TRF modelling are realistic and feasible.

## 8.2 Recommendations

The following issues remain open to further research and enhancement:

1. Space-Time covariance/variogram models are crucial for S/TRF modelling. Further research could be directed to investigate various types of permissible space-time covariance models in addition to joint-distance models and separable models.
2. Spatiotemporal estimation techniques are extensively used in geoscience applications. It would be interesting to consider the development of other estimation techniques such as spatiotemporal indicator kriging and IRF-k methods. As for spatiotemporal IRF-k, the permissible models would be deliberately investigated.
3. The SGGs greatly improves Gaussian simulations in terms of running time. The strategy of the SGGs could also apply to multivariate Gaussian simulations without

huge modifications. The SEA loss of multivariate simulations could be discussed in a similar manner.

4. The simulated annealing technique with experimental variogram reproduction has the great benefit of generating simulations with more natural properties of space-time continuity. However, its computing time greatly constrains its capacity for large-scale spatiotemporal conditional simulations. The further research should focus on the improvement of implementation in terms of running time.
5. Sampling investigation of spring contaminants focused on the evaluation of average local estimation error and associated uncertainty using different sampling grids. The economic impact on sampling investigation was not taken into account due to the lack of information. In environmental engineering, it is more interesting to estimate optimal sampling with regard to sampling and remediation costs. Further research could construct economic objective functions and evaluate their uncertainties as a function of different sampling grids.

## BIBLIOGRAPHY

- Agnew, J., 1978, *Linear Algebra with Applications*. Brooke/cole Co., Monterey, California.
- Agterberg, F.P., 1974, *Geomathematics*. Elsevier Scientific Publishing Company. Amsterdam.
- Alabert, F., 1987, *The practice of fast conditional simulations through the LU decomposition of the covariance*. *Mathematical Geology*, 19(5), p. 369-386.
- Aziz, K., 1979, *Petroleum Reservoir Simulation*. Applied Science Publishers LTD, London.
- Berg, C., et al., 1984, *Theory of Positive Definite and Related Functions*. Springer-Verlog, New York.
- Berger, J.O., 1985, *Statistical Decision Theory and Bayesian Analysis*. Springer-Verlag Inc., New York.
- Berkowitz, B., et al., 1992, *A spatial, time-dependent approach to estimation of hydrologic data*. *J. Hydrology*, 135, p. 133-142.
- Bilonick, R.A., 1983, *Risk-qualified maps of hydrogen ion concentration for the New York state area for 1966-1978*. *Atmospheric Environment*, 17 (12), p. 2513-2524.
- Bilonick, R.A., 1985, *The space-time distribution of sulfate deposition in the northeastern U. S.* *Atmospheric Environment*, 19(11), p. 1829-1845.
- Bilonick, R.A., 1987, *Monthly hydrogen ion deposition maps for the northeastern U. S. from July 1982 to September 1984*. Consolidation Coal Co., Pittsburgh.
- Bochner, S., 1959, *Lectures on Fourier Integrals*. Princeton University Press, Princeton.
- Bras, R. L., Rodriguez-Iturbe, I., 1976, *Rainfall generation: a nonstationary time-varying multidimensional model*. *Water Resources Research*, 12(3), p. 450-456.
- Bras, R. L., and Rodriguez-Iturbe, I., 1985, *Random Functions and Hydrology*. Addison Wesley, Reading, Massachusetts.
- Buxton, B. E. and Pate, A. D., 1994, *Joint temporal-spatial modelling of concentrations of hazardous pollutants in urban air*. In R. Dimitrakopoulos, editor, *Geostatistics for the Next Century*, Kluwer Academic Publishers, Dordrecht. p. 75-87.

- Christakos, G., 1984, *On the problem of permissible covariance and variogram models*. Water Resources Research, 20(2), p. 251-265.
- Christakos, G., 1992, *Random Field Models in Earth Sciences*. Academic Press, New York.
- Cormen, T.H., Leiserson, C.E., and Rivest, R.L., 1990, *Introduction to Algorithms*. The MIT Press. Cambridge.
- Dake, L. P., 1978, *Fundamentals of Reservoir Engineering*. Elsevier Scientific Publishing Company, Amsterdam.
- David, M., 1977, *Geostatistical ore Reserve Estimation*. Elsevier, Amsterdam.
- Davis, J. C., 1973, *Statistics and Data Analysis in Geology*, John Wiley & Sons Inc., New York.
- Davis, M. W., 1987a, *Production of conditional simulations via the LU triangular decomposition of the covariance matrix*. Mathematical Geology, 21(2), p. 91-98.
- Davis, M. W., 1987b, *Generating large stochastic simulations-the matrix polynomial approximation method*, Mathematical Geology, 21(2), p. 99-107.
- Deutsch, C. V., and Journel, A.G., 1992, *Geostatistical Software Library and User's Guide*. Oxford University Press, New York.
- Deutsch, C. V., 1993, *Conditioning reservoir models to well test information*. In Soares A., editor, Geostatistics Troia '92, p. 505-518.
- Dietrich, C. R., 1993, *Computationally efficient generation of Gaussian conditional simulations over regular sample grids*. Mathematical Geology, 25(4), p. 439-452.
- Dietrich, C. R., and Newsam, G. N., 1995, *Efficient generation of conditional simulations by Chebyshev matrix polynomial approximations to the symmetric square root of the covariance matrix*. Mathematical-Geology. 27(2). p. 207-228.
- Dimitrakopoulos, R., 1989, *Conditional simulation of IRF-k in the petroleum industry and the expert system perspective*. PhD thesis, Ecole Polytechnique, Montreal, QC.
- Dimitrakopoulos, R., 1990, *Conditional simulation of intrinsic random function of order k*. Mathematical Geology, 22(3), p. 361-380.
- Dimitrakopoulos, R. and Luo, X., 1994, *Spatiotemporal modelling: covariances and ordinary kriging systems*. in R. Dimitrakopoulos, editor, Geostatistics for the Next Century, Kluwer Academic Publishers, Dordrecht. p. 88-93.

- Dowd, P. A., 1992, *A review of recent developments in geostatistics*. Computers & Geosciences, 17(10), p. 1481-1500.
- Egbert G., and Lettenmaier, D. P., 1986, *Stochastic modeling of the space-time structure of atmospheric chemical deposition*, Water Resources Research, 22(2), p. 165-179.
- Englund, E. V., and Heravi, N., 1993, *Conditional simulation: practical application for sampling design optimization*. In Soares A., editor, Geostatistics Troia '92, p. 613-624.
- Eynon, B. P. and Switzer, P., 1983, *The variability of rainfall acidity*. Can. J. Stat., 11, p. 11-24.
- Farmer, C., 1991, *Numerical Rocks*. In F. Fayers and P. King, editors, The Mathematical Generation of Reservoir Geology, Oxford Univ. Press, New York.
- Gandin, L. S., 1963, *Objective Analysis of Meteorological fields*. Gidrometeorologicheskoe Izdatel'stvo, Leningrad.
- Gelfand, I.M. and Vilenkin, N., 1964, *Generalized Functions 4*. Academic Press, New York.
- Geman, S. and Geman, D. 1984, *Stochastic relaxation, Gibbs distributions and the Bayesian restoration of images*. IEEE Transactions on Pattern Analysis and Machine Intelligence, PAMI-6(6), p. 721-741.
- Gilbert, R.O., 1987, *Statistical Methods for Environmental Pollution Monitoring*, Van Nostrand-reinhold, New York.
- Gomez, H. J., 1992, *Joint sequential simulation of multigaussian fields*. In Soares A., editor, Geostatistics Troia '92, 4 (Suppl. 3). p. 12-18.
- Goovaerts, P., Sonnet, P., and Navarre, A., 1993, *Factorial kriging analysis of Springwater contents in the Dyle River Basin, Belgium*. Water Resources Research, 29(7), p. 2215-2125.
- Granger, C.W.J., 1975, *Aspects of the analysis and interpretation of temporal and spatial data*, The Statistician, 24, p. 197-210.
- Gunst, R.F. and Mason, R.L., 1980, *Regression Analysis and Its Applications*. Marcel Dekker, Inc., New York.
- Haslett, J., Raftery, A.E., 1989, *Space-Time modelling with long memory dependence: assessing Ireland's wind power resource*. Appl. Statist., 38 (1), p. 1-50.

- Issaks, E. and Srivastava, E. H., 1988, *Spatial continuity measures for probabilistic and deterministic geostatistics*. *Mathematical Geology*, 20(4), p. 313-342.
- Issaks, E. and Srivastava, E. H., 1989, *Applied Geostatistics*. Oxford University Press, New York.
- Issaks, E., 1991, *The application of Monte Carlo methods to the analysis of spatially correlated data*. PhD thesis, Stanford University, Stanford, CA.
- Johnson, M. E., 1987, *Multivariate Statistical Simulation*. Wiley & Sons, New York.
- Journel, A.G., 1974, *Geostatistics for conditional simulation of ore bodies*. *Econ. Geol.*, 69, p. 673-687.
- Journel, A.G. and Huijbregts, Ch. J., 1978, *Mining Geostatistics*. Academic Press, London.
- Journel, A.G., 1989, *Fundamentals of Geostatistics in Five Lessons*. American Geophysical Union, Washington, D.C.
- Journel, A.G., 1994, *Modelling uncertainty: some conceptual thoughts*. in R. Dimitrakopoulos, editor, *Geostatistics for the Next Century*, Kluwer Academic Publishers, Dordrecht. p. 30-43.
- Kirkpatrick, S., et al., 1983, *Optimization by simulated annealing*. *Science*, 220(4598), p.671-680.
- Kolmogorov, A. N., 1941, *The distribution of energy in locally isotropic turbulence*. *Dokl. Akad. Nauk SSSR*, 32, p. 19-21.
- Loutfi, H. and Khtira, A., 1992, *Stochastic analysis and generation of synthetic sequences of daily global solar irradiation: Rabat site (Morocco)*. *Renewable Energy*, 2(2), p. 129-138.
- Mantoglou, A., 1987, *Digital simulation of multivariate two and three dimensional stochastic processes with a spectral turning bands method*. *Mathematical Geology*, 19(2), p. 129-149.
- Matern, B., 1960, *Spatial Variation*. Medd. Stens Skogsforskniginst. Swed.
- Matheron, G., 1971, *The theory of regionalized variables and its applications*. Les Cahiers du CMM. Fasc. no. 5, ENSMP, Paris.

- Matheron, G., 1973, *The intrinsic random functions and their applications*. Advances in Probability, 5, p. 439-468.
- Myers, D. E. and Journel A.G., 1990, *Variograms with zonal anisotropies and noninvertible kriging systems*. Mathematical Geology, 22(7), p. 779-786.
- Mejia, J.M., Rodriguez-Iturbe I., 1974, *On the synthesis of random field sampling from the spectrum: an application to the generation of hydrologic spatial processes*. Water Resources Research, 10(1), p. 705-711.
- Neuman, S. P. and Jacobson, E. A., 1984, *Analysis of Nonintrinsic spatial variability by residual kriging with application to regional groundwater levels*. Mathematical Geology, 16(5), p. 499-521.
- Rodriguez-Iturbe, I., Mejia, J.M., 1974, *The design of rainfall networks in time and space*. Water Resources Research, 10(4), p. 713-728.
- Rodriguez-Iturbe, I., Eagleson, P., 1987, *Mathematical models of rainstorm events in space and time*. Water Resources Research, 23(1), p. 181- 190.
- Rouhani, S. and Hall, T. J., 1989, *Space-Time kriging of groundwater data*. in M. Armstrong, editor, Geostatistics, Kluwer Academic Publishers, p. 639-651.
- Rouhani, S. and Myers, D., 1990, *Problems in space-time kriging of geohydrological data*. Mathematical Geology, 22(5), p. 611-623.
- Rouhani, S., Wackernagel, H., 1990, *Multivariate geostatistical approach to space-time data analysis*. Water Resources Research, 26(4), p. 585-591.
- Rouhani, S., et al., 1992, *Multivariate geostatistical trend detection and network evaluation of space-time acid deposition data -I. Methodology*. Atmospheric Environment, 26A(14), p. 2603 - 2614.
- Sarac, C. and Dowd, P.A., 1993, *A modified approach to large scale geostatistical simulation via the decomposition method*. Luma 1993, p. 95-102.
- Solow, A. R. and Gorelick, S. M., 1986, *Estimating monthly streamflow values by cokriging*. Mathematical Geology, 18(8), p. 785-810.
- Steinberg, D., 1974, *Computational Matrix Algebra*. McGraw-Hill Inc. New York.
- Switzer, P., 1988, *Non-stationary spatial correlations estimated from monitoring data*. in M. Armstrong, editor, Geostatistics, Kluwer Academic Publishers, 1, p. 56-67.

- Vanmarcke, E., 1983, *Random Fields: Analysis and Synthesis*. The MIT Press, Cambridge.
- Verly, G., 1993, *Sequential Gaussian co-simulation: a simulation method integrating several types of information*. In Soares A., editor, *Geostatistics Troia '92*, p. 543-554.
- Wackernagel, H., 1988, *Geostatistical techniques for interpreting multivariate spatial information*. in C.F. Chung et al., editors, *Quantitative Analysis of Mineral and Energy Resources*, D. Reidel Publishers, Dordrecht, p. 393-409.
- Waymire, E., et al., 1984, *A spatial theory of rainfall intensity at the meso- scale*. *Water Resources Research*, 20(10), p. 1453-1465.
- Wiener, N., 1949, *Time Series*. MIT Press. Cambridge.
- Yaglom, A. M., 1962, *An Introduction to the Theory of Stationary Random Functions*. Prentice-Hall. Englewood Cliffs.
- Zawadzki, I.I., 1973, *Statistical properties of precipitation patterns*. *J. of Applied Meteorology*, 12, p. 459-472.
- Zhu, H., 1991, *Modeling mixture of spatial distributions with integration of soft data*. PhD thesis, Stanford University, Stanford, CA.